Small Molecule Tools for Structural and Functional Studies of 2OG Oxygenases

Robert K Leśniak

A thesis submitted to the Board of the Faculty of Mathematical, Physical & Life Sciences in partial fulfilment of the requirements for the degree of Doctor of Philosophy at the University of Oxford





Hertford College

Michaelmas Term 2016

Authors Declaration

The work presented in this thesis was conducted at the Chemistry Research Laboratory at the University of Oxford between Michaelmas Term 2012 and Michaelmas Term 2016 under the supervision of Professor Christopher J. Schofield. All the work is my own, except where otherwise stated, and has not been submitted for any other degree at this or any other university.

Robert K Leśniak

January 2017

Small Molecule Tools for Structural and Functional Studies of 2OG Oxygenases

Abstract

Robert Kazimierz Leśniak, University of Oxford, a thesis submitted for the degree of Doctor of Philosophy, Michaelmas 2016

The work described in this thesis focused on members of the $Fe^{(II)}$, 2-oxoglutarate dependent oxygenase family that are involved in the biosynthesis of L-carnitine in mammals and in hypoxia sensing. Work on metallo β-lactamases was also carried out. *N*ε-Trimethyllysine hydroxylase (TMLH) and γ-butyrobetaine hydroxylase (BBOX) catalyse the first and final steps in carnitine biosynthesis, respectively. Chapter 1 provides an overview of the current literature regarding the 2OG oxygenases involved in the biosynthesis of L-carnitine from a therapeutic perspective. A discussion concerning the clinically used inhibitor of carnitine biosynthesis, Mildronate (Meldonium, THP, Met-88), is also included.

In Chapter 2 the stereochemical elucidation of the product of TMLH catalysis as (2*S*,3*S*)-3-hydroxy-*N*ε-trimethyllysine is described. This was achieved via the successful implementation of a silver(I) catalysed asymmetric aldol reaction to obtain (2*S*,3*R*)-3-hydroxy-*N*ε-trimethyllysine which enabled elucidation of the TMLH catalysed product using 1D and 2D NMR spectroscopic techniques.

Chapter 3 explores the use of a ^{19}F labelled cysteine mutant of BBOX from *Pseudomonas sp. AK1* to monitor conformational changes upon ligand binding using ^{19}F NMR spectroscopy. The results validate the use of ^{19}F chemical labelling to monitor ligand binding to 2OG-dependent oxygenases and identifies a potential new class of small molecule inhibitor of BBOX. Synthetic work towards novel BBOX inhibitors is described in Appendix I.

Chapter 4 describes the design and synthesis of novel, broad-spectrum class B metallo β-lactamase inhibitors. The predicted binding modes of the potent mercaptopropionic acid derivative RL368 and its diastereomer RL369 were validated by X-ray crystallography. RL368, in particular, showed superior inhibition to the known inhibitors L- and D-captopril, and, pleasingly displays cell-based potential as an antibiotic following antimicrobial susceptibility assays against Gram negative pathogens of clinical origin; *E. coli*, *E. aerogenes* and *K. pneumoniae*.

Chapter 5 concerns the design, synthesis and implementation of a multifunctional PHD2-selective covalent probe compound RL409, which is aimed at irreversibly binding PHD2. By functionalising a reversibly binding PHD2 inhibitor with electrophilic and photoreactive moieties, it was possible to attach a biotin tag to PHD2 using a copper-free 'click' reaction with the aim to capture PHD2 from cell lysates.

Overall the results provide new insights into metallo-enzyme catalysis and describe new ways to inhibit them.

Acknowledgements

Firstly I would like to thank my supervisor, Professor Christopher Schofield for providing me with support, inspiration and the opportunity to pursue my research interests and further develop a passion for organic chemistry. In addition I would like to thank the British Heart Foundation for providing support for my Dphil research.

The work discussed in this thesis could not have been completed without the help of many co-workers within the University. I am especially grateful to Anna Rydzik and Jürgen Brem for their advice and help on multiple occasions through my time in Oxford. I would also like to thank Suzana Markolovic, James Holt-Martyn, Martine Abboud, Guo-Bo Li, Jacob Bush, Cyrille Thinnes, Duncan Hay, Marina Demetriades, Tzu-Lan Yeh, Roman Belle, David Wang, Klaus-Daniel Umland, Dong Zhang and Hidenori Someya for their invaluable support, guidance and friendship. Furthermore, I would like to thank all members of the Schofield group for promoting a kind, friendly and truly inspirational working environment which has made the lab a great place to work. Wendy Sobey, Adam Hardy and Jenny Houlsby deserve a huge thanks for keeping the lab running as efficiently as possible.

Thanks to the community of Hertford College for providing a supporting atmosphere where I formed many close friendships. Particular thanks should go to Gregory Coussa, Christopher Jones, Oscar Rahnama, Gregory McSweeney, Sangseraima Ujeed, Matthew Collins, Victoria Harsch and Robert Carlsson for making my time in Oxford so memorable.

Most importantly, I would like to thank my parents and my brother for providing love, support and encouragement throughout the last 4 years, and without which I could not have achieved what I have today.

Author contributions

All experiments described within the text were carried out by myself unless otherwise stated. A list of all work carried out by others is given here:

All figures obtained from external sources are used with prior permission.

Chapter 2

Purified recombinant TMLH-MBP fusion protein was prepared by Prof. Kaspars Tars. Derivatisation and LCMS analyses were carried out by Suzanna Markolovic.

Chapter 3

- Mutagenesis, protein mass-spec, and T_m shift data were provided by Dr Anna Rydzik. ^{1}H NMR dual reporter assays were performed by Dr. Amjad Kahn. P-GBB was synthesised by Jos Kamps. Compounds (**12**)-(**19**) were synthesised by Dr. Anna Rydzik.

Chapter 4

Computational work, compound screening and X-ray crystallography were performed by Dr Guo-Bo Li and Dr Michael McDonough. *In vitro* cell-based screening of (**15**) and (**16**) was carried out by Dr Matthew Avison. Synthesis of (**1**) and (**2**), was performed by Dr. Anna Rydzik.

Chapter 5

Compounds (**4**)-(**7**) were synthesised by Dr. Jasmin Mecinovic. MS reaction monitoring of PHD2 with compounds (**4**), (**6**), (**7**) and (**18**) were performed by Dr. Jacob Bush. Western blot experiments were performed by Dr. Tzu-Lan Yeh.

Appendix I

Synthesis of compound (**14**) was performed by Dr. Anna Rydzik.

General Contents

Acknowledgements

Abbreviations

1.0 INTRODUCTION 3

1.1 2-OXOGLUTARATE-DEPENDENT OXYGENASES 3
1.2 2OG OXYGENASES IN LIPID METABOLISM: CARNITINE BIOSYNTHESIS 6
1.3 TMLH AND BBOX 10
1.4 CARNITINE BIOSYNTHESIS IN CARDIOVASCULAR DISEASE 14
1.5 MILDRONATE: FACT OR FICTION? 16
1.6 MILDRONATE AS A MEDICINE: WHAT IS THE CLINICAL EVIDENCE? 22
1.7 THESIS OUTLINE 28
1.8 REFERENCES 30

2.0 THE STEREOCHEMISTRY OF TMLH CATALYSIS 46

2.1 INTRODUCTION: THE FIRST STEP IN CARNITINE BIOSYNTHESIS 46
2.2 β-HYDROXY-α-AMINO ACID SYNTHESIS 48
2.3 PUBLISHED SYNTHESES OF 3-HYDROXYLYSINES 49
2.4 ACCESSING VICINAL AMINO ALCOHOL FRAGMENTS WITH THE ALDOL REACTION 52
2.5 SYNTHESIS OF 3-HYDROXY-N^{ε}-TRIMETHYLLYSINE 54
2.6 (2*S*,3*R*)-3-HYDROXYLYSINE (24) AS A STANDARD FOR AMINO ACID ANALYSIS 65
2.7 DETERMINATION OF THE TMLH PRODUCT 67
2.8 MODELLING OF THE TMLH ACTIVE SITE 75
2.9 SUMMARY AND FUTURE PERSPECTIVES 79
2.10 GENERAL EXPERIMENTAL 81
2.11 NMR MATERIALS AND METHODS 82
2.12 AMINO ACID ANALYSIS 83
2.13 SYNTHESIS 84
2.14 SYNTHESIS OF MOSHER'S ESTERS FOR STEREOCHEMICAL INVESTIGATION OF (51) 94
2.15 SYNTHESIS OF MOSHER'S AMIDES OF (48) 94
2.16 NMR SPECTRA 96
2.17 REFERENCES 99

3.0 ^{19}F NMR STUDIES OF BBOX FROM *PSEUDOMONAS* SP. AK1 110

3.1 INTRODUCTION 110
3.2 ^{19}F LABELLING OF PSBBOX 119

3.3 INITIAL NMR EXPERIMENTS ON PSBBOX* 122
3.4 EFFECTS ON PSBBOX* ^{19}F SIGNAL WITH CO/SUBSTRATES 126
3.5 EFFECTS OF OTHER SUBSTRATES ON PSBBOX*-ZN$^{(II)}$ 134
3.6 EFFECT OF INHIBITORS ON THE PSBBOX*-ZN$^{(II)}$ COMPLEX 139
3.7 SUMMARY AND FUTURE PERSPECTIVES 153
3.8 ACKNOWLEDGEMENTS 158
3.9 MATERIALS AND METHODS 158
3.10 REFERENCES 164

4.0 NOVEL METALLO-β-LACTAMASE INHIBITORS 173

4.1 INTRODUCTION 173
4.2 METALLO-β-LACTAMASE MEDIATED RESISTANCE 174
4.2 BBOX INHIBITORS: BROAD SPECTRUM MBL INHIBITORS? 176
4.3 *IN SILICO* VIM INHIBITOR DESIGN 179
4.4 DISCOVERY OF CAPTOPRIL ANALOGUES 180
4.4 CELLULAR SCREENING 184
4.5 SUMMARY AND FUTURE PERSPECTIVES 185
4.6 ACKNOWLEDGEMENTS 186
4.7 MATERIALS AND METHODS 186
4.8 SYNTHESIS 186
4.9 REFERENCES 194

5.0 DESIGN OF A MULTI-FUNCTIONAL CHEMICAL PROBE FOR PHD2 201

5.1 INTRODUCTION – PHD2 201
5.2 COVALENT CAPTURE OF PHD2 203
5.3 CONJUGATION OF PHD2 WITH RL409 (18) 210
5.4 SUMMARY AND FUTURE PERSPECTIVES 212
5.5 ACKNOWLEDGEMENTS 214
5.6 SYNTHESIS 214
5.7 REFERENCES 219

6.0 SUMMARY 223

APPENDIX I – SYNTHESIS OF NOVEL BBOX INHIBITORS 231

1.1 BBOX INHIBITION 231
1.2 FLUORIDE RELEASE ASSAY 232
1.3 3-HYDROXY-PYRIDINES – AR692B 233
1.4 BBOX ACTIVE SITE MIMETICS 234

1.5 PYRROLO PYRIDINES 237
1.6 TRIAZOLYL PYRIDINES 238
1.7 'METATHESIS' COMPOUND 239
1.8 SUMMARY 240
1.9 EXPERIMENTAL 241
1.10 REFERENCES 258

Abbreviations

2OG	2-oxoglutarate
3HO-TML	3-hydroxy-N^{ϵ}-trimethyllysine
AcOH	acetic acid
AQC	6-aminoquinolyl-*N*-hydroxysuccinimidyl carbamate
ATP	adenosine triphosphate
BBOX	γ-butyrobetaine hydroxylase
BCN	*N*-[(1*R*,8*S*,9*s*)-bicyclo[6.1.0]non-4-yn-9-ylmethyloxycarbonyl]-*N'*-biotinyl-1,8-diamino-3,6-dioxaoctane
BFA	3-bromo-1,1,1-trifluoroacetone
boc	*tert*-butyloxy carbonyl
Bn	benzyl
CACT	carnitine/acyl-carnitine translocase
CAD	coronary artery disease
CAS	clavaminic acid synthase
CAT	carnitine acetyl-transferase
Cbz	carboxybenzyl
CoA	coenzyme A
CODD	*C*-terminal oxygen dependent degradation domain
COSY	homonuclear correlation spectroscopy
CPMG	carr-purcell-meiboom-gill
CPTI	carnitine palmitoyltransferase-I
CPTII	carnitine palmitoyltransferase-II
CV	column volumes
CVD	cardiovascular disease
Da	daltons
DBU	1,8-diazabicyclo[5.4.0]undec-7-ene
DCM	dichloromethane
DIAD	diisopropyl azodicarboxylate
DIPEA	*N*,*N*-diisopropylethylamine
DMAP	4-(dimethylamino)pyridine
DMSO	dimethylsulfoxide
DNA	deoxyribonucleic acid
DPPA	diphenyl phosphoryl azide
d.r.	diastereomeric ratio
DSBH	double-stranded β-helix
EDAC	*N*-(3-dimethylaminopropyl)-*N*-ethylcarboiimide
EDTA	ethylenediaminetetraacetic acid
e.e.	enantiomeric excess
ESI	electrospray ionisation

Et	ethyl
EtOAc	ethyl acetate
EtOH	ethanol
e.r.	enantiomeric ratio
FAs	fatty acids
FPLC	fast protein liquid chromatography
GBB	γ-butyrobetaine
GLUT1	glucose transporter type 1
GLUT4	glucose transporter type 4
HATU	(1-[Bis(dimethylamino)methylene]-1H-1,2,3-triazolo[4,5-b]pyridinium-3-oxid-hexafluorophosphate)
hBBOX	human γ-butyrobetaine hydroxylase
HCl	hydrogen chloride
HIF	αβ-heterodimeric hypoxia-inducible factor
HPLC	high-performance liquid chromatography
HSQC	heteronuclear single quantum correlation
HTMLA	3-hydroxytrimethyllysine aldolase
IA	iodoacetamide
IPNS	isopenicillin N synthase
iPr	isopropyl
IR	infrared
JMJD	jumonji domain-containing
LCFAs	long-chain fatty acids
MBL	metallo-β-lactamase
MBP	maltose-binding protein
Me	methyl
MeCN	acetonitrile
MeOH	methanol
MHz	megahertz
MI	myocardial ischemia
MS	mass spectrometry
MRI	magnetic resonance imaging
M.S.	molecular sieves
MTPA	α-methoxy-α-trifluoromethylphenylacetic acid
m/*z*	mas to charge
NAD	nicotinamide adenine dinucleotide
NDM	new delhi metallo-β-lactamase
NMR	nuclear magnetic resonance
NODD	*N*-terminal oxygen dependent degradation domain
NOG	*N*-oxalylglycine
OCTN2	organic cation/carnitine transporter type 2
PBP	penicillin binding protein

PBS	phosphate buffer
Pd/C	palladium on carbon
PDC	pyruvate dehydrogenase complex
PDK	pyruvate dehydrogenase kinase
PHD2	prolyl hydroxylase domain-containing enzyme 2
Pht	phthalamide
PLOD	pro-collagen lysine 2-oxoglutarate 5-dioxygenase
PLP	pyridoxal-5'-phosphate
ppm	parts per million
psBBOX	bacterial γ-butyrobetaine hydroxylase from *Pseudomonas* sp. AK1
RCM	ring-close metathesis
SBL	serine-β-lactamase
TauD	taurine dioxygenase
^{t}Bu	*tert*-butyl
TEA	triethylamine
TEV	tobacco etch virus
TFA	trifluoroacetic acid
THF	tetrahydrofuran
TLC	thin layer chromatography
TMABADH	4-*N*-trimethylaminobutyraldehyde dehydrogenase
TMAO	*N*-trimethylamine oxide
TML	N^{ϵ}-trimethyllysine
TMLH	N^{ϵ}-trimethyllysine hydroxylase
TOF	time of flight
TRIS	*tris*(hydroxymethyl)aminomethane
UV	ultraviolet
VIM	verona integrin-encoded metallo-β-lactamase
v/v	volume per volume

Chapter 1

Introduction

Contents

1.0 INTRODUCTION 3

1.1 2-OXOGLUTARATE-DEPENDENT OXYGENASES 3

1.1.1 Structural and mechanistic properties of 2-oxoglutarate-dependent oxygenases 3

1.2 2OG OXYGENASES IN LIPID METABOLISM: CARNITINE BIOSYNTHESIS 6

1.2.1 Fatty acid metabolism: the carnitine shuttle 7

1.2.2 Carnitine tissue distribution and biosynthesis 9

1.3 TMLH AND BBOX 10

1.3.1 N^{ε}-Trimethyllysine hydroxylase (TMLH) 10

1.3.2 γ-Butyrobetaine hydroxylase (BBOX) 12

1.4 CARNITINE BIOSYNTHESIS IN CARDIOVASCULAR DISEASE 14

1.5 MILDRONATE: FACT OR FICTION? 16

1.5.1 Biochemical functions of Mildronate: more than just a BBOX inhibitor? 17

1.5.1.1 Mildronate and carnitine biosynthesis enzymes 18

1.5.1.2 Mildronate and carnitine transport enzymes 20

1.5.1.3 Mildronate: effect on enzymes involved in mitochondrial fatty acid metabolism 21

1.6 MILDRONATE AS A MEDICINE: WHAT IS THE CLINICAL EVIDENCE? 22

1.6.1 Cardioprotection 22

1.6.2 Influence on glucose metabolism and diabetes 23

1.6.3 Role in neurological conditions 25

1.6.4 Role in performance enhancement 26

1.7 THESIS OUTLINE 28

1.8 REFERENCES 30

1.0 Introduction

1.1 2-Oxoglutarate-dependent oxygenases

Since the discovery of the first members in the 1960s,[1] the 2-oxoglutarate-(2OG) dependent oxygenase enzyme superfamily has been found to perform a diverse range of biological functions in most aerobic organisms, with the likely exception of archaea.[2,3] Approximately 70 2OG-dependent oxygenases exist in humans and other higher animals with many more predicted to exist in plants.[4,5] The 2OG oxygenases require O_2, 2OG and $Fe^{(II)}$ for activity; in some cases their activity is stimulated by ascorbate.[6,7] They catalyse reactions including hydroxylations, ring expansions, ring closures, desaturations and halogenations amongst others.[2,3] In the context of animals and humans, 2OG oxygenases are at present known to only catalyse hydroxylations and hydroxylation-mediated demethylations. These reactions involve a 2OG-coupled, two-electron oxidation of the substrate in the presence of $Fe^{(II)}$ to give succinate and CO_2 as byproducts.[2,4] Although they often catalyse simple reactions, some 2OG oxygenase mediated transformations are involved in physiologically crucial processes such as fatty acid metabolism, epigenetic regulation and hypoxic sensing.[4,8]

1.1.1 Structural and mechanistic properties of 2-oxoglutarate-dependent oxygenases

The therapeutic potential of the human 2OG oxygenases has promoted studies focused on elucidating their structures and mechanisms; this work has enabled the design of inhibitors of 2OG oxygenases, ultimately aimed at pharmaceutical use.[9-11] The structure of the 'pseudo'-2OG oxygenase isopenicillin N synthase (IPNS) was the first enzyme of the 2OG oxygenase structural superfamily to be crystallised.[12] However, IPNS does not actually utilise a 2OG co-substrate. Crystallographic analysis of IPNS revealed the presence of a double-stranded β-helix (DSBH) fold at its core. Indeed, the DSBH or 'jelly roll' fold, has

been found to be present in all structurally characterised 2OG oxygenases (Figure 1).[4] The DSBH of IPNS (which is closely related to the 2OG oxygenases) was found to support three key iron-binding residues: two histidinyl- and one aspartyl-residues. Subsequently, the HXD/E…H motif was found to be present in most characterised 2OG oxygenases. The DSBH forms two β-sheets formed from eight β-strands. The active-site of 2OG oxygenases is typically found at the more open end of the 'barrel' of the DSBH core and is flanked by at least one α-helix on the *C*-terminal side. Further structural motifs surrounding the DSBH core are more flexible and can be involved in substrate binding. Structural studies on taurine dioxygenase (TauD) and clavaminic acid synthase (CAS) (Figure 1) led to the identification of conserved structural motifs involved in substrate and 2OG binding.[13,14] Notably, residues from the first and second beta-strands of the DSBH, and depending on the specific 2OG oxygenase subfamily, other DSBH strands and flexible loops are often involved in substrate binding.[4,9]

Solution phase mechanistic information regarding the 2OG oxygenases came from

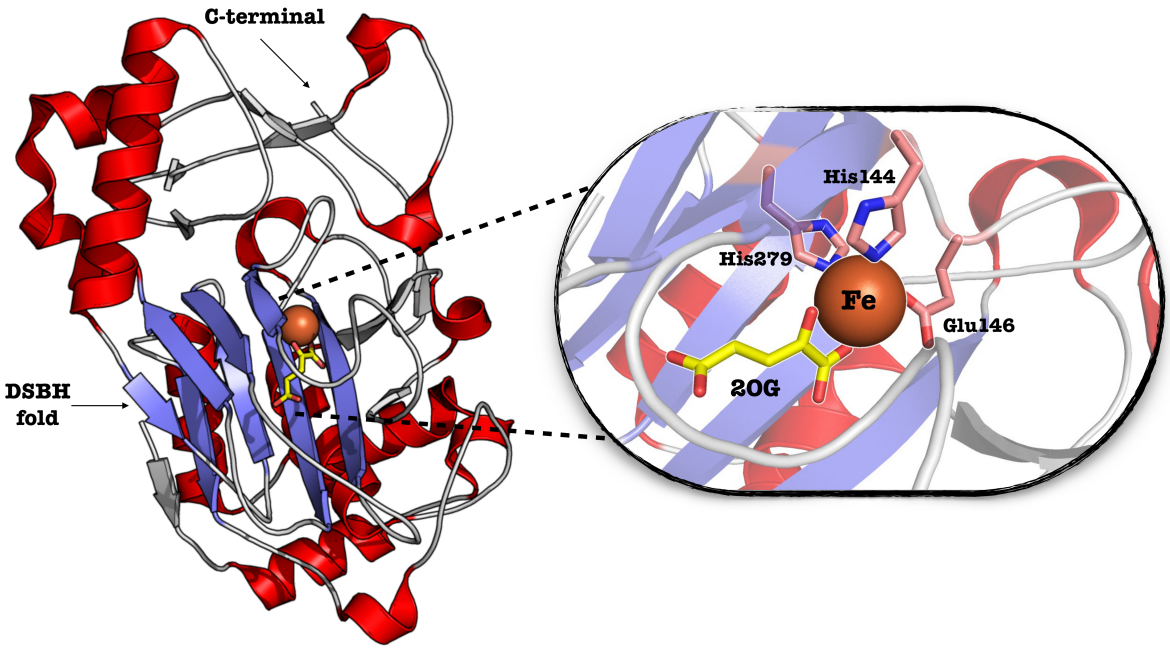


Figure 1 View from a crystal structure of the trifunctional 2OG oxygenase clavaminic acid synthase (CAS) in complex with $Fe^{(II)}$ (orange sphere) and 2OG (yellow sticks). The DSBH, which is characteristic of all 2OG oxygenases, is highlighted in blue; surrounding α-helices are shown in red. Residues involved in the conserved 2OG oxygenase HXD/E…H metal chelating motif are highlighted in the expanded active site view. (peach sticks).

studies on enzymes including TauD and CAS.[13,14] A general mechanism for a 2OG oxygenase catalysed hydroxylation reaction is displayed in Figure 2,[3] where the conserved HXD/E…H motif of the enzyme shown.[12,15,16] The $Fe^{(II)}$ octahedral complex (B) is formed following the 2OG-mediated displacement of two molecules of water from complex (A). 2OG chelation occurs *via* its C-1 carboxylate and C-2 carbonyl oxygens. Complex (C) forms following the loss of a molecule of water as a result of substrate (R-H) binding; subsequently dioxygen binds to the vacant coordination site to give an $Fe^{(III)}$-superoxo species (E).[17] Decaboxylation of 2OG to succinate and CO_2 gives an $Fe^{(IV)}$-oxo intermediate (E), which abstracts a hydrogen from the substrate yielding the $Fe^{(III)}$-hydroxide complex (F). A subsequent radical rebound reaction promotes departure of the hydroxylated substrate (R-OH) and restores the enzyme, to its initial $Fe^{(II)}$ state. Characterisation of the $Fe^{(IV)}$ ferryl species has been achieved using spectroscopic techniques.[18-20] The presence of this intermediate highlights similarities between the 2OG oxygenases and the haem oxygenases,

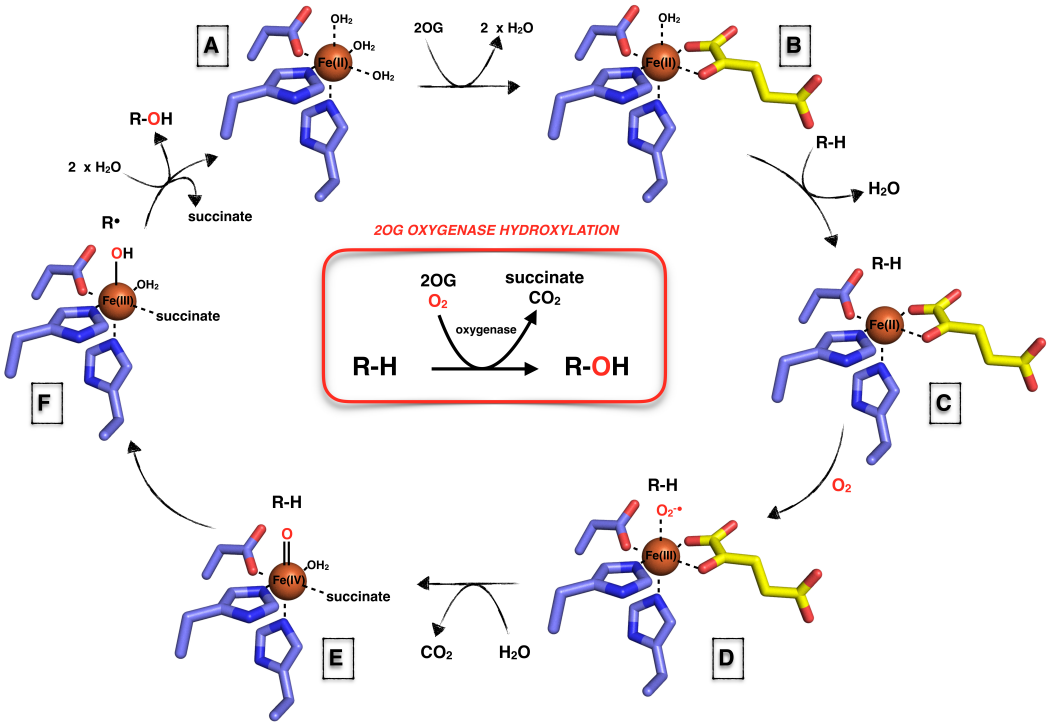
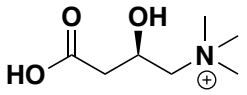


Figure 2 A simplified, general 2OG oxygenase hydroxylation mechanism. One atom of dioxygen is inserted into a substrate (R-H) to give an oxygenated product (R-OH) *via* decarboxylation of 2OG to succinate and CO_2. CO_2 derives from the C-1 carboxylate of 2OG, and the second atom of dioxygen is incorporated into succinate.

which are also proposed to react *via* a radical rebound mechanism.[18-22]

1.2 2OG oxygenases in lipid metabolism: carnitine biosynthesis

Two 2OG dependent oxygenases N^{ε}-trimethyllysine hydroxylase (TMLH) and γ-butyrobetaine hydroxylase (BBOX), catalyse the first and last steps in the biosynthesis of the metabolite β-hydroxy-γ-(trimethylammonio)butyrate, more commonly known as L-carnitine (**1**), in mammals. Carnitine was first isolated from muscle extracts in the early 20th century[23,24] and thus was named after the Latin *carnis* meaning flesh. The structure of carnitine was elucidated in the late 1920s[25] and the stereochemistry of its hydroxyl function was determined to be L-(-) in the 1960s.[26] Since then, the biological functions,[26,27]



L-carnitine (1)

Figure 3 Chemical structure of carnitine.

biosynthesis and the quintessential role of carnitine in mammalian fatty acid metabolism have been well studied.[26-28] Carnitine has been considered as a 'quasi-vitamin' because its endogenous biosynthesis does not always meet the requirements of the human body.[28,29] In animals carnitine was found to accumulate in the heart, skeletal muscle tissue and to a lesser extent in the kidney, brain and testis.[30,31] In humans, 98% of total carnitine is present in muscular tissue.[32] Daily alimentation of carnitine provides around 75% of total carnitine concentration in the human body, with 25% originating from endogenous synthesis. The main dietary sources of carnitine are diary products and red meat, with red meat containing the highest concentrations (~ 80 μg/ 100 g).[28] Recently, the link between red meat consumption and heart disease was proposed to be carnitine mediated (Section 1.4).[33,34] Carnitine supplementation has also been clinically examined as a potential treatment of cardiovascular related diseases (Section 1.4);[35-39] however, there is conflicting evidence regarding its efficacy,[40,41] and further clinical research is required. Treatment of patients with

primary carnitine deficiency with carnitine supplementation (100-300 mg, kg^{-1}, d^{-1}), provides one of only a few clinically validated uses of carnitine as a medical treatment.[42] Carnitine has been reported as an effective treatment in patients with common cancer related fatigue, thought to stem from carnitine deficiency.[43-46]

Carnitine supplementation has also been subject to numerous studies attempting to validate its clinical efficacy and use within the sporting community.[47-49] Carnitine is commonly available as a supplement in the fitness industry,[49,50] with claims of aiding fat loss and boosting athletic performance.[51] However research validating these claims is lacking.[48] The majority of studies investigating the athletic benefit of carnitine supplementation do not provide compelling evidence supporting its use.[51,52]

1.2.1 Fatty acid metabolism: the carnitine shuttle

In humans and other animals, fatty acids (FAs) are predominantly obtained from the diet and are stored as triglycerides.[53] FAs are used as a form of energy storage, because their metabolism, *via* β-oxidation and the citric acid cycle, efficiently yields more energy (adenosine triphosphate, ATP) per gram when compared to other macronutrients, *e.g.* carbohydrates and proteins.[53,54] The prime metabolic function of carnitine is to act as a molecular 'chaperone' in the transport of long-chain fatty acids (LCFAs) across the mitochondrial membrane,[55] from the cytosol to the mitochondrial matrix where most β-oxidation occurs. Carnitine enables the essential transport of acyl-CoA activated long-chain fatty acids *via* formation of acyl-carnitine esters. A schematic representation of this process, known as the 'carnitine shuttle', is displayed in Figure 4. The hydroxyl group of carnitine is crucial to its metabolic function, because it reacts covalently with long-chain acyl coenzyme A (acyl-CoA) activated fatty acids (FAs) to give long-chain acyl-carnitine esters. This process is catalysed by carnitine palmitoyltransferase-1 (CPTI) and is reported as the rate limiting step in FA transport into mitochondria.[56] Long-chain acyl-carnitine transport across

the mitochondrial membrane is completed by the carnitine/acyl-carnitine translocase (CACT).[57,58] Following reaction with carnitine palmitoyltransferase-II (CPTII) the acyl-carnitines are converted to free carnitine and acyl-CoA activated long-chain FAs.[58] Whilst activated FAs are then metabolised for energy production *via* β-oxidation,[59] free carnitine is acted upon by carnitine acetyl-transferase (CAT), which catalyses the reversible transfer of the acetyl group of acetyl-CoA to carnitine.[60-62] Acetyl-carnitine can then be transported back to the cytosol by CACT. The actions of CAT and CACT on acetyl-carnitine, enable the regulation of the cellular acetyl-CoA/CoA ratio,[63] the homeostasis of which, affects glucose metabolism *via* inhibition of the pyruvate dehydrogenase complex (PDC).[64] An increase in the acetyl-CoA/CoA ratio, upregulates pyruvate dehydrogenase kinase (PDK) which catalyses the phosphorylation and consequent inhibition of PDC, which is known to catalyse the rate limiting step in carbohydrate oxidation.[65,66]

Overall, given the role of carnitine in long-chain FA and carbohydrate metabolism, it can be concluded that carnitine plays a crucial role in the regulation of cellular energy production. The roles of carnitine in energy metabolism have promoted the targeting of

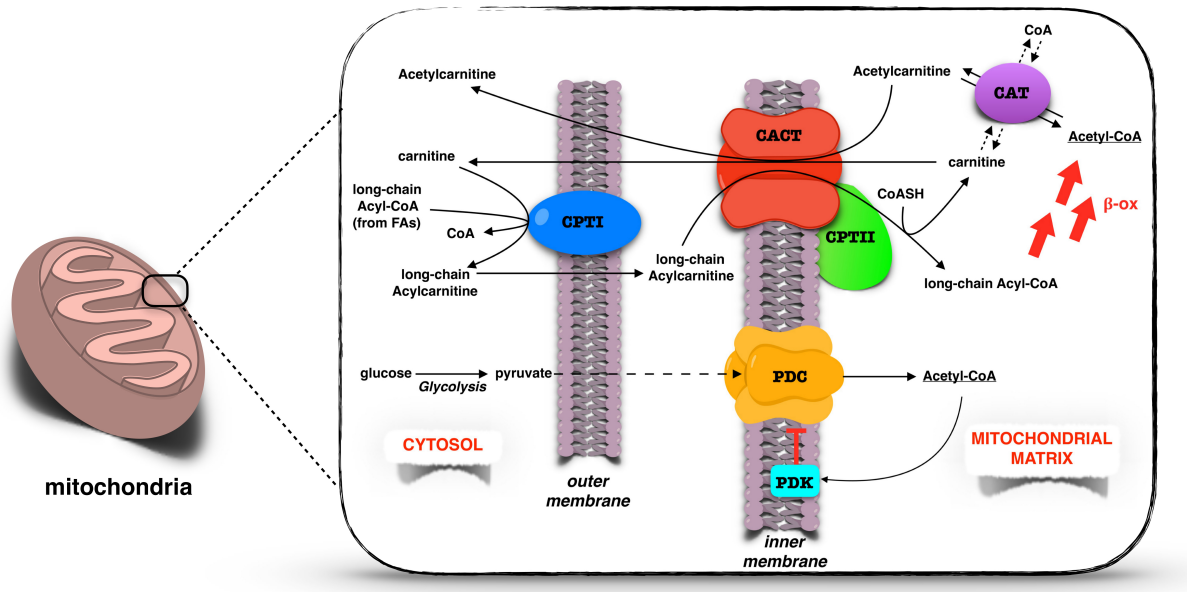


Figure 4 Once transported across the mitochondrial membrane, long-chain FAs provide a source of cellular energy through β-oxidation. Carnitine in the mitochondrial matrix is used to regulate the cellular acetyl-CoA/CoA ratio which inturn affects the rate-limiting step in carbohydrate oxidation, which is mediated by the pyruvate dehydrogenase complex (PDC).

carnitine biosynthesis as a means to therapeutically regulate energy metabolism in the heart as a means to treat cardiovascular diseases (Section 1.4).

1.2.2 Carnitine tissue distribution and biosynthesis

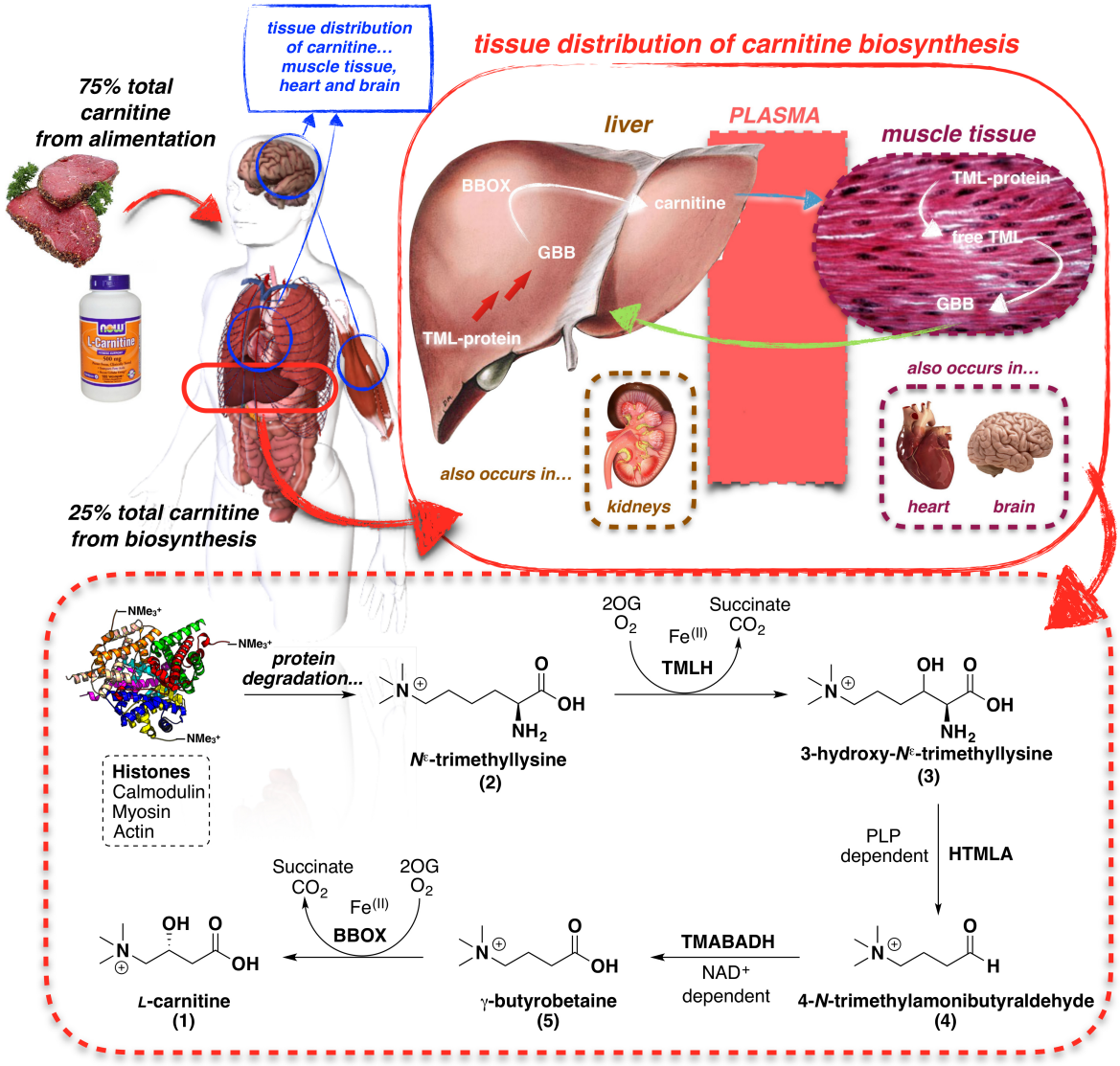


Figure 5 The majority of carnitine in humans is obtained from dietary sources. Carnitine is also synthesised *in vivo via* a highly conserved biosynthetic pathway found in animals. Carnitine accumulates in skeletal and heart muscle tissue, the brain and testis. In humans, the full carnitine biosynthetic pathway occurs in most tissues, excluding the final hydroxylation step (catalysed by the 2OG oxygenase BBOX), which has been found to occur only in the liver and kidneys. From the liver/kidneys, carnitine is transported to other tissues *via* plasma.

Carnitine accumulates predominantly in muscle tissue including the heart, with lower but detectable levels in the brain, kidneys and testis.[30,31] As described above, the majority of carnitine in humans is obtained from dietary sources such as red meat.[33] It is also synthesised *de novo* from lysine[67,68] and methionine[68] in a highly conserved biosynthetic

pathway in animals (Figure 5).[69,70] Steps in the biosynthesis of carnitine are reported to take place in all studied tissues studied in humans, namely the liver, kidneys and skeletal and cardiovascular muscle tissue.[71] An exception is the final step in carnitine biosynthesis, which is catalysed by the 2OG oxygenase BBOX and takes place exclusively in the liver and kidneys.[71]

Biosynthesis of carnitine is initiated by TMLH mediated C-3 hydroxylation of the amino acid N^{ε}-trimethyllsine (TML) (**2**), to give 3-hydroxy-N^{ε}-trimethyllysine (**3**).[72] (**3**) then undergoes cleavage catalysed by the pyridoxal-5'-phosphate dependent (PLP) aldolase, 3-hydroxytrimethyllysine aldolase (HTMLA). This reaction gives 4-*N*-trimethylaminobutyraldehyde (**4**) and glycine.[70] γ-Butyrobetaine (GBB, **5**) is then formed, *via* an NAD^+ dependent dehydrogenase, 4-*N*-trimethylaminobutyraldehyde dehydrogenase (TMABADH).[73] The final step of carnitine biosynthesis is then carried out by the 2OG oxygenase BBOX.[74-76] BBOX catalyses a pro-*R*, C-3 hydroxylation of GBB to give carnitine (**1**).[75]

1.3 TMLH and BBOX

1.3.1 N^{ε}-Trimethyllysine hydroxylase (TMLH)

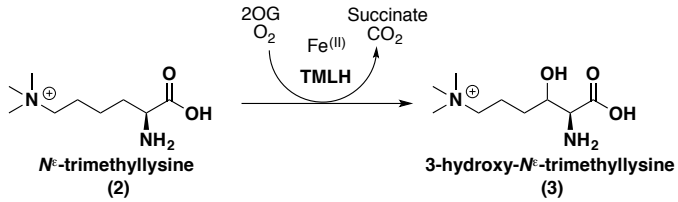


Figure 6 TMLH catalysed hydroxylation of (**2**).

The first step in carnitine biosynthesis is catalysed by the $Fe^{(II)}$, 2OG-dependent oxygenase N^{ε}-trimethyllysine hydroxylase (Figure 6) (TMLH, E.C. 1.14.11.8).[70,72] 3-hydroxy-N^{ε}-trimethyllysine (**3**) is generated *via* TMLH mediated hydroxylation of N^{ε}-trimethyllysine (TML, **2**) (Figure 6), the precursor for caritine biosynthesis.[77] The bioavailability of TML is thought to be a rate-limiting factor in carnitine biosynthesis although its exact origins are not definitively defined.[26] Degradation of proteins containing methylated lysine such as

histones, calmodulin, myosin and actin may act as sources of TML.[78-80] A recent study suggests that TML is found in relatively large quantities in many plant-based foods and therefore might be the primary source of TML in the body.[79] Early studies showed that TML was converted to 4-*N*-trimethylaminobutyraldehyde (TMABA, **4**), and γ-butyrobetaine (GBB, **5**) in rats[81] and isolated liver tissue.[82,83] TMLH activity was observed for the first time in rat liver mitochondria, whereby conversion of TML to 3HO-TML, (**3**) was observed exclusively in the presence of $Fe^{(II)}$, 2OG and ascorbate.[84] The chemical structure of the product of TMLH catalysis was identified as 3HO-TML by the use of chemical and enzymatic analysis.[84] Reacting the TMLH product with periodate or a serine transhydroxymethylase both yielded TMABA (**4**) and glycine as products. To-date the exact stereochemistry of 3HO-TML has not been assigned categorically. However, an attempt was made *via* comparison to enantiopure 3-hydroxylysine standards and 3HO-TML was predicted to exist as the *erythro* isomer *i.e.* (2*S*,3*S*)-3-hydroxy-trimethyllysine.[85]

The liver, kidney, brain, heart and skeletal muscle tissues have all been shown to have TMLH activity (Figure 5).[71,86] TMLH has been reported to reside in the mitochondrial matrix, which is a unique characteristic when compared to the other cytosolic carnitine biosynthesis enzymes.[87] Transport of TML across the mitochondrial membrane has been reported to be a limiting factor in the production of 3HO-TML and thus a TML/3HO-TML transport system may exist.[87] TML availability directly affects the rate of carnitine production,[88] thus regulation of carnitine biosynthesis could be achieved *via* inhibition of a putative TML/3HO-TML transport system. cDNA in rats[72] encoding for a human TMLH homologue was identified and the gene was shown to encode for a protein consisting of 405 amino acids amounting to a weight of 47.5 kDa. However, in solution, TMLH exists as a homodimer with a mass of 87 kDa (the loss in mass has been proposed to be a consequence of mitochondrial transport).[72]

Although no high-resolution structural data of human TMLH has been reported, high sequence similarity between human BBOX and TMLH exists (26%).[75,89] As discussed in Chapter 2, given the availability of hBBOX structural data, BBOX provides a suitable template for TMLH homology modeling. Chapter 2 describes the elucidation of the stereochemical outcome of TMLH-mediated hydroxylation of TML, and given this knowledge it was possible able to manually dock TML into the active site of a TMLH homology model based on hBBOX structural data. TMLH has received considerably less attention when compared to its homologue BBOX, which is surprising given its key biological role in carnitine biosynthesis. Moreover, impairments in carnitine biosynthesis and higher TML levels were observed as a result of mutations in the TMLH gene.[90] TMLH gene mutations have been linked to autism,[91,92] especially in the male population given its location on the X chromosome.[90]

1.3.2 γ-Butyrobetaine hydroxylase (BBOX)

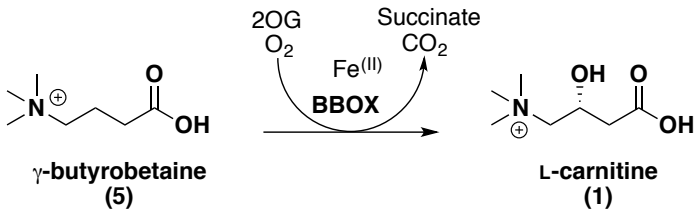


Figure 7 BBOX catalysed hydroxylation of GBB (**5**)

The conversion of γ-butyrobetaine (GBB, **5**) to L-carnitine is catalysed by γ-butyrobetaine hydroxylase (BBOX, E.C. 1.14. 11.1) (Figure 7).[75,93] Similarly to TMLH, BBOX is a member of the 2OG-dependent oxygenase superfamily, requiring $Fe^{(II)}$, 2OG and molecular oxygen for activity.[75] BBOX was first isolated from rat[94] and calf liver[95] and human kidneys.[96] Subsequently, BBOX activity in humans has been found to take place in (at least) the kidney, liver, and at low levels, in the brain (Figure 5).[59] Human BBOX (hBBOX) is

comprised of 387 amino acids,[76] which amounts to a 44.7 kDa protein and similarly to TMLH was found to exist as a homodimer in solution.[97 98]

A crystal structure of hBBOX in complex with GBB (**5**), *N*-oxalylglycine (NOG, a non-reactive 2OG analogue) and $Zn^{(II)}$ (a non-reactive $Fe^{(II)}$ replacement) was solved within the Schofield group (PDB id: 3O2G) (Figure 8).[75] The obtained structure revealed a hBBOX homodimer, in support of the previously observed[98] hBBOX dimerisation in solution. Characteristic structural motifs of 2OG-oxygenases were observed, including a *C*-terminal DSBH fold, along with a HXD…H active-site metal chelating motif (His202, Aps204, His347). In contrast to other members of the 2OG-oxygenase family hBBOX dimerises through its *N*-terminal domain. Moreover, the *N*-terminal domain was found to possess a $Zn^{(II)}$ binding site involving Cys38, Cys40, Cys43 and His 82 as zinc chelating residues. The prime substrate, GBB, binds adjacent to the active site $Zn^{(II)}$ ion, and adopts a conformation that allows for a C-3, pro-*R* hydroxylation to take place to give (2*R*)-L-carnitine. The quaternary ammonium moiety of GBB is flanked by aromatic residues, Trp181, Tyr 194 and Tyr177, that form an 'aromatic cage' (Figure 8), thought to be highly involved in substrate

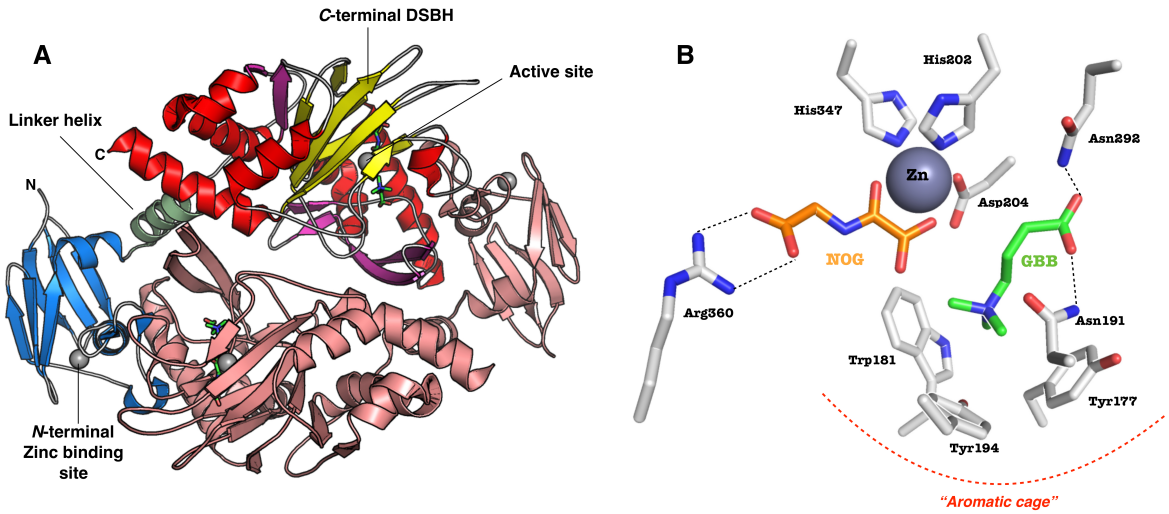


Figure 8 Two views from a crystal structure of hBBOX in the presence of GBB, NOG and $Zn^{(II)}$ (PDB id: 3O2G). **A**) A view of a crystal structure of homodimeric hBBOX. One monomer is represented as a cartoon, coloured according to various structural motifs, and the other monomer is highlighted as a pink cartoon. **B**) Enlarged and simplified view of the active site of hBBOX, with important metal and co/substrate binding residues highlighted as white sticks. GBB and NOG are highlighted as green and orange sticks respectively.

recognition. The carboxylate of GBB interacts with two asparagine residues (Asn191 and Asn292). The inactive co-substrate *N*-oxalylglycine (NOG), binds adjacent to GBB, with the C-1 and C-2 carbonyl oxygens allowing for bidentate chelation of the active site zinc. As with other 2OG-oxygenases, an arginine residue (Arg360) interacts with the C-5 carboxylate of NOG, and by implication, 2OG.

1.4 Carnitine biosynthesis in cardiovascular disease

Myocardial ischemia (MI) belongs to a group of cardiovascular diseases (CVDs) commonly known as coronary artery diseases (CADs). CADs are a common cause of mortality in the western world.[99] MI occurs as a result of decreased blood flow to the heart, usually as a result of atherosclerosis, which in turn reduces local oxygen concentration towards anoxia.[100] Heart tissue, under such ischemic conditions, can be permanently damaged and therefore significantly affects the ability of the heart to pump efficiently, leading to cardiac arrest, heart failure and irregular heartbeat. A notable trait of MI is altered cellular energy metabolism, whereby the tightly regulated homeostasis between fatty acid and glucose metabolism is altered.[101] Under anoxic conditions resulting from MI a shift in cellular energy homeostasis towards glucose metabolism occurs, probably to aid in the recovery of damaged heart tissue.[101,102] This shift is proposed to arise from the lower oxygen requirement per ATP molecule generated, in glucose compared to FA metabolism.[101] Interestingly, anoxia induced by MI has been linked to depletion of carnitine.[103-105] Consequently long-chain FA ester metabolites (free, acyl-CoA and acyl carnitine FAs) which are toxic to mitochondria,[64] are reported to accumulate as a result of decreased FA metabolism *via* β-oxidation in mitochondria.[104] The lack of carnitine is also reflected in the decreased ATP concentration in heart tissue during MI.[103] Direct carnitine supplementation as a means to alleviate the sudden decreased carnitine levels observed with some CVDs, is reported to be an effective treatment in ischemic heart disease.[38] However, some reports in the literature

describe no beneficial effect following carnitine treatment of cardiometabolic disorders.[106] Recently, the excessive consumption of red meat in the developed world has been linked to increasing rates of CVD.[33,107] Originally an increased risk of CVD was thought to be a result of the high saturated fat and cholesterol content of red meat.[108,109] However, it has now been suggested that the high levels of carnitine in red meat may be the cause. In a recent study human subjects were given a diet containing red meat or a diet supplemented with isolated carnitine.[33] Subjects ingesting red meat or carnitine supplements produced significantly more *N*-trimethylamine oxide (TMAO) than control groups.[33] Furthermore, using heavy isotope d_3-labelled carnitine it was also shown that the quaternary ammonium group of TMAO is obtained from ingested carnitine.[33] This study is important as high concentrations of TMAO in the blood can lead to atherosclerosis and an increased risk of CVD.[33,107]

Promoting a shift in cellular energy preference towards glucose metabolism in the failing heart is reported to be beneficial in recovery after heart failure, in both the short and long term.[102,110] The regulation of the preferred cellular energy use in the failing heart has been achieved *via* inhibiting FA metabolism, by interfering with FA transport into mitochondria.[64,101,111] Thus, given carnitine plays an essential role in the regulation of energy production in cardiovascular tissue, its biosynthesis has been targeted as a means to therapeutically manipulate preferred cellular energy metabolism for the treatment of MI and CVD. The only clinically used inhibitor of carnitine biosynthesis currently used is Mildronate.[112]

1.5 Mildronate: fact or fiction?

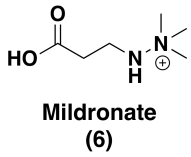




Figure 9 The chemical structure of the drug Mildronate, manufactured by the Latvian pharmaceutical company Grindex.

Mildronate (**6**) (Meldonium, Met-88, THP), which is manufactured by the Latvian pharmaceutical company Grindex (Figure 9), is a clinically used drug in Eastern Europe.[64,112,113] Mildronate is the subject of numerous, albeit small, clinical trials with regards to its purported anti-ischemic and cardioprotective properties.[64,114,115] Outside of its application in treaing CVDs, multiple claims have been made regarding its application towards treating health conditions such as diabetes[116] and neurodegenerative diseases.[117,118] Mildronate has received considerable media attention recently, following its abuse in high-profile sports.[113]

Mildronate was developed by Ivars Kalviņš in research supposedly aiming to exploit excess Soviet hydrazine which is used as a rocket fuel.[119,120] The work was carried out in the 1970s at the Latvian Institute for Organic Synthesis.[113] Latvia was then known as the Latvian SSR, and as such early clinical data for the drug is near impossible to obtain. However, according to the patent literature its original applications were in agricultural and veterinary.[121] Mildronate is apparently able to control growth in plants whilst potentiating growth in animals.[121] Interestingly in 2009, in an interview with the Latvian news paper Diena, Kalviņš identified alternate uses of Mildronate.[122] Kalviņš stated that Mildronate was frequently used by soviet army personnel for training at high altitude, although clinical

evidence from that era is likely very difficult to obtain.[119,120,122,123] Klintsevich Franz, head of the Russian Union of Afghan veterans stated in an interview with Russian media, that Mildronate was used by Soviet Special Forces before dangerous engagements.[120,124]

Mildronate has received considerable attention in the media, following its recent classification as a "hormone and metabolic-regulator" by the World Anti-Doping Agency (WADA).[125] Mildronate was classified as a performance enhancer as a result of a year-long monitoring program carried out by WADA, attempting to eludicate the prevalence of Mildronate in doping controls.[126,127] The prevalence of Mildronate was substantial, as highlighted by a study contributing to the WADA monitoring program, where a high number of athletes competing in 15 out of 21 sports at the 2015 Baku European Games, including 13 medallists, tested positive for Mildronate.[127] A few months following Mildronate's appreance on the WADA prohibited list, in April 2016, 172 athletes (almost all of Russian origin) including the former world No.1 tennis player Maria Sharapova, tested positive for the Mildronate.[128,129]

Mildronate can be obtained in Azerbaijan, Belarus, Georgia, Kazakhstan, Kyrgyzstan, Latvia, Moldova, Urkraine, Uzbekistan and Russia, as a prescribed and registered drug for human therapeutic use.[127,130] The typical daily dose of Mildronate is between 0.5-1.0 g and can be administered orally or intravenously.[130] Regardless of its widespread medical use in Eastern Europe and in the sporting world, definitive data supporting the use of Mildronate in either clinical or sporting contexts is scarce.[112,113] Furthermore, to-date clear clinical evidence for the application of Mildronate as a 'first-line' medication is lacking.[112,113]

1.5.1 Biochemical functions of Mildronate: more than just a BBOX inhibitor?

Although numerous biochemical functions of Mildronate have been reported in the literature the overall evidence implies Mildronate performs two (at least) roles; *i.e.* it (1) perturbs the cellular energy metabolism towards glucose oxidation, lowering the cellular oxygen

requirement, and (2), it reduces accumulation of free, long-chain acyl-CoA and acyl carnitine FAs which can be toxic in large amounts (Section 1.4). The latter is achieved by potentiating peroxisomal FA metabolism and mitochondrial free FA oxidation.

1.5.1.1 Mildronate and carnitine biosynthesis enzymes

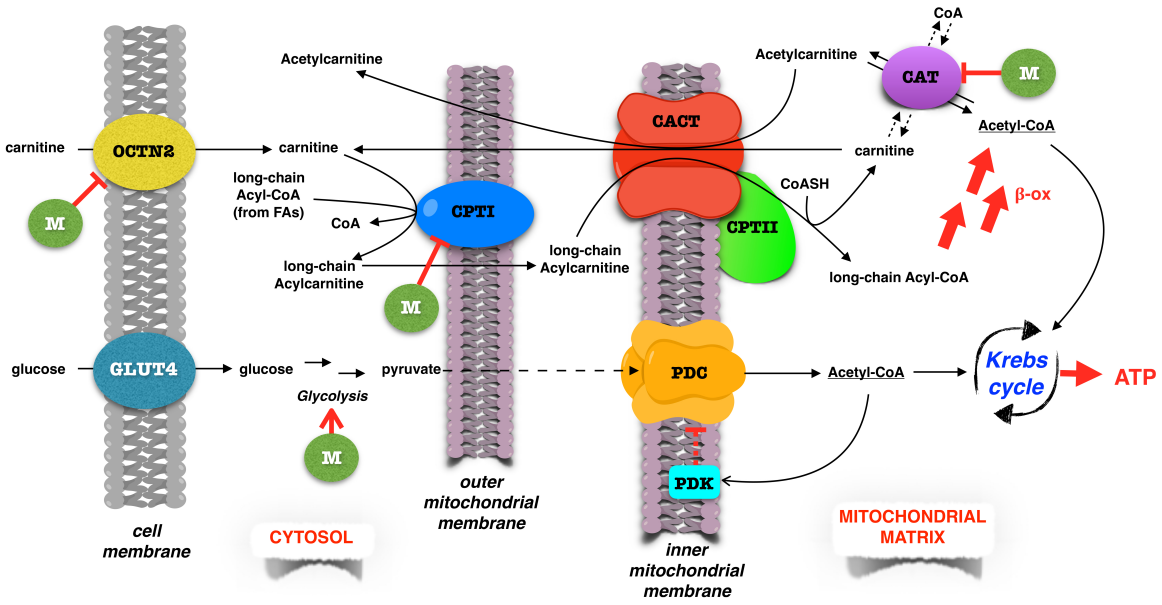


Figure 10 Schematic representation of the enzymology involved in carnitine and glucose uptake and its role in cellular energy metabolism. The points at which Mildronate (**6**) (green circles) has an inhibitory or upregulatory activities are highlighted. Mildronate is a substrate and an inhibitor of BBOX and has also been shown to interact with proteins involved in carnitine transport and FA metabolism in cells, namely OCTN2, CPT1 and CAT.

Mildronate (**6**) has been shown to be an inhibitor of carnitine biosynthesis, 2OG-oxygenase, BBOX, which catalyses the final step in the biosynthesis of carnitine in animals (Section 1.2 and Figure 5).[111,131] As such, Mildronate decreases the local concentration of carnitine and is able to affect cellular energy pathways.[64] Key interactions of Mildronate with mitochondrial enzymes are shown in (Figure 10). BBOX inhibition by Mildronate was initially observed in rats (K_m = 37 μM, K_i = 16 μM, IC_{50} = 13-18 μM),[94,131] with a consequent reduction of carnitine levels by 64%.[111] Following the characterisation of human BBOX (hBBOX),[98] Mildronate was also found to be an inhibitor of hBBOX (K_i = 19 μM,[132] IC_{50} = 34-62 μM[75,98]). Work within the Schofield group identified Mildronate as a competitive substrate

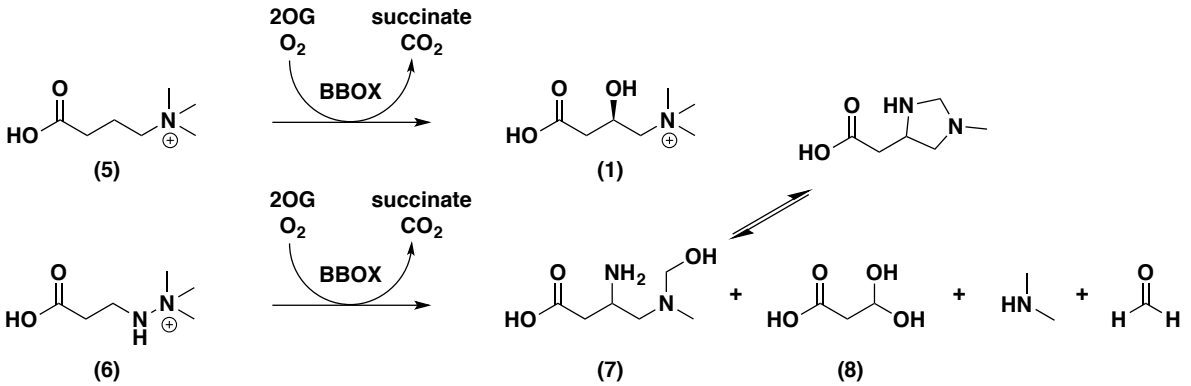


Figure 11 GBB (**5**) and Mildronate (**6**) have been shown to be substrates for hBBOX. Whilst BBOX catalyses a pro-*R*, C-3 hydroxylation of GBB to give carnitine, *N*-demethylation and radical rearrangement reactions occur with Mildronate.

for hBBOX (Figure 11).[75] Mildronate reacts with hBBOX *via* an unprecedented radical rearrangement mechanism to give compunds (**7**) and (**8**) as products with dimethylamine and formaldehyde as lower level 'co-products' (Figure 11).[75] A crystal structure of hBBOX in complex with Mildronate has been solved (PDB id: 3MS5);[75] Mildronate is observed to bind in a near-identical fashion to that observed with GBB (Figure 12). All key metal and co/substrate binding residues are maintained and support the observed reactivity of Mildronate with hBBOX. Interestingly, although the first enzyme in carnitine biosynthesis, TMLH (Section 1.2), has a high sequence similarity to hBBOX (26%),[75] Mildronate does not inhibit rat[133] or human TMLH.[134] Furthermore, Mildronate addition does not affect

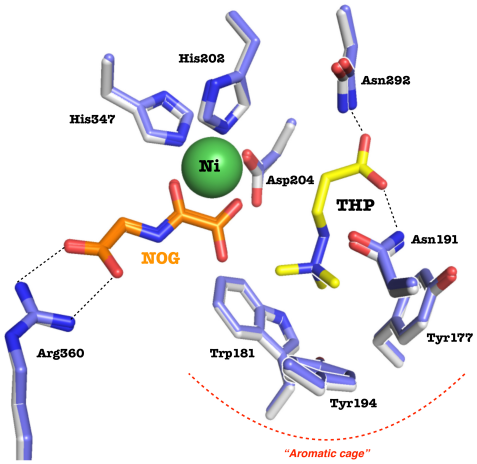


Figure 12 A view from a crystal structure of hBBOX (blue sticks) in complex with $Ni^{(II)}$(green sphere), NOG (orange sticks) and Mildronate (**6**)(yellow sticks) (PDB id: 3MS5). Mildronate can be seen to bind in a near-identical fashion to GBB (**5**)(**Figure 8**). Overlaid residues involved in binding of metal, NOG and GBB are highlighted as white sticks (PDB id: 3O2G).

expression of any of the carnitine biosynthesis genes in rats.[133]

1.5.1.2 Mildronate and carnitine transport enzymes

In the late 1990s it was discovered that Mildronate inhibits carnitine transport in mouse kidneys to a significantly higher extent than in isolated myocytes (K_i = 52 μM vs K_i = 1340 μM respectively).[135] The ability of Mildronate to lower carnitine concentrations, and hence function as a cardioprotective agent, was therefore attributed, at least in part, to the inhibition of carnitine reabsorption at the kidney, increasing carnitine clearance.[135] This observation was supported by a later study, again in rats, where an increased excretion of carnitine *via* urine was observed using ^{13}C-labelled carnitine following Mildronate administration.[136] Mildronate was subsequently found to be an inhibitor of the organic cation/carnitine transporter type 2 (OCTN2, K_i = 41 μM, Figure 10)[131] in rats. OCTN2 plays a key physiological role in the human heart, given carnitine is not biosynthesised in the heart, the active transport of carnitine by OCTN2 and others from plasma is required.[137] Mutations in the OCTN2 gene result in severe cardiomyopathy.[137] A recent study in rats reported that inhibition of OCTN2 by Mildronate was a method of reducing carnitine concentration in heart tissues; and a 35% reduction of the myocardial infarction size of isolated rat hearts was observed.[138] The same study also reported the inhibition by Mildronate of carnitine transport into human embryonic kidney cells (HEK293, producing OCTN2 but not synthesising carnitine) by several OCTN2 selective Mildronate analogues.[138] This study supported the observations that Mildronate can compete with carnitine for the carnitine transporter OCTN2.[131] Further studies also confirmed the efficacy of Mildronate for OCTN2 in human 293 and MDCK-II cell lines (K_m = 26 μM[139] and EC_{50} = 21 μM[140] respectively).

1.5.1.3 Mildronate: effect on enzymes involved in mitochondrial fatty acid metabolism

Carnitine palmitoyltransferase-1 (CPT1) catalyses the carnitine-dependent formation and subsequent transport of acyl-carnitine FAs across the outer mitochondrial membrane (Figure 10);[64] this is the rate-limiting step in the transfer of FAs.[56] CPT1 was not shown to be directly inhibited by Mildronate in rats. An increase in CPT1 gene expression[141,142] was observed although CPT1 activity decreased by 25%;[136] the latter was attributed to decreased availability of carnitine due to the interactions of Mildronate with carnitine biosynthesis enzymes.[64] The reduction of CPT1 activity can be expected to lead to the accumulation of long-chain FA oxidation intermediates, which cannot be transported into mitochondria, as a result of a reduced carnitine concentration (Figure 13).[111,114] However, under ischemic conditions, overall cardiac FA oxidation was shown to be unaffected following Mildronate treatment as a result of potentiation of FA oxidation by peroxisomes.[142,143] Peroxisomal FA oxidation, metabolises long-chain FA intermediates to short and medium-chain acylcarnitines, which can be transported into mitochondria (Figure 13).[64] Thus, Mildronate-induced potentiation of peroxisomal FA oxidation (*via* lowering of local carnitine

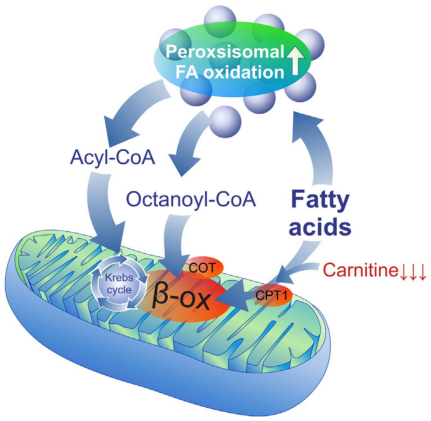


Figure 13 Accumulation of long-chain FA intermediates that cannot be metabolised by mitochondria occurs due to the reduction in local carnitine concentraion following Mildronate administration. Peroxisomal FA oxidation is upregulated as a result of Mildronate-induced re-direction of FA intermediates to peroxisomes. Following peroxisomal oxidation to short- and medium-chain FAs can be transported into mitochondria *via* other transporters such as carnitine-*O*-octanoyltransferase (COT). The shorter chain-FA intermediates can now be metabolised *via* β-oxidation in the mitochondiral matrix. The overall effect of Mildronate on FA oxidation is a protective one, preventing build-up of long-chain FA intermediates. *Figure obtained from Dambrova, et al.*[64]

concentration) has been proposed as one of its cardioprotective biochemical functions.[114,143]

Mildronate was shown to be a poor inhibitor of isolated CAT (K_i = 5.2 mM),[144] the carnitine dependent enzyme responsible for the maintenance of cellular acetyl-CoA/CoA homeostasis (Figure 10). However, CAT inhibition by Mildronate was not observed in rat heart tissue.[136]

Mildronate was found to be a weak, competitive inhibitor of the carnitine translocase CACT (K_i = 530 μM),[145] which transports carnitine and acylcarnitine activated FAs across the inner mitochondrial membrane (Figure 10).[146,147] It was also reported that CACT can also transport Mildronate and enables its interaction with other mitochondrial enzymes such as CAT.[145]

1.6 Mildronate as a medicine: what is the clinical evidence?

1.6.1 Cardioprotection

Since the discovery of the apparent cardioprotective properties of Mildronate,[111,148] multiple studies have been published in apparent support of this observation in healthy and diabetic rats.[136,149-152] The observed cardioprotective effects of Mildronate have been largely attributed to the Mildronate-induced reduction of FA metabolism and increase in glucose metabolism.[114] Although other studies exist linking Mildronate-induced cardio-protection to additional factors, such as its potentiation of nitric-oxide synthase (enzyme involved in proper cardiac function) *via* increasing GBB concentration[153,154] and its involvement in Ca^{2+} re-uptake.[155] The prime substrate of BBOX, GBB (Section 1.3.2), is also known to reduce endothelial dysfunction in animal models of atherosclerosis and hypertension.[153,156,157] As mentioned in Section 1.5.1.3, Mildronate is reported to be transported into mitochondria *via* CACT (Figure 10).[145] This is another way Mildronate is proposed to act as a cardio-protectant; preventing the reduced production of the sarcoplasmic reticulum Ca^{2+}-ATPase

(SERCA) under ischemic conditions, and thus preventing a reduced Ca^{2+} uptake.[149,155,158] This is important as Ca^{2+} ions are essential to cardiac tissue for ensuring the efficient coupling between cardiac excitation and contraction and at low Ca^{2+} concentrations increase the risk of damage to heart tissue.[159]

Mildronate has been involved in clinical trials for treatment of myocardial ischemia (MI),[64,160-170] where it was observed to provide multiple beneficial outcomes *i.e.* (1) high blood pressure reduction, proposed to be *via* lowering of peripheral arterial resistance, (2) decreased pressure of the pulmonary artery, (3) myocardial dilation and hypertrophy inhibition and (4) improved left and right ventricular systolic function. Although these clinical trials show some positive results, most are published in the Russian language. Those written, at least in part, in English do not provide sufficient evidence, which would be required by trials conducted in Western countries.[112,113] Overall, it would seem that the body of evidence supporting the therapeutic potential of Mildronate to treat CVDs is inadequate. The lack of clinical evidence has not, however, resulted in a reduced rate of the prescription of Mildronate in Eastern Europe where it is clinically used in Latvia, Lithuania, Russia, Ukraine and Georgia, for the treatment of patients with stable angina.[112]

1.6.2 Influence on glucose metabolism and diabetes

As mentioned in Section 1.6.1, a Mildronate-induced reduction of carnitine concentration is proposed to prevent the accumulation of long-chain acyl-carnitines under ischemic conditions.[143] Long-chain acyl-carnitine concentration has been suggested to have an effect on glucose/fatty-acid oxidation homeostasis[171] and an increase in long-chain acyl-carnitine concentration has been implied in cellular diabetic phenotypes.[172,173] Consequently, given Mildronate's effect on acyl-carnitine concentration, the downstream effect on glucose metabolism and its potential as a novel diabetic treatment have been studied.[64,112]

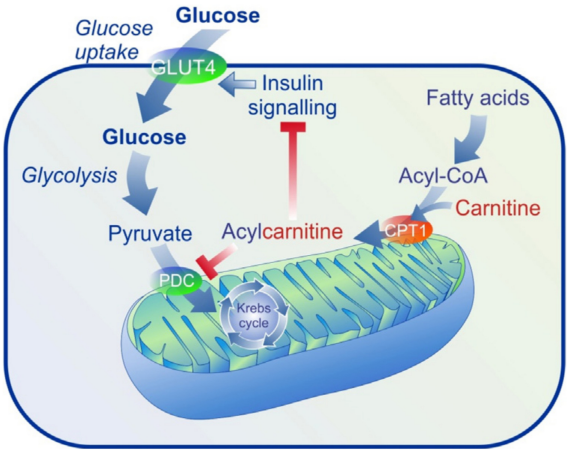


Figure 14 Acyl-carnitines play a key role in the regulation of glucose uptake by mitochondria. Accumulation of long-chain acyl-carnitines can inhibit insulin signalling and hence reduce glucose transporter type 4 (GLUT4) activity. A build-up of acyl-carnitines is also associated with preventing glucose metabolism via inhibition of the pyruvate dehydrogenase complex (PDC). *Figure obtained from Dambrova, et al.*[64]

An increase in long-chain acyl-carnitines in cellular diabetic phenotypes is thought to result from an acyl-carnitine mediated reduction of glucose metabolism.[172,173] This is achieved *via* decreased pyruvate dehydrogenase complex (PDC)[171] and glucose transporter type 4 (GLUT4)[172] activity (Figure 10 and Figure 14). Following a 20-day treatment of isolated rat hearts with Mildronate, an increase in expression of glucose transporter type 4 (GLUT4), (Figure 10 and Figure 14) and the insulin receptor protein was observed.[141] This is associated with the lowering of long-chain acyl-carnitine concentration by Mildronate.[141,174] Therefore, Mildronate treatment is suggested to restore a balance between FA and glucose metabolism,[175] stemming from a lowering of carnitine concentration, as a novel means to treat diabetes.[175]

Although concrete clinical evidence is lacking for patients with diabetes, Mildronate has been reported to provide beneficial effects on type 2 diabetes mellitus animal models such as a decreased blood glucose concentration and an improved glucose tolerance.[152,176,177] Glucose tolerance is achieved *via* reduction of glycated haemoglobin and normalising the expression of the glucose transporter 1 (GLUT1) gene.[177] Mildronate supplementation of human and mouse models showed a reversal of insulin resistance induced by high acyl-carnitine concentration.[172] This is important given fluctuation in FA β-oxidation occurs in

patients with diabetes type 2 mellitus.[178] This is proposed to be a result of accumulation of acyl-carnitines which induce mitochondrial dysfunction (Section 1.5.1.3).[178]

1.6.3 Role in neurological conditions

Via its primary involvement in mitochondrial carnitine transporters (*Section* 1.5.1, Figure 10) and nerve cell protein expression, Mildronate is proposed to be beneficial as based on various studies using animal models of neuroregeneration, neuroinflammation, and apoptosis.[179-185] Following Mildronate administration in animal models of ischaemic brain damage, improved brain function[186] and protection against anoxia-reoxygenation was observed.[187] Benefits in memory and learning capabilities have also been observed following Mildronate treatment in rats.[183,188]

Treatment of oxidative brain damage with carnitine supplementation has been reported, with carnitine supposedly acting as a free-radical scavenger.[189] Interestingly, much of the positive effects of Mildronate on neurological conditions have been attributed to its structural similarity to carnitine, rather than its inhibitory action on carnitine biosynthesis.[112,182] High concentrations of Mildronate have been suggested to reduce local carnitine concentrations *via* a negative feedback mechanism, acting as a 'false carnitine'.[182] Given that there is a significantly lower level of BBOX activity in the brain compared to other organs such as the kidneys and liver, inhibition of BBOX by Mildronate most likely plays an insignificant part in the effects of Mildronate on neurological diseases, as based on the model research. This may explain why Mildroante has been proposed as a replacement treatment for carnitine,[182] rather than as an inhibitor of carnitine biosynthesis in the brain. In summary, although a significant amount of speculation persists with regards to the application of Mildonrate to neurological disorders such as Parkinson's disease, human clinical trials are non-existent and further studies are required to validate the numerous claims.[112,113]

1.6.4 Role in performance enhancement

It is generally accepted that a shift from FA metabolism to glucose metabolism is observed during intensive bouts of exercise;[190,191] oxidation of carbohydrates has a lower oxygen demand per molecule of ATP produced than FA metabolism.[53,54] As mentioned in Section 1.2.1, carnitine is thought to play a key role in FA oxidation in muscular tissue. Carnitine is reported to regulate the transition of FA to glucose oxidation following the increase from moderate (~65% VO_{2max}) to high intensity exercise (>65% VO_{2max}) in working muscles.[191,192] Consequently, the use of carnitine supplementation to improve physical performance has been studied, with both positive and non-effective results reported.[51,52,193,194] However, the efficacy of carnitine supplementation in improving muscular endurance and energy metabolism during physical exercise remains uncertain.[51,112]

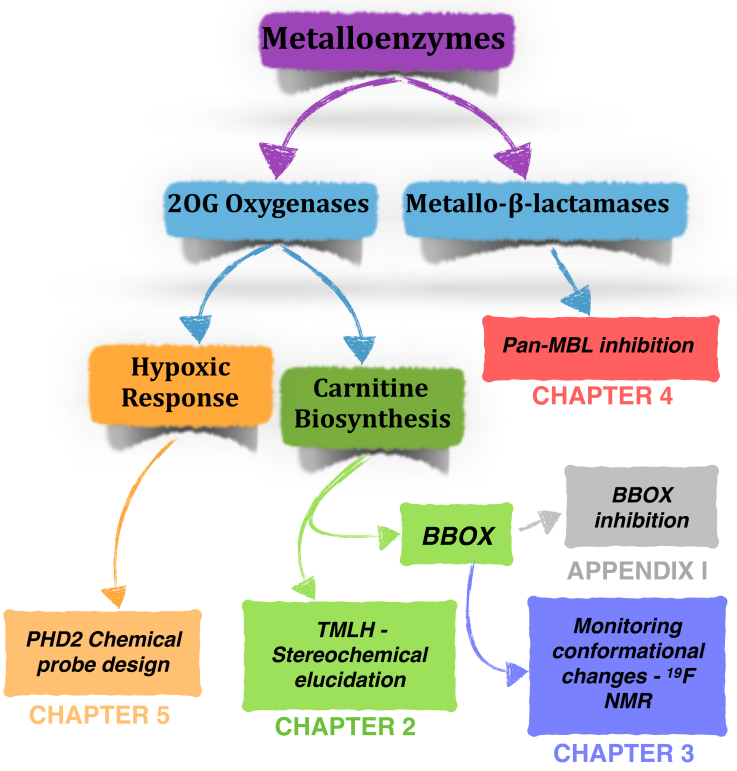
The overall literature implies that the available clinical data, reporting on the ability of Mildronate to improve physical performance in healthy or athletic individuals, is ambiguous. The effect of Mildronate supplementation (250 mg per day for 20 days) on 7 Georgian Judo athletes was conducted in 2002.[195] The results revealed improvements in their physical working capacity using judo-specific mixed aerobic-anaerobic tests. Although the trials reported good results, with an apparent increase in physical capacity, the study remains ambiguous for several reasons (only 7 athletes were screened and no clear description of the exercise tests used is provided). Mildronate was shown more recently to improve the physical working capacity of rats.[196] Following completion of a forced swimming test when compared to control groups, overall 'recovery rate' and 'performance' was shown to be improved by 65% and 49.4% respectively.

Overall the published evidence in the scientific literature is inconclusive on the use of Mildronate as a performance-enhancing drug in healthy or athletically trained individuals.[112,127] However, since its ban by WADA,[125] the number of athletes testing

positive for Mildronate has increased, primarily as a result of the discovery of its prolonged residency in red blood cells.[118] Numerous clinical studies assessing the short-term pharmacokinetics of Mildronate, reported the blood plasma elimination half-life ($t_{1/2}$) to be between 6-18 hours.[111,197-200] However a recent pilot study provided evidence for a prolonged, second release of Mildronate with urinary concentrations still reaching 200 ng/mL up to 49 days after only 500 mg supplementation.[118] In part, it is this discovery of the high affinity of Mildronate for red blood cells that has led to an increase in competitive athletes testing positive for the drug.[112] Although it is not yet known why Mildronate has such a high affinity for erythrocytes, this discovery is important as some competitive bans received by athletes from anti-doping panels will need to be reassessed.[113] Moreover, whether or not Mildronate's mode of action stems from its ability to inhibit carnitine biosynthesis *via* the 2OG oxygenase BBOX, novel BBOX inhibitors have been disclosed as improved analogues of Mildronate.[201] It is therefore possible that BBOX inhibitors will appear on the pharmaceutical market in the near future.[112]

Chapters 1-3, of this thesis, discuss further the 2OG oxygenases involved in carnitine biosynthesis. Relatively little is known about TMLH, which may be a target of Mildronate, is discussed in detail in Chapter 2. Indeed, TMLH may be a therapeutic target for carnitine biosynthesis. The effect of Mildronate and other inhibitors on the conformation of BBOX is examined in Chapter 3 using NMR spectroscopy. This is interesting given X-ray crystallographic studies of Mildroante and hBBOX, discovered Mildronate binds in a near-identical fashion to GBB. However, Mildronate is known to react with hBBOX,[75] and its effect on BBOX in solution has not been previously observed. Synthetic attempts to identify novel BBOX inhibitors in the Schofield lab are disclosed in Appendix I. It is hoped that following screening of the compounds disclosed, that more potent inhibitors of hBBOX, compared to Mildronate, can be identified.

1.7 Thesis outline



The first part work in this thesis focused on the development of chemical tools to further our understanding of the 2OG oxygenases involved in the biosynthesis of carnitine. The specific aims were as follows:

- To elucidate the stereochemical outcome of the first enzyme of human carnitine biosynthesis, the $Fe^{(II)}$, 2OG-dependent oxygenase, N^{ε}-trimethyllysine hydroxylase (TMLH). **(Chapter 2)**
- To explore conformational changes in the $Fe^{(II)}$, 2OG-dependent oxygenase, γ-butyrobetaine hydroxylase (BBOX) in solution, using ^{19}F NMR spectroscopy. Changes in enzyme conformation, as a result of various co-factors and co/substrates is explored, including Mildronate. **(Chapter 3)**
- Synthetic work involved in the development of novel inhibitors of BBOX is presented in **Appendix I**.

Chapters **4** and **5** describe work on other related metallo-enzymes, but outside of the direct realm of carnitine biosynthesis:

- **Chapter 4** describes the design and synthesis of novel metallo-β-lactamase (MBL) inhibitors, derived from the BBOX inhibitor FG2216 and L- and D-captopril.
- **Chapter 5** concerns the synthesis and *in vitro* application of a multi-functional chemical tool selective for the prolyl hydroxylase domain-containing enzyme 2 (PHD2). PHD2 is a $Fe^{(II)}$, 2OG-dependent oxygenase involved in oxygen sensing.

Overall the aim of the work described in this thesis was to further our understanding of metallo-enzyme catalysis and inhibition from a therapeutic perspective.

1.8 References

1. J. J. Hutton, Jr., A. Kaplan and S. Udenfriend, Conversion of the amino acid sequence gly-pro-pro in protein to gly-pro-hyp by collagen proline hydroxylase, *Arch. Biochem. Biophys.*, 1967, **121**, 384-391.
2. C. Loenarz and C. J. Schofield, Expanding chemical biology of 2-oxoglutarate oxygenases, *Nat. Chem. Biol.*, 2008, **4**, 152-156.
3. R. P. Hausinger and C. Schofield, *2-oxoglutarate-dependent oxygenases*, Royal Society of Chemistry, Cambridge, 2015.
4. M. A. McDonough, C. Loenarz, R. Chowdhury, I. J. Clifton and C. J. Schofield, Structural studies on human 2-oxoglutarate dependent oxygenases, *Curr. Opin. Struct. Biol.*, 2010, **20**, 659-672.
5. A. G. Prescott and M. D. Lloyd, The iron(II) and 2-oxoacid-dependent dioxygenases and their role in metabolism, *Nat. Prod. Rep.*, 2000, **17**, 367-383.
6. M. Costas, M. P. Mehn, M. P. Jensen and L. Que, Jr., Dioxygen activation at mononuclear nonheme iron active sites: enzymes, models, and intermediates, *Chem. Rev.*, 2004, **104**, 939-986.
7. A. Ozer and R. K. Bruick, Non-heme dioxygenases: cellular sensors and regulators jelly rolled into one?, *Nat. Chem. Biol.*, 2007, **3**, 144-153.
8. C. Loenarz and C. J. Schofield, Physiological and biochemical aspects of hydroxylations and demethylations catalyzed by human 2-oxoglutarate oxygenases, *Trends Biochem. Sci.*, 2011, **36**, 7-18.
9. I. J. Clifton, M. A. McDonough, D. Ehrismann, N. J. Kershaw, N. Granatino and C. J. Schofield, Structural studies on 2-oxoglutarate oxygenases and related double-stranded beta-helix fold proteins, *J. Inorg. Biochem.*, 2006, **100**, 644-669.
10. W. G. Kaelin, Jr. and P. J. Ratcliffe, Oxygen sensing by metazoans: the central role of the HIF hydroxylase pathway, *Mol. Cell.*, 2008, **30**, 393-402.
11. N. R. Rose, M. A. McDonough, O. N. King, A. Kawamura and C. J. Schofield, Inhibition of 2-oxoglutarate dependent oxygenases, *Chem. Soc. Rev.*, 2011, **40**, 4364-4397.
12. P. L. Roach, I. J. Clifton, V. Fulop, K. Harlos, G. J. Barton, J. Hajdu, I. Andersson, C. J. Schofield and J. E. Baldwin, Crystal structure of isopenicillin N synthase is the first from a new structural family of enzymes, *Nature*, 1995, **375**, 700-704.
13. Z. Zhang, J. Ren, D. K. Stammers, J. E. Baldwin, K. Harlos and C. J. Schofield, Structural origins of the selectivity of the trifunctional oxygenase clavaminic acid synthase, *Nat. Struct. Biol.*, 2000, **7**, 127-133.
14. J. M. Elkins, M. J. Ryle, I. J. Clifton, J. C. Dunning Hotopp, J. S. Lloyd, N. I. Burzlaff, J. E. Baldwin, R. P. Hausinger and P. L. Roach, X-ray crystal structure of Escherichia coli taurine/alpha-ketoglutarate dioxygenase complexed to ferrous iron and substrates, *Biochemistry*, 2002, **41**, 5185-5192.
15. K. Valegard, A. C. van Scheltinga, M. D. Lloyd, T. Hara, S. Ramaswamy, A. Perrakis, A. Thompson, H. J. Lee, J. E. Baldwin, C. J. Schofield, J. Hajdu and I. Andersson, Structure of a cephalosporin synthase, *Nature*, 1998, **394**, 805-809.
16. M. Costas, M. P. Mehn, M. P. Jensen and L. Que, Dioxygen activation at mononuclear nonheme iron active sites: Enzymes, models, and intermediates, *Chem. Rev.*, 2004, **104**, 939-986.
17. R. P. Hausinger, Fe(II)/alpha-ketoglutarate-dependent hydroxylases and related enzymes, *Crit. Rev. Biochem. Mol. Biol.*, 2004, **39**, 21-68.

18. J. C. Price, E. W. Barr, T. E. Glass, C. Krebs and J. M. Bollinger, Jr., Evidence for hydrogen abstraction from C1 of taurine by the high-spin Fe(IV) intermediate detected during oxygen activation by taurine:alpha-ketoglutarate dioxygenase (TauD), *J. Am. Chem. Soc.*, 2003, **125**, 13008-13009.
19. J. C. Price, E. W. Barr, B. Tirupati, J. M. Bollinger, Jr. and C. Krebs, The first direct characterization of a high-valent iron intermediate in the reaction of an alpha-ketoglutarate-dependent dioxygenase: a high-spin FeIV complex in taurine/alpha-ketoglutarate dioxygenase (TauD) from Escherichia coli, *Biochemistry*, 2003, **42**, 7497-7508.
20. D. A. Proshlyakov, T. F. Henshaw, G. R. Monterosso, M. J. Ryle and R. P. Hausinger, Direct detection of oxygen intermediates in the non-heme Fe enzyme taurine/alpha-ketoglutarate dioxygenase, *J. Am. Chem. Soc.*, 2004, **126**, 1022-1023.
21. K. Majamaa, H. M. Hanauske-Abel, V. Gunzler and K. I. Kivirikko, The 2-oxoglutarate binding site of prolyl 4-hydroxylase. Identification of distinct subsites and evidence for 2-oxoglutarate decarboxylation in a ligand reaction at the enzyme-bound ferrous ion, *Eur. J. Biochem.*, 1984, **138**, 239-245.
22. S. Sinnecker, N. Svensen, E. W. Barr, S. Ye, J. M. Bollinger, Jr., F. Neese and C. Krebs, Spectroscopic and computational evaluation of the structure of the high-spin Fe(IV)-oxo intermediates in taurine: alpha-ketoglutarate dioxygenase from Escherichia coli and its His99Ala ligand variant, *J. Am. Chem. Soc.*, 2007, **129**, 6168-6179.
23. W. Gulewitsch and R. Krimberg, Zur Kenntnis der Extractivstoffe der Muskeln., *Z Physiol Chem*, 1905, **45**, 326-328.
24. F. Kutscher, Zur Kenntnis des Novains., *Z. Physiol. Chem.*, 1905, **49**, 47-49.
25. M. Tomita and Y. Sendju, Über die Oxyaminverbindungen welche die Biuret Reaktionen zeigen. III. Spaltung der γ -amino- β -oxybuttersäure in die optisch-aktiven Komponente, *Z. Physiol. Chem.*, 1927, **169**, 263-277.
26. C. Hoppel, The role of carnitine in normal and altered fatty acid metabolism, *Am. J. Kidney Dis.*, 2003, **41**, S4-12.
27. G. Wolf, The discovery of a vitamin role for carnitine: The first 50 years, *J. Nutr.*, 2006, **136**, 2131-2134.
28. J. Odle, S. H. Adams and J. Vockley, Carnitine, *Adv. Nutr.*, 2014, **5**, 289-290.
29. S. Alesci, I. Manoli, R. Costello, P. Coates, P. W. Gold, G. P. Chrousos and M. R. Blackman, Carnitine: the science behind a conditionally essential nutrient., *Ann. NY. Acad. Sci.*, 2004, **1033**, 1-197.
30. N. R. Marquis and I. B. Fritz, The Distribution of Carnitine, Acetylcarnitine, and Carnitine Acetyltransferase in Rat Tissues, *J. Biol. Chem.*, 1965, **240**, 2193-2196.
31. M. Fischer, J. Keller, F. Hirche, H. Kluge, R. Ringseis and K. Eder, Activities of gamma-butyrobetaine dioxygenase and concentrations of carnitine in tissues of pigs, *Comp. Biochem. Physiol. A. Mol. Integr. Physiol.*, 2009, **153**, 324-331.
32. A. G. Engel and C. J. Rebouche, Carnitine metabolism and inborn errors, *J. Inherit. Metab. Dis.*, 1984, **7** , 38-43.
33. R. A. Koeth, Z. Wang, B. S. Levison, J. A. Buffa, E. Org, B. T. Sheehy, E. B. Britt, X. Fu, Y. Wu, L. Li, J. D. Smith, J. A. DiDonato, J. Chen, H. Li, G. D. Wu, J. D. Lewis, M. Warrier, J. M. Brown, R. M. Krauss, W. H. Tang, F. D. Bushman, A. J. Lusis and S. L. Hazen, Intestinal microbiota metabolism of L-carnitine, a nutrient in red meat, promotes atherosclerosis, *Nat. Med.*, 2013, **19**, 576-585.
34. J. M. Brown and S. L. Hazen, The gut microbial endocrine organ: bacterially derived signals driving cardiometabolic diseases, *Annu. Rev. Med.*, 2015, **66**, 343-359.
35. K. K. Witte, A. L. Clark and J. G. Cleland, Chronic heart failure and micronutrients, *J. Am. Coll. Cardiol.*, 2001, **37**, 1765-1774.

36. K. K. Witte and A. L. Clark, Micronutrients and their supplementation in chronic cardiac failure. An update beyond theoretical perspectives, *Heart Fail. Rev.*, 2006, **11**, 65-74.
37. Y. Z. Xue, L. X. Wang, H. Z. Liu, X. W. Qi, X. H. Wang and H. Z. Ren, L-carnitine as an adjunct therapy to percutaneous coronary intervention for non-ST elevation myocardial infarction, *Cardiovasc. Drugs Ther.*, 2007, **21**, 445-448.
38. R. Lango, R. T. Smolenski, M. Narkiewicz, J. Suchorzewska and W. Lysiak-Szydlowska, Influence of L-carnitine and its derivatives on myocardial metabolism and function in ischemic heart disease and during cardiopulmonary bypass, *Cardiovasc. Res.*, 2001, **51**, 21-29.
39. B. J. Lee, J. S. Lin, Y. C. Lin and P. T. Lin, Effects of L-carnitine supplementation on oxidative stress and antioxidant enzymes activities in patients with coronary artery disease: a randomized, placebo-controlled trial, *Nutr. J.*, 2014, **13**, 79.
40. M. Najafi and A. Garjani, Short term administration of L-carnitine can be detrimental to the ischemic heart, *Adv. Pharm. Bull.*, 2014, **4**, 1-3.
41. F. Dastan, A. Hajhossein Talasaz, M. Mojtahedzadeh, A. Karimi, A. Salehiomran, P. Bina, A. Jalali and Z. Aghaie, Potential Effect of L-Carnitine on the Prevention of Myocardial Injury after Coronary Artery Bypass Graft Surgery, *J. Tehran Heart Cent.*, 2015, **10**, 74-79.
42. P. L. Magoulas and A. W. El-Hattab, Systemic primary carnitine deficiency: an overview of clinical manifestations, diagnosis, and management, *Orphanet. J. Rare. Dis.*, 2012, **7**, 68.
43. R. A. Cruciani, E. Dvorkin, P. Homel, S. Malamud, B. Culliney, J. Lapin, R. K. Portenoy and N. Esteban-Cruciani, Safety, tolerability and symptom outcomes associated with L-carnitine supplementation in patients with cancer, fatigue, and carnitine deficiency: a phase I/II study, *J. Pain Symptom Manage*, 2006, **32**, 551-559.
44. R. A. Cruciani, E. Dvorkin, P. Homel, B. Culliney, S. Malamud, J. Lapin, R. K. Portenoy and N. Esteban-Cruciani, L-carnitine supplementation in patients with advanced cancer and carnitine deficiency: a double-blind, placebo-controlled study, *J. Pain Symptom Manage*, 2009, **37**, 622-631.
45. R. A. Cruciani, E. Dvorkin, P. Homel, B. Culliney, S. Malamud, L. Shaiova, S. Fleishman, J. Lapin, E. Klein, P. Lesage, R. Portenoy and N. Esteban-Cruciani, L-carnitine supplementation for the treatment of fatigue and depressed mood in cancer patients with carnitine deficiency: a preliminary analysis, *Ann. N. Y. Acad. Sci.*, 2004, **1033**, 168-176.
46. R. A. Cruciani, J. J. Zhang, J. Manola, D. Cella, B. Ansari and M. J. Fisch, L-carnitine supplementation for the management of fatigue in patients with cancer: an eastern cooperative oncology group phase III, randomized, double-blind, placebo-controlled trial, *J. Clin. Oncol.*, 2012, **30**, 3864-3869.
47. E. P. Brass, Supplemental carnitine and exercise, *Am. J. Clin. Nutr.*, 2000, **72**, 618s-623s.
48. O. J. Heinonen, Carnitine and physical exercise, *Sports Med.*, 1996, **22**, 109-132.
49. E. P. Brass, Carnitine and sports medicine: use or abuse?, *Ann. N. Y. Acad. Sci.*, 2004, **1033**, 67-78.
50. C. Alves and R. V. Lima, Dietary supplement use by adolescents, *J Pediatr (Rio J)*, 2009, **85**, 287-294.
51. F. Le Borgne and J. Demarquoy, Carnitine and athletic performance, *Sci. Sport.*, 2003, **18**, 125-133.

52. R. G. Villani, J. Gannon, M. Self and P. A. Rich, L-Carnitine supplementation combined with aerobic training does not promote weight loss in moderately obese women, *Int. J. Sport Nutr. Exerc. Metab.*, 2000, **10**, 199-207.
53. J. M. Berg, J. L. Tymoczko and L. Stryer, *Biochemistry*, W. H. Freeman, New York, 6th edn., 2007.
54. R. S. Schofield and J. A. Hill, Role of metabolically active drugs in the management of ischemic heart disease, *Am. J. Cardiovasc. Drugs*, 2001, **1**, 23-35.
55. J. Bremer, Carnitine--metabolism and functions, *Physiol. Rev.*, 1983, **63**, 1420-1480.
56. F. P. Kuhajda and G. V. Ronnett, Modulation of carnitine palmitoyltransferase-1 for the treatment of obesity, *Curr. Opin. Investig. Drugs*, 2007, **8**, 312-317.
57. C. Indiveri, V. Iacobazzi, A. Tonazzi, N. Giangregorio, V. Infantino, P. Convertini, L. Console and F. Palmieri, The mitochondrial carnitine/acylcarnitine carrier: Function, structure and physiopathology, *Mol. Aspects. Med.*, 2011, **32**, 223-233.
58. S. Violante, L. IJlst, H. T. Brinke, I. T. de Almeida, R. J. A. Wanders, F. V. Ventura and S. M. Houten, Carnitine palmitoyltransferase 2 and carnitine/acylcarnitine translocase are involved in the mitochondrial synthesis and export of acylcarnitines, *FASEB J.*, 2013, **27**, 2039-2044.
59. F. M. Vaz and R. J. Wanders, Carnitine biosynthesis in mammals, *Biochem. J.*, 2002, **361**, 417-429.
60. J. Bremer, Carnitine - Metabolism and Functions, *Physiol. Rev.*, 1983, **63**, 1420-1480.
61. G. Jogl and L. Tong, Crystal structure of carnitine acetyltransferase and implications for the catalytic mechanism and fatty acid transport, *Cell*, 2003, **112**, 113-122.
62. S. Violante, L. Ijlst, J. Ruiter, J. Koster, H. van Lenthe, M. Duran, I. T. de Almeida, R. J. A. Wanders, S. M. Houten and F. V. Ventura, Substrate specificity of human carnitine acetyltransferase: Implications for fatty acid and branched-chain amino acid metabolism, *BBA-Mol. Basis. Dis.*, 2013, **1832**, 773-779.
63. R. R. Ramsay, R. D. Gandour and F. R. van der Leij, Molecular enzymology of carnitine transfer and transport, *Biochim. Biophys. Acta*, 2001, **1546**, 21-43.
64. M. Dambrova, M. Makrecka-Kuka, R. Vilskersts, E. Makarova, J. Kuka and E. Liepinsh, Pharmacological effects of meldonium: Biochemical mechanisms and biomarkers of cardiometabolic activity, *Pharmacol. Res.*, 2016, **113**, 771-780.
65. G. D. Lopaschuk, Optimizing cardiac energy metabolism: how can fatty acid and carbohydrate metabolism be manipulated?, *Coronary. Artery Dis.*, 2001, **12**, S8-S11.
66. C. J. Rebouche, Kinetics, pharmacokinetics, and regulation of L-carnitine and acetyl-L-carnitine metabolism, *Ann. N. Y. Acad. Sci.*, 2004, **1033**, 30-41.
67. V. Tanphaichitr and H. P. Broquist, Role of lysine and -N-trimethyllysine in carnitine biosynthesis. II. Studies in the rat, *J. Biol. Chem.*, 1973, **248**, 2176-2181.
68. V. Tanphaichitr, D. W. Horne and H. P. Broquist, Lysine, a precursor of carnitine in the rat, *J. Biol. Chem.*, 1971, **246**, 6364-6366.
69. C. J. Rebouche, Carnitine Function and Requirements during the Life-Cycle, *FASEB J.*, 1992, **6**, 3379-3386.
70. K. Strijbis, F. M. Vaz and B. Distel, Enzymology of the Carnitine Biosynthesis Pathway, *IUBMB. Life*, 2010, **62**, 357-362.
71. C. J. Rebouche and A. G. Engel, Tissue distribution of carnitine biosynthetic enzymes in man., *Biochim. Biophys. Acta*, 1980, **630**, 22-29.
72. F. M. Vaz, R. Ofman, K. Westinga, J. W. Back and R. J. A. Wanders, Molecular and biochemical characterization of rat epsilon-N-Trimethyllysine hydroxylase, the first enzyme of carnitine biosynthesis, *J. Biol. Chem.*, 2001, **276**, 33512-33517.

73. J. D. Hulse and L. V. M. Henderson, Carnitine Biosynthesis - Purification of 4-N-Trimethylaminobutyraldehyde Dehydrogenase from Beef-Liver, *J. Biol. Chem.*, 1980, **255**, 1146-1151.
74. C. Rigault, F. Le Borgne and J. Demarquoy, Genomic structure, alternative maturation and tissue expression of the human BBOX1 gene, *BBA-Mol. Cell. Biol. L*, 2006, **1761**, 1469-1481.
75. I. K. Leung, T. J. Krojer, G. T. Kochan, L. Henry, F. von Delft, T. D. Claridge, U. Oppermann, M. A. McDonough and C. J. Schofield, Structural and mechanistic studies on gamma-butyrobetaine hydroxylase, *Chem. Biol.*, 2010, **17**, 1316-1324.
76. F. M. Vaz, S. van Gool, R. Ofman, L. Ijlst and R. J. A. Wanders, Carnitine biosynthesis: Identification of the cDNA encoding human gamma-butyrobetaine hydroxylase, *Biochem. Biophys. Res. Commun.*, 1998, **250**, 506-510.
77. J. LaBadie, W. A. Dunn and N. N. Aronson, Jr., Hepatic synthesis of carnitine from protein-bound trimethyl-lysine. Lysosomal digestion of methyl-lysine-labelled asialo-fetuin, *Biochem. J*, 1976, **160**, 85-95.
78. G. Huszar, Tissue-Specific Biosynthesis of Epsilon-N-Monomethyllysine and Epsilon-N-Trimethyllysine in Skeletal and Cardiac-Muscle Myosin - Model for Cell-Free Study of Post-Translational Amino-Acid Modifications in Proteins, *J. Mol. Biol.*, 1975, **94**, 311-326.
79. L. Servillo, A. Giovane, D. Cautela, D. Castaldo and M. L. Balestrieri, Where does N(epsilon)-trimethyllysine for the carnitine biosynthesis in mammals come from?, *PLoS One*, 2014, **9**, e84589.
80. R. K. Morse, J. P. Vergnes, J. Malloy and I. R. Mcmanus, Sites of Biological Methylation of Proteins in Cultured Chick Muscle-Cells, *Biochemistry*, 1975, **14**, 4316-4325.
81. R. A. Cox and C. L. Hoppel, Biosynthesis of carnitine and 4-N-trimethylaminobutyrate from 6-N-trimethyl-lysine, *Biochem. J*, 1973, **136**, 1083-1090.
82. R. A. Cox and C. L. Hoppel, Carnitine Biosynthesis in Rat-Liver Slices, *Biochim. Biophys. Acta*, 1974, **362**, 403-413.
83. W. A. Dunn, G. Rettura, E. Seifter and S. Englard, Carnitine biosynthesis from gamma-butyrobetaine and from exogenous protein-bound 6-N-trimethyl-L-lysine by the perfused guinea pig liver. Effect of ascorbate deficiency on the in situ activity of gamma-butyrobetaine hydroxylase, *J. Biol. Chem.*, 1984, **259**, 10764-10770.
84. J. D. E. Hulse, S. R.; Henderson, L. M., Carnitine biosynthesis. beta-Hydroxylation of trimethyllysine by an alpha-ketoglutarate-dependent mitochondrial dioxygenase., *J. Biol. Chem.*, 1978, **253**, 1654-1659.
85. R. F. Novak, T. J. Swift and C. L. Hoppel, N6-Trimethyl-lysine metabolism. Structural identification of the metabolite 3-hydroxy-N6-trimethyl-lysine, *Biochem. J.*, 1980, **188**, 521-527.
86. R. Stein and S. Englard, Properties of rat 6-N-trimethyl-L-lysine hydroxylases: similarities among the kidney, liver, heart, and skeletal muscle activities, *Arch. Biochem. Biophys.*, 1982, **217**, 324-331.
87. N. van Vlies, R. Ofman, R. J. Wanders and F. M. Vaz, Submitochondrial localization of 6-N-trimethyllysine dioxygenase - implications for carnitine biosynthesis, *FEBS J.*, 2007, **274**, 5845-5851.
88. A. L. Carter and R. Frenkel, Role of the Kidney in the Biosynthesis of Carnitine in the Rat, *J. Biol. Chem.*, 1979, **254**, 670-674.
89. A. Kazaks, M. Makrecka-Kuka, J. Kuka, T. Voronkova, I. Akopjana, S. Grinberga, O. Pugovics and K. Tars, Expression and purification of active, stabilized trimethyllysine hydroxylase, *Protein. Expr. Purif.*, 2014, **104**, 1-6.

90. C. Nava, F. Lamari, D. Heron, C. Mignot, A. Rastetter, B. Keren, D. Cohen, A. Faudet, D. Bouteiller, M. Gilleron, A. Jacquette, S. Whalen, A. Afenjar, D. Perisse, C. Laurent, C. Dupuits, C. Gautier, M. Gerard, G. Huguet, S. Caillet, B. Leheup, M. Leboyer, C. Gillberg, R. Delorme, T. Bourgeron, A. Brice and C. Depienne, Analysis of the chromosome X exome in patients with autism spectrum disorders identified novel candidate genes, including TMLHE, *Transl. Psychiatry*, 2012, **2**, e179.
91. R. O. Rosti, A. A. Sadek, K. K. Vaux and J. G. Gleeson, The genetic landscape of autism spectrum disorders, *Dev. Med. Child. Neurol.*, 2014, **56**, 12-18.
92. E. T. Lim, S. Raychaudhuri, S. J. Sanders, C. Stevens, A. Sabo, D. G. MacArthur, B. M. Neale, A. Kirby, D. M. Ruderfer, M. Fromer, M. Lek, L. Liu, J. Flannick, S. Ripke, U. Nagaswamy, D. Muzny, J. G. Reid, A. Hawes, I. Newsham, Y. Q. Wu, L. Lewis, H. Dinh, S. Gross, L. S. Wang, C. F. Lin, O. Valladares, S. B. Gabriel, M. dePristo, D. M. Altshuler, S. M. Purcell, M. W. State, E. Boerwinkle, J. D. Buxbaum, E. H. Cook, R. A. Gibbs, G. D. Schellenberg, J. S. Sutcliffe, B. Devlin, K. Roeder, M. J. Daly and N. E. S. Project, Rare Complete Knockouts in Humans: Population Distribution and Significant Role in Autism Spectrum Disorders, *Neuron*, 2013, **77**, 235-242.
93. S. Englard, J. S. Blanchard and C. F. Midelfort, Gamma-Butyrobetaine Hydroxylase - Stereochemical Course of the Hydroxylation Reaction, *Biochemistry*, 1985, **24**, 1110-1116.
94. S. Galland, F. Le Borgne, D. Guyonnet, P. Clouet and J. Demarquoy, Purification and characterization of the rat liver gamma-butyrobetaine hydroxylase, *Mol. Cell. Biochem.*, 1998, **178**, 163-168.
95. A. Kondo, J. S. Blanchard and S. Englard, Purification and Properties of Calf Liver Gamma-Butyrobetaine Hydroxylase, *Arch. Biochem. Biophys.*, 1981, **212**, 338-346.
96. G. Lindstedt, S. Lindstedt and I. Nordin, Gamma-Butyrobetaine Hydroxylase in Human-Kidney, *Scand. J Clin. Lab. Inv.*, 1982, **42**, 477-485.
97. G. Lindstedt, S. Lindstedt and I. Nordin, Purification and properties of gamma-butyrobetaine hydroxylase from Pseudomonas sp AK 1, *Biochemistry*, 1977, **16**, 2181-2188.
98. K. Tars, J. Rumnieks, A. Zeltins, A. Kazaks, S. Kotelovica, A. Leonciks, J. Sharipo, A. Viksna, J. Kuka, E. Liepinsh and M. Dambrova, Crystal structure of human gamma-butyrobetaine hydroxylase, *Biochem. Biophys. Res. Commun.*, 2010, **398**, 634-639.
99. J. J. McMurray and M. A. Pfeffer, Heart failure, *Lancet*, 2005, **365**, 1877-1889.
100. NIH: National Heart, Lung and Blood Institue, What is a heart attack?, *NIH: Health information for the public*, https://www.nhlbi.nih.gov/health/health-topics/topics/heartattack/.
101. J. S. Jaswal, W. Keung, W. Wang, J. R. Ussher and G. D. Lopaschuk, Targeting fatty acid and carbohydrate oxidation--a novel therapeutic intervention in the ischemic and failing heart, *Biochim. Biophys. Acta*, 2011, **1813**, 1333-1350.
102. G. D. Lopaschuk, Optimizing cardiac fatty acid and glucose metabolism as an approach to treating heart failure, *Semin. Cardiothorac. Vasc. Anesth.*, 2006, **10**, 228-230.
103. A. L. Shug, J. H. Thomsen, J. D. Folts, N. Bittar, M. I. Klein, J. R. Koke and P. J. Huth, Changes in tissue levels of carnitine and other metabolites during myocardial ischemia and anoxia, *Arch. Biochem. Biophys.*, 1978, **187**, 25-33.
104. N. A. Silverman, G. Schmitt, M. Vishwanath, H. Feinberg and S. Levitsky, Effect of carnitine on myocardial function and metabolism following global ischemia, *Ann. Thorac. Surg.*, 1985, **40**, 20-24.
105. L. G. Spagnoli, M. Corsi, S. Villaschi, G. Palmieri and F. Maccari, Myocardial carnitine deficiency in acute myocardial infarction, *Lancet*, 1982, **1**, 1419-1420.

106. C. Mingorance, R. Rodriguez-Rodriguez, M. L. Justo, M. Alvarez de Sotomayor and M. D. Herrera, Critical update for the clinical use of L-carnitine analogs in cardiometabolic disorders, *Vasc. Health Risk Manag.*, 2011, **7**, 169-176.
107. E. Randrianarisoa, A. Lehn-Stefan, X. L. Wang, M. Hoene, A. Peter, S. S. Heinzmann, X. J. Zhao, I. Konigsrainer, A. Konigsrainer, B. Balletshofer, J. Machann, F. Schick, A. Fritsche, H. U. Haring, G. W. Xu, R. Lehmann and N. Stefan, Relationship of Serum Trimethylamine N-Oxide (TMAO) Levels with early Atherosclerosis in Humans, *SCI. REP-UK.*, 2016, **6**, 26745.
108. A. M. Bernstein, Q. Sun, F. B. Hu, M. J. Stampfer, J. E. Manson and W. C. Willett, Major Dietary Protein Sources and Risk of Coronary Heart Disease in Women, *Circulation*, 2010, **122**, 876-883.
109. R. Micha, S. K. Wallace and D. Mozaffarian, Red and Processed Meat Consumption and Risk of Incident Coronary Heart Disease, Stroke, and Diabetes Mellitus A Systematic Review and Meta-Analysis, *Circulation*, 2010, **121**, 2271-U2252.
110. J. R. Dyck, T. A. Hopkins, S. Bonnet, E. D. Michelakis, M. E. Young, M. Watanabe, Y. Kawase, K. Jishage and G. D. Lopaschuk, Absence of malonyl coenzyme A decarboxylase in mice increases cardiac glucose oxidation and protects the heart from ischemic injury, *Circulation*, 2006, **114**, 1721-1728.
111. B. Z. Simkhovich, Z. V. Shutenko, D. V. Meirena, K. B. Khagi, R. J. Mezapuke, T. N. Molodchina, I. J. Kalvins and E. Lukevics, 3-(2,2,2-Trimethylhydrazinium)propionate (THP)--a novel gamma-butyrobetaine hydroxylase inhibitor with cardioprotective properties, *Biochem. Pharmacol.*, 1988, **37**, 195-202.
112. W. Schobersberger, T. Dunnwald, G. Gmeiner and C. Blank, Story behind meldonium-from pharmacology to performance enhancement: a narrative review, *Br. J. Sports Med.*, 2017, **51**, 22-25.
113. H. K. Greenblatt and D. J. Greenblatt, Meldonium (Mildronate): A Performance-Enhancing Drug?, *Clin. Pharm. Drug Dev.*, 2016, **5**, 167-169.
114. M. Dambrova, E. Liepinsh and I. Kalvinsh, Mildronate: cardioprotective action through carnitine-lowering effect, *Trends Cardiovasc. Med.*, 2002, **12**, 275-279.
115. E. Liepinsh, R. Vilskersts, D. Loca, O. Kirjanova, O. Pugovichs, I. Kalvinsh and M. Dambrova, Mildronate, an inhibitor of carnitine biosynthesis, induces an increase in gamma-butyrobetaine contents and cardioprotection in isolated rat heart infarction, *J. Cardiovasc. Pharmacol.*, 2006, **48**, 314-319.
116. M. Dambrova, G. Latkovskis, J. Kuka, I. Strele, I. Konrade, S. Grinberga, D. Hartmane, O. Pugovics, A. Erglis and E. Liepinsh, Diabetes is Associated with Higher Trimethylamine N-oxide Plasma Levels, *Exp. Clin. Endocrinol. Diabetes*, 2016, **124**, 251-256.
117. N. Sjakste, A. Gutcaits and I. Kalvinsh, Mildronate: An antiischernic drug for neurological indications, *Cns. Drug Rev.*, 2005, **11**, 151-168.
118. L. Tretzel, C. Gorgens, H. Geyer, A. Thomas, J. Dib, S. Guddat, V. Pop, W. Schanzer and M. Thevis, Analyses of Meldonium (Mildronate) from Blood, Dried Blood Spots (DBS), and Urine Suggest Drug Incorporation into Erythrocytes, *Int. J. Sports. Med.*, 2016, **37**, 500-502.
119. M. Kugel and T. Balmforth, 'Sharapova Drug' Is Not Doping, Says Its Latvian Inventor, *RadioFreeEuropeRadioLiberty*, 10th March 2016, http://www.rferl.org/a/sharapova-drug-meldonium-mildronate-not-doping-latvian-inventor/27603162.html.
120. M. Kugel, Профессор Мельдоний (Professor Meldonium), *Радио Свобода (Radio svoboda)*, March 9th 2016, http://www.svoboda.org/a/27601071.html.

121. I. Y. K. Anatoly Eremeev, Valentina G. Semenikhina, Edvards E. Liepinsh, Yan Y. Latvietis, Paul P. Anderson, Elena B. Astapenok, Yazep Y. Spruzh, Petr T. Trapentsiers, Gennady I. Podoprigora, Solomon A. Giller, deceased, 3-(2,2,2-Trimethylhydrazinium)propionate and method for the preparation and use thereof, Institut Organicheskogo Sinteza Akademii Nauk Latviiskoi SSR, US4481218 A, *USSR Pat.*, Jul 8, 1982.
122. M. Birnbaum, The drug taken by Maria Sharapova was used by the Soviet Union to help soldiers combat stress, *The Washington Post*, 8th March 2016, https://www.washingtonpost.com/news/worldviews/wp/2016/03/08/the-drug-linked-to-tennis-great-sharapova-has-roots-in-soviet-military/.
123. E. Cohen, The secret Cold War origins of Sharapova's doping drug, *CNN*, 8th June 2016, http://edition.cnn.com/2016/03/21/health/maria-sharapova-drug-meldonium-cold-war-origins/.
124. ВЕСТИ.ru, Советские солдаты принимали мельдоний перед заброской в тыл афганских душманов (A Soviet soldier taking meldonium before getting to the rear of the Afghan dushmans), http://www.vesti.ru/doc.html?id=2729021, (accessed March 9th 2016).
125. W. A. D. A, The 2016 Prohibited List, https://wada-main-prod.s3.amazonaws.com/resources/files/wada-2016-prohibited-list-en.pdf).
126. W. A. D. A, The 2015 Monitoring Program, https://wada-main-prod.s3.amazonaws.com/resources/files/wada-2015-monitoring-program-en.pdf).
127. M. Stuart, C. Schneider and K. Steinbach, Meldonium use by athletes at the Baku 2015 European Games, *Br. J. Sports Med.*, 2016, **50**, 694-698.
128. K. Soong, Maria Sharapova provisionally suspended after admitting to failing drug test, *The Washington Post*, 7th March 2016, https://www.washingtonpost.com/news/early-lead/wp/2016/03/07/maria-sharapova-says-she-failed-drug-test-at-australian-open/?tid=a_inl.
129. W. A. D. A, WADA statement on Meldonium-Notice issued to stakeholders., https://www.wada-ama.org/en/media/news/2016-04/wada-statement-on-meldonium-notice-issued-to-stakeholders, (accessed 13 April 2016).
130. S. C. Sweetman and W. Martindale, *Martindale : the complete drug reference*, Pharmaceutical Press, London, 33rd edn., 2002.
131. M. Spaniol, H. Brooks, L. Auer, A. Zimmermann, M. Solioz, B. Stieger and S. Krahenbuhl, Development and characterization of an animal model of carnitine deficiency, *Eur. J. Biochem.*, 2001, **268**, 1876-1887.
132. E. Liepinsh, I. Kalvinsh and M. Dambrova, (2011). The Regulation of Energy Metabolism Pathways Through L-Carnitine Homeostasis, Role of the Adipocyte in Development of Type 2 Diabetes. D. C. Croniger, *InTech*, 10.5772/22478, http://www.intechopen.com/books/role-of-the-adipocyte-in-development-of-type-2-diabetes/the-regulation-of-energy-metabolism-pathways-through-l-carnitine-homeostasis.
133. A. T. Davis, T. J. Monroe, K. E. Ingersoll, L. VanWyk and M. Wojtas, Dietary mildronate supplementation has no effect on carnitine biosynthetic enzyme mRNA expression in rat, *Nutr. Res.*, 2007, **27**, 225-229.
134. A. H. K. Al Temimi, B. J. G. E. Pieters, Y. Reddy Vijayendar, P. B. White and J. Mecinović, Substrate scope for trimethyllysine hydroxylase catalysis, *Chem. Commun.*, 2016, **52**, 12849-12852.

135. M. Kuwajima, H. Harashima, M. Hayashi, S. Ise, M. Sei, K. Lu, H. Kiwada, Y. Sugiyama and K. Shima, Pharmacokinetic analysis of the cardioprotective effect of 3-(2,2, 2-trimethylhydrazinium) propionate in mice: inhibition of carnitine transport in kidney, *J. Pharmacol. Exp. Ther.*, 1999, **289**, 93-102.
136. J. Kuka, R. Vilskersts, H. Cirule, M. Makrecka, O. Pugovics, I. Kalvinsh, M. Dambrova and E. Liepinsh, The cardioprotective effect of mildronate is diminished after co-treatment with L-carnitine, *J. Cardiovasc. Pharmacol. Ther.*, 2012, **17**, 215-222.
137. J. Nezu, I. Tamai, A. Oku, R. Ohashi, H. Yabuuchi, N. Hashimoto, H. Nikaido, Y. Sai, A. Koizumi, Y. Shoji, G. Takada, T. Matsuishi, M. Yoshino, H. Kato, T. Ohura, G. Tsujimoto, J. Hayakawa, M. Shimane and A. Tsuji, Primary systemic carnitine deficiency is caused by mutations in a gene encoding sodium ion-dependent carnitine transporter, *Nat. Genet.*, 1999, **21**, 91-94.
138. E. Liepinsh, M. Makrecka, J. Kuka, H. Cirule, E. Makarova, E. Sevostjanovs, S. Grinberga, R. Vilskersts, D. Lola, E. Loza, I. Stonans, O. Pugovics and M. Dambrova, Selective inhibition of OCTN2 is more effective than inhibition of gamma-butyrobetaine dioxygenase to decrease the availability of l-carnitine and to reduce myocardial infarct size, *Pharmacol. Res.*, 2014, **85**, 33-38.
139. S. Grigat, C. Fork, M. Bach, S. Golz, A. Geerts, E. Schomig and D. Grundemann, The carnitine transporter SLC22A5 is not a general drug transporter, but it efficiently translocates mildronate, *Drug Metab. Dispos.*, 2009, **37**, 330-337.
140. M. Grube, H. E. Meyer zu Schwabedissen, D. Prager, J. Haney, K. U. Moritz, K. Meissner, D. Rosskopf, L. Eckel, M. Bohm, G. Jedlitschky and H. K. Kroemer, Uptake of cardiovascular drugs into the human heart: expression, regulation, and function of the carnitine transporter OCTN2 (SLC22A5), *Circulation*, 2006, **113**, 1114-1122.
141. E. Liepinsh, R. Vilskersts, E. Skapare, B. Svalbe, J. Kuka, H. Cirule, O. Pugovics, I. Kalvinsh and M. Dambrova, Mildronate decreases carnitine availability and up-regulates glucose uptake and related gene expression in the mouse heart, *Life Sci.*, 2008, **83**, 613-619.
142. P. Degrace, L. Demizieux, J. Gresti, M. Tsoko, A. Andre, L. Demaison and P. Clouet, Fatty acid oxidation and related gene expression in heart depleted of carnitine by mildronate treatment in the rat, *Mol. Cell. Biochem.*, 2004, **258**, 171-182.
143. E. Liepinsh, E. Skapare, J. Kuka, M. Makrecka, H. Cirule, E. Vavers, E. Sevostjanovs, S. Grinberga, O. Pugovics and M. Dambrova, Activated peroxisomal fatty acid metabolism improves cardiac recovery in ischemia-reperfusion, *Naunyn Schmiedebergs Arch. Pharmacol.*, 2013, **386**, 541-550.
144. K. Jaudzems, J. Kuka, A. Gutsaits, K. Zinovjevs, I. Kalvinsh, E. Liepinsh, E. Liepinsh and M. Dambrova, Inhibition of carnitine acetyltransferase by mildronate, a regulator of energy metabolism, *J. Enzyme Inhib. Med. Chem.*, 2009, **24**, 1269-1275.
145. F. Oppedisano, D. Fanello, M. Calvani and C. Indiveri, Interaction of mildronate with the mitochondrial carnitine/acylcarnitine transport protein, *J. Biochem. Mol. Toxicol.*, 2008, **22**, 8-14.
146. S. V. Pande and R. Parvin, Characterization of carnitine acylcarnitine translocase system of heart mitochondria, *J. Biol. Chem.*, 1976, **251**, 6683-6691.
147. M. S. Murthy and S. V. Pande, Mechanism of carnitine acylcarnitine translocase-catalyzed import of acylcarnitines into mitochondria, *J. Biol. Chem.*, 1984, **259**, 9082-9089.
148. N. Sjakste and I. Kalvinsh, Mildronate: An antiischemic drug with multiple indications, *Pharmacologyonline*, 2006, **1**, 1-18.
149. Y. Hayashi, H. Ishida, M. Hoshiai, K. Hoshiai, T. Kirimoto, T. Kanno, M. Nakano, K. Tajima, H. Miyake, N. Matsuura and H. Nakazawa, MET-88, a gamma-butyrobetaine

hydroxylase inhibitor, improves cardiac SR Ca2+ uptake activity in rats with congestive heart failure following myocardial infarction, *Mol. Cell. Biochem.*, 2000, **209**, 39-46.
150. Y. Hayashi, T. Kirimoto, N. Asaka, M. Nakano, K. Tajima, H. Miyake and N. Matsuura, Beneficial effects of MET-88, a gamma-butyrobetaine hydroxylase inhibitor in rats with heart failure following myocardial infarction, *Eur. J. Pharmacol.*, 2000, **395**, 217-224.
151. M. Nakano, T. Kirimoto, N. Asaka, Y. Hayashi, T. Kanno, H. Miyake and N. Matsuura, Beneficial effects of MET-88 on left ventricular dysfunction and hypertrophy with volume overload in rats, *Fundam. Clin. Pharmacol.*, 1999, **13**, 521-526.
152. E. Liepinsh, R. Vilskersts, L. Zvejniece, B. Svalbe, E. Skapare, J. Kuka, H. Cirule, S. Grinberga, I. Kalvinsh and M. Dambrova, Protective effects of mildronate in an experimental model of type 2 diabetes in Goto-Kakizaki rats, *Br. J. Pharmacol.*, 2009, **157**, 1549-1556.
153. R. Vilskersts, J. Kuka, B. Svalbe, H. Cirule, E. Liepinsh, S. Grinberga, I. Kalvinsh and M. Dambrova, Administration of L-carnitine and mildronate improves endothelial function and decreases mortality in hypertensive Dahl rats, *Pharmacol. Rep.*, 2011, **63**, 752-762.
154. M. Akahira, A. Hara and Y. Abiko, Effect of MET-88, a gamma-butyrobetaine hydroxylase inhibitor, on myocardial derangements induced by hydrogen peroxide in the isolated perfused rat heart, *Fundam. Clin. Pharm.*, 1997, **11**, 356-364.
155. K. Yonekura, Y. Eto, I. Yokoyama, A. Matsumoto, S. Sugiura, S. Momomura, T. Kirimoto, Y. Hayashi, M. Omata and T. Aoyagi, Inhibition of carnitine synthesis modulates protein contents of the cardiac sarcoplasmic reticulum Ca2+-ATPase and hexokinase type I in rat hearts with myocardial infarction, *Basic Res. Cardiol.*, 2000, **95**, 343-348.
156. R. Vilskersts, O. Zharkova-Malkova, R. Mezhapuke, S. Grinberga, H. Cirule and M. Dambrova, Elevated vascular gamma-butyrobetaine levels attenuate the development of high glucose-induced endothelial dysfunction, *Clin Exp Pharmacol Physiol*, 2013, **40**, 518-524.
157. R. Vilskersts, E. Liepinsh, L. Mateuszuk, S. Grinberga, I. Kalvinsh, S. Chlopicki and M. Dambrova, Mildronate, a Regulator of Energy Metabolism, Reduces Atherosclerosis in apoE/LDLR-/- Mice, *Pharmacology*, 2009, **83**, 287-293.
158. T. Kirimoto, N. Asaka, Y. Hayashi, T. Maeda, T. Irimura and N. Matsuura, MET-88: SR Ca2+-uptake stimulator for treating chronic heart failure, *Cardiovasc. Drug. Rev.*, 1999, **17**, 75-86.
159. P. Braveny, Heart, calcium and time, *Exp. Clin. Cardiol.*, 2002, **7**, 3-6.
160. C. Sesti, B. Z. Simkhovich, I. Kalvinsh and R. A. Kloner, Mildronate, a novel fatty acid oxidation inhibitor and antianginal agent, reduces myocardial infarct size without affecting hemodynamics, *J. Cardiovasc. Pharmacol.*, 2006, **47**, 493-499.
161. H. P. Kutuschenko, N. A. Dimtrijeva and J. B. Lukina, Influence of mildronate on efficiency of antianginal therapy in patients with stable burden angina., *Rational Pharmacother. Cardiol.*, 2005, **2**, 37-47.
162. I. V. Sergijenko, M. E. Burgij, T. V. Balachonova and *e. al.*, The possiblity of usage of metabolic correction therapy in patients with ischemic heart diesase and heart failure., *Rational Pharmacother. Cardiol.*, 2007, **4**, 25-31.
163. A. T. Teplyakov, T. V. Sankevitch, T. A. Stepatcheva and S. E. Mamchur, The use fatty acid of beta-oxidation inhibitor mildronate as monotherapy or in combination with atenolol in patients with left ventricular dysfunction after myocardial infarction, *Kardiologiya*, 2003, **43**, 15-18.

164. V. Dzerve, D. Matisone, I. Kukulis and e. al., Mildronate improves peripheral circulation in patients with chronic heart failure: results of clinical trial (the first report). *Sem Cardiol*, 2005, **11**, 56-64.
165. V. Dzerve and M. I. S. Group, A dose-dependent improvement in exercise tolerance in patients with stable angina treated with mildronate: a clinical trial "MILSS I", *Medicina (Kaunas)*, 2011, **47**, 544-551.
166. M. D. Tsverava, Influence of mildronat on left ventricular systolic, diastolic functional parameters, pulmonary arterial flow and systolic dyssynchrony in patients with congestive heart failure., *Georgian Med. News.*, 2013, **218**, 34-40.
167. V. Dzerve, D. Matisone, Y. Pozdnyakov and e. al., Mildronate improves the exercise tolerance in patients with stable angina results of a long term clinical trial., *Sem. Cardiol.*, 2010, **16**, 3.
168. V. Dzerve, D. Matisone, I. Kukulis and A. Vitols, Efficacy of combined treatment of chronic heart failure with mildronate: Results of clinical trial, *Int. J. Cardiol.*, 2007, **119**, S17-S17.
169. V. Y. Dzerve and Y. M. Pozdnyakov, Exercise capacity in patients with coronary heart disease and peripheral artery disease, receiving long-term mildronate therapy, *Russ. J. Cardiol.*, 2011, 49-55.
170. V. Dzerve, I. Kukulis, D. Matisone, L. Putane, V. Grabauskiene, I. Skarda, J. Strautmanis and L. I. C. R. Latvia, Influence of mildronate on myocardial contractility in patients with chronic heart failure: Results of a clinical trial, *Eur. Heart. J.*, 2006, **27**, 343-343.
171. M. Makrecka, J. Kuka, K. Volska, U. Antone, E. Sevostjanovs, H. Cirule, S. Grinberga, O. Pugovics, M. Dambrova and E. Liepinsh, Long-chain acylcarnitine content determines the pattern of energy metabolism in cardiac mitochondria, *Mol. Cell. Biochem.*, 2014, **395**, 1-10.
172. C. Aguer, C. S. McCoin, T. A. Knotts, A. B. Thrush, K. Ono-Moore, R. McPherson, R. Dent, D. H. Hwang, S. H. Adams and M. E. Harper, Acylcarnitines: potential implications for skeletal muscle insulin resistance, *FASEB J.*, 2015, **29**, 336-345.
173. T. R. Koves, J. R. Ussher, R. C. Noland, D. Slentz, M. Mosedale, O. Ilkayeva, J. Bain, R. Stevens, J. R. B. Dyck, C. B. Newgard, G. D. Lopaschuk and D. M. Muoio, Mitochondrial overload and incomplete fatty acid oxidation contribute to skeletal muscle insulin resistance, *Cell Metab.*, 2008, **7**, 45-56.
174. N. Asaka, Y. Muranaka, T. Kirimoto and H. Miyake, Cardioprotective profile of MET-88, an inhibitor of carnitine synthesis, and insulin during hypoxia in isolated perfused rat hearts, *Fundam. Clin. Pharmacol.*, 1998, **12**, 158-163.
175. W. Wang and G. D. Lopaschuk, Metabolic therapy for the treatment of ischemic heart disease: reality and expectations, *Expert Rev. Cardiovasc. Ther.*, 2007, **5**, 1123-1134.
176. E. Liepinsh, R. Vilskersts, E. Skapare, B. Svalbe, J. Kuka, H. Cirule, O. Pugovics, I. Kalvinsh and M. Dambrova, Mildronate decreases carnitine availability and up-regulates glucose uptake and related gene expression in the mouse heart, *Life Sci.*, 2008, **83**, 613-619.
177. J. Sokolovska, S. Isajevs, O. Sugoka, J. Sharipova, L. Lauberte, D. Svirina, E. Rostoka, T. Sjakste, I. Kalvinsh and N. Sjakste, Correction of glycaemia and GLUT1 level by mildronate in rat streptozotocin diabetes mellitus model, *Cell Biochem. Funct.*, 2011, **29**, 55-63.
178. E. J. Anderson, M. E. Lustig, K. E. Boyle, T. L. Woodlief, D. A. Kane, C. T. Lin, J. W. Price, L. Kang, P. S. Rabinovitch, H. H. Szeto, J. A. Houmard, R. N. Cortright, D. H. Wasserman and P. D. Neufer, Mitochondrial H2O2 emission and cellular redox state

link excess fat intake to insulin resistance in both rodents and humans, *J. Clin. Invest.*, 2009, **119**, 573-581.
179. U. Beitnere, S. Isajevs, D. Svirina, S. Sausa, E. Rostoka and V. Klusa, Neurorestorative properties of mildronate in the rat model of Parkinson's disease, *Eur. Neuropsychopharm.*, 2011, **21**, S268-S269.
180. S. Isajevs, D. Isajeva, U. Beitnere, B. Jansone, I. Kalvinsh and V. Klusa, Mildronate as a Regulator of Protein Expression in a Rat Model of Parkinson's Disease, *Med. Lith.*, 2011, **47**, 552-559.
181. S. Isajevs, D. Svirina, J. Pupure, J. Rumaks, S. Svirskis, Z. Dzirkale, B. Jansone and V. Z. Klusa, Long-term mildronate neuroprotective effects in a rat model of Parkinson's disease, *Virchows. Arch.*, 2011, **459**, S270-S270.
182. V. Klusa, U. Beitnere, J. Pupure, S. Isajevs, J. Rumaks, S. Svirskis, Z. Dzirkale and I. Kalvinsh, Mildronate and its Neuroregulatory Mechanisms: Targeting the Mitochondria, Neuroinflammation, and Protein Expression, *Med. Lith.*, 2013, **49**, 301-309.
183. V. Klusa, R. Muceniece, S. Isajevs, D. Isajeva, U. Beitnere, I. Mandrika, J. Pupure, J. Rumaks, B. Jansone, I. Kalvinsh and H. V. Vinters, Mildronate enhances learning/memory and changes hippocampal protein expression in trained rats, *Pharmacol. Biochem. Be.*, 2013, **106**, 68-76.
184. V. Z. Klusa, S. Isajevs, D. Svirina, J. Pupure, U. Beitnere, J. Rumaks, S. Svirskis, B. Jansone, Z. Dzirkale, R. Muceniece, I. Kalvinsh and H. V. Vinters, Neuroprotective Properties of Mildronate, a Small Molecule, in a Rat Model of Parkinson's Disease, *Int. J. Mol. Sci.*, 2010, **11**, 4465-4487.
185. J. Pupure, S. Isajevs, E. Skapare, J. Rumaks, S. Svirskis, D. Svirina, I. Kalvinsh and V. Klusa, Neuroprotective properties of mildronate, a mitochondria-targeted small molecule, *Neurosci. Lett.*, 2010, **470**, 100-105.
186. B. Svalbe, L. Zvejniece, E. Vavers, O. Pugovics, R. Muceniece, E. Liepinsh and M. Dambrova, Mildronate treatment improves functional recovery following middle cerebral artery occlusion in rats, *Behav. Brain Res.*, 2011, **222**, 26-32.
187. M. Makrecka, B. Svalbe, K. Volska, E. Sevostjanovs, J. Liepins, S. Grinberga, O. Pugovics, E. Liepinsh and M. Dambrova, Mildronate, the inhibitor of L-carnitine transport, induces brain mitochondrial uncoupling and protects against anoxia-reoxygenation, *Eur. J. Pharmacol.*, 2014, **723**, 55-61.
188. U. Beitnere, Z. Dzirkale, S. Isajevs, J. Rumaks, S. Svirskis and V. Klusa, Carnitine congener mildronate protects against stress-and haloperidol-induced impairment in memory and brain protein expression in rats, *Eur. J. Pharmacol.*, 2014, **745**, 76-83.
189. G. S. Ribas, C. R. Vargas and M. Wajner, L-carnitine supplementation as a potential antioxidant therapy for inherited neurometabolic disorders, *Gene*, 2014, **533**, 469-476.
190. K. Sahlin, E. K. Sallstedt, D. Bishop and M. Tonkonogi, Turning down Lipid Oxidation during Heavy Exercise - What Is the Mechanism?, *J. Physiol. Pharmacol.*, 2008, **59**, 19-30.
191. J. Jeppesen and B. Kiens, Regulation and limitations to fatty acid oxidation during exercise, *J. Physiol. London*, 2012, **590**, 1059-1068.
192. J. A. Romijn, E. F. Coyle, L. S. Sidossis, X. J. Zhang and R. R. Wolfe, Relationship between fatty acid delivery and fatty acid oxidation during strenuous exercise, *J. Appl. Physiol.*, 1995, **79**, 1939-1945.
193. L. Vecchiet, F. Dilisa, G. Pieralisi, P. Ripari, R. Menabo, M. A. Giamberardino and N. Siliprandi, Influence of L-Carnitine Administration on Maximal Physical Exercise, *Eur. J. Appl. Physiol. O.*, 1990, **61**, 486-490.
194. B. T. Wall, F. B. Stephens, D. Constantin-Teodosiu, K. Marimuthu, I. A. Macdonald and P. L. Greenhaff, Chronic oral ingestion of L-carnitine and carbohydrate increases

muscle carnitine content and alters muscle fuel metabolism during exercise in humans, *J. Physiol. London*, 2011, **589**, 963-973.
195. J. Kakhabrishvili, N. Chabashvili, V. Akhalkatsi and e. al., Effect of Mildronate on physical working capacity of highly qualified judoka, *Ann. Biomed. Res. Educ. Tbilisi State Med. Univ.*, 2002, **2**, 263-266.
196. S. I. Baulin, S. M. Rogacheva, S. V. Afanaseva, E. V. Zabanova and Y. V. Karagaycheva, Pharmaceutical Composition for Improving Physical Working Capacity, *B. Exp. Biol. Med.*, 2015, **160**, 45-48.
197. Y. Peng, J. Yang, Z. R. Wang, J. W. Wang, Y. Liu, Z. J. Luo and A. D. Wen, Determination of mildronate by LC-MS/MS and its application to a pharmacokinetic study in healthy Chinese volunteers, *J. Chromatogr. B.*, 2010, **878**, 551-556.
198. J. Zhang, L. J. Cai, J. Yang, Q. Z. Zhang and W. X. Peng, Nonlinear pharmacokinetic properties of mildronate capsules: a randomized, open-label, single- and multiple-dose study in healthy volunteers, *Fundam. Clin. Pharm.*, 2013, **27**, 120-128.
199. Y. Zhu, G. Y. Zhang, J. Zhao, D. S. Li, X. D. Yan, J. F. Liu, X. D. Liu, H. B. Zhao, J. L. Xia, X. Zhang, Z. Y. Li, B. R. Zhang, Z. C. Guo, L. Y. Feng, Z. D. Zhang, F. Qu and G. Zhao, Efficacy and Safety of Mildronate for Acute Ischemic Stroke: A Randomized, Double-Blind, Active-Controlled Phase II Multicenter Trial, *Clin. Drug Invest.*, 2013, **33**, 755-760.
200. Z. Zhao, J. Chen, W. Peng, X. Wang, Z. Chen, H. Tang, Y. Liang, Z. Ma, J. Chen, X. Chen, G. Zhong and M. Huang, Single- and Multiple-dose Pharmacokinetic, Safety and Tolerability Study of Mildronate Injection in Healthy Chinese Subjects Pharmacokinetic of Mildronate Injection, *Drug. Res.*, 2016, **66**, 251-256.
201. K. Tars, J. Leitans, A. Kazaks, D. Zelencova, E. Liepinsh, J. Kuka, M. Makrecka, D. Lola, V. Andrianovs, D. Gustina, S. Grinberga, E. Liepinsh, I. Kalvinsh, M. Dambrova, E. Loza and O. Pugovics, Targeting carnitine biosynthesis: discovery of new inhibitors against gamma-butyrobetaine hydroxylase, *J. Med. Chem.*, 2014, **57**, 2213-2236.

Chapter 2

The stereochemistry of TMLH catalysis

Contents

2.0 THE STEREOCHEMISTRY OF TMLH CATALYSIS 46

2.1 INTRODUCTION: THE FIRST STEP IN CARNITINE BIOSYNTHESIS 46

2.1.1 Structural determination of the TMLH product 47

2.2 B-HYDROXY-A-AMINO ACID SYNTHESIS 48

2.3 PUBLISHED SYNTHESES OF 3-HYDROXYLYSINES 49

2.3.1 Chemical Syntheses 49

2.3.2 Biocatalytic synthesis 51

2.4 ACCESSING VICINAL AMINO ALCOHOL FRAGMENTS WITH THE ALDOL REACTION 52

2.4.1 Synthesis of (-)-chloramphenicol (8) and other amino alcohols 52

2.4.2 Synthesis of (2R,3S)-3-hydroxylysine (19) using a stereoselective aldol 53

2.5 SYNTHESIS OF 3-HYDROXY-N^{ε}-TRIMETHYLLYSINE 54

2.5.1 Previous attempts 3-hydroxylysine synthesis – work by M. Muenzel 54

2.5.2 Towards 3-hydroxy-Nε-trimethyllysine: Implementing the asymmetric aldol 55

2.5.3 Chiral oxazoline formation 56

2.5.4 Utilising the formamide protecting group 58

2.5.5 Mosher's method for determination of e.r and absolute stereochemistry 60

2.6 (2*S*,3*R*)-3-HYDROXYLYSINE (24) AS A STANDARD FOR AMINO ACID ANALYSIS 65

2.7 DETERMINATION OF THE TMLH PRODUCT 67

2.7.1 TML Turnover by ^{1}H NMR 67

2.7.2 Assignment of the TMLH product 68

2.7.2.1 2D NMR Analysis 68

2.7.2.2 Proving the TMLH product stereochemistry and amino acid analysis 69

2.8 MODELLING OF THE TMLH ACTIVE SITE 75

2.8.1 Sequence alignment 75

2.8.2 Analysis of TMLH homology modeling 77

2.8.2.1 Structural comparison and active site mutations 77

2.8.2.3 BBOX vs. TMLH hydroxylation 78

2.9 SUMMARY AND FUTURE PERSPECTIVES 79

2.10 GENERAL EXPERIMENTAL 81

2.10.1 Enzyme Production 81

2.11 NMR MATERIALS AND METHODS 82

2.12 AMINO ACID ANALYSIS 83

2.13 SYNTHESIS 84

Dibenzyl-4,4-diethoxybutan-1-amine 85
4-(dibenzylamino)butanal (49) 86
N-[(9*R*)-10,11-dihydrocinchonan-9-yl]-2-(diphenylphosphino)benzamide (33)[55] 86
tert-Butyl(2*S*,3*R*)-3-(6-(dibenzylamino)propyl)-2,3-dihydrooxazole-2-carboxylate (50) 88
tert-Butyl (2*S*,3*R*)-6-(dibenzylamino)-2-formamido-3-hydroxyhexanoate (51) 89
tert-Butyl (2*S*,3*R*)-6-amino-2-formamido-3-hydroxyhexanoate (51a) 90
(2*S*,3*R*)-2-amino-2-carboxy-3-hydroxy-*N,N,N*-trimethylpentan-6-aminium (48) 91
(2*S*,3*R*)-2,6-diamino-3-hydroxyhexanoic acid (24) 92

2.14 SYNTHESIS OF MOSHER'S ESTERS FOR STEREOCHEMICAL INVESTIGATION OF (51) 94

2.15 SYNTHESIS OF MOSHER'S AMIDES OF (48) 94

2.16 NMR SPECTRA 96

2.16.1 ^{1}H NMR spectrum of (2*S*,3*R*)/(2*R*,3*S*)-3HO-Lys (24). 96
2.16.2 ^{13}C NMR spectrum of (2*S*,3*R*)/(2*R*,3*S*)-3HO-Lys (24). 96
2.16.3 ^{1}H NMR spectrum of (2*S*,3*R*)/(2*R*,3*S*)-3HO-Lys (24). 97
2.16.4 ^{13}C NMR spectrum of (2*S*,3*R*)/(2*R*,3*S*)-3HO-Lys (24). 97
2.16.5 ^{1}H NMR spectrum of (2*S*,3*R*)/(2*R*,3*S*)-3HO-TML (48). 98
2.16.6 ^{13}C NMR spectrum of (2*S*,3*R*)/(2*R*,3*S*)-3HO-TML (48). 98

2.17 REFERENCES 99

2.0 The stereochemistry of TMLH catalysis

2.1 Introduction: the first step in carnitine biosynthesis

The essential metabolite L-carnitine is utilised by mammalian cells as a transport molecule,[1] enabling long-chain fatty acids to pass from the cytosol into the mitochondrial matrix where β-oxidation occurs.[2-4] Mammals obtain carnitine *via* biosynthesis from the amino acids lysine and methionine and from daily alimentation.[5-8] Carnitine biosynthesis itself has been the focus of numerous studies attempting to evaluate the 'druggabilty' of carnitine biosynthesis as a potential therapeutic target for the prevention and treatment of cardiovascular diseases, through the design of small molecule chemical probes targeting the $Fe^{(II)}$, 2-oxoglutarate (2OG) dependent oxygenase γ-butyrobetaine hydroxylase (BBOX). [9-17] In catalysing the final step in carnitine biosynthesis, BBOX carries out a pro-*R*, C-3 hydroxylation of gamma-butyrobetaine (**3**) to yield L-carnitine (**4**) (Figure 1).[16,18,19]

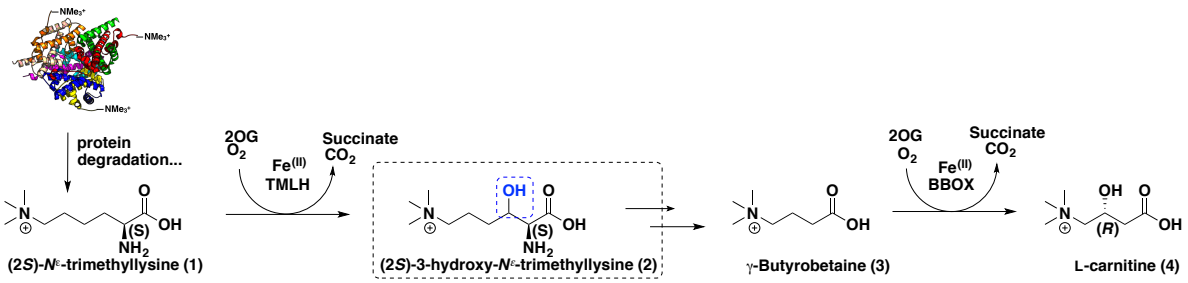


Figure 1 First and last steps of L-carnitine (**1**) biosynthesis in mammals. Both are catalysed by two 2-oxoglutarate oxygenases.

The first step of carnitine biosynthesis is catalysed by the 2OG-dependent, $Fe^{(II)}$ oxygenase N^{ε}-trimethyllysine hydroxylase (TMLH) (Figure 1).[20] TMLH catalyses the C-3 hydroxylation of N^{ε}-trimethyllysine (TML) (**1**) to 3-hydroxy-N^{ε}-trimethyllysine (3HO-TML) (**2**) in the mitochondrial matrix.[21] 3HO-TML is subsequently transported to the cytosol where the remaining three steps in carnitine biosynthesis take place.[21] TML is proposed to be a rate-limiting factor[1] in carnitine biosynthesis and it can be obtained from

the degradation of certain proteins such as histones and calmodulin that contain multiple *N*-methylated lysine residues.[22,23] Following methylation at the lysine ε-nitrogen and protein degradation by the lysosome, free TML is proposed to be liberated,[24,25] which can then be utilised in carnitine biosynthesis (Figure 1).[23] However, the exact origin of TML remains uncertain; and it has also been suggested that obtaining TML through diet could be more energetically economical.[23] Relatively little research has been conducted with regards to TMLH, which is surprising given its importance with regards to carnitine biosynthesis. Its submitochondrial locality for instance, was only established relatively recently.[21] Of the four carnitine biosynthesis enzymes, TMLH and BBOX are likely the most tractable candidates for the design of small molecule probes intended to alter carnitine levels.

Outside of being a potential target for carnitine biosynthesis inhibition, as mentioned in Chapter 1, TMLH has potential health implications with regards to autism, following several studies linking the condition to mutations in the *TMLHE* gene.[26-30] Here the synthetic and enzymatic studies are reported that describe the stereochemistry of the TMLH product (**2**).

2.1.1 Structural determination of the TMLH product

TMLH and BBOX share a common evolutionary ancestry as reflected in their sequence similarity (26%).[18,31] Greater conservation can be observed in their active site residues; and this is unsurprising for two reasons; (1) they both belong to the $Fe^{(II)}$, 2OG-dependent superfamily of enzymes and (2) catalyse a C-3 stereospecific hydroxylation of a quaternary ammonium substrate (Figure 1).[32-37] The stereochemistry of BBOX mediated GBB hydroxylation is well documented, however the stereochemistry of TMLH hydroxylation has never been absolutely defined. Early attempts at elucidating the structure of the TMLH product were successful in identifying functional groups present and a C-3 mode of hydroxylation.[20] Using ^{1}H and ^{13}C NMR, attempts were also made to identify the

stereochemical relationship between the C-2 and C-3 moieties of the TMLH product via comparison to synthetic, enantiopure 3-hydroxy lysine standards. Given the low resolution of NMR spectroscopy at the time (90 MHz) only a prediction of an '*erythro*' or (2*S*,3S) configuration of (**2**) could be made.[38] Thus taking a similar approach, an asymmetric synthesis of a diastereomer of (**2**) was undertaken, in order to prove absolutely, the stereochemistry of TMLH mediated hydroxylation of TML using NMR techniques.

2.2 β-Hydroxy-α-amino acid synthesis

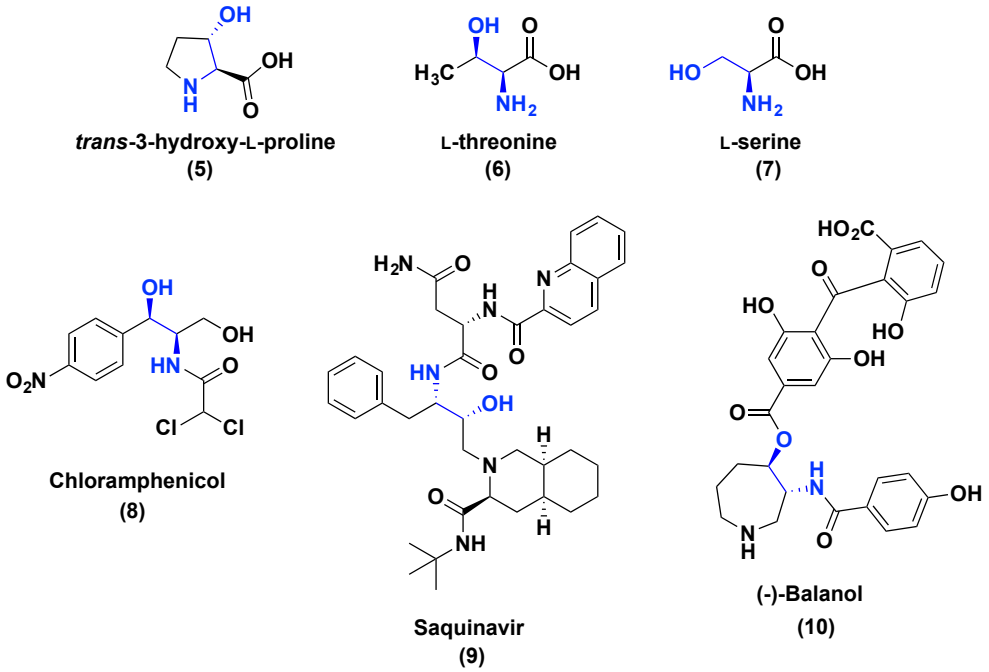


Figure 2 Naturally occurring amino acids and examples of pharmaceuticals containing the vicinal amino alcohol fragment.

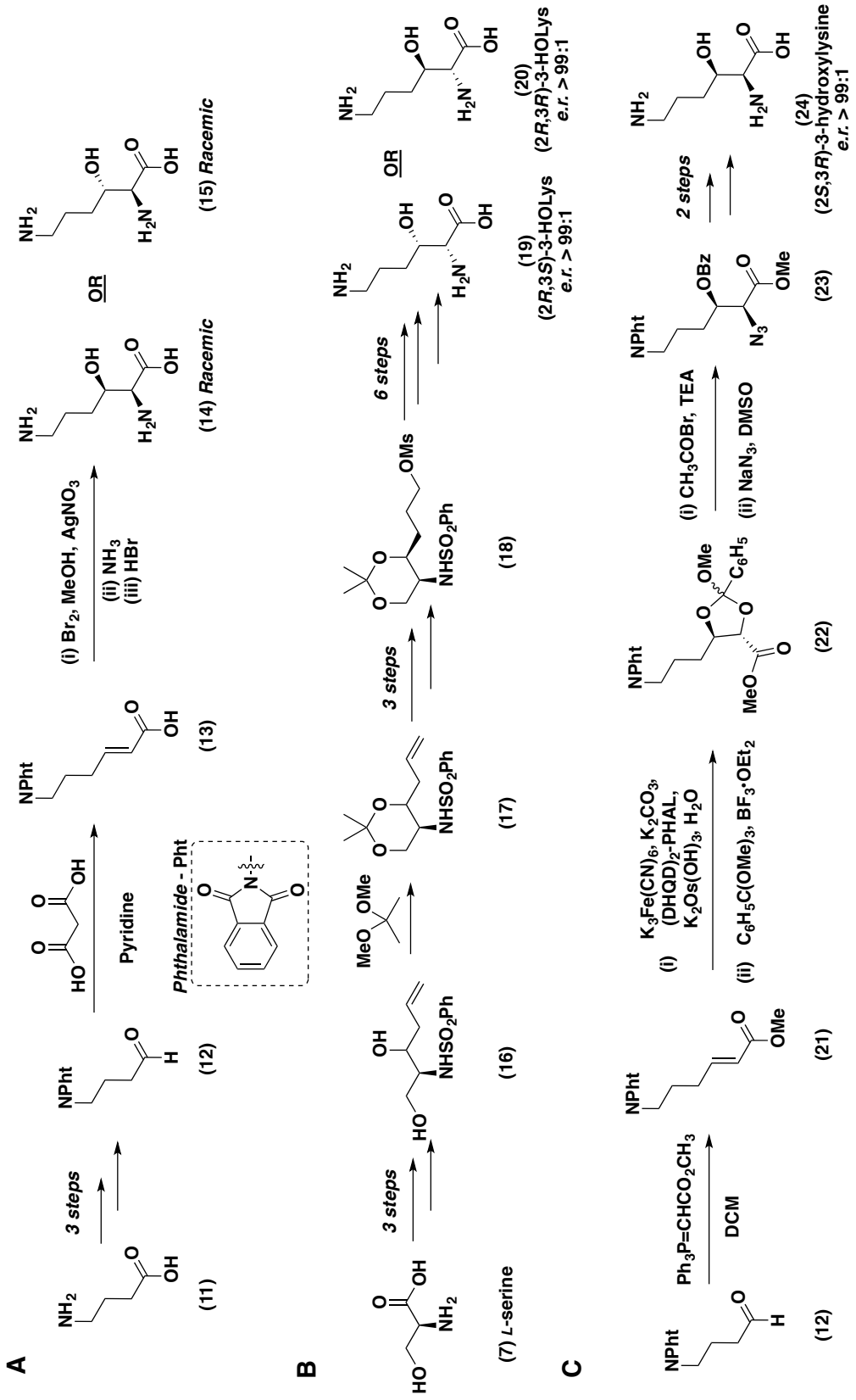
Vicinal amino alcohols are an important class of compounds that can manifest themselves as single β-hydroxy-α-amino acids (*e.g.* 3-hydroxy proline (**5**), serine (**7**) and threonine (**6**)) or as part of valuable, biologically active natural products such as the antibiotic chloramphenicol (**8**)[39,40] and the protease inhibitor for HIV treatement, saquinavir (**9**).[41] Many such compounds possessing chiral vicinal amino alcohol fragments are of interest in the field of synthetic organic chemistry, not only for their pharmacological activity but also for their potential as building blocks and chiral auxiliaries in organic synthesis.[42] Fuelled by

their high biological and synthetic value, numerous elegant synthetic strategies have emerged over the years to obtain these compounds in a diastereo- and enantioselective manner.[42,43] Given the nature of the target compound (**2**) the final synthesis was designed following analysis of published syntheses of the naturally occurring amino acid 3-hydroxy-lysine.

2.3 Published syntheses of 3-hydroxylysines

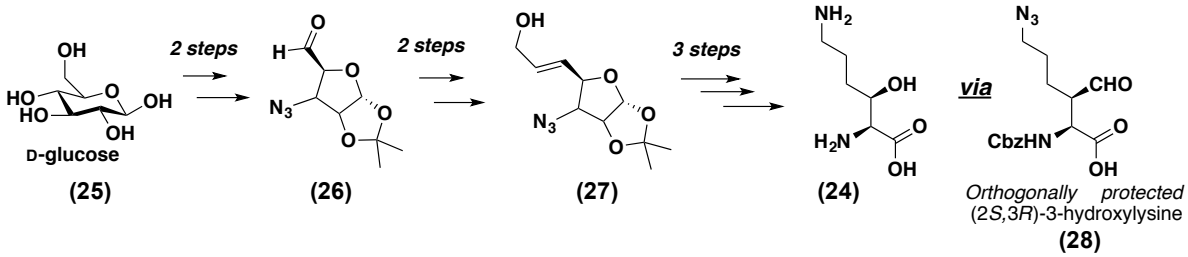
2.3.1 Chemical Syntheses

In efforts to synthesise cycloserine derivatives in the late 1960's Stammer and Webb required an achiral synthesis of 3-hydroxylysine (3HO-Lys) for use as an intermediate (Scheme 1 (**A**)),[44] aiming to have access to both *cis*- (**14**) and *trans*- (**15**) β-hydroxy amino fragments. One of the first asymmetric syntheses of 3HO-Lys was reported by Roemmele and Rapoport in 1989 (Scheme 1 (**B**)).[45] Through their broad investigation into synthesising various β-hydroxy amino acids involving the use of the chirally pure starting amino acid L-serine, they were able to access both *cis* (**19**) and *trans* (**20**) functionalities *i.e.* (2*R*,3*R*) and (2*R*,3*S*). A few years later in their attempts to synthesise (-)-Balanol (**10**), Hughes and co-workers utilised a Sharpless *cis*-hydroxylation to obtain (2*S*,3*R*)-3-hydroxylysine (**24**) with optical purity of > 99% in 7 steps (Scheme 1 (**C**)).[46-48] They also presented a second synthesis utilising an aldol condensation to obtain (2*R*,3*S*)-3-hydroxylysine (**23**) in an equally impressive optical purity of > 99% in a much shorter synthetic procedure.[46] More recently in 2000, a shorter synthesis of (**10**), again via (2*S*,3*R*)-3-hydroxylysine was published.[49] This was also achieved *via* an asymmetric Sharpless reaction, although this time the substrate for aminohydroxylation was an α,β-unsaturated aryl ester derivative of (**21**).[49] Although the synthesis is of similar length to the procedure followed by Hughes (7 steps),[46] the use of an aryl-ester derivative allowed successful introduction of the correct stereochemistry at the C-3 and C-4 positions in a one-pot asymmetric reaction. Recently, the



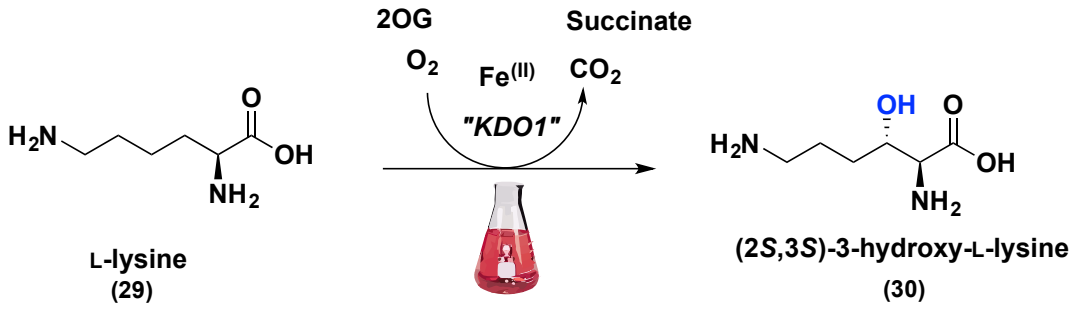
Scheme 1 Early syntheses of 3-HOLys. **A**) The first achiral synthesis of 3HO-Lys by Stammer *et al*.[44] **B**) A chiral synthesis of 3HO-Lys using the chirally pure *L*-serine as a starting point. Roemmele *et al*.[45] **C**) A chiral synthesis of 3HO-Lys utilising a chiral Sharpless *cis*-hydroxylation. Hughes *et al*.[46-48]

use of a chiron approach (utilising naturally occurring small molecules as starting materials) to the synthesis of 3HO-Lys (**24**) was published (scheme 2).[50] From chirally pure D-glucose (**25**) the authors were able to obtain (**24**) in 8 steps in excellent yield and optical purity. Importantly, aside from presenting a novel synthesis of (**24**), the method enabled the synthesis of an orthogonally protected 3HO-Lys (**28**) over 7 steps. This synthesis provided inspiration for an orthogonal protecting group strategy towards 3-hydroxy-N^{ε}-trimethyllysine (**39**), (Section 2.5.2). Although synthetically lengthy, given the biological importance of modified amino acids, the authors present a novel method of potentially incorporating 3HO-Lys into solid phase peptide synthesis via a Boc/Fmoc strategy.[50]



Scheme 2 Chiron approach used by Kumar *et al*,[50] to obtain orthogonally protected 3HO-Lys (**28**).

2.3.2 Biocatalytic synthesis



Scheme 3 The 2OG-oxygenase "KDO1" catalyses a C-3 pro-*S* hydroxylation of the free amino acid L-lysine (**29**).[51,52]

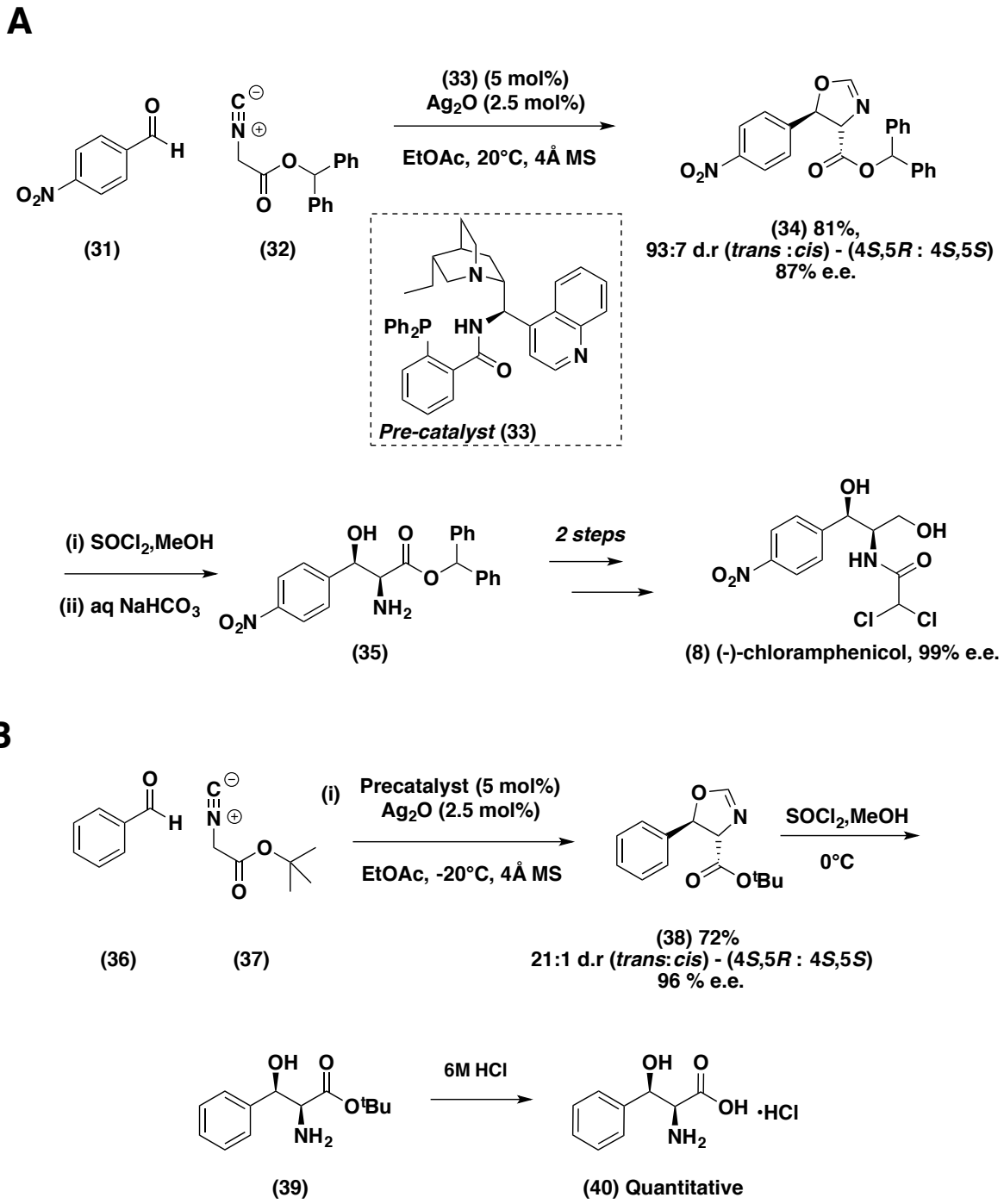
Recently, several previously uncharacterised $Fe^{(II)}$, 2OG-dependent oxygenases, discovered using a genome mining approach, were utilised for a large-scale production of hydroxylated amino acids.[51,52] An enzyme originating from *Catenullispora acidiphila* (DSM 44928,

UniProtKB ID: C7QJ42) named "KDO1" was shown to catalyse a C-3 pro-*S* hydroxylation of L-lysine (**29**) to give (2*S*,3*S*)-3-hydroxylysine (**30**). The stereochemistry of the product was determined by Mosher's analysis (Figure 3 and 4, Section 2.14).[51-53]

2.4 Accessing vicinal amino alcohol fragments with the aldol reaction

2.4.1 Synthesis of (-)-chloramphenicol (8) and other amino alcohols

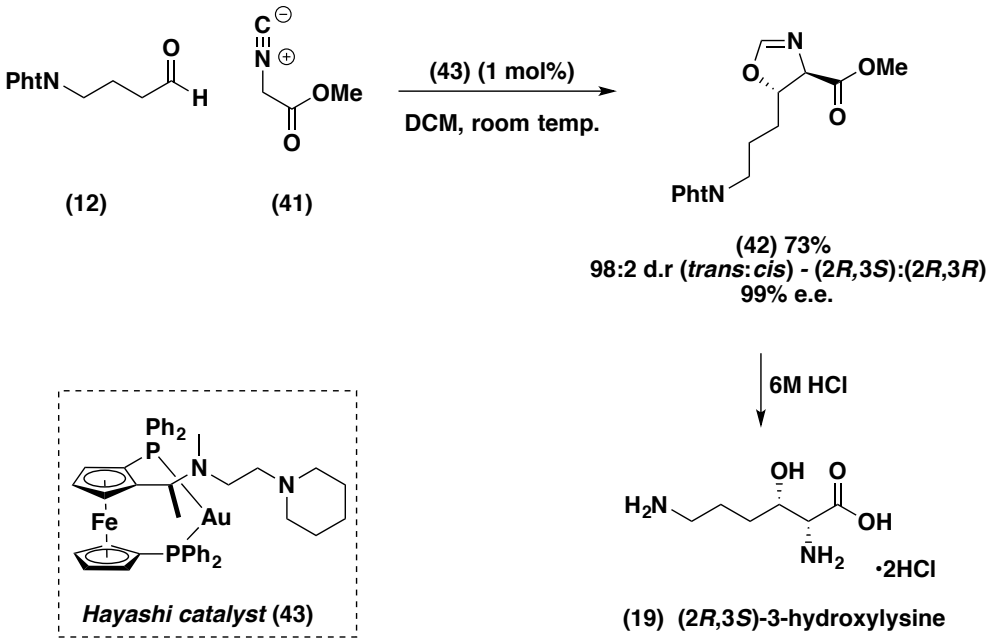
In 2015 an elegant synthesis of (-)-chloramphenicol (**8**) was published (Scheme 4).[40] Access to the chiral vicinal amino alcohol fragment of (**8**) was achieved by using a silver(I)-catalysed asymmetric isocyanoacetate aldol reaction involving a cinchona-derived amino-phosphine ligand (**33**) to generate a chiral *trans*-oxazoline (**34**).[54,55] Through tailoring chirally pure epicinchona-alkaloid starting materials to bear both Brønsted and Lewis basic sites, it was possible to provide activation sites for isocyanoacetate pronucleophiles (**32**, **37**) towards electrophiles such as aldehydes (**31**) and (**37**).[54,55] As a result, high diastereo- and enantio-control was achieved for oxazoline formation (Scheme 4). Moreover, formation of chiral *trans*-oxazolines allows for direct access to *trans*-amino alcohol motifs such as (**35**) and (**39**); the authors successfully screened a wide variety of aldehydes and isocyanoacetates for use with the asymmetric system. The elegance of this method in the context of accessing complex amino alcohol moieties is clear when further chemistry from the oxazoline is envisaged. With appropriate protection of the carboxylate function adjacent to the oxazoline, not only is it possible to directly access chiral β-hydroxy-α-amino acids such as (**40**) in one step, but by changing the strength of the acid used, α-amino protection *via* oxazoline hydrolysis is also achievable.[40,54] Compared to alternative syntheses of vicinal amino alcohols an attraction of this method is the mildness of the conditions used making it potentially suited to large-scale synthesis.



Scheme 4 A) Synthetic route used to obtain (-)-chloramphenicol (**8**), making use of an asymmetric aldol reaction.[40] **B**) Accessing β-hydroxy-α-amino acid (**40**) *via* silver(I)-catalysed asymmetric oxazoline synthesis.[54]

2.4.2 Synthesis of (2*R*,3*S*)-3-hydroxylysine (19) using a stereoselective aldol reaction

In the same publication as mentioned above (Section 2.3.1), Hughes *et al* were able to utilise a stereoselective aldol reaction to synthesise (2*R*,3*S*)-3-hydroxylysine (**19**) in 4 steps with excellent yield and optical retention (Scheme 5).[46,48] The authors presented the first use



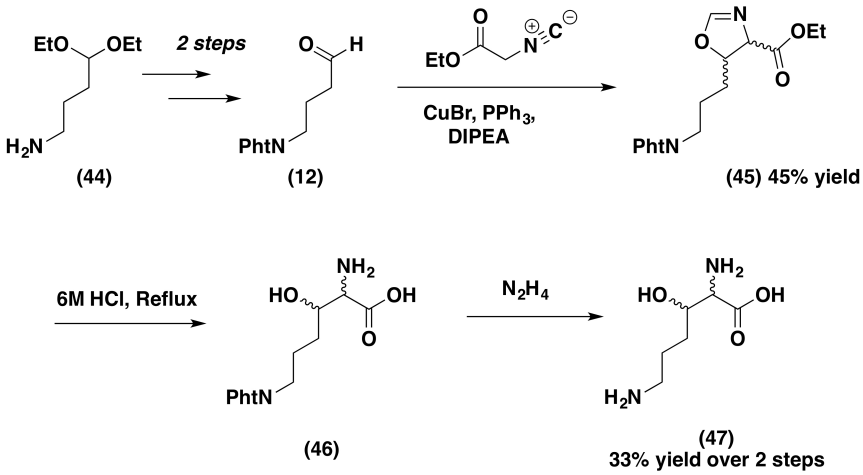
Scheme 5 Synthetic route followed by Hughes *et al* in their synthesis of (2*S*,3*R*)-3-hydroxylysine (**19**), making use of an asymmetric aldol reaction catalysed by Hayashi's ferroceno gold catalyst (**43**).[46,48]

of Hayashi's ferroceno gold catalyst (**43**)[56] (which had been used previously to synthesise β-hydroxy-α-amino acids)[57,58] towards the synthesis of chiral 3-hydroxylysine (**19**). The downfall of using the Hayashi catalyst (**43**) used by Hughes is that the opposite stereochemistry is obtained at the α-amino function (2*R*), when natural lysine (**29**) is usually (2*S*). Although the Hayashi catalytic system has been used to generate oxazolines providing the correct (2*S*)-stereochemistry, Hayashi catalysts can be difficult and expensive to synthesise.[58]

2.5 Synthesis of 3-hydroxy-N^{ε}-trimethyllysine

2.5.1 Previous attempts 3-hydroxylysine synthesis – work by M. Muenzel

The synthesis of racemic 3HO-Lys (**47**) was recently required for use as a biological standard in the Schofield laboratory. Using an achiral synthesis it was possible to obtain (**47**) as a racemic mixture of *cis*- and *trans*-diastereomers over 5 steps (Scheme 6). This was achieved *via* an achiral aldol to give oxazoline (**45**). (**45**) was hydrolysed in refluxing 6M HCl at the oxazoline and ester functions to give vicinal amino alcohol (**46**).

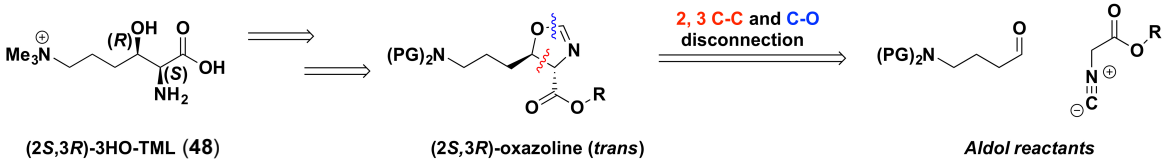


Scheme 6 An achiral synthetic route used within the Schofield laboratory (Martin Muenzel) to obtain 3-hydroxylysine as a diastereomeric mixture.

One issue encountered with this synthesis is that, the ε-amino phthalimide protecting group of (**46**) was troublesome to remove under the published conditions.[46] Although treatment with hydrazine eventually liberated the free 3HO-Lys (**47**), a significantly reduced overall yield was observed. From this synthesis and that presented in Section 2.4.2 however, it was clear that the correct α-amino stereochemistry could be achieved *via* an asymmetric aldol if the correct chiral ligand could be used.

2.5.2 Towards 3-hydroxy-*N*$^{\varepsilon}$-trimethyllysine: Implementing the asymmetric aldol

Overall, the published syntheses and initial attempts to synthesise 3HO-Lys, suggested that the easiest isomer of 3HO-TML (**2**) to produce could be (**48**), *i.e*. the (2*S*,3*R*) isomer. This could be achieved *via* a 2,3 C-C disconnection making use of an aldol reaction to create a chiral (2*S*,3*R*) oxazoline and hence a C-C bond (Scheme 7).

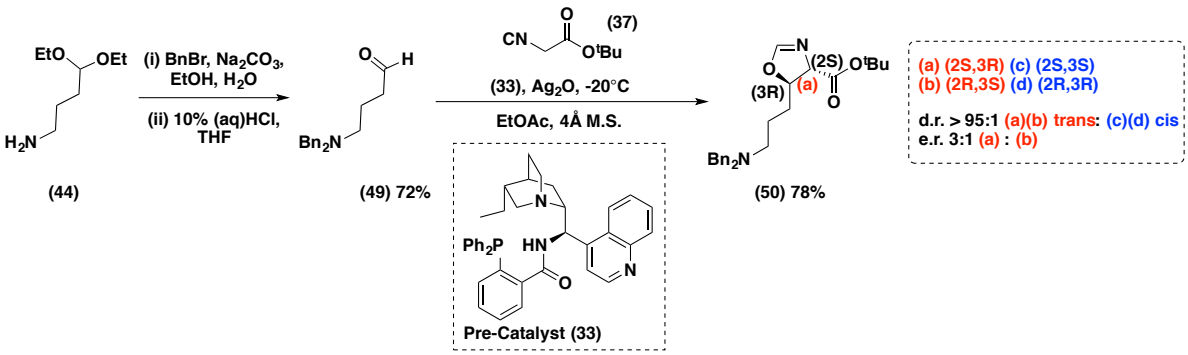


Scheme 7 Disconnection strategy used to generate proposed aldol reagents required for (2*S*,3*R*)-3HO-TML (**48**).

It was envisaged that *via* the use of the Dixon silver asymmetric oxazoline synthesis[54] it would be possible to introduce the desired (2*S*)-stereochemistry at the *N*-α position. This would also enable access to an orthogonally protected 3HO-Lys derivative (**28**, Section 2.3) in order to alkylate the *N*-ε whilst keeping the *N*-α protected. Focus then turned to which *N*-ε protecting group would be most suitable. From previous attempts at synthesising 3HO-Lys mentioned in (Section 2.5.1), the phthalimide protecting group seemed difficult to remove and was sparingly soluble in many solvents. Given the Dixon oxazoline synthesis uses EtOAc it was thought best to avoid this protecting group. Taking inspiration from the work of Kumar,[50] where the *N*-ε was maintained as a Pd/C reducible azide (**28**), it was decided to use a di-benzyl protection of the *N*-ε, thus providing an orthogonally protected 3HO-Lys derivative. A di-benzyl protection seemed necessary as a protecting group given the early work of Stammer (Section 2.3) showed a mono-Cbz, *N*-ε protection led to cyclisation.[44] As a carboxylate protecting group, a *t*-butyl ester was employed; the work of Dixon showed *t*-butyl esters conveyed stereochemical information better than Me, Et, and iPr analogues and that the *t*-butyl ester survived oxazoline hydrolysis.[40,54] Secondly, it was envisaged that removal of the *t*-butyl ester could be carried out in tandem with any acid labile *N*-α protecting group, so reducing the number of total steps to the target compound (**48**).

2.5.3 Chiral oxazoline formation

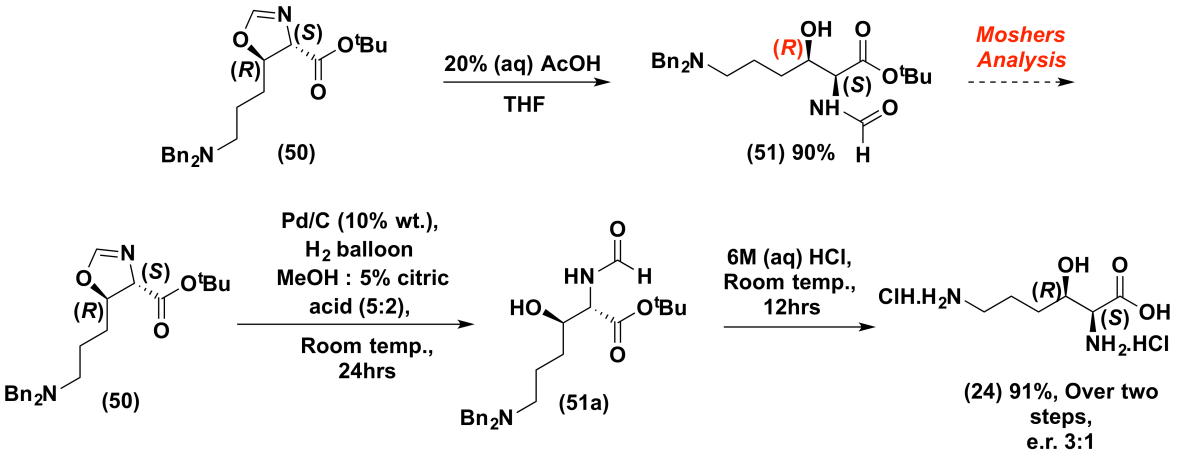
From commercially available 4-aminobutyraldehyde diethylacetal (**44**) it was possible to synthesise aldehyde (**49**) over two steps in excellent yield (Scheme 8). After synthesising pre-catalyst (**33**), following the literature protocols,[55,59] oxazoline (**50**) was obtained with high diastereoselectivity (2*S*,3*R*/2*R*,3*S* : 2*S*,3*S*/2*R*,3*R*; d.r. > 95 : 1, *trans*:*cis*). By comparison of ^{1}H NMR α- and β-proton coupling constants to values obtained in the literature for similar oxazolines ($J_{2\text{-}3}$ = 7.0 Hz),[40,54,60] it was concluded that the reaction



Scheme 8 Synthetic route used to obtain oxazoline (**50**) in a diastereo- and stereo-selective manner.

selectively produced the *trans*-diastereomer *i.e.* (2*S*,3*R*). The employed Dixon methodology yields *trans*-oxazolines; however, to identify the absolute stereochemistry, the configuration of the β-hydroxy function was then examined. Mosher's analysis proved a useful NMR-based method (described in full in Section 2.5.5),[53,61] not only for the determination of absolute configuration, but also for determining the optical purity of the Dixon aldol reaction (Figure 3 and 4) (2*S*,3*R* : 2*R*,3*S*; e.r. 3 : 1 inferred from analyses on (**51**)). Thus, it was possible to obtain corresponding Mosher's esters at the β-hydroxy function by making use of the natural degradation of oxazoline (**50**) to formamide (**51**), which was promoted using mild acid (Scheme 9) as reported.[54] The stereochemistry of the major stereoisomer of formamide (**51**) was assigned as (2*S*,3*R*) by ^{1}H NMR analysis of the corresponding Mosher's esters.[62] Assuming no inversion from (**50**) to (**51**), Mosher's analysis of (**50**) revealed an e.r. of 3:1 (2*S*,3*R* : 2*R*,3*S* and the C-3 alcohol was found to have an (*R*)-configuration. Interestingly, work published by Dixon revealed unfunctionalised aliphatic aldehydes do not show much diastereo- or enantio-control.[54] However, given that the aim was to obtain at least diastereomerically pure 3HO-TML (**48**), the level of stereocontrol achieved was useful.

2.5.4 Utilising the formamide protecting group

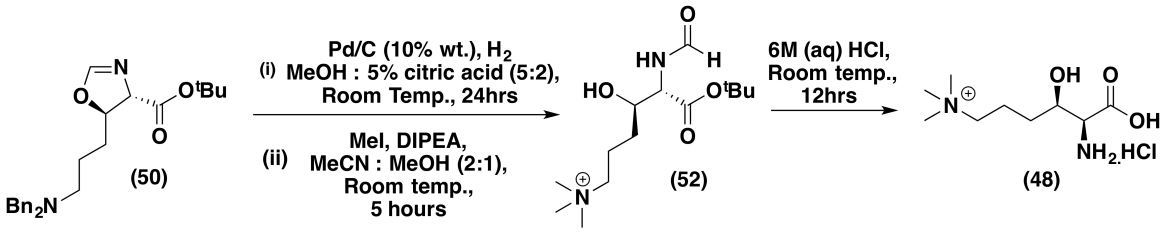


Scheme 9 2-step synthesis of (2*S*,3*R*)-3-hydroxy-lysine (**24**) from oxazoline (**50**). Hydrolysis of the oxazoline and di-benzyl reduction of (**50**) to give (**24**) can be carried out separately *via* (**51**) or in a one-pot reaction as displayed.

It was initially assumed there would be need to protect the free *N*-α after oxazoline cleavage with a protecting group such as the Boc group. However, after oxazoline (**50**) was observed to degrade to formamide (**51**) over time, even at -20°C, it was decided to utilise this natural degradation and use the formamide as a protecting group (Scheme 9).

Thus, a similar procedure to that utilised by Dixon and co-workers was employed, where the authors were able to promote formamide production, whilst maintaining the *t*-butyl ester by use of a mild acid.[54] Stirring oxazoline (**50**) in 5% (v/v) aqueous citric acid yielded, in a near quantitative manner, formamide (**51**). It was observed however, that a much faster chemo-selective oxazoline hydrolysis to formamide (**51**) was possible using 20% (v/v) aqueous AcOH in THF (1 hr versus 12 hrs).

Following from this reaction, one-pot reduction and oxazoline hydrolysis (Scheme 9) was attempted. It was hoped that this would shorted the synthesis of 3HO-Lys (**24**), and at the same time test the lability of the di-benzyl protecting groups. Pleasingly, oxazoline (**50**) was cleaved to the formamide along with both benzyl protecting groups being efficiently removed to give amine (**51a**). An excellent yield (91%) and optical retention (e.r. 3:1) was observed, after treatment with 6M HCl overnight at room temperature to give



Scheme 10 Synthetic route used to obtain (2*S*,3*R*)-3-hydroxy-*N*$^{\varepsilon}$-trimethyllysine (**48**)

(2*S*,3*R*)-3-hydroxylysine (**24**) over two steps. Use of 20% (v/v) AcOH for the one-pot reduction-hydrolysis was attempted; however, multiple products and incomplete conversion were observed. The approximate enantiomeric ratio was obtained for the final compound (**24**) by comparison to literature optical rotation values for optically pure (2*S*,3*R*)-3-hydroxylysine ($[\alpha]_D^{25}$ = +6.8 versus +16.9[46,50] (c = 1.83 in MeOH)). (**24**) was used within the laboratory as a diastereomerically pure biological standard for amino acid analysis. Consequently, the stereochemical outcome of two novel enzymes involved in epigenetic regulation was determined (described in Section 2.6). Following the successful synthesis of diastereomerically pure (**24**), the focus then returned to the synthesis of 3-hydroxy-*N*$^{\varepsilon}$-trimethyllysine (**48**). From (**50**) it was possible to trimethylate the *N*-ε after repeating the one-pot oxazoline hydrolysis and benzyl reduction procedure (Scheme 10). Pleasingly, normal-phase silica purification of quaternary amine (**52**) proved effective, given the presence of the *t*-butyl ester and formamide moieties, providing sufficient non-polar interactions. Thus, after treatment of quaternary amine (**52**) with 6M HCl at room temperature it was possible to obtain (2*S*,3*R*)-3-hydroxy-*N*$^{\varepsilon}$-trimethyllysine (**48**) over 6 steps. Reacting the *N*-α with Mosher's acid chloride, showed an identical e.r. to that observed from the Mosher's esters derived from formamide (**51**) (Figure 3, 4 and section 2.14).

2.5.5 Mosher's method for determination of e.r and absolute stereochemistry

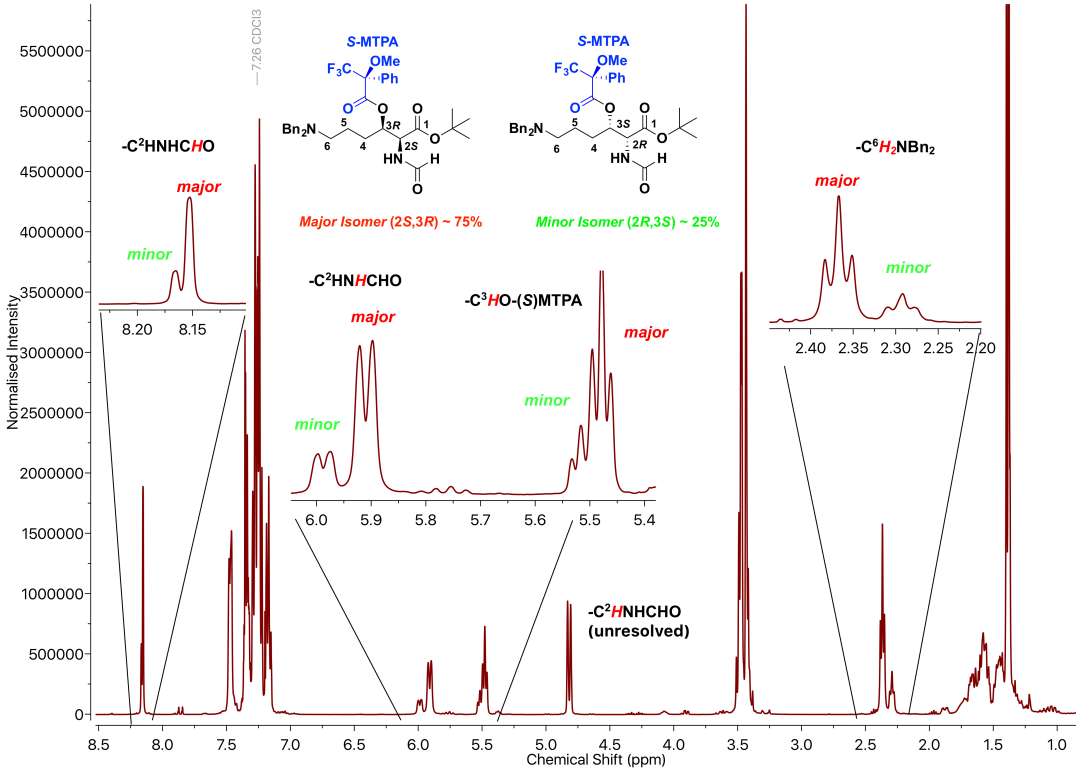


Figure 3 ^{1}H NMR spectrum of the Mosher's esters resulting from the reaction of formamide (**51**) with (*S*)-Mosher's acid. The signals used in the stereochemical assignment are enlarged.

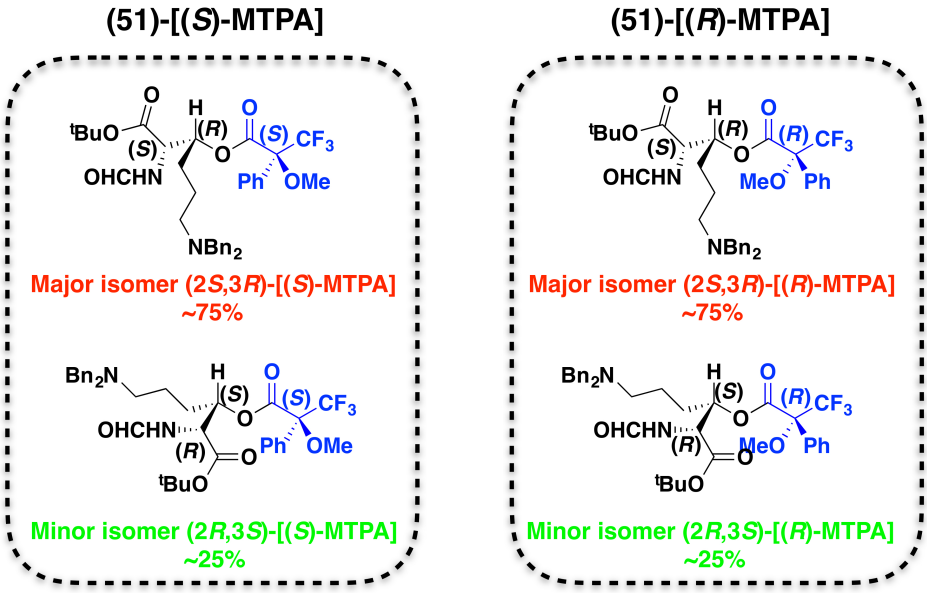
As yet, separation of the mixture of stereoisomers of oxazoline (**50**) has been unsuccessful by HPLC or crystallisation, hence the Mosher's method was used.[53] Mosher's analysis can be used to determine not only the enantiomeric ratio of certain chiral compounds but it can also be utilised for the determination of absolute stereochemistry.[61] Although initially described in 1973 by Dale and Mosher,[53] the method remains the most frequently applied NMR-based method used in the determination of otherwise unknown chiral carbon centers of secondary amines or alcohols.[61] The 'Mosher ester/amide analysis' is implemented *via*; (1) derivatisation of the enantiomeric mixture with (*S*)-α-methoxy-α-trifluoromethylphenylacetic acid (MTPA) and (*R*)-MTPA (Figure 4) and (2) ^{1}H NMR analysis (Figure 4) of both resulting (*S*)-MTPA (Figure 3) and (*R*)-MTPA (Figure 5) esters. Following derivatisation of the enantiomeric mixture with either (*S*)-MTPA or (*R*)-MTPA,

step (1) resolves the mixture into diastereomers, which display different chemical shifts in the ^{1}H NMR spectrum thus, allowing for e.r determination (*via* integration), provided the resolved signals are sufficiently separated. If both (*S*)-MTPA and (*R*)-MTPA esters are synthesised, step (2) can be applied, whereby the difference in chemical shifts between (*S*)-MTPA and (*R*)-MTPA esters ($\Delta\delta^{SR}$) can be determined. Following the determination of the chemical shift sign difference of $\Delta\delta^{SR}$ of the (*S*)-MTPA and (*R*)-MTPA esters, the absolute configuration of the chiral carbon center can be assigned (Figure 4).

The Mosher's analysis relies on an empirically derived and validated conformational model, which explains the observed effects of MTPA derivatisation on ^{1}H NMR spectra of chiral mixtures. Each diastereomer is arranged so that the $-CF_3$ group of the MTPA moiety and the C-H of the chiral alcohol/amine in question are *syn*-coplanar with the carbonyl group *i.e*. $R_1R_2\underline{C}(\underline{H})\text{-}\underline{O}\text{-}\underline{C}(=\underline{O})\text{-}\underline{C}\text{-}\underline{C}F_3$.[61] Once this arrangement is constructed, the observed differential (upfield/downfield) chemical shift changes observed between (*S*)-MTPA and (*R*)-MTPA esters can be attributed to differential anisotropic shielding induced by the phenyl substituent of the MTPA moiety on R_1 and R_2 substructures. Affected protons therefore are more or less shielded and thus more or less upfield respectively.[61]

Another reason for the popularity of the Mosher's method is likely a result of the ^{19}F NMR spectra that can be obtained of the resulting (*S*)-MTPA and (*R*)-MTPA esters (Figure 6).[63] Assuming the aforementioned *syn*-coplanar configuration, differences in ^{19}F NMR signals between diasteromeric (*S*)-MTPA and (*R*)-MTPA esters are attributed to the movement of the CF_3 moiety out of coplanarity in either the (*R*)- or (*S*)-ester with the other atoms of the Mosher model. This shift out of coplanarity, induces a lowering of induced shielding in one MTPA ester, which manifests as an observed upfield shift in the ^{19}F NMR spectrum relative to the opposite MTPA ester.

Successful derivatisation of the C-3 carbinol of formamide (**51**) with (*S*)-MTPA (Figure 3) and (*R*)-MTPA (Figure 6) acids enabled Mosher's ester analysis to be carried out using ^{1}H (Figure 4) and ^{19}F (Figure 6) NMR. Derivatisation of amide (**48**) (*R*)-Mosher's acid chloride allowed for the determination of the e.r of (**48**) (Figure 7).



Resolved proton signals	Major isomer of (51)-(*S*)-MTPA ^{1}H NMR δ^{S} (ppm)	Major isomer of (51)-(*R*)-MTPA ^{1}H NMR δ^{R} (ppm)	$\Delta\delta^{SR} = (\delta^{S} - \delta^{R})$ / (ppm)
-C*H*O	8.15	8.17	-0.02
-C^{2}N*H*CHO	5.91	6.03	-0.12
-C^{3}*H*O-MTPA	5.48	5.52	-0.04
-C^{6}*H*$_2$NBn$_2$	2.37	2.30	+0.07

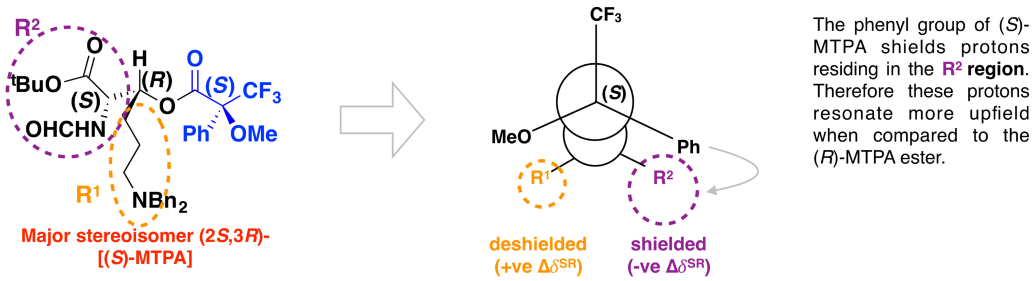


Figure 4 ^{1}H NMR Mosher ester analysis of the C-3 alcohol of formamide (**51**). $\Delta\delta^{SR}$ values obtained from analysis of ^{1}H NMR (400 MHz) spectra of (*S*)- and (*R*)-Mosher's ester derivatives, (**51**)-[(*S*)-MTPA] and (**51**)-[(*R*)-MTPA]. Calculation of $\Delta\delta^{SR}$ values enables assignment of the stereochemistry at C-3 of (9). $\Delta\delta^{SR} = (\delta^{S} - \delta^{R})$ i.e. $\Delta\delta^{SR} = \delta$(*S*-MTPA ester) - δ(*R*-MTPA ester). The basis of the Mosher's method is exemplified above for (2*S*,3*R*)-[(*S*)-MTPA].

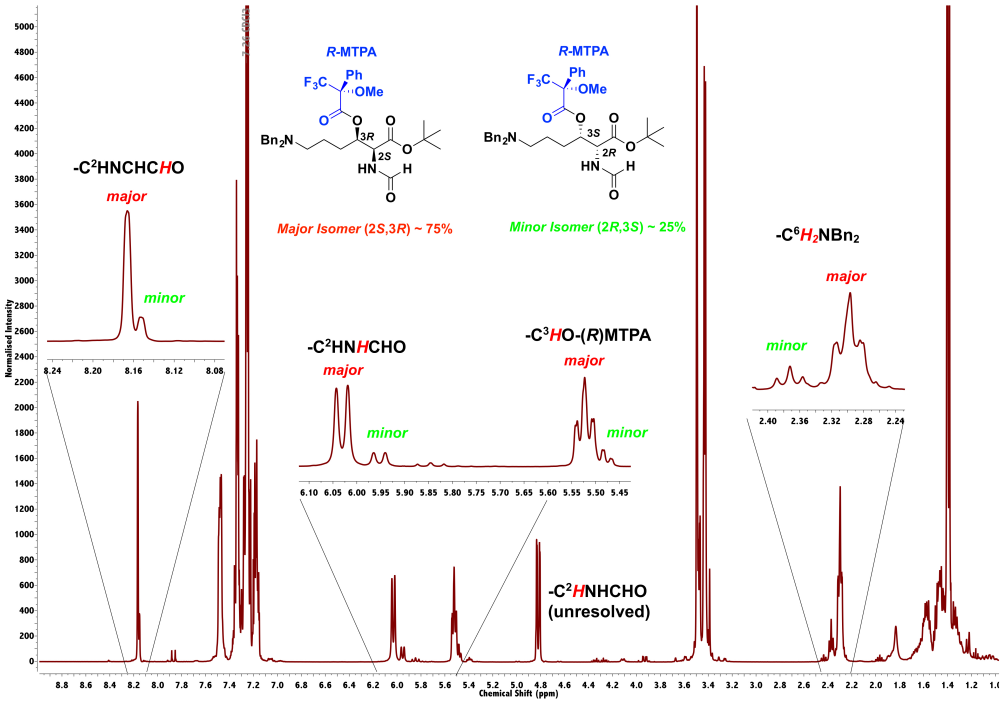


Figure 5 [1]H NMR spectrum of the Mosher's esters resulting from the reaction of formamide (**51**) with (*R*)-Mosher's acid. The signals used in the stereochemical assignment are enlarged.

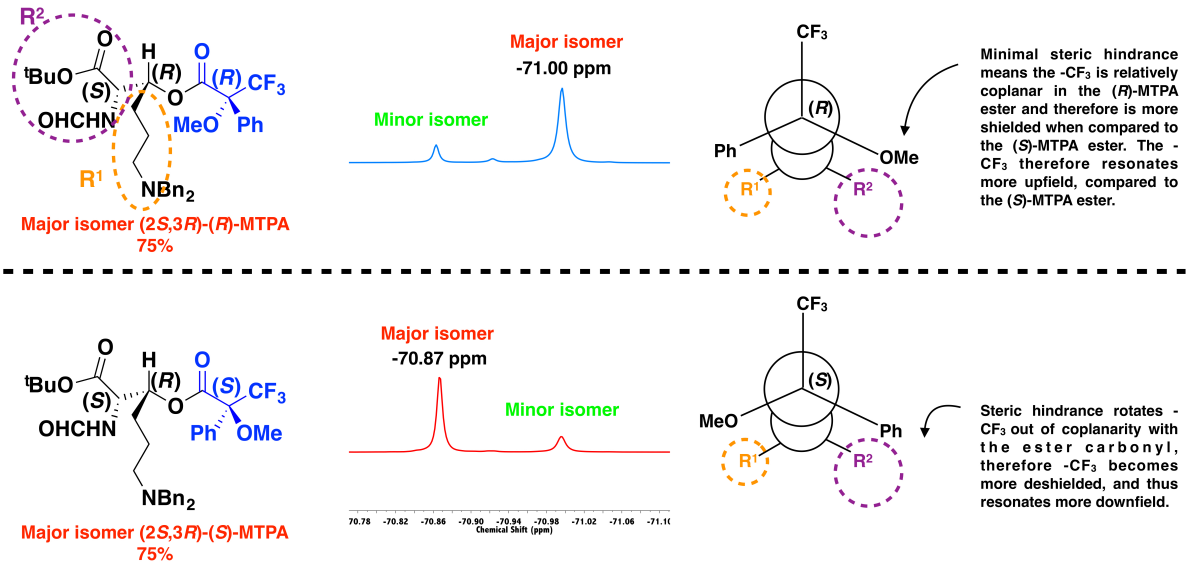


Figure 6 [19]F NMR Mosher ester analysis of the C-3 alcohol of formamide (**51**). Analysis of [19]F NMR (377 MHz) spectra of (*S*)- and (*R*)-Mosher's ester derivatives, (**51**)-[(*S*)-MTPA] and (**51**)-[(*R*)-MTPA]. Comparing [19]F resonances of both (**51**)-[(*S*)-MTPA] and (**51**)-[(*R*)-MTPA] supports the stereochemical assignment at C-3 of (**51**) as described in Figure 4.

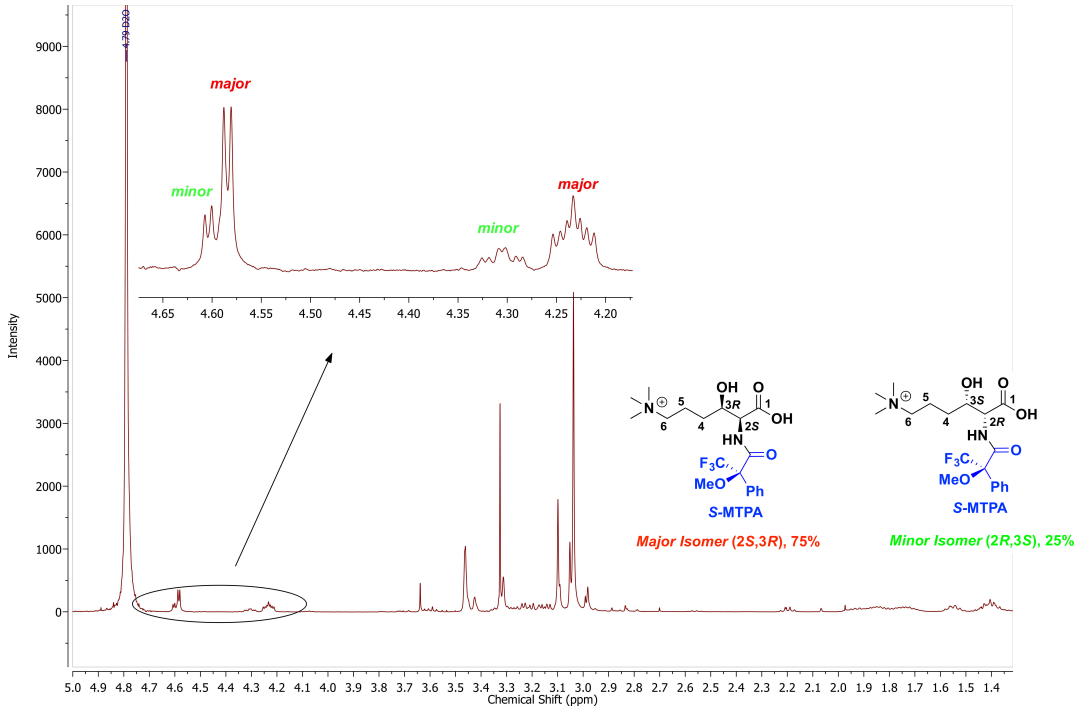


Figure 7 ^{1}H NMR spectrum of the crude aqueous reaction mixture of quaternary amine (**48**) and (*R*)-Mosher's acid chloride. The signals used in the stereochemical assignment are enlarged.

2.6 (2*S*,3*R*)-3-Hydroxylysine (24) as a standard for amino acid analysis

Lysyl hydroxylation is an important post-translational modification with physiological roles in collagen biosynthesis and protein synthesis.[64] The pro-collagen lysine 2-oxoglutarate 5-dioxygenase enzymes (PLODs) help maintain the structural integrity of the collagen triple helix by catalysing 5*R* lysyl hydroxylation of pro-collagen.[65] Lysyl hydroxylation occurs at the post-transcriptional level of protein synthesis *via* the 5*S* lysyl hydroxylation of splicing regulatory proteins by Jumonji domain-containing 6 (JMJD6).[64,65] Furthermore, C-4 lysyl hydroxylation (stereochemistry yet to be determined) of eukaryotic release factor 1 increases the efficiency of translation termination.[66] To date, no human C-3 lysyl hydroxylases have been reported.

Two uncharacterised human enzymes (which will be called Enzyme R and Enzyme S here), were identified by members of the Schofield Laboratory to catalyse C-3 lysyl hydroxylation (Markolovic, S. *et al*., manuscript in preparation; Gannon, J. *et al*., manuscript in preparation), though the stereochemistry of the modifications were unknown. (2*S*,3*R*)/(2*S*,3*R*)-3HO-Lys (**24**) was therefore used as a synthetic standard for amino acid analysis to determine the stereochemistry of Enzyme R- and Enzyme S-catalysed hydroxylation of their respective substrates. Comparison of (2*S*,3*R*)/(2*R*,3*S*)-3-hydroxylysine (**24**) with a racemic mixture of 3-hydroxylysine diastereomers [(2*S*,3*R*)/(2*R*,3*S*)/(2*S*,3*S*)/(2*R*,3*R*)] resolved the sets of stereoisomers (Figure 8A, 8B). Comparison of the standards with respective hydrolysed Enzyme R- and Enzyme S-treated substrate peptides revealed that the Enzyme R catalyses formation of the (3*R*) product, while Enzyme S catalyses the opposite stereochemistry (Figure 8). Given the physiological importance of lysyl hydroxylation, the work here illustrates the value of characterising the stereochemistry of new post-translational modifications with synthetic standards.

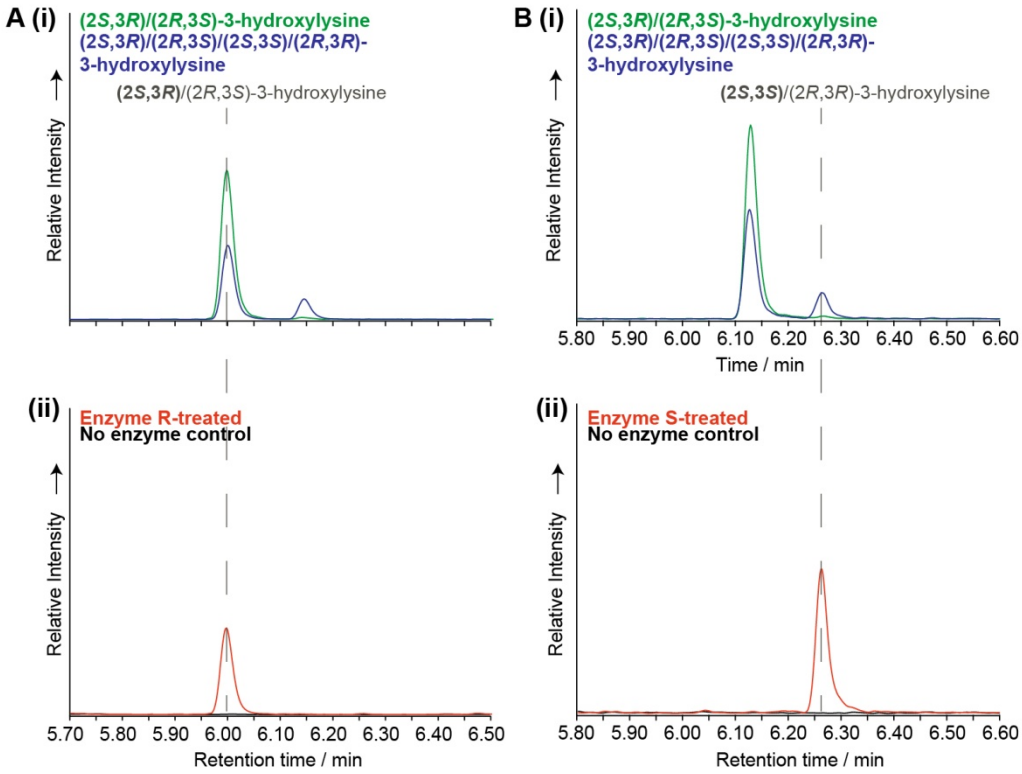


Figure 8 Using (2*S*,3*R*)/(2*R*,3*S*)-3-hydroxylysine as a standard for amino acid analysis and stereochemical determination. **A**) Overlaid extracted mass chromatograms (m/z = 503.2) of (**i**) the C-3 hydroxylysine standard (dark blue, a mixture of all stereoisomers) and the (2*S*,3*R*)/(2*R*,3*S*)-3-hydroxylysine standard (green), which co-elutes with the first C-3 hydroxylysine standard peak, and (**ii**) the hydrolysed Enzyme R substrate peptide, incubated without (black) or with Enzyme R (red) prior to hydrolysis and amino acid analysis. A new peak corresponding to the mass of derivatised hydroxylysine is observed in the Enzyme R-treated sample (red); it elutes at the same retention time as the first C-3 hydroxylysine peak, corresponding to the (2*S*,3*R*)/(2*R*,3*S*)-3-hydroxylysine stereoisomers. **B**) (**i**) See description for (**A**,**i**). (**ii**) Overlaid extracted mass corresponding to the hydrolyzed Enzyme S substrate peptide, incubated without (black) or with Enzyme S (red) prior to hydroylsis and amino acid analysis. A new peak corresponding to the mass of derivatised hydroxylysine is observed in the Enzyme S-treated sample (red), which elutes at the same retention time as the second C-3 hydroxylysine peak, corresponding to the (2*S*,3*S*)/(2*R*,3*R*)-3-hydroxylysine stereoisomers, opposite to that of Enzyme R.

2.7 Determination of the TMLH product

2.7.1 TML Turnover by ^{1}H NMR

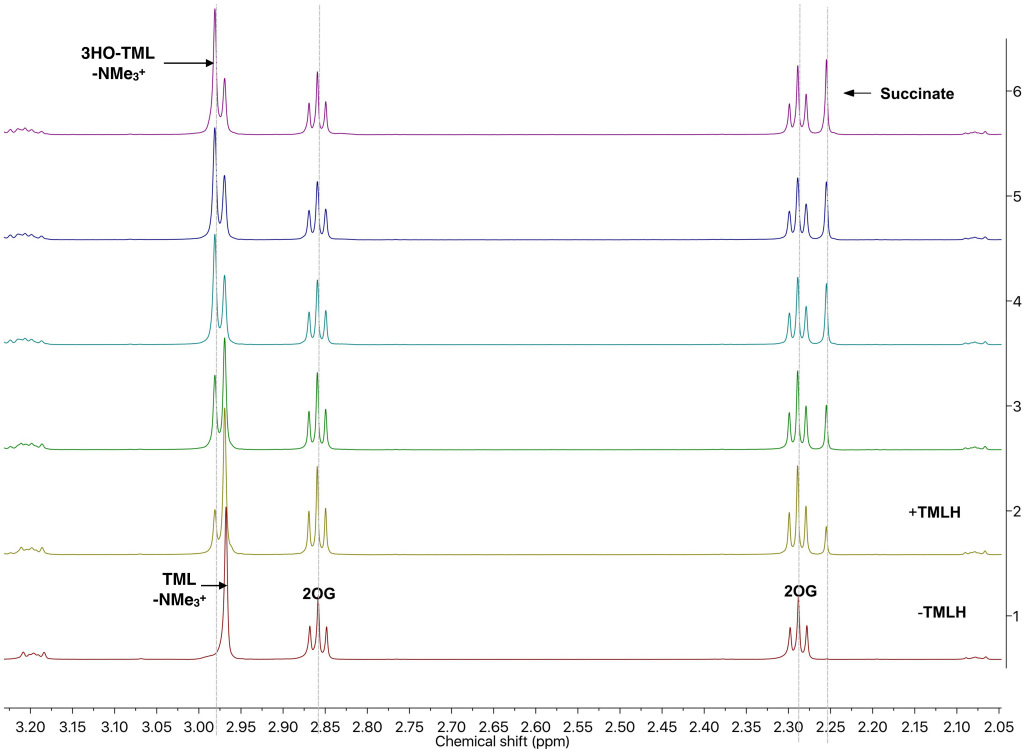


Figure 9 ^{1}H NMR spectra of TMLH catalysed TML hydroxylation (δ = 2.05-3.20 ppm). Reaction conditions: 500 μM TML, 1500 μM 2OG (mono-sodium), 500 μM L-ascorbate (di-sodium), 150 μM $Fe^{(II)}$ (from $(NH_4)_2Fe(SO_4)_2$) in 20 mM HCl), 10 μM TMLH, 50 mM Tris-d_{11}, 200 mM NaCl, pH 8.0.

After obtaining recombinant human TMLH (Section 2.10.1),[31] NMR, and crystallographic studies were initiated. From monitoring the reaction of TMLH with TML by ^{1}H NMR, in the presence of 2OG, and $Fe^{(II)}$, the activity of TMLH was confirmed, as evident by the observation of a new quaternary ammonium signal forming over time, apparently coupled to 2OG turnover to succinate (Figure 9). An approximate initial rate of formation of 3HO-TML was 1.30 μM.s^{-1} The first attempts at elucidating the TMLH product peaks proved challenging; formation of a new signal (doublet of triplets) resulting from C-3 hydroxylation was visible; however, the expected C-2 proton doublet was not observed (Figure 10).

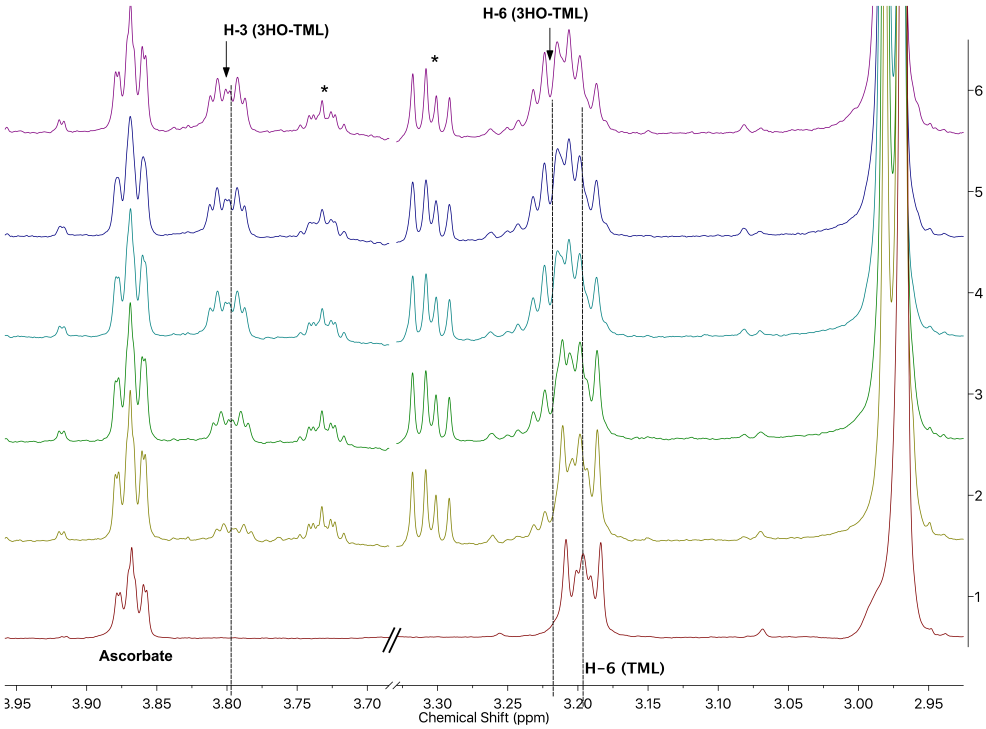


Figure 10 ^{1}H NMR spectrum of TMLH catalysed TML Hydroxylation (δ = 2.95-3.95 ppm). Reaction conditions: 500μM TML, 1500 μM 2OG (mono-sodium), 500 μM L-ascorbate (di-sodium), 150 μM $Fe^{(II)}$ (from $(NH_4)_2Fe(SO_4)_2$) in 20 mM HCl), 10μM TMLH, 50 mM Tris-d_{11}, 200 mM NaCl, pH 8.0. Signals arising between δ = 3.5 – 3.65 ppm (mainly glycerol) have been omitted for clarity.

2.7.2 Assignment of the TMLH product

2.7.2.1 2D NMR Analysis

Initial 2D ^{1}H-^{1}H COSY and ^{1}H-^{13}C HSQC indicated the missing signal was hidden underneath large glycerol impurities resulting from the protein preparation procedure (Section 2.7.2, 2.10.1). Adjustment of the reaction pH to 7.5 enabled clear observation of two new signals in the 1D ^{1}H NMR spectrum as a doublet (3.81 ppm, J = 3.3 Hz) and doublet of triplets (4.10 ppm, J = 10.1 Hz, J = 3.3 Hz) respectively (Section 2.7.2, Figure 12). Furthermore, near complete turnover of TML was observed. The TMLH product was thus confirmed as (2S)-3-hydroxy-trimethyllysine (Figure 12).

In order to conclusively assign the signals in ^{1}H NMR spectra resulting from TMLH incubations, further COSY and HSQC NMR experiments were carried out (Figure 13 and Figure 14, respectively). As expected, a distinct vicinal coupling pattern was observed

between the signals at 3.81 ppm and 4.10 ppm ($J_{2\text{-}3}$ = 3.3 Hz). These signals were thus assigned as H-2 and H-3 (Figure 11A, Figure 13, Figure 14) respectively. Further support for the assignment was obtained from the HSQC spectrum (Figure 14) where proton signals H-2 and H-3 were both confirmed to be part of tertiary carbon environments ($R_1R_2R_3C$-***H***) respectively (represented as blue spots in Figure 14). The COSY signal of H-3 showed the triplet splitting was due to coupling to a doublet of multiplets at 1.88 ppm and 1.78 ppm (Figure 13). These signals could therefore be assigned as the aliphatic protons on C-4, which was confirmed (a $R_1R_2C\boldsymbol{H_AH_B}$ environment is shown as red spots in Figure 14). The C-4 protons showed coupling to another doublet of multiplets in the COSY spectrum (Figure 13) which was assigned as C-5 following analysis of the HSQC spectrum (an $R_1R_2C\boldsymbol{H_AH_B}$ environment, Figure 14). The C-5 protons were observed to couple to a multiplet at a higher shift (3.34 ppm, Figure 13) and this signal was assigned at the $R_1R_2C\boldsymbol{H_AH_B}$ environment of C-6 after which concurred with the HSQC data (Figure 14).

2.7.2.2 Proving the TMLH product stereochemistry and amino acid analysis

Having identified the TMLH product using 2D NMR techniques, attention was focused on elucidating the stereochemistry of the C-3 hydroxy moiety. Given the inability of 'normal' ^{1}H NMR to discern between enantiomeric species, the objective was to observe an additive effect on the ^{1}H NMR spectrum of TMLH catalysed hydroxylation upon addition of (**48**) to the TMLH incubation. If this scenario proved to be true then this would suggest the TMLH product posesses the same stereochemistry as (**48**), *i.e.* the (2*S*,3*R*)-isomer. If the opposite situation was observed (TMLH product ^{1}H NMR signals differing to those of (**48**)), then it would be concluded that the TMLH product has the opposite stereochemistry to the synthetic standard (**48**), *i.e.* is the (2*S*,3*S*)-isomer.

On supplementing the reaction mixture with (**48**) a non-additive effect on the reaction product species (Figure 12 and Figure 15) was observed, indicating that the TMLH

product was the (2*S*,3*S*)-isomer. Following HPLC purification of the TMLH incubation (Figure 15) and assuming an inherent (*S*)-stereochemistry of the α-nitrogen of TML (**2**) and assuming no epimerisation, it was possible to assign the catalytic product of TMLH as (2S,3S)-3-hydroxy-*N*$^{\varepsilon}$-trimethyllysine (**30**). As further proof of the diastereoisomeric relationship between (**30**) and (**48**) amino acid analysis following AQC derivitisation of freeze-dried TMLH incubations with and without enzyme were carried out (Figure 11B and C).

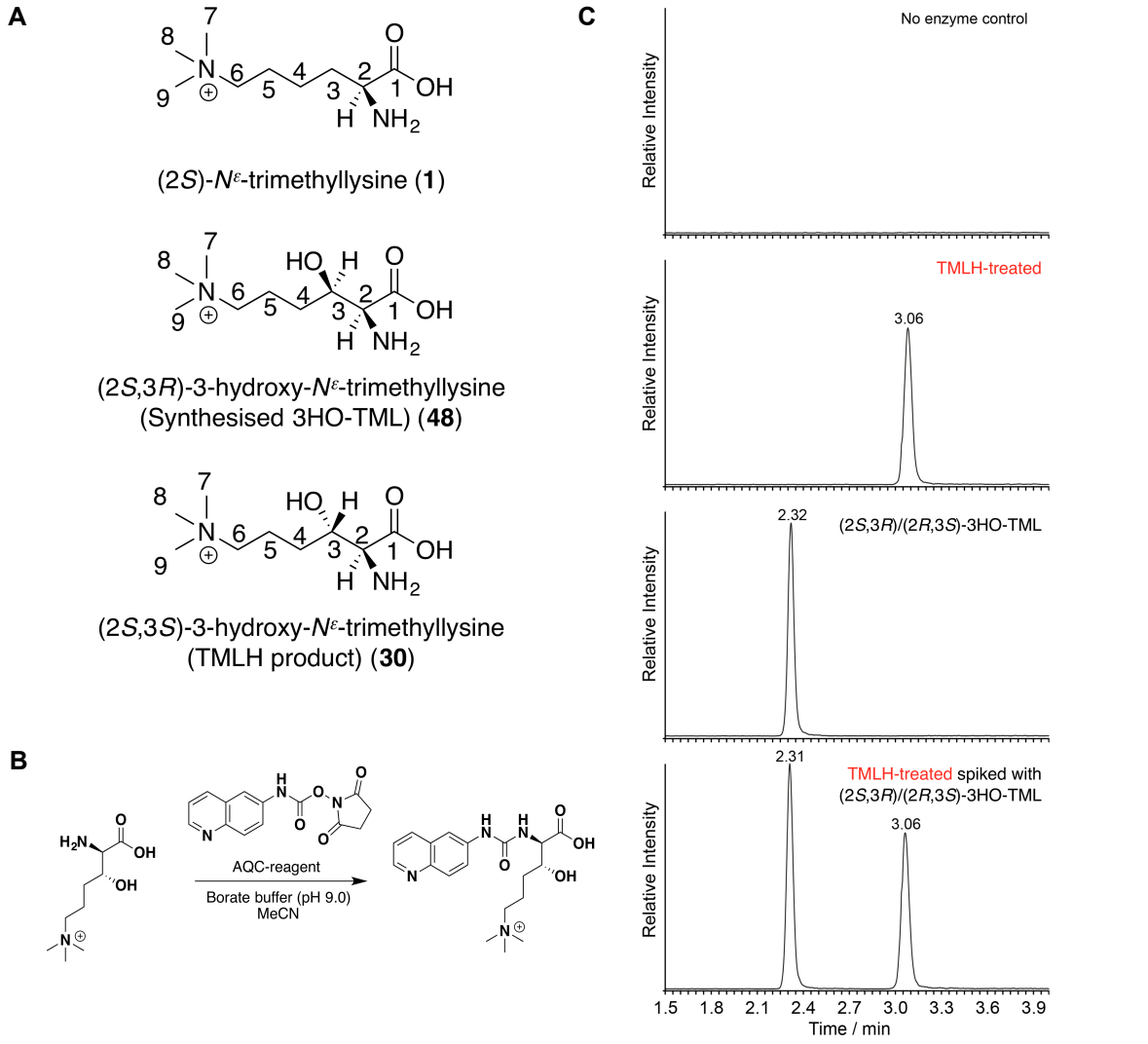


Figure 11 A) Numbering used in TMLH product assignment. **B**) Amino acid analysis of TML-catalysed hydroxylation product. Schematic representation of derivatisation of standard/product for amino acid analysis. **C**) Non-overlaid extracted ion chromatograms (m/z = 375.2) corresponding to the theoretical exact mass of AQC-derivatised 3HO-TML (theoretical m/z = 375.2032; observed m/z = 375.2114).

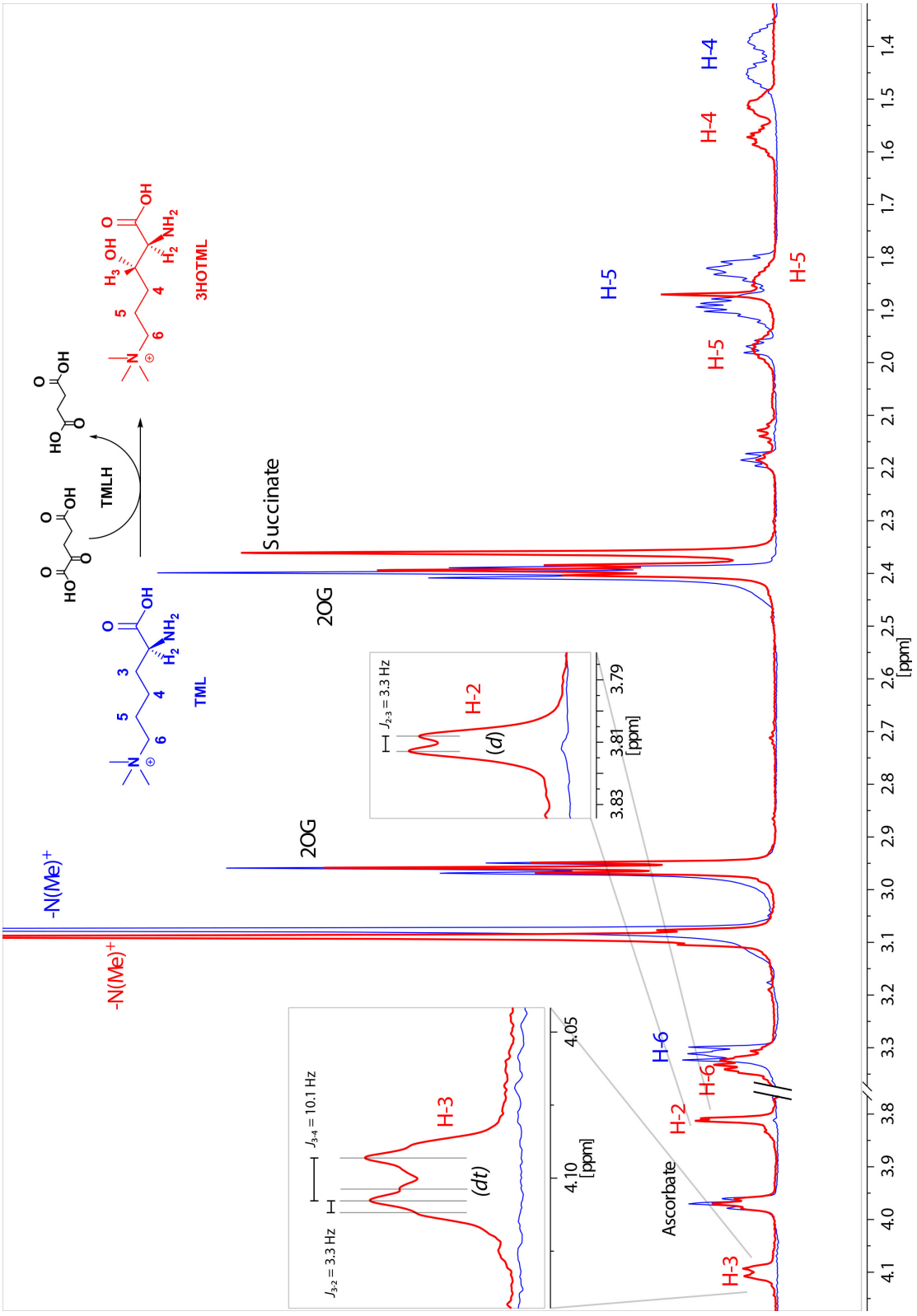


Figure 12 ^{1}H NMR assignments of the product resulting from TMLH catalysed hydroxylation of N^{ε}-trimethyllysine (**2**). Superimposing the ^{1}H NMR spectrum of the reaction mixture before (blue) and after (red) addition of TMLH displays product formation (**30**). Analysis of the splitting patterns of H2 and H3 reveal that the hydroxylation is occurring at the C-3 position. Signals arising between δ = 3.5 – 3.75 ppm (mainly glycerol) have been omitted for clarity.

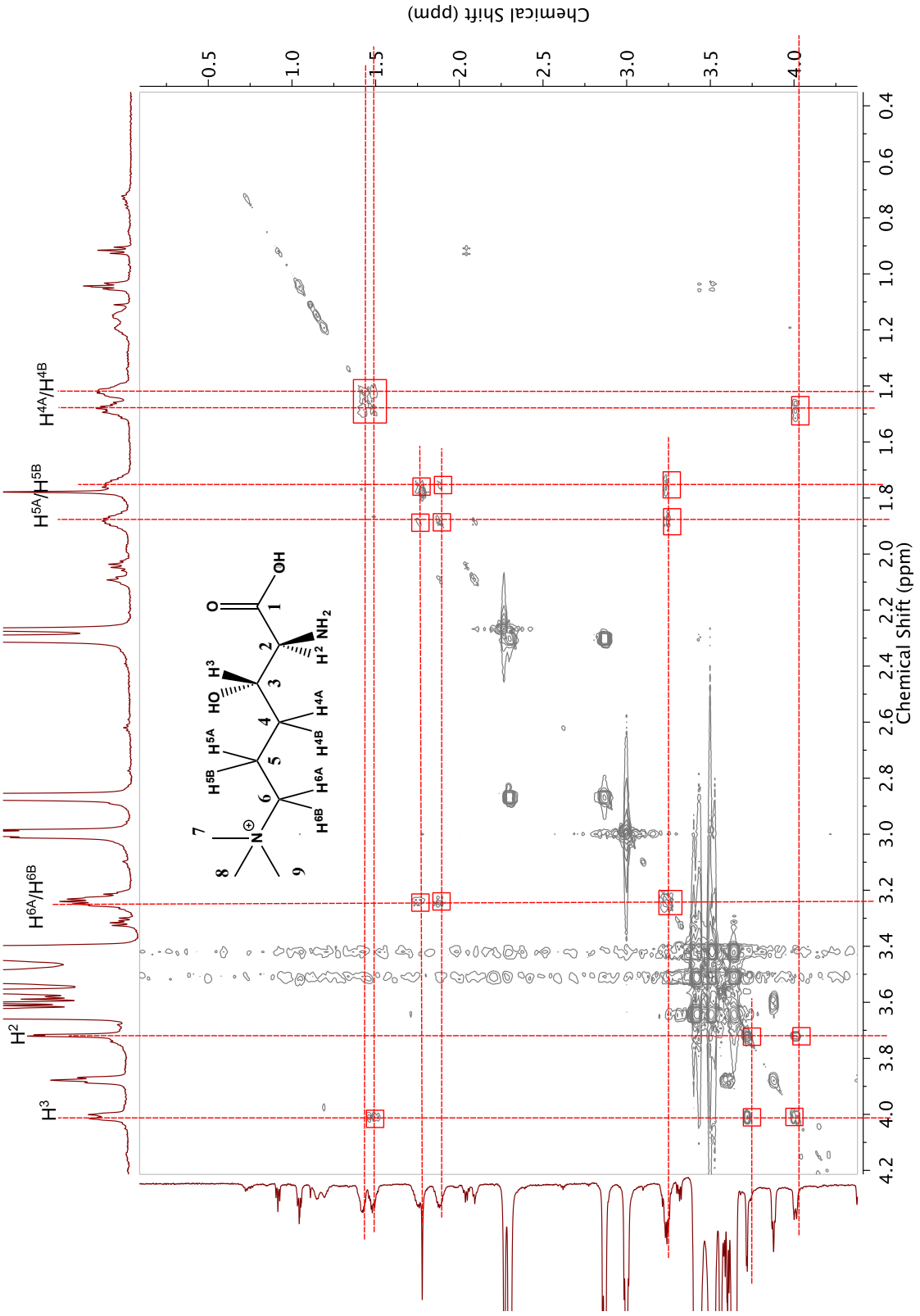


Figure 13 ^{1}H-^{1}H COSY spectrum of TMLH catalysed TML hydroxylation. Reaction conditions: 500 µM TML, 1500 µM 2OG, 500 µM L-ascorbate, 150 µM $Fe^{(II)}$, 10 µM TMLH, 50 mM Tris-d_{11}, 200 mM NaCl, pH 7.5.

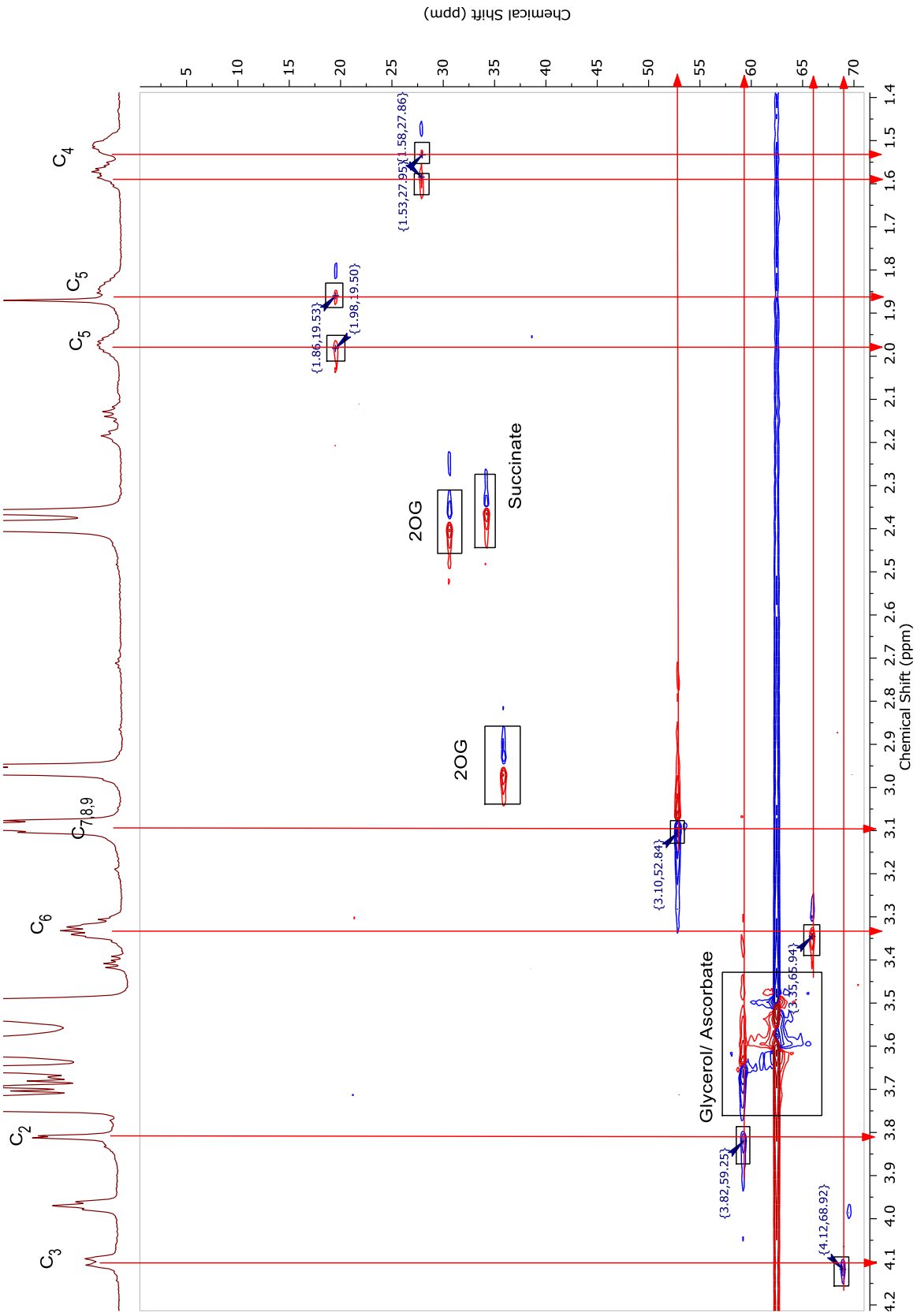


Figure 14 ^{1}H-^{13}C HSQC spectrum of TMLH-catalysed TML hydroxylation. Reaction conditions: 500 μM TML, 1500 μM 2OG, 500 μM L-ascorbate, 150 μM $Fe^{(II)}$, 10 μM TMLH, 50 mM Tris-d_{11}, 200 mM NaCl, pH 7.5.

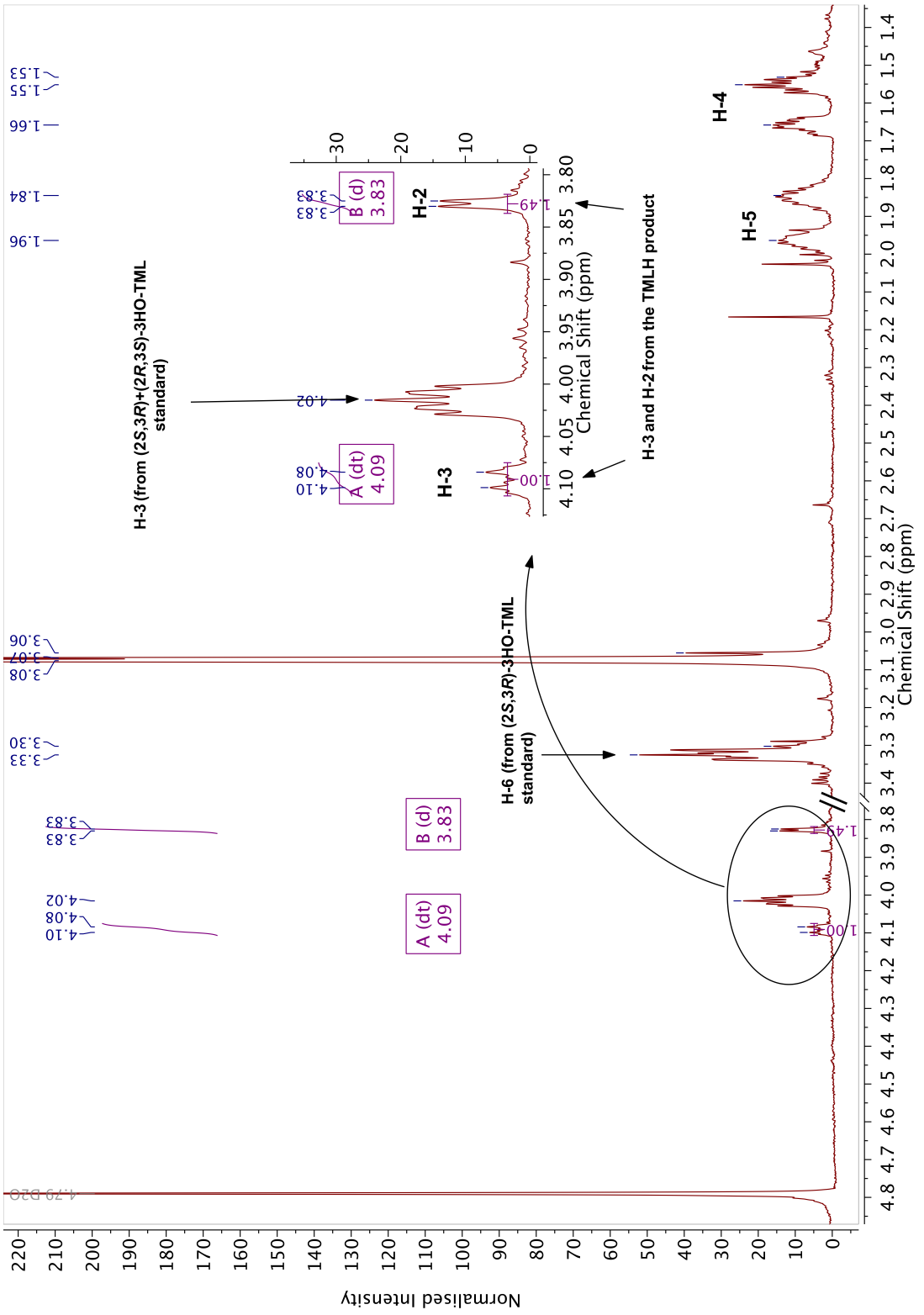


Figure 15 ^{1}H NMR spectrum of TMLH-catalysed (2*S*,3*S*)-3HO-TML (**30**) spiked with synthetic (2*S*,3*R*)/(2*R*,3*S*)-3HO-TML (**48**) post-HPLC purification. A TMLH incubation with TML spiked with synthetic (2*S*,3*R*)-3HO-TML (**48**) was purified by HPLC, as described in the General Experimental Methods section. Signals arising between δ = 3.50 – 3.75 ppm (glycerol and ascorbate) are omitted for clarity.

2.8 Modelling of the TMLH active site

Since crystallographic analyses of recombinant human TMLH have failed to date (Section 2.10.1), it was hoped that a homology model of TMLH based on known structural data of human BBOX would provide some insight into the TMLH structure. Given TMLH and BBOX likely share a common evolutionary ancestry and have a high sequence similarity (~26%) (Figure 17),[18,31] structure homology-modelling server SWISS-MODEL[67-71] was used to obtain a suitable model for the purposes of visualising the TMLH active site.

2.8.1 Sequence alignment

TMLH homology models were made using the SWISS-MODEL server homology modelling pipeline and using ProMod3. By searching for sequence similarity to TMLH, numerous potential modelling templates based on hBBOX were obtained. Using conserved residues between the target and template sequences as a starting point, the rest of the model was constructed. TMLH homology models generated from hBBOX structural data where the 'flexible-loop' region (strand $\beta 11^{I}$) in the *C*-terminus DSBH region of hBBOX was not well defined (*i.e.* PDB id: 3N6W) gave poor results. The highest scoring TMLH homology models, based on a global quality score, was generated from a crystal structure of human BBOX with *N*-oxalylglycine (NOG) and GBB (PDB id: 3O2G). The generated model is shown in Figure 16 as a comparison to a hBBOX crystal structure.

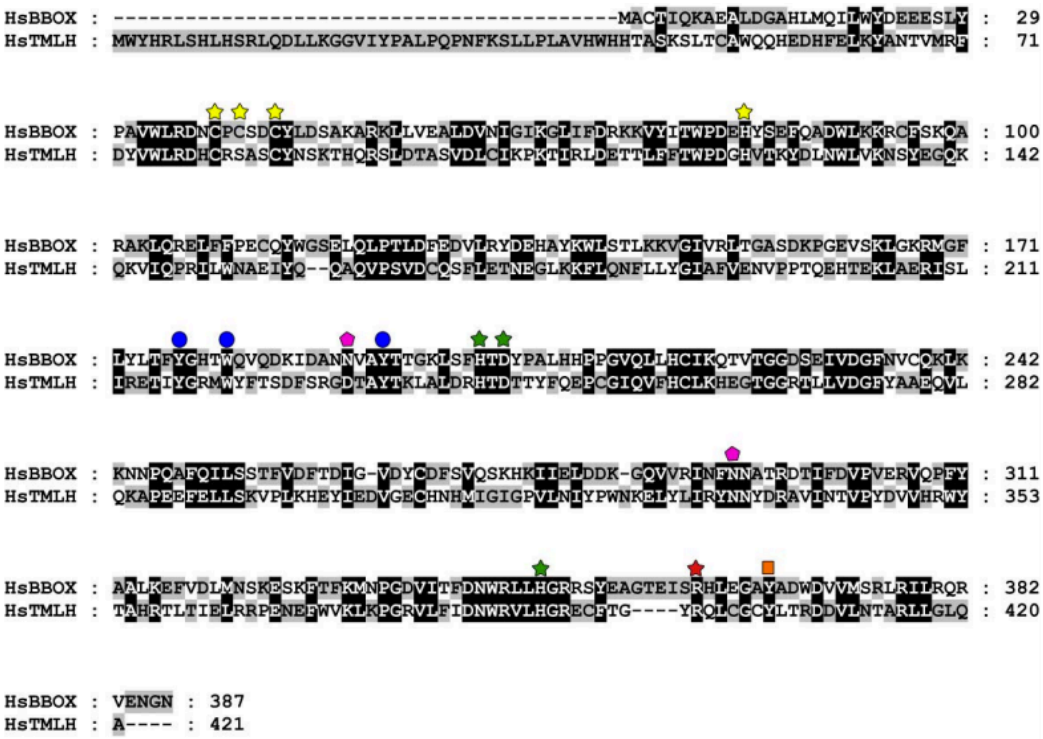


Figure 17 Alignment of human TMLH (gil8922625) and human BBOX (gil4502369) sequences. For sequence homology modeling, the large mitochondrial targeting sequence at the start of the TMLH sequence is omitted. Magenta pentagons represent GBB carboxylate interacting residues; residues responsible for the recognition of the quaternary ammonium moiety of GBB are highlighted by blue circles; the red star highlights the 2OG, C-5 interacting residue; yellow stars indicate $Zn^{(II)}$ chelating residues; residues binding $Fe^{(II)}$ are shown with yellow stars. Figure obtained from Leung *et al*.[18]

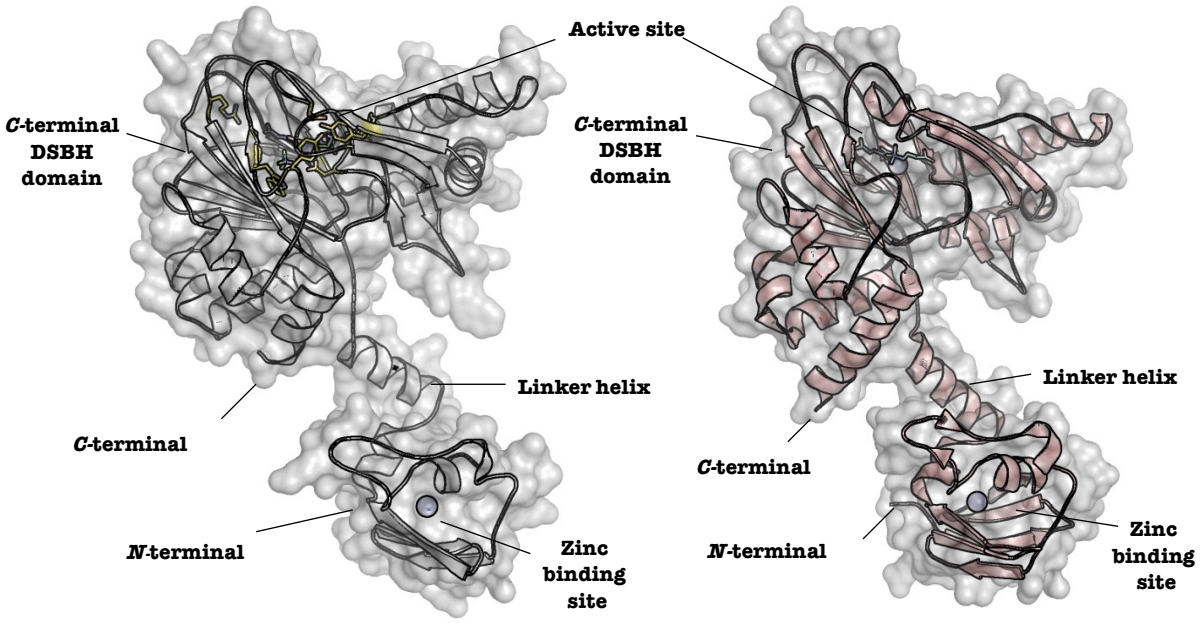


Figure 16 View of the overall structural homology between a TMLH model (left) and the structural template used to create the TMLH model, hBBOX (PDB id: 3O2G). Both enzymes have been shown to exist as homo-dimers. Above, only the monomer in each case is displayed.

2.8.2 Analysis of TMLH homology modeling

2.8.2.1 Structural comparison and active site mutations

As expected, the TMLH model maintains a double-stranded β-helix (DSBH domain, Figure 16) structural motif carrying the $Fe^{(II)}$-binding sequence HxD/E…H (His242, Asp244, His389, Figure 17, Figure 16, Figure 18) characteristic of the 2OG-dependent oxygenase family of enzymes.[36] Also typical of the 2OG oxygenases the 2OG C-5 carboxylate-binding residue is conserved (Arg398, Figure 18).[36]

Several differences can be seen when substrate binding residues of BBOX and the TMLH model are compared. Interestingly, the 'aromatic cage' residues required for quaternary ammonium recognition in BBOX are conserved in the TMLH model (Tyr216, Trp221, Tyr234) (Figure 18). The presence of a tyrosine (Tyr301) in the TMLH active site, 6Å away from the $–NH_3^+$ of TML, which substitutes for Asp261 in BBOX, suggests it may function in stabilising the quaternary ammonium species (Figure 18). One noticeable difference between the hBBOX structure and the TMLH model is a valine to phenylalanine substitution (Val183→Phe223, Figure 18). Given TML is effectively longer than GBB, the quaternary ammonium moiety of TML may be pushed in the direction of Phe223, in order to better obtain stabilisation via π-π interactions. Interestingly, Asn191, a basic residue responsible for binding the carboxylate of GBB in BBOX, is substituted for an aspartic acid in the TMLH model (Asp231)(Figure 18). Together with a mutation from Thr295 in BBOX to Asp337 in the TMLH model, possible placement of the $–NH_3^+$ moiety of TML was obvious; *i.e.* positioning TML to form two equidistant hydrogen bonding interactions with both Asp231 and Asp337. The GBB carboxylate binding residue in BBOX, Asn292 is conserved in TMLH (Asn334) suggesting the carboxylate of TML may bind in a similar way (Figure 18).

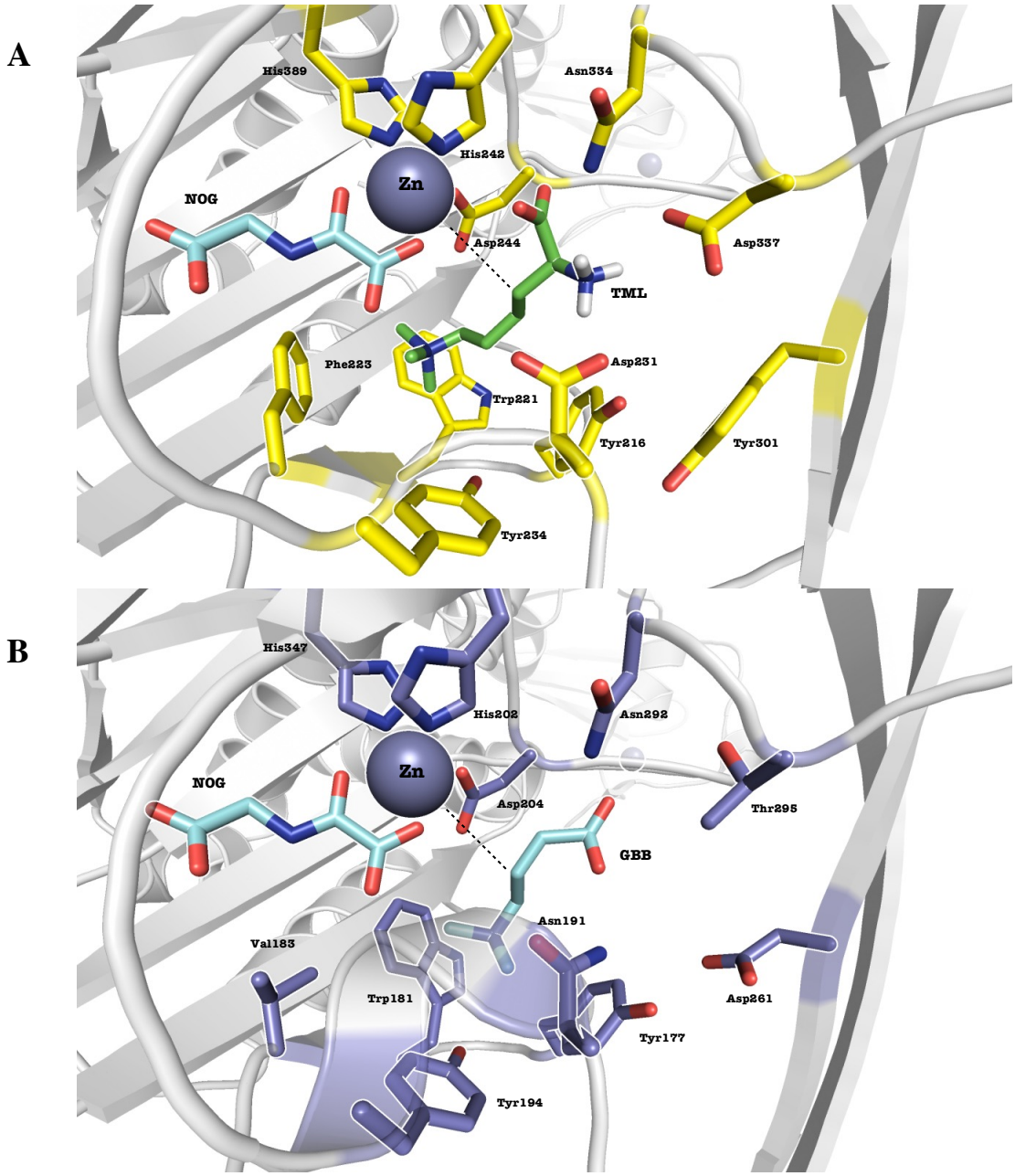


Figure 18 Stick representation of key residues in the active site of the modelled TMLH model (**A**) and BBOX (PDB id: 3O2G) (**B**). **A**) Manual docking of TML (green sticks) in the model TMLH active site. Residues determined to be key in binding of TML are indicated (yellow sticks). NOG is highlighted as cyan sticks. Assuming correct orientation of the $-NH_3^+$ moiety of TML, correct stereochemistry of a C-3, pro-*S* hydroxylation can be envisaged (dotted line). **B**) Close up of the BBOX active site. GBB and 2OG are represented as cyan sticks and key active site residues are indicated as purple sticks.

2.8.2.3 BBOX vs. TMLH hydroxylation

BBOX and TMLH both catalyse C-3 hydroxylations of quaternary ammonium substrates. The results presented here suggest that whereas BBOX catalyses a pro-*R* hydroxylation of GBB (**4**), TMLH catalyses a pro-*S* hydroxylation of TML (**2**). At first glance, the stereochemical assignment using Cahn-Ingold-Prelog (CIP) rules[72] would suggest different

modes of hydroxylation; however, relative to the $-NMe_3^+$ moiety both BBOX and TMLH catalyse hydroxylations with the same spatial orientation (Figure 19).

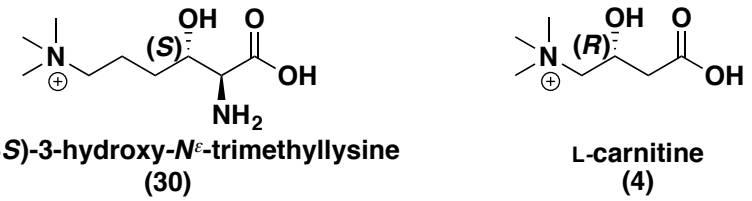


Figure 19 Chemical structures of the enzymatic products of TMLH catalysed hydroxylation of TML (**2**) to give (2*S*,3*S*)-3-hydroxy-N^{ε}-trimethyllysine (**30**) and the BBOX catalysed hydroxylation of GBB (**3**) to give carnitine (**4**). Stereochemistries of the C-3 alcohols in both cases are assigned using CIP-rules.

2.9 Summary and future perspectives

Little research on TMLH is described in the literature. No crystal structures of TMLH are available, and the stereochemical outcome of TMLH catalysis has previously not been assigned. Through the use of NMR techniques and synthesis of the diastereomerically pure standard (2*S*,3*R*)-3-hydroxy-N^{ε}-trimethyllysine (**48**), it was possible to assign the stereochemical outcome of the catalytic hydroxylation reaction of the natural amino acid (2*S*)-N^{ε}-trimethyllysine (**2**) and the 2OG oxygenase TMLH as (2*S*,3*S*). Novel and short syntheses of (2*S*,3*R*)-3-hydroxy-lysine (**24**) (5 steps) and (2*S*,3*R*)-3-hydroxy-N^{ε}-trimethyllysine (**48**) (6 steps) *via* the use of an established silver(I)-catalysed asymmetric aldol condensation involving an epicinchona-derived pre-catalyst were developed.[54] These challenging β-hydroxy α-amino acid scaffolds were obtained in a mild and atomically efficient manner using an orthogonal protecting group strategy. The developed route maybe used for the inclusion of hydroxylated lysines into peptide synthesis given its economy and likely scalability. Using sequence homology modeling, based on a known crystal structure of human BBOX, it was possible to generate a model for the human TMLH structure, with which it was possible to dock the TMLH substrate TML. TML can be orientated in such a way that supports the finding that TMLH catalyses a pro-*S* hydroxylation. From a medicinal perspective TMLH potentially offers an alternate carnitine biosynthesis inhibition strategy.

It is hoped that the results will enable further kinetic, biophysical and structural studies on the TMLH and carnitine biosynthesis.

2.10 General Experimental

The work in this chapter has been published in an altered form: R .K. Leśniak, S. Markolovic, K. Tars, C. J. Schofield, *Chemical Communications*, **2016**.[62]

2.10.1 Enzyme Production

Purified recombinant TMLH-MBP (MBP, maltose binding protein) fusion protein was prepared by Prof. Kaspars Tars (Latvian Biomedical Research and Study Centre, Riga, Latvia), and the MBP tag was cleaved as described.[31] TMLH-MBP was incubated with rTEV protease (20:1; TMLH-MBP:rTEV; kind gift from Dr. Illaria Pettinati, University of Oxford) in 20 mM Tris, 200 mM NaCl, pH 7.5 overnight at 4°C. Following the protease-catalysed cleavage reaction, the resultant solution was incubated with dithiothreitol (1 mM final concentration) overnight at 4°C, then purified by gel-filtration using a 16/600 Superdex S200 120 ml HiLoad column (GE Healthcare Life Sciences) attached to an AKTA FPLC system; the protein was eluted in 50 mM Tris, 200 mM NaCl, pH 7.5. In our hands TMLH did not crystallise; all of the crystalline materials obtained were determined to be salt (Section 2.9.1).

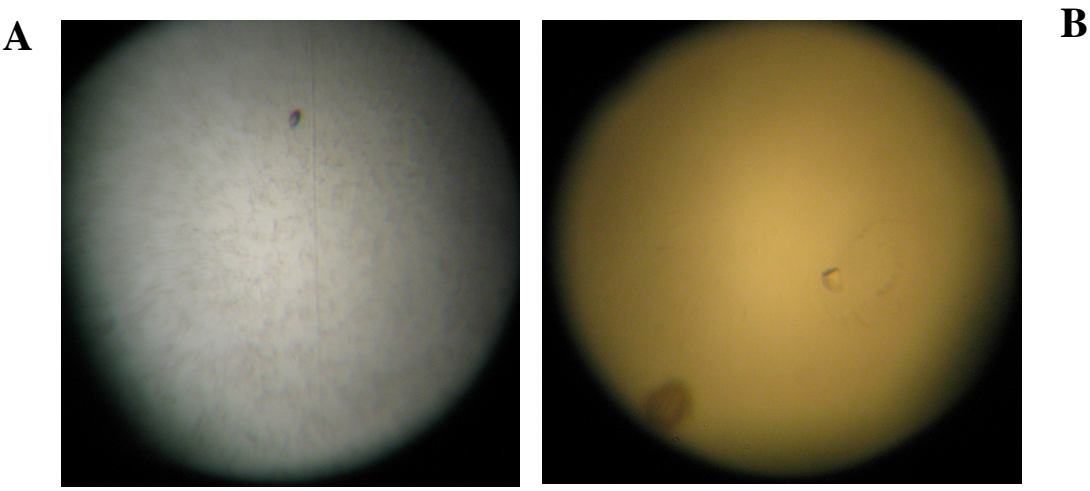


Figure 15 TMLH Crystallisation attempts. Both A) and B) present examples where crystals were observed but were later shown to be salt crystals.

A **B**

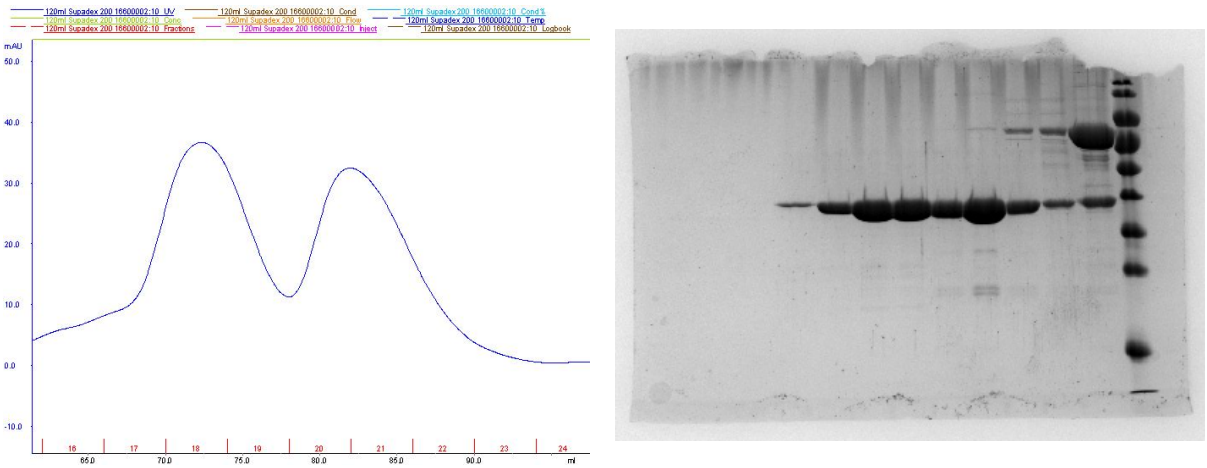


Figure 16 TMLH protein purification A) S200 gel filtration chromatogram. B) SDS PAGE gel, lanes: 1. Ladder, 2. 1min after addition of TEV protease, 3. Fraction 16(mixture of cleaved and uncleaved TMLH, 4. Fraction 17 (as for fraction 16), 5. Fraction 18 (pure TMLH), 6. Fraction 19 (pure TMLH), 7-10. Fractions 20-23 (cleaved MBP protein).

2.11 NMR materials and methods

NMR experiments were carried out using a Bruker AVIII 700 MHz instrument equipped with a 5mm inverse TCI cryoprobe and 3mm Bruker Match tubes. The single-pulse nutation method was used to calibrate pulses (Bruker pulsecal routine). Tris-d_{11} and D_2O were obtained from Sigma-Aldrich.

TMLH assay incubations for NMR comprised: 500 μM N^{ε}-trimethyllysine hydrochloride, 1500 μM 2-oxoglutarate (2OG, monosodium salt), 500 μM L-ascorbate (disodium salt), 150 μM ammonium iron(II) sulfate hexahydrate ($Fe^{(II)}$), 10 μM TMLH, and 50 mM Tris-d_{11}, 200 mM NaCl, pH 8.0 buffer. The $Fe^{(II)}$ solution was freshly prepared before each reaction by diluting a 100 mM $Fe^{(II)}$ solution stock in 20 mM HCl with D_2O, as required, prior to addition to the reaction mixture. Reagent stock solutions were made up in D_2O immediately prior to use; the enzyme stock solution was made up in 50 mM Tris-d_{11} with 200 mM NaCl by buffer exchanging the original enzyme solution (50 mM Tris, 200 mM NaCl, pH 7.5). Reactions were initiated by addition of the $Fe^{(II)}$ solution. The first NMR spectrum was

measured 240 sec after the start of reaction. All ^{1}H spectra were obtained using 64 scans. Control reactions were recorded without enzyme and metal.

2D NMR experiments used to assign the TMLH-catalysed turnover product were recorded after no further conversion of TML to 3HO-TML or 2OG to succinate was observed by ^{1}H NMR. Initial reactions were performed in Tris-d_{11} pH 8.0, although pH 7.5 was determined to be optimal. All subsequent reactions were performed at pH 7.5 unless otherwise stated. 2D experiments used were ^{1}H-^{1}H COSY and multiplicity edited ^{1}H-^{13}C HSQC NMR. Synthetic standards were characterised using a Bruker AVIII HD 400 instrument and 5 mm tubes.

2.12 Amino acid analysis

Amino acid derivatisation and LCMS analyses were carried out by Suzanna Markolovic (Chemistry Research Laboratory, University of Oxford)

Samples were prepared as described for NMR analyses and subsequently freeze-dried. Freeze-dried samples were resuspended in borate buffer pH 9.0 and derivatised by 6-aminoquinolyl-*N*-hydroxysuccinimidyl carbamate (AQC) in acetonitrile at 25°C according to the AccQ-Tag Ultra Derivatisation Protocol (Waters, USA). LC-MS analyses were performed as described[73] using a Waters Acquity ultra performance liquid chromatography system coupled to a Xevo G2-S QTof mass spectrometer equipped with an electrospray ionisation source (Waters, USA). Gradient conditions for separation were carried out as described in the AccQ-Tag Ultra Derivatisation Protocol (Waters, USA).

Conditions for positive ion mode ESI-MS detection were as follows: desolvation temperature, 600°C; source temperature, 100°C, capillary voltage, 3000 V; sample cone voltage, 20 V; cone gas flow, 30 L/min; and desolvation gas flow 1000 L/min. MS data were acquired and extracted ion chromatograms were produced for m/z values of either 359.2 or 375.2, corresponding to the theoretical masses of AQC-derivatized N^{ε}-

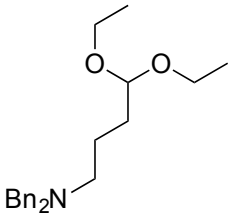
trimethyllysine (359.2083) or hydroxy-N^{ε}-trimethyllysine (375.2032), respectively. Extracted ion chromatograms were smoothed to the mean (number of smooths, 2; smooth window channels, 3), and total ion current chromatograms were further baseline subtracted (polynomial order, 1; below curve %, 40; tolerance, 0.01).

2.13 Synthesis

All chemicals, reagents, and solvents were obtained from Sigma-Aldrich (Dorset, UK) and used without further purification. HPLC grade solvents were used for reactions, chromatography, and work-ups. Aqueous solutions were made using de-ionized water. Thin layer chromatography (TLC) was carried out using Merck (Darmstadt, Germany) silica gel 60 F254 TLC plates. TLC visualisation was carried out under UV light and stained with one of three stains: ninhydrin, potassium permanganate, or anisaldehyde. Chromatographic purifications were carried out using a Biotage® (Uppsala, Sweden) Isolera One or Biotage® SP4 flash purification system, using Biotage® pre-packed SNAP columns. Reactions were monitored using an Agilent (Cheshire, UK) 1200 series, 6120 quadrupole LC-MS system using a Merck Chromolith® Performance RP-18 HPLC column. Deuterated solvents were obtained from Sigma-Aldrich, and ^{1}H NMR spectra were obtained on a Bruker AVANCE AVIII HD 400 nanobay (400 MHz), Bruker AV500 (500M Hz) with a ^{13}C cryoprobe, and/or Bruker AVIII 700 (700 MHz) with an inverse TCI cryoprobe. All signals are described in δ ppm with multiplets being denoted as singlet, doublet, triplet, quartet, and multiplet using the abbreviations s, d, t, q, and m, respectively. Chemical shifts in presented NMR spectra were referenced using residual solvent peaks with coupling constants, *J*, reported in hertz (Hz) to an accuracy of 0.5 Hz. For high-resolution mass spectrometry (HR-MS), a Bruker MicroTOF instrument with an ESI source and Time of Flight (TOF) analyser was used. MS data are represented as a ratio of mass to charge (m/z) in Daltons. A Bruker Tensor 27

instrument was used to obtain Fourier transform infrared spectra (FT-IR). Spectroscopic grade solvents and a Perkin Elmer 241 Polarimeter were used to obtain optical rotations.

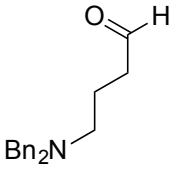
Dibenzyl-4,4-diethoxybutan-1-amine



4-Aminobutyraldehyde diethyl acetal (**44**) (12.4 ml, 71.5 mmol) was dissolved in a 4:1 (v/v) of EtOH:distilled water (70 ml). Sodium carbonate (22.73 g, 214.5 mmol) was then added, followed by a solution of benzyl bromide (29.8 ml, 250.3 mmol) in EtOH (14 ml), which was added dropwise over 30 minutes. The resultant mixture was refluxed overnight. The solvent was then removed *in vacuo,* and the resulting material diluted with water (60 ml) and CH_2Cl_2 (30 ml). The aqueous layer was washed with CH_2Cl_2 (2 x 30 ml), and the organic layers combined, dried over $MgSO_4$, and filtered. After evaporation of the solvent *in vacuo,* the crude reaction mixture was loaded onto a silica column and purified using flash column chromatography with an isocratic gradient (50:50 EtOAc/cyclohexane). After collecting the appropriate fractions, the solvent was removed *in vacuo* to yield dibenzyl-4,4-diethoxybutan-1-amine as a thin, colourless oil (21.8 g, 63.9 mmol, 89%).

^{1}H NMR (400 MHz, $CDCl_3$) δ = 7.4 – 7.2 (10H, m, *Ph*), 4.4 – 4.3 (1H, m, C*H*O_2Et_2), 3.7 – 3.3 (m, 8H, OC*H*$_2$$CH_3$, C*H*$_2$Ph), 2.4 (2H, t, *J* = 6.5 Hz, NC*H*$_2$$CH_2$), 1.7 – 1.5 (4H, m, $NCH_2CH_2CH_2$), 1.2 (6H, t, *J* = 7.0 Hz, OCH_2CH_3) ppm. **^{13}C NMR** (101 MHz, $CDCl_3$) δ = 140.0, 128.9, 128.3, 126.9, 102.9, 61.1, 53.1, 31.2, 22.3, 15.5 ppm. **FT-IR** ν_{max} (film) 3028, 2973, 2928, 2874, 2795, 1494, 1453, 1372, 1124, 1060, 743, 698 cm^{-1}. **HRMS** (ESI-TOF) calcd for $C_{22}H_{32}NO_2$ $[M+H]^+$: 342.2428, found: 342.2429.

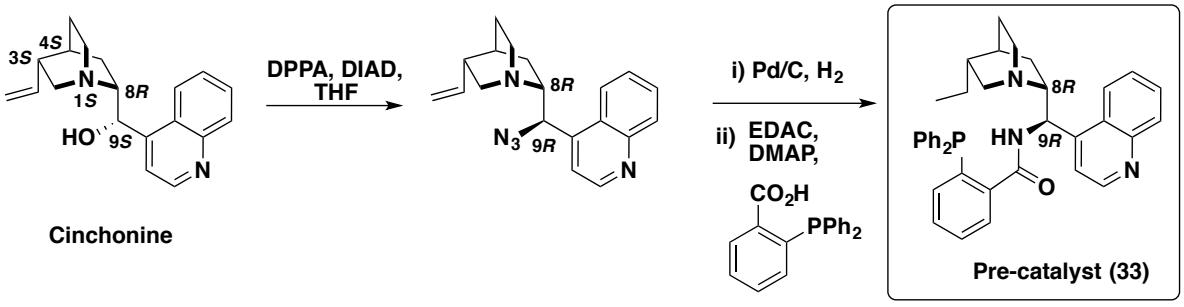
4-(dibenzylamino)butanal (49)



Dibenzyl-4,4-diethoxybutan-1-amine (2.0 g, 5.87 mmol) was dissolved in THF (2.93 ml); 20% (v/v) $HCl_{(aq)}$ solution (2.93 ml) was then added. This mixture was stirred for 1 h at room temperature until complete reaction was observed by TLC (4:1 cyclohexane/EtOAc). The reaction was quenched by the addition of saturated $NaHCO_{3(aq)}$. The organic material was then extracted with EtOAc (3 x 20ml); the combined organic layers were washed with saturated $NaHCO_3$ and brine, then dried over $MgSO_4$ and filtered. After removal of volatiles by evaporation *in vacuo*, the crude reaction material was purified via flash column chromatography (0-20% cyclohexane/EtOAc over ~10 column volumes). The appropriate fractions were combined and the solvent removed to yield (**49**) as a pale yellow oil (1.13 g, 4.23 mmol, 72%).

^{1}H NMR (400 MHz, $CDCl_3$) δ = 9.7 (1H, t, *J* = 1.5 Hz, C*H*O), 7.3 (10H, s, *Ph*), 3.6 (4H, s, NCH_2Ph), 2.5 – 2.4 (4H, m, NCH_2CH_2CH_2), 1.8 (2H, p, *J* = 7.0 Hz, NCH_2CH_2CH_2) ppm. **^{13}C NMR** (101 MHz, $CDCl_3$) δ = 202.7, 139.6, 128.9, 128.3, 127.0, 58.5, 52.5, 41.8, 20.0 ppm. **FT-IR** ν_{max} (film) 3027, 2802, 1721, 1493, 1452, 745, 698 cm^{-1}. **HRMS** (ESI-TOF) calcd for $C_{18}H_{22}NO$ $[M+H]^+$: 268.1696, found: 268.1693.

N-[(9R)-10,11-dihydrocinchonan-9-yl]-2-(diphenylphosphino)benzamide (33)[55]



The procedures of Sladojevich *et al*.[54] and Cassani *et al*.[59] were used. Cinchonine[74] (3.0 g, 10.2 mmol) and triphenylphosphine (3.2 g, 12.2 mmol) were suspended in dry THF (51 ml). The mixture was cooled in an ice bath to 0°C, after which diisopropyl azodicarboxylate (2.41 ml, 12.2 mmol) was added. Diphenyl phosphoryl azide (2.64 ml, 12.2 mmol) was then dissolved in dry THF (21 ml); the resultant solution was added dropwise to the reaction mixture. Upon removing the ice bath, the reaction mixture was allowed to warm to room temperature and stirred overnight. The resultant solution was heated for 2 h at 50°C, after which the volatiles were removed *in vacuo*. The resultant crude mixture was dissolved in CH_2Cl_2 (150 ml), and 4M hydrochloric acid was added. The aqueous phase was removed, and solid $NaHCO_3$ was then added to the aqueous phase until the pH was ~10 (litmus paper). The basic aqueous phase was then extracted with CH_2Cl_2 (3 x 100 ml), dried over $MgSO_4$, the CH_2Cl_2 was then removed *in vacuo* to give the desired azide in 94% crude yield.

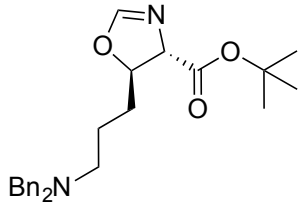
The crude azide was then dissolved in MeOH (50 ml), and 10% Pd/C (750 mg) was added. The reaction flask was placed under a H_2 atmosphere by fitting the vessel with a septum, H_2 balloon, and syringe. The flask was evacuated and filled with H_2 three times, then stirred at room temperature at 1 atm overnight. The reaction mixture was then filtered through a short pad of Celite®; volatiles were removed *in vacuo* to yield the crude amine in apparent quantitative yield as a yellow oil, which was used without further purification.

The crude amine (1.70 g, 5.7 mmol) was dissolved in anhydrous CH_2Cl_2 (50 ml). 2-(diphenylphosphino)-benzoic acid (1.94 g, 6.3 mmol) and 4-dimethylaminopyridine (7 mg, 0.057 mmol) were then added. The resultant mixture was cooled to 0°C, then *N*-(3-dimethylaminopropyl)-*N*-ethylcarbodiimide hydrochloride (1.1 g, 5.7 mmol) was added. The reaction mixture was allowed to warm to room temperature, after which it was stirred

overnight at room temperature. After removing volatiles *in vacuo*, the resultant crude mixture was dissolved in EtOAc (50 ml), then washed with water, 10% $NaHCO_{3(aq)}$, and brine. After drying the organic phase over Na_2SO_4 and removing the solvent *in vacuo*, the crude mixture was purified by flash chromatography using an isocratic elution system (EtOAc/CH_2Cl_2/MeOH 5:2:1) to yield the desired compound as a pale yellow foam (3.2 g, 5.51 mmol, 54%, over three steps).

^{1}H NMR (400 MHz, $CDCl_3$) δ = 8.75 (1H, d, *J* = 4.5 Hz), 8.38 (1H, d, *J* = 8.5 Hz), 8.11 (1H, dd, *J* = 8.5, 1.5 Hz), 7.74 – 7.55 (4H, m), 7.40 – 7.15 (13H, m), 6.89 (1H, dd, *J* = 7.0, 4.0 Hz), 5.37 (1H, s), 3.05 – 2.63 (4H, m), 2.59 – 2.41 (1H, m), 1.52 (1H, s), 1.47 – 1.32 (5H, m), 1.25 – 1.18 (1H, m), 0.89 (3H, t, *J* = 7.0 Hz), 0.89 – 0.80 (1H, m) ppm. **^{13}C NMR** (101 MHz, $CDCl_3$) δ = 169.1, 150.2, 148.5, 146.7, 141.3, 141.0, 137.8, 137.7, 137.3, 137.1, 135.9, 135.7, 134.3, 133.9, 133.8, 133.7, 133.6, 130.3, 127.4, 126.6, 123.5, 119.6, 60.5, 49.0, 37.3, 27.1, 26.0, 25.7, 25.0, 12.1 ppm. **^{31}P NMR** (162 MHz, $CDCl_3$) δ = -10.3 ppm. **FT-IR** ν_{max} (film) 2980, 1654, 1457, 745, 697 cm^{-1}. $[\alpha]_D^{25}$ = + 60.6 (c = 0.2 in CH_2Cl_2)(Lit $[\alpha]_D^{25}$ = +67.2, c = 0.5 CH_2Cl_2). **HRMS** (ESI-TOF): calcd for $C_{38}H_{39}N_3O_1P_1$ $[M+H]^+$ 584.2825, found 584.2825. Spectroscopic data are consistent with those reported.[54]

***tert-Butyl(2S,3R)-3-(6-(dibenzylamino)propyl)-2,3-dihydrooxazole-2-carboxylate* (50)**

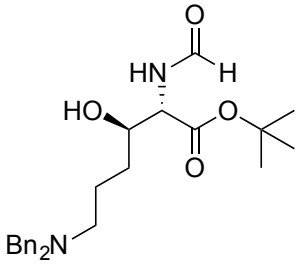


Pre-catalyst (**33**) (53 mg, 0.09 mmol) was dissolved in anhydrous EtOAc (5 ml) prior to addition of Ag_2O (9.3 mg, 0.04 mmol). The mixture was stirred for ~5 min at room temperature, then cooled in a dry ice/acetone bath. On cooling, *tert*-butyl isocyanoacetate (0.22 ml, 1.47 mmol) was added, followed by crushed, dried 4Å molecular sieves. A solution of aldehyde (**49**) (470 mg, 1.76 mmol) in anhydrous EtOAc (1 ml) was added; the

reaction was quickly placed in a -20°C freezer with occasional stirring. The reaction was left overnight; consumption of the isocyanoacetate was monitored by TLC (50:50 EtOAc/cyclohexane), staining with anisaldehyde solution. After 16 h, the reaction mixture was quickly filtered through a short pad of silica gel eluting with EtOAc. The filtered reaction mixture was concentrated *in vacuo*, then purified using silica flash chromatography (0–40% EtOAc/cyclohexane over ~10 column volumes). Concentration of the appropriate fractions gave oxazoline (**50**) (468 mg, 1.15 mmol, 78%, d.r. > 95:1) as a viscous, colourless oil. An e.r. of 3:1 was determined by analysis of the ^{1}H NMR spectra of the corresponding Mosher's ester of formamide (**51**) (Section 2.5.5).

^{1}H NMR (500 MHz, toluene-d_8) δ = 7.32 – 7.26 (m, 4H, *Ph*), 7.19 – 7.14 (m, 4H, *Ph*), 7.11 – 7.07 (m, 2H, *Ph*), 6.36 (d, J = 2.0, 1H, OC*H*N), 4.62 – 4.54 (m, 1H, CH_2CH(O)CH(N)), 4.06 (dd, J = 7.0, 2.1, 1H, CH_2CH(O)C*H*(N)), 3.40 – 3.31 (m, 4H, NCH_2Ph), 2.24 (t, J = 6.5, 2H, NCH_2CH_2), 1.49 – 1.36 (m, 3H, $NCH_2CH_2CH_A$), 1.35 (s, 9H, ^{t}Bu), 1.29 – 1.20 (m, 1H, $NCH_2CH_2CH_B$) ppm. **^{13}C NMR** (126 MHz, toluene-d_8) δ = 170.1, 155.6, 140.1, 129.0, 128.5, 127.2, 81.5, 81.1, 74.1, 58.7, 53.1, 32.8, 27.9, 22.8 ppm. **FT-IR** ν_{max} (film) 3027, 2979, 2797, 1732, 1624, 1367, 1155, 1110, 745, 698 cm^{-1}. $[\alpha]_D^{25}$ = + 66.2° (c = 2.65 in CH_2Cl_2). **HRMS** (ESI-TOF): calcd for $C_{25}H_{32}O_3N_2Na_1$ $[M+Na]^+$ 431.2305, found 431.2306.

tert-Butyl (2S,3R)-6-(dibenzylamino)-2-formamido-3-hydroxyhexanoate (51)

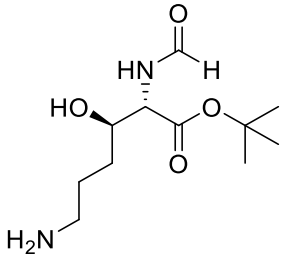


tert-Butyl(2*S*,3*R*)-3-(6-(dibenzylamino)propyl)-2,3-dihydrooxazole-2-carboxylate (**50**) (400 mg, 0.98 mmol) was dissolved in THF (6 ml) prior to addition of 20% (v/v) $AcOH_{(aq)}$ (4 ml).

This mixture was stirred for 30 min (TLC monitor, 100% EtOAc) before the addition of saturated aqueous sodium hydrogen carbonate until a pH ~ 8 was reached. CH_2Cl_2 was then added and the organic material extracted with CH_2Cl_2 (3 x 20 ml). The organic layers were combined, dried over $MgSO_4$, and then evaporated *in vacuo*. The crude reaction material was purified using flash chromatography (0-100% EtOAc/cyclohexane over ~10 column volumes). The appropriate fractions were combined, and the solvent removed *in vacuo* to yield formamide (**51**) as a clear, viscous oil (379 mg, 0.89 mmol, 91%).

^{1}H NMR (400 MHz, $CDCl_3$) δ = 8.1 (1H, s, NHC*H*O), 7.3 – 7.1 (10H, m, *Ph*), 6.5 (1H, d, *J* = 9.0 Hz, CHN*H*CHO), 4.5 (1H, dd, *J* = 10.0, 2.0 Hz, C*H*NHCHO), 4.0 (1H, dt, *J* = 10.0, 2.0 Hz, C*H*OH), 3.7 (2H, d, *J* = 13.0 Hz, NCH_2Ph), 3.3 (2H, d, *J* = 13.0 Hz, NCH_2Ph), 2.5 – 2.3 (2H, m, NCH_2CH$_2$CH$_2$), 2.0 (1H, s, O*H*), 1.7 – 1.6 (3H, m, NCH$_2$CH_2CH_A), 1.4 (9H, s, ^{t}*Bu*), 1.2 – 1.1 (1H, m, NCH$_2$CH$_2$CH_B) ppm. ^{13}C NMR (101 MHz, $CDCl_3$) δ = 169.8, 161.4, 137.3, 129.8, 128.4, 127.5, 82.2, 72.0, 58.3, 55.8, 54.0, 33.9, 28.1, 24.1 ppm. **FT-IR** ν_{max} (film) 3356, 2934, 1738, 1669, 1369, 1158, 746, 699 cm^{-1}. $[\alpha]_D^{25}$ = + 10.4° (c = 0.414 in CH_2Cl_2). **HRMS** (ESI-TOF): calcd for $C_{25}H_{35}O_4N_2$ $[M+H]^+$ 427.2591, found 427.2577.

tert-Butyl (2S,3R)-6-amino-2-formamido-3-hydroxyhexanoate (51a)

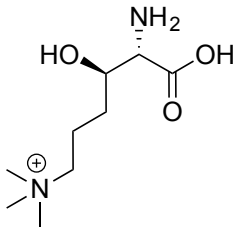


tert-Butyl (2*S*,3*R*)-3-(6-(dibenzylamino)propyl)-2,3-dihydrooxazole-2-carboxylate (**50**) (250 mg, 0.61 mmol) was dissolved in MeOH (5 ml) prior to addition of 5% (v/v) aqueous citric acid (2 ml). 10% palladium on carbon (100 mg/mmol) was added to the solution, and the reaction vessel was subsequently placed under an atmosphere of H_2 and stirred at room temperature for 24 h until complete conversion was observed (by TLC and/or LC-MS). The

reaction mixture was filtered through a short pad of Celite®, then evaporated *in vacuo*. The residue was dissolved in CH_2Cl_2 (10 ml) and washed with a solution of saturated $NaHCO_3$ (10 ml). The aqueous fractions were frozen in liquid nitrogen and lyophilized. The resultant material was purified by loading onto a silica column pre-equilibrated with 100% CH_2Cl_2 and eluted with a gradient of 0-70% MeOH over 10 column volumes. The appropriate fractions were then concentrated *in vacuo* to yield amine (**51a**) as a colourless oil (145 mg, 0.59 mmol, 96%).

^{1}H NMR (CD_4OD, 400 MHz) δ = 8.2 (1H, s, NHC*H*O), 4.5 (1H, d, *J* = 3.0 Hz, C*H*NHCHO), 4.1 (1H, td, *J* = 6.5, 3.0 Hz, C*H*OH), 2.9 (2H, t, *J* = 7.5 Hz, $NH_2CH_2CH_2$), 1.8 – 1.5 (4H, m, $NH_2CH_2CH_2CH_2$), 1.5 (9H, s, ^tBu) ppm. **^{13}C NMR** (CD_4OD, 101 MHz) δ = 170.5 , 164.2 , 83.5, 71.9, 57.2 , 32.1, 28.3 , 26.2 ppm. **FT-IR** ν_{max} (film) 3286, 2934, 1732, 1665, 1522, 1157, 1084 cm^{-1}. $[\alpha]_D^{25}$ = + 14.7° (c = 0.08 in MeOH). **HRMS** (ESI-TOF): calcd for $C_{11}H_{23}N_2O_4$ $[M+H]^+$ 247.1652, found 247.1664.

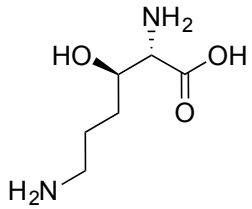
***(2S,3R)-2-amino-2-carboxy-3-hydroxy-N,N,N-trimethylpentan-6-aminium* (48)**



tert-Butyl (2*S*,3*R*)-6-amino-2-formamido-3-hydroxyhexanoate (**51a**) (200 mg, 0.81 mmol) was dissolved in a 2:1 (v/v) MeCN/MeOH solution (8.1 ml). Methyl iodide (252 µl, 4.05 mmol) and *N*,*N*-diisopropylethylamine (183 µl, 1.05 mmol) were then added. The reaction mixture was stirred at room temperature until complete reaction was observed after ~4 h by TLC (5:4:1, $CHCl_3$/MeOH/AcOH). The reaction mixture was concentrated *in vacuo*, dissolved in a small amount of $CHCl_3$, then loaded onto a pre-equilibrated silica column

(100% $CHCl_3$) and purified by flash column chromatography (0-100% MeOH (+10% formic acid) over ~10 column volumes). Ninhydrin active fractions were collected and concentrated. The residue was then dissolved in 6M $HCl_{(aq)}$ (8.1 ml) and stirred at room temperature overnight until complete reaction was observed by LC-MS. The reaction mixture was then concentrated to dryness. The resultant material was taken up in a minimal amount of H_2O, then purified using a cation exchange chromatography (Dowex® 1X8 200-400, Cl^- form) eluting in water. The ninhydrin active fractions were evaporated to dryness. The resultant residue was triturated several times with iPrOH to yield (**48**) a hygroscopic white powder (67 mg, 0.24 mmol, 30% over two steps); an e.r. of 3:1 was observed, as calculated by analysing the ^{1}H NMR spectra of the corresponding Mosher amides (Section 2.5.5) . **^{1}H NMR** (D_2O, 400 MHz) δ = 4.1 (1H, dt, *J* = 9.0, 4.5 Hz, C*H*OH), 3.6 (1H, d, *J* = 5.0 Hz, C$H_2$$NH_2$), 3.4 (2H, t, *J* = 8.5 Hz, NH_2C$H_2$$CH_2$), 3.1 (9H, s, N(C$H_3$)), 2.1 – 1.8 (2H, m, $NH_2CH_2CH_2CH_2$), 1.8 – 1.5 (2H, m, $NH_2CH_2CH_2CH_2$) ppm. **^{13}C NMR** (D_2O, 101 MHz) δ = 173.1 , 69.7 , 60.0 , 53.5, 30.7, 19.8 ppm. **FT-IR** ν_{max} (film) 3363, 3026, 2919, 1735, 1622, 1489, 1222, 984 cm^{-1}. $[\alpha]_D^{25}$ = + 14.7° (c = 0.1 in H_2O/MeOH (1:1)). **HRMS** (ESI-TOF): calcd for $C_9H_{21}N_2O_3$ $[M]^+$ 205.1547, found 205.1547.

(2S,3R)-2,6-diamino-3-hydroxyhexanoic acid (24)



To a solution of *tert*-Butyl (2*S*,3*R*)-3-(6-(dibenzylamino)propyl)-2,3-dihydrooxazole-2-carboxylate (**50**) (336 mg, 0.82 mmol) in MeOH (6 ml) and 5% (v/v) aqueous citric acid (2.3 ml) 10% palladium on carbon (100 mg/mmol) was added, and the reaction vessel was put under a H_2 atmosphere using a balloon. The reaction mixture was stirred for 24 h (until

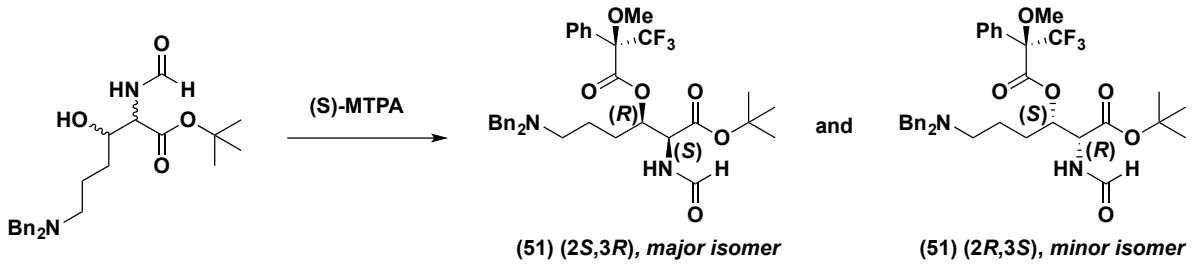
complete conversion occurred, by LC-MS/TLC), then filtered through a short pad of Celite®, which was then further washed with MeOH. The filtrate was concentrated *in vacuo* and purified by flash column chromatography (CH_2Cl_2/MeOH, 100/0 to 30/70). Ninhydrin active fractions were collected and concentrated to give a clear oil, which was analysed by ^{1}H NMR. The oil was dissolved in 3M $HCl_{(aq)}$ and stirred overnight until complete reaction was observed by LC-MS and TLC. The reaction mixture was then concentrated to dryness to yield amine (**24**) as a white powder (di-hydrochloride salt, 176 mg, 0.75 mmol, 91%).

^{1}H NMR (400 MHz, D_2O) δ 4.16 (1H, dt, *J* = 9.6, 3.6 Hz, C*H*OH), 3.91 (1H, d, *J* = 4.5 Hz, C*H*NH_2), 3.04 (2H, t, *J* = 7.4 Hz, C*H*$_2$$NH_2$), 1.94 – 1.55 (4H, m, $NH_2CH_2CH_2CH_2$) ppm. **^{13}C NMR** (101 MHz, D_2O) δ 171.0, 68.6, 58.1, 39.0, 30.0, 23.3 ppm.

The so-obtained (**24**) was purified by cation exchange column chromatography using Dowex® 50WX8 200-400 (hydrogen form) resin that was washed with H_2O. Crude (**24**) was dissolved in a minimal amount of H_2O, then loaded onto the pre-equilibrated ion-exchange column, followed by a wash phase with at least 3 column volumes of water. The product was eluted with 3% (v/v) NH_4OH in MeOH to give purified product as a clear oil .

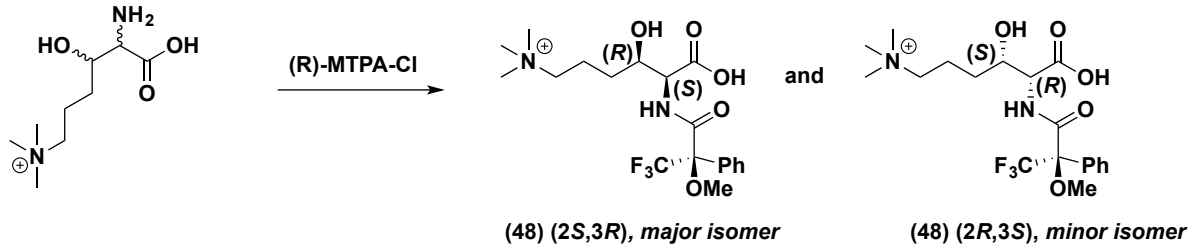
^{1}H NMR (400 MHz, D_2O) δ 4.01 – 3.90 (1H, m, C*H*OH), 3.55 (1H, d, *J* = 5.0 Hz, C*H*NH_2), 2.96 (2H, t, *J* = 7.0 Hz, C*H*$_2$$NH_2$), 1.85 – 1.46 (4H, m, $NH_2CH_2CH_2CH_2$) ppm. **^{13}C NMR** (101 MHz, D_2O) δ 172.6, 69.1, 59.3, 39.1, 30.3, 23.3 ppm. **FT-IR** ν_{max} (film) 3033, 2923, 1698 cm^{-1}. $[\alpha]_D^{25}$ = + 6.8 (c = 1.83 in MeOH) (Lit $[\alpha]_D^{25}$ = +16.9, c = 1.83 MeOH)[46]. **HRMS** (ESI-TOF): calcd for $C_6H_{15}O_3N_2$ $[M+H]^+$ 163.1077, found 163.1078.

2.14 Synthesis of Mosher's esters for stereochemical investigation of (51)



Formamide (**51**) (1.0 eq., a mixture of stereoisomers) was dissolved in a solution of (*S*)-Mosher's acid (0.1 M, 1.5 eq) in CH_2Cl_2. A solution of *N*,*N*'-dicyclohexylcarbodiimide in CH_2Cl_2 (0.1 M, 2 eq.) was then added, followed by 4-dimethylaminopyridine (DMAP) in CH_2Cl_2 (0.1 M, 0.1 eq.). The resultant mixture was stirred at room temperature overnight to yield a precipitate that was subsequently filtered through a short pad of Celite®. The filtrate was then passed through a short pad of silica eluting with 100% EtOAc. After evaporating the filtrate to dryness, the residue was dissolved in $CDCl_3$ for analysis by ^{1}H NMR. The ^{1}H NMR spectra of the resultant Mosher amides are shown in Section 2.5.5. The procedure was repeated with (*R*)-Mosher's acid to investigate the absolute stereochemistry of the C-3 position.

2.15 Synthesis of Mosher's amides of (48)

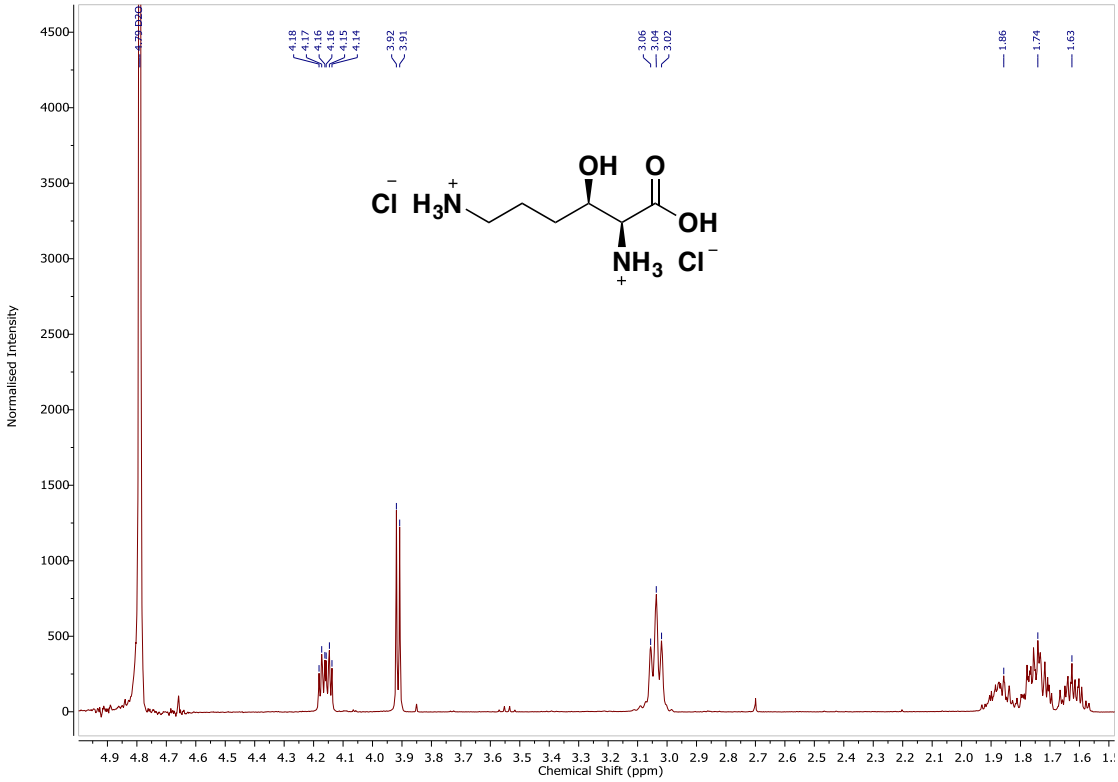


Amine (**48**) (1.0 eq., a mixture of stereoisomers) was dissolved in a 10% $NaCO_3$ solution (0.2 M). (*R*)-Mosher's acid chloride solution in dioxane (0.2 M, 1.2 eq.) was then added to give a final reaction concentration of 0.1 M. This mixture was stirred for 3 h before being neutralized with a 1.0 M $HCl_{(aq)}$ solution and concentrated. The crude reaction mixture was

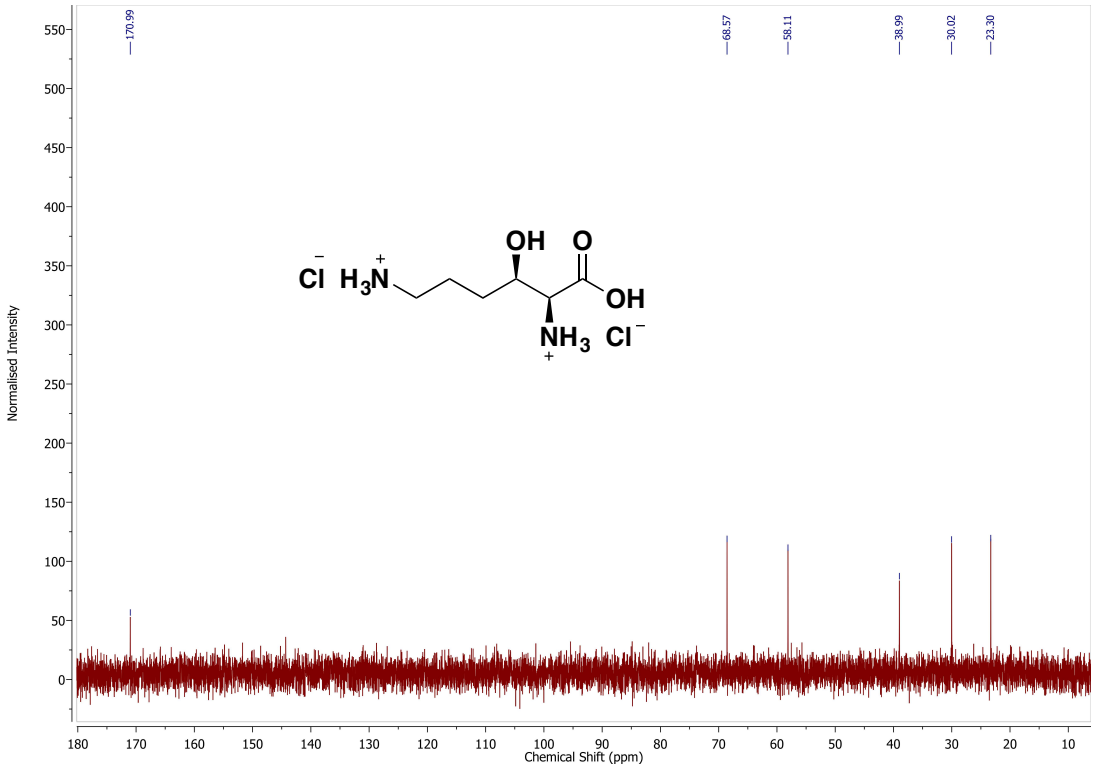
concentrated to dryness and dissolved in D_2O for ^1H NMR analysis and e.r. determination; an e.r. of 3:1 was observed. The ^1H NMR spectra are shown in (Figure 7).

2.16 NMR Spectra

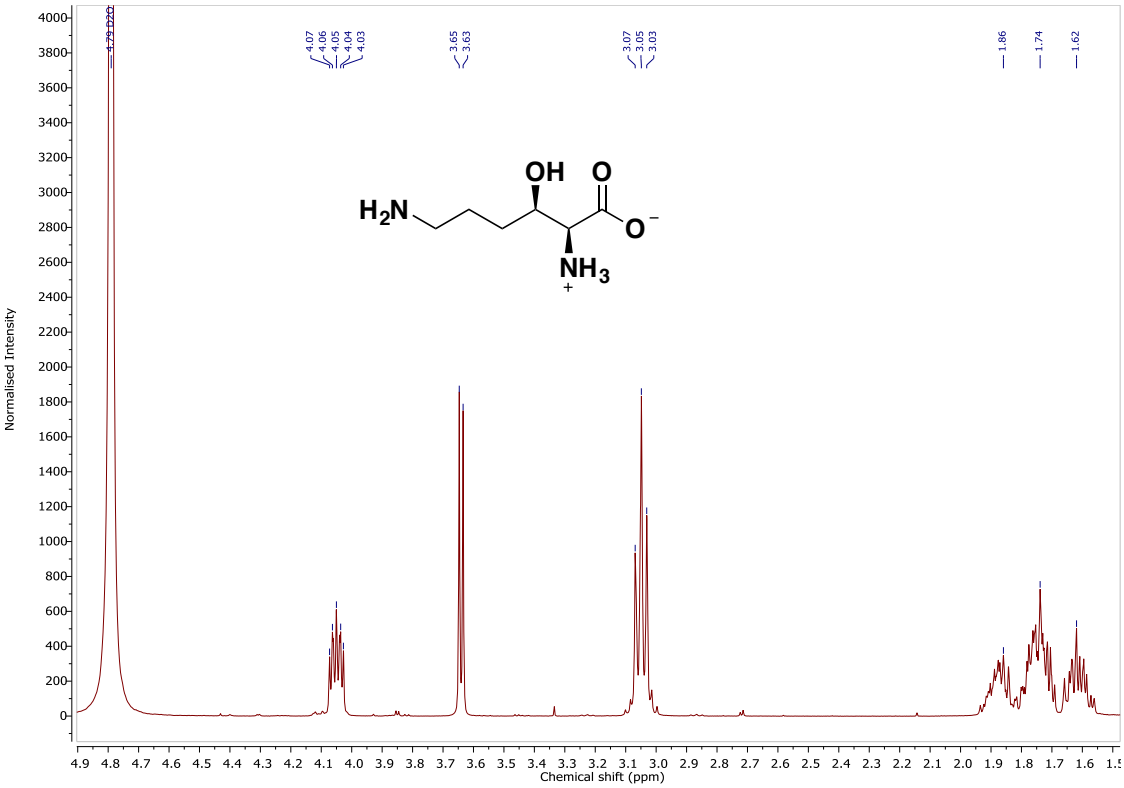
2.16.1 ^{1}H NMR spectrum of (2S,3R)/(2R,3S)-3HO-Lys (24).



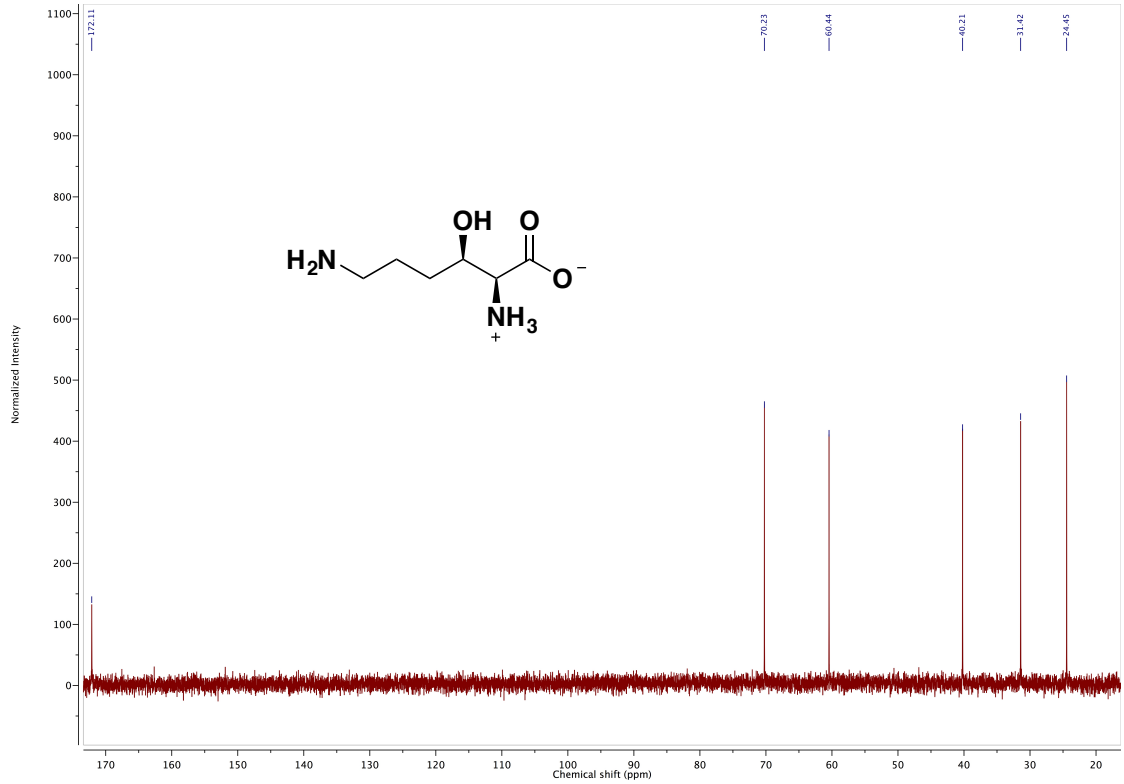
2.16.2 ^{13}C NMR spectrum of (2S,3R)/(2R,3S)-3HO-Lys (24).



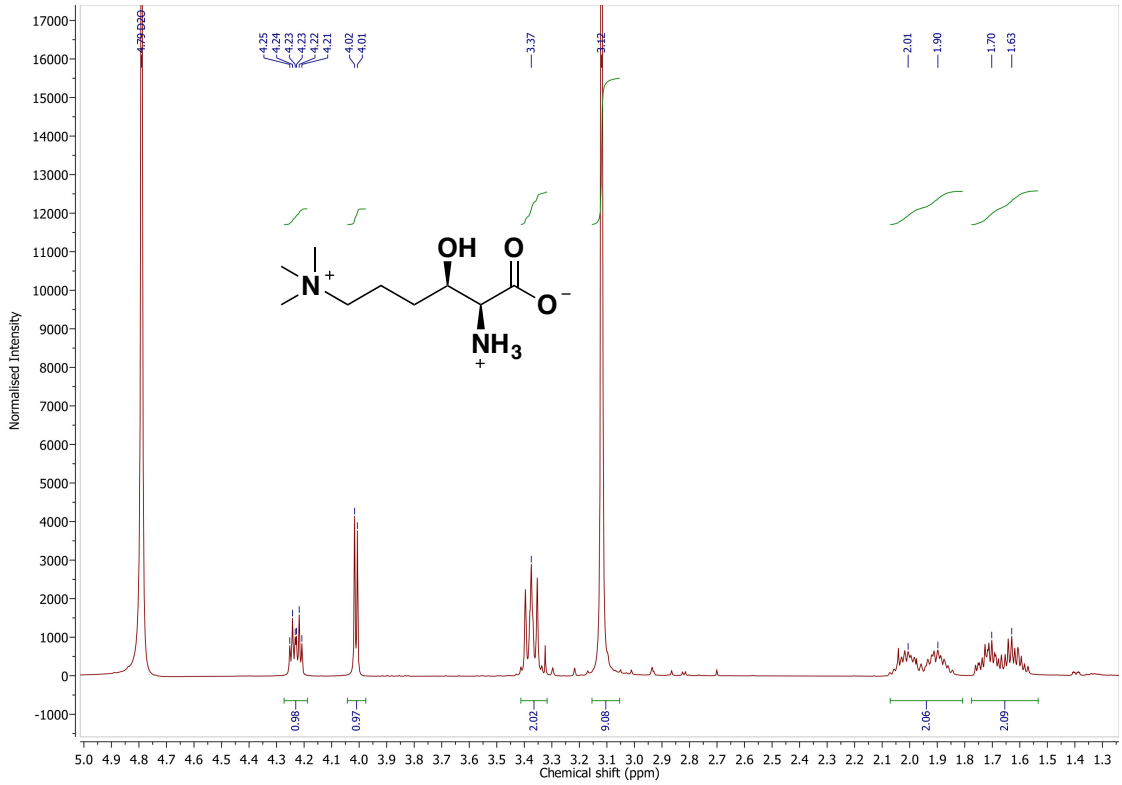
2.16.3 ^{1}H NMR spectrum of (2S,3R)/(2R,3S)-3HO-Lys (24).



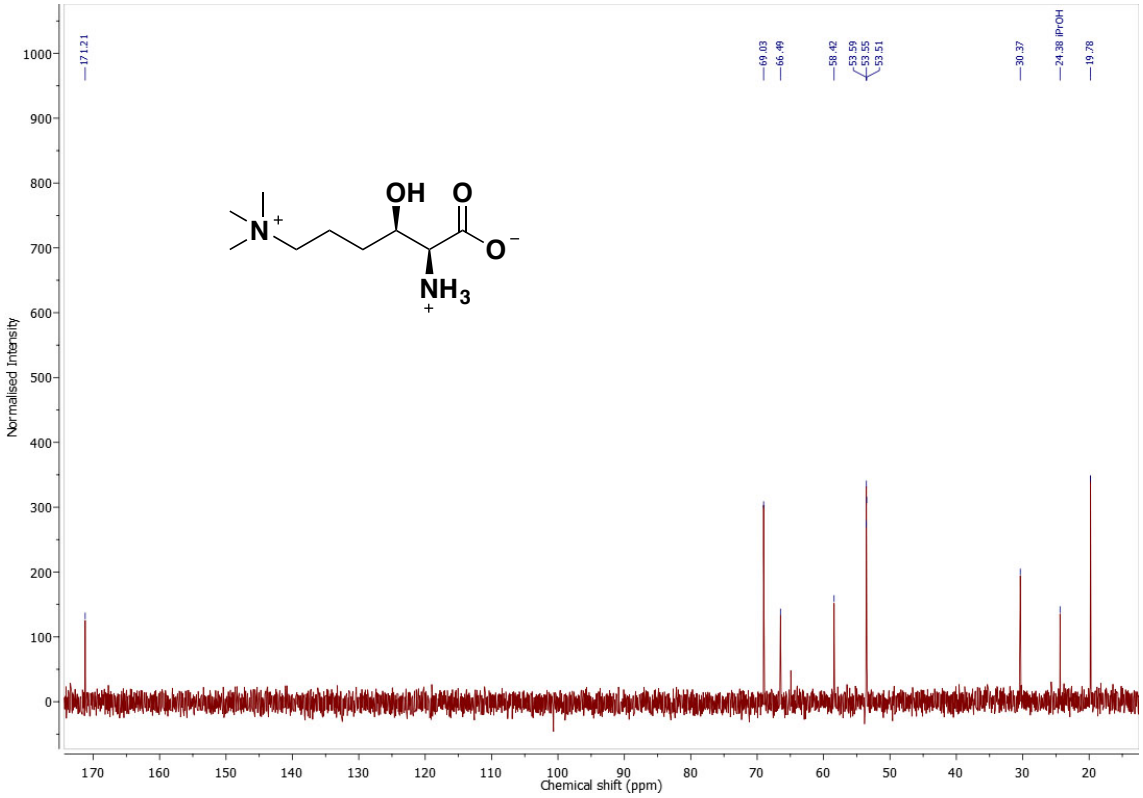
2.16.4 ^{13}C NMR spectrum of (2S,3R)/(2R,3S)-3HO-Lys (24).



2.16.5 ^{1}H NMR spectrum of (2S,3R)/(2R,3S)-3HO-TML (48).



2.16.6 ^{13}C NMR spectrum of (2S,3R)/(2R,3S)-3HO-TML (48).



2.17 References

1. C. Hoppel, The role of carnitine in normal and altered fatty acid metabolism, *Am. J. Kidney Dis.*, 2003, **41**, S4-12.
2. R. R. Ramsay, R. D. Gandour and F. R. van der Leij, Molecular enzymology of carnitine transfer and transport, *Biochim. Biophys. Acta*, 2001, **1546**, 21-43.
3. J. D. McGarry, The mitochondrial carnitine palmitoyltransferase system: its broadening role in fuel homoeostasis and new insights into its molecular features, *Biochem. Soc. Trans.*, 1995, **23**, 321-324.
4. J. D. McGarry and N. F. Brown, The mitochondrial carnitine palmitoyltransferase system. From concept to molecular analysis, *Eur. J. Biochem.*, 1997, **244**, 1-14.
5. V. Tanphaichitr, D. W. Horne and H. P. Broquist, Lysine, a precursor of carnitine in the rat, *J. Biol. Chem.*, 1971, **246**, 6364-6366.
6. V. Tanphaichitr and H. P. Broquist, Role of lysine and -N-trimethyllysine in carnitine biosynthesis. II. Studies in the rat, *J. Biol. Chem.*, 1973, **248**, 2176-2181.
7. D. W. Horne, V. Tanphaichitr and H. P. Broquist, Role of lysine in carnitine biosynthesis in Neurospora crassa, *J. Biol. Chem.*, 1971, **246**, 4373-4375.
8. W. K. Paik and S. Kim, Protein methylation, *Science*, 1971, **174**, 114-119.
9. M. Dambrova, S. Chlopicki, E. Liepinsh, O. Kirjanova, O. Gorshkova, V. I. Kozlovski, S. Uhlen, I. Liepina, R. Petrovska and I. Kalvinsh, The methylester of gamma-butyrobetaine, but not gamma-butyrobetaine itself, induces muscarinic receptor-dependent vasodilatation, *Naunyn Schmiedebergs Arch. Pharmacol.*, 2004, **369**, 533-539.
10. N. Sjakste, L. Baumane, J. L. Boucher, M. Dzintare, D. Meirena, J. Sjakste, L. Lauberte and I. Kalvinsh, Effects of gamma-butyrobetaine and mildronate on nitric oxide production in lipopolysaccharide-treated rats, *Basic Clin. Pharmacol. Toxicol.*, 2004, **94**, 46-50.
11. E. Liepinsh, R. Vilskersts, D. Loca, O. Kirjanova, O. Pugovichs, I. Kalvinsh and M. Dambrova, Mildronate, an inhibitor of carnitine biosynthesis, induces an increase in gamma-butyrobetaine contents and cardioprotection in isolated rat heart infarction, *J. Cardiovasc. Pharmacol.*, 2006, **48**, 314-319.

12. K. Tars, J. Rumnieks, A. Zeltins, A. Kazaks, S. Kotelovica, A. Leonciks, J. Sharipo, A. Viksna, J. Kuka, E. Liepinsh and M. Dambrova, Crystal structure of human gamma-butyrobetaine hydroxylase, *Biochem. Biophys. Res. Commun.*, 2010, **398**, 634-639.
13. E. Liepinsh, I. Konrade, E. Skapare, O. Pugovics, S. Grinberga, J. Kuka, I. Kalvinsh and M. Dambrova, Mildronate treatment alters gamma-butyrobetaine and l-carnitine concentrations in healthy volunteers, *J. Pharm. Pharmacol.*, 2011, **63**, 1195-1201.
14. K. Tars, J. Leitans, A. Kazaks, D. Zelencova, E. Liepinsh, J. Kuka, M. Makrecka, D. Lola, V. Andrianovs, D. Gustina, S. Grinberga, E. Liepinsh, I. Kalvinsh, M. Dambrova, E. Loza and O. Pugovics, Targeting carnitine biosynthesis: discovery of new inhibitors against gamma-butyrobetaine hydroxylase, *J. Med. Chem.*, 2014, **57**, 2213-2236.
15. E. Liepinsh, M. Makrecka-Kuka, J. Kuka, R. Vilskersts, E. Makarova, H. Cirule, E. Loza, D. Lola, S. Grinberga, O. Pugovics, I. Kalvins and M. Dambrova, Inhibition of L-carnitine biosynthesis and transport by methyl-gamma-butyrobetaine decreases fatty acid oxidation and protects against myocardial infarction, *Br. J. Pharmacol.*, 2015, **172**, 1319-1332.
16. A. M. Rydzik, I. K. Leung, G. T. Kochan, A. Thalhammer, U. Oppermann, T. D. Claridge and C. J. Schofield, Development and application of a fluoride-detection-based fluorescence assay for gamma-butyrobetaine hydroxylase, *Chembiochem*, 2012, **13**, 1559-1563.
17. A. M. Rydzik, R. Chowdhury, G. T. Kochan, S. T. Williams, M. A. McDonough, A. Kawamura and C. J. Schofield, Modulating carnitine levels by targeting its biosynthesis pathway - selective inhibition of gamma-butyrobetaine hydroxylase, *Chem. Sci.*, 2014, **5**, 1765-1771.
18. I. K. Leung, T. J. Krojer, G. T. Kochan, L. Henry, F. von Delft, T. D. Claridge, U. Oppermann, M. A. McDonough and C. J. Schofield, Structural and mechanistic studies on gamma-butyrobetaine hydroxylase, *Chem. Biol.*, 2010, **17**, 1316-1324.
19. L. Henry, I. K. Leung, T. D. Claridge and C. J. Schofield, gamma-Butyrobetaine hydroxylase catalyses a Stevens type rearrangement, *Bioorg. Med. Chem. Lett.*, 2012, **22**, 4975-4978.
20. J. D. E. Hulse, S. R.; Henderson, L. M., Carnitine biosynthesis. beta-Hydroxylation of trimethyllysine by an alpha-ketoglutarate-dependent mitochondrial dioxygenase., *J. Biol. Chem.*, 1978, **253**, 1654-1659.

21. N. van Vlies, R. Ofman, R. J. Wanders and F. M. Vaz, Submitochondrial localization of 6-N-trimethyllysine dioxygenase - implications for carnitine biosynthesis, *FEBS J.*, 2007, **274**, 5845-5851.
22. G. Huszar, Tissue-Specific Biosynthesis of Epsilon-N-Monomethyllysine and Epsilon-N-Trimethyllysine in Skeletal and Cardiac-Muscle Myosin - Model for Cell-Free Study of Post-Translational Amino-Acid Modifications in Proteins, *J. Mol. Biol.*, 1975, **94**, 311-326.
23. L. Servillo, A. Giovane, D. Cautela, D. Castaldo and M. L. Balestrieri, Where does N(epsilon)-trimethyllysine for the carnitine biosynthesis in mammals come from?, *PLoS One*, 2014, **9**, e84589.
24. J. LaBadie, W. A. Dunn and N. N. Aronson, Jr., Hepatic synthesis of carnitine from protein-bound trimethyl-lysine. Lysosomal digestion of methyl-lysine-labelled asialo-fetuin, *Biochem. J*, 1976, **160**, 85-95.
25. W. A. Dunn, G. Rettura, E. Seifter and S. Englard, Carnitine biosynthesis from gamma-butyrobetaine and from exogenous protein-bound 6-N-trimethyl-L-lysine by the perfused guinea pig liver. Effect of ascorbate deficiency on the in situ activity of gamma-butyrobetaine hydroxylase, *J. Biol. Chem.*, 1984, **259**, 10764-10770.
26. R. O. Rosti, A. A. Sadek, K. K. Vaux and J. G. Gleeson, The genetic landscape of autism spectrum disorders, *Dev. Med. Child Neurol.*, 2014, **56**, 12-18.
27. C. Nava, F. Lamari, D. Heron, C. Mignot, A. Rastetter, B. Keren, D. Cohen, A. Faudet, D. Bouteiller, M. Gilleron, A. Jacquette, S. Whalen, A. Afenjar, D. Perisse, C. Laurent, C. Dupuits, C. Gautier, M. Gerard, G. Huguet, S. Caillet, B. Leheup, M. Leboyer, C. Gillberg, R. Delorme, T. Bourgeron, A. Brice and C. Depienne, Analysis of the chromosome X exome in patients with autism spectrum disorders identified novel candidate genes, including TMLHE, *Transl. Psychiatry*, 2012, **2**, e179.
28. E. T. Lim, S. Raychaudhuri, S. J. Sanders, C. Stevens, A. Sabo, D. G. MacArthur, B. M. Neale, A. Kirby, D. M. Ruderfer, M. Fromer, M. Lek, L. Liu, J. Flannick, S. Ripke, U. Nagaswamy, D. Muzny, J. G. Reid, A. Hawes, I. Newsham, Y. Wu, L. Lewis, H. Dinh, S. Gross, L. S. Wang, C. F. Lin, O. Valladares, S. B. Gabriel, M. dePristo, D. M. Altshuler, S. M. Purcell, N. E. S. Project, M. W. State, E. Boerwinkle, J. D. Buxbaum, E. H. Cook, R. A. Gibbs, G. D. Schellenberg, J. S. Sutcliffe, B. Devlin, K. Roeder and M. J. Daly, Rare complete knockouts in humans: population distribution and significant role in autism spectrum disorders, *Neuron*, 2013, **77**, 235-242.

29. P. B. Celestino-Soper, C. A. Shaw, S. J. Sanders, J. Li, M. T. Murtha, A. G. Ercan-Sencicek, L. Davis, S. Thomson, T. Gambin, A. C. Chinault, Z. Ou, J. R. German, A. Milosavljevic, J. S. Sutcliffe, E. H. Cook, Jr., P. Stankiewicz, M. W. State and A. L. Beaudet, Use of array CGH to detect exonic copy number variants throughout the genome in autism families detects a novel deletion in TMLHE, *Hum. Mol. Genet.*, 2011, **20**, 4360-4370.
30. P. B. Celestino-Soper, S. Violante, E. L. Crawford, R. Luo, A. C. Lionel, E. Delaby, G. Cai, B. Sadikovic, K. Lee, C. Lo, K. Gao, R. E. Person, T. J. Moss, J. R. German, N. Huang, M. Shinawi, D. Treadwell-Deering, P. Szatmari, W. Roberts, B. Fernandez, R. J. Schroer, R. E. Stevenson, J. D. Buxbaum, C. Betancur, S. W. Scherer, S. J. Sanders, D. H. Geschwind, J. S. Sutcliffe, M. E. Hurles, R. J. Wanders, C. A. Shaw, S. M. Leal, E. H. Cook, Jr., R. P. Goin-Kochel, F. M. Vaz and A. L. Beaudet, A common X-linked inborn error of carnitine biosynthesis may be a risk factor for nondysmorphic autism, *Proc. Natl. Acad. Sci. U. S. A.*, 2012, **109**, 7974-7981.
31. A. Kazaks, M. Makrecka-Kuka, J. Kuka, T. Voronkova, I. Akopjana, S. Grinberga, O. Pugovics and K. Tars, Expression and purification of active, stabilized trimethyllysine hydroxylase, *Protein. Expr. Purif.*, 2014, **104**, 1-6.
32. R. Stein and S. Englard, Properties of rat 6-N-trimethyl-L-lysine hydroxylases: similarities among the kidney, liver, heart, and skeletal muscle activities, *Arch. Biochem. Biophys.*, 1982, **217**, 324-331.
33. D. S. Sachan and H. P. Broquist, Synthesis of carnitine from epsilon-N-trimethyllysine in post mitochondrial fractions of Neurospora crassa, *Biochem. Biophys. Res. Commun.*, 1980, **96**, 870-875.
34. D. S. Sachan and C. L. Hoppel, Carnitine biosynthesis. Hydroxylation of N6-trimethyl-lysine to 3-hydroxy-N6-trimethyl-lysine, *Biochem. J.*, 1980, **188**, 529-534.
35. A. G. Prescott and M. D. Lloyd, The iron(II) and 2-oxoacid-dependent dioxygenases and their role in metabolism, *Nat. Prod. Rep.*, 2000, **17**, 367-383.
36. M. A. McDonough, C. Loenarz, R. Chowdhury, I. J. Clifton and C. J. Schofield, Structural studies on human 2-oxoglutarate dependent oxygenases, *Curr. Opin. Struct. Biol.*, 2010, **20**, 659-672.
37. C. Loenarz and C. J. Schofield, Expanding chemical biology of 2-oxoglutarate oxygenases, *Nat. Chem. Biol.*, 2008, **4**, 152-156.

38. R. F. Novak, T. J. Swift and C. L. Hoppel, N6-Trimethyl-lysine metabolism. Structural identification of the metabolite 3-hydroxy-N6-trimethyl-lysine, *Biochem. J.*, 1980, **188**, 521-527.
39. J. Ehrlich, Q. R. Bartz, R. M. Smith, D. A. Joslyn and P. R. Burkholder, Chloromycetin, a New Antibiotic From a Soil Actinomycete, *Science*, 1947, **106**, 417.
40. A. Franchino, P. Jakubec and D. J. Dixon, Enantioselective synthesis of (-)-chloramphenicol via silver-catalysed asymmetric isocyanoacetate aldol reaction, *Org. Biomol. Chem*, 2016, **14**, 93-96.
41. E. D. Clercq, Antiviral drugs in current clinical use, *J. Clin. Virol.*, 2004, **30**, 115-133.
42. S. C. Bergmeier, The Synthesis of Vicinal Amino Alcohols, *Tetrahedron*, 2000, **56**, 2561-2576.
43. O. K. Karjalainen and A. M. Koskinen, Diastereoselective synthesis of vicinal amino alcohols, *Org. Biomol. Chem.*, 2012, **10**, 4311-4326.
44. C. H. Stammer and R. G. Webb, Synthesis of Racemic Threo- and Erythro-Beta-Hydroxylysines, *J. Org. Chem.*, 1969, **34**, 2306-&.
45. R. C. Roemmele and H. Rapoport, Chirospecific Synthesis of Beta-Hydroxy Alpha-Amino-Acids, *J. Org. Chem.*, 1989, **54**, 1866-1875.
46. P. F. Hughes, S. H. Smith and J. T. Olson, Two Chiral Syntheses of threo-3-Hydroxylysine, *J. Org. Chem.*, 1994, **59**, 5799-5802.
47. J. W. Lampe, P. F. Hughes, C. K. Biggers, S. H. Smith and H. Hu, Total Synthesis of (-)-Balanol, *J. Org. Chem.*, 1994, **59**, 5147-5148.
48. J. W. Lampe, P. F. Hughes, C. K. Biggers, S. H. Smith and H. Hu, Total synthesis of (-)- and (+)-balanol, *J. Org. Chem.*, 1996, **61**, 4572-4581.
49. C. E. Masse, A. J. Morgan and J. S. Panek, An asymmetric aminohydroxylation approach to the azepine core of (-)-balanol, *Org. Lett.*, 2000, **2**, 2571-2573.
50. K. S. A. Kumar, A chiron approach towards the synthesis of 3-hydroxy lysine and its derivatives, *Biorg. Med. Chem.*, 2013, **21**, 3609-3613.
51. D. Baud, P.-L. Saaidi, A. Monfleur, M. Harari, J. Cuccaro, A. Fossey, M. Besnard, A. Debard, A. Mariage, V. Pellouin, J.-L. Petit, M. Salanoubat, J. Weissenbach, V. de Berardinis and A. Zaparucha, Synthesis of Mono- and Dihydroxylated Amino Acids with New α-Ketoglutarate-Dependent Dioxygenases: Biocatalytic Oxidation of C-H Bonds, *Chem. Cat. Chem.*, 2014, **6**, 3012-3017.

52. A. Zaparucha, B. De Veronique, P. L. Saaidi and D. Baud, New enzymes and method for preparing hydroxylated L-lysine and or L-ornithine and analogues thereof, EP 28976156 A1 / WO2015078889 A1, Nov 26th 2013.
53. H. S. M. J. A. Dale, Nuclear magnetic resonance enantiomer regents. Configurational correlations via nuclear magnetic resonance chemical shifts of diastereomeric mandelate, O-methylmandelate, and .alpha.-methoxy-.alpha.-trifluoromethylphenylacetate (MTPA) esters, *J. Am. Chem. Soc.*, 1973, **95**, 512-519.
54. F. Sladojevich, A. Trabocchi, A. Guarna and D. J. Dixon, A new family of cinchona-derived amino phosphine precatalysts: application to the highly enantio- and diastereoselective silver-catalyzed isocyanoacetate aldol reaction, *J. Am. Chem. Soc.*, 2011, **133**, 1710-1713.
55. F. Sladojevich, A. L. Fuentes de Arriba, I. Ortin, T. Yang, A. Ferrali, R. S. Paton and D. J. Dixon, Mechanistic investigations into the enantioselective Conia-ene reaction catalyzed by cinchona-derived amino urea pre-catalysts and Cu(I), *Chemistry*, 2013, **19**, 14286-14295.
56. Y. S. Ito, M.; Hayashi, T., Catalytic Asymmetric Aldol Reaction: Reaction of Aldehydes with Isocyanoacetate Catalyzed by a Chiral Ferrocenylphosphine-Gold(1) Complex, *J. Am. Chem. Soc.*, 1986, **108**, 6406-6407.
57. M. S. Yoshihiko Ito, Eiji Shirakawa, Keiichi Hayashizaki, Tamio Hayashi, Asymmetric synthesis of β-hydroxy-α-alkylamino acids by asymmetric aldol reaction of α-isocyanocarboxylates catalyzed by chiral ferrocenylphosphine-gold(I) complexes, *Tetrahedron*, 1988, **44**, 5253-5262.
58. Y. U. Tamio Hayashi, Akiko YamazakiMasaya Sawamura, Hitoshi Hamashima, Yoshihiko Ito, Silver(I)-catalyzed asymmetric aldol reaction of isocyanoacetate, *Tetrahedron Lett.*, 1991, **32**, 2799–2802.
59. C. Cassani, R. Martin-Rapun, E. Arceo, F. Bravo and P. Melchiorre, Synthesis of 9-amino(9-deoxy) epi cinchona alkaloids, general chiral organocatalysts for the stereoselective functionalization of carbonyl compounds, *Nat. Protoc.*, 2013, **8**, 325-344.
60. M. Kirihata, Y. Nakao, M. Fukuari and I. Ichimoto, Synthesis and Structural Confirmation of (2S,3R,4R,6E)-2-Acetylamino-3-hydroxy-4-methyl-6-octenoic Acid, a New Amino Acid Produced by Neocosmospora vasinfecta, *Biosci. Biotech. Biochem.*, 1995, **59**, 2228-2230.

61. T. R. Hoye, C. S. Jeffrey and F. Shao, Mosher ester analysis for the determination of absolute configuration of stereogenic (chiral) carbinol carbons, *Nat. Protoc.*, 2007, **2**, 2451-2458.
62. R. K. Lesniak, S. Markolovic, K. Tars and C. J. Schofield, Human carnitine biosynthesis proceeds via (2S,3S)-3-hydroxy-Nepsilon-trimethyllysine, *Chem. Commun.*, 2016, **53**, 440-442.
63. G. R. Sullivan, J. A. Dale and H. S. Mosher, Correlation of Configuration and F-19 Chemical-Shifts of Alpha-Methoxy-Alpha-Trifluoromethylphenylacetate Derivatives, *J. Org. Chem.*, 1973, **38**, 2143-2147.
64. S. Markolovic, S. E. Wilkins and C. J. Schofield, Protein Hydroxylation Catalyzed by 2-Oxoglutarate-dependent Oxygenases, *J. Biol. Chem.*, 2015, **290**, 20712-20722.
65. M. Mantri, N. D. Loik, R. B. Hamed, T. D. Claridge, J. S. McCullagh and C. J. Schofield, The 2-oxoglutarate-dependent oxygenase JMJD6 catalyses oxidation of lysine residues to give 5S-hydroxylysine residues, *Chem. Bio. chem.*, 2011, **12**, 531-534.
66. T. Feng, A. Yamamoto, S. E. Wilkins, E. Sokolova, L. A. Yates, M. Munzel, P. Singh, R. J. Hopkinson, R. Fischer, M. E. Cockman, J. Shelley, D. C. Trudgian, J. Schodel, J. S. O. McCullagh, W. Ge, B. M. Kessler, R. J. Gilbert, L. Y. Frolova, E. Alkalaeva, P. J. Ratcliffe, C. J. Schofield and M. L. Coleman, Optimal Translational Termination Requires C4 Lysyl Hydroxylation of eRF1, *Mol. Cell.*, 2014, **53**, 645-654.
67. S. B. Marco Biasini, Andrew Waterhouse, Konstantin Arnold, Gabriel Studer, Tobias Schmidt, Florian Kiefer, Tiziano Gallo Cassarino, Martino Bertoni, Lorenza Bordoli, Torsten Schwede, SWISS-MODEL: modelling protein tertiary and quaternary structure using evolutionary information. , *Nucleic Acids Res.*, 2014, **42**.
68. K. Arnold, F. Kiefer, J. Kopp, J. N. Battey, M. Podvinec, J. D. Westbrook, H. M. Berman, L. Bordoli and T. Schwede, The Protein Model Portal, *J. Struct. Funct. Genomics*, 2009, **10**, 1-8.
69. F. Kiefer, K. Arnold, M. Kunzli, L. Bordoli and T. Schwede, The SWISS-MODEL Repository and associated resources, *Nucleic Acids Res.*, 2009, **37**, D387-392.
70. K. Arnold, L. Bordoli, J. Kopp and T. Schwede, The SWISS-MODEL workspace: a web-based environment for protein structure homology modelling, *Bioinformatics*, 2006, **22**, 195-201.

71. N. Guex, M. C. Peitsch and T. Schwede, Automated comparative protein structure modeling with SWISS-MODEL and Swiss-PdbViewer: a historical perspective, *Electrophoresis*, 2009, **30**, S162-173.

72. J. March, *Advanced Organic Chemistry* Wiley, 3rd edn.

73. M. Mantri, T. Krojer, E. A. Bagg, C. A. Webby, D. S. Butler, G. Kochan, K. L. Kavanagh, U. Oppermann, M. A. McDonough and C. J. Schofield, Crystal Structure of the 2-Oxoglutarate- and Fe(II)-Dependent Lysyl Hydroxylase JMJD6, *J. Mol. Biol.*, 2010, **401**, 211-222.

74. L. Sidorowicz and J. Skarzewski, Easy Access to 9-Epimers of Cinchona Alkaloids: One-Pot Inversion by Mitsunobu Esterification-Saponification, *Synthesis*, 2011, **5**, 708-710.

Chapter 3

^{19}F NMR studies of BBOX from *Pseudomonas* sp. AK1

Contents

3.0 ^{19}F NMR STUDIES OF BBOX FROM *PSEUDOMONAS* SP. AK1 110

3.1 INTRODUCTION 110

3.1.1 BBOX from Pseudomonas sp. AK1 (psBBOX) 110

3.1.2 Mildronate and BBOX inhibition 112

3.1.3 Previous NMR Studies on psBBOX 113

3.1.4 Protein-observed ^{19}F NMR spectroscopy 115

3.1.5 ^{19}F labelling of proteins 116

3.2 ^{19}F LABELING OF PSBBOX 119

3.3 INITIAL NMR EXPERIMENTS ON PSBBOX* 122

3.3.1 Metal screening 123

3.3.1.1 T_m Shift - psBBOX 123

3.3.1.2 ^{19}F NMR spectra of psBBOX*-Metal complexes: $Zn^{(II)}$and $Ni^{(II)}$ 124

3.3.1.3 psBBOX*-Metal complexes: $Fe^{(II)}$, $Co^{(II)}$ and $Mn^{(II)}$ 125

3.4 EFFECTS ON PSBBOX* ^{19}F SIGNAL WITH CO/SUBSTRATES 126

3.4.1 Effects of GBB 126

3.4.2 Effects of 2OG 128

3.4.3 Effects of 2OG on psBBOX-$Zn^{(II)}$-GBB 129*

3.4.4 Effect of NOG on psBBOX-$Zn^{(II)}$ 132*

3.4.4.1 Effect of GBB on psBBOX*-$Zn^{(II)}$-NOG 133

3.5 EFFECTS OF OTHER SUBSTRATES ON PSBBOX*-$ZN^{(II)}$ 134

3.5.1 L/D-Carnitine 134

3.5.2 P-GBB 135

3.5.3 GBBNF 137

3.6 EFFECT OF INHIBITORS ON THE PSBBOX*-$ZN^{(II)}$ COMPLEX 139

3.6.1 Effect of substrate analogues 139

3.6.1.1 Mildronate 139

3.6.1.2 AR758 140

3.6.2 Effect of FG2216 analogues on psBBOX 142*

3.6.2.1 FG2216 142

3.6.2.2 FG-L-Ala 144

3.6.2.3 FG-D-Ala 145

3.6.2.4 FG-L/D-Trp 147

3.6.3 Effect of AR92B on psBBOX 149*

3.6.4 Effect of RL190B on psBBOX 151*

3.6.5 Effect of DMSO 152

3.7 SUMMARY AND FUTURE PERSPECTIVES 153

3.8 ACKNOWLEDGEMENTS **158**
3.9 MATERIALS AND METHODS **158**
3.9.1 NMR - instrumentation *158*
3.9.2 NMR – Sample preparation and data aquisition *158*
3.9.3 Enzyme production and purification *159*
3.9.3.1 Reagents for molecular biology 159
3.9.3.2 Expression 160
3.9.3.3 Cell lysis and protein purification[19] 160
3.9.3.4 BFA labelling of psBBOX-Y201C 161
3.9.3.5 Expression materials 162
3.9.3.6 T_m Measurements on psBBOX 162
3.10 REFERENCES **164**

3.0 ^{19}F NMR studies of BBOX from *Pseudomonas* sp. AK1

3.1 Introduction

3.1.1 BBOX from *Pseudomonas* sp. AK1 (psBBOX)

L-Carnitine (**1**) (Figure 1) is used prevalently in the supplement industry as a fat-loss aid.[1,2] Its biosynthesis is also targeted as a means to treat cardiac conditions and carnitine deficiencies.[3-5] Consequently, high-scale biosynthesis of carnitine has been investigated for commercial production.[6,7] Although *de novo* biosynthesis of carnitine does not occur in the majority of microbes, a number of *Pseudomonas* bacterial strains produce a γ-butyrobetaine hydroxylase (BBOX) homologue which catalyses the conversion of γ-butyrobetaine (**2**) (GBB) to L-carnitine.[8-11] A specific carnitine biosynthesis pathway in bacteria has not been elucidated and most literature concerns carnitine catabolism.[12,13] The role of carnitine itself in bacteria is not well defined; it is reported to act as a nitrogen and carbon source,[13] an osmoprotectant,[14] and a growth stimulant.[15] In animal systems, carnitine biosynthesis has been well established.[16,17] A BBOX homologue, isolated from *Pseudomonas* ps. AK1 (psBBOX), was found to be dependent on $Fe^{(II)}$ and 2-oxoglutarate (2OG) (**3**), possessing a $Zn^{(II)}$ binding domain, and existing as a homodimer.[10,11,18] This is consistent with the 30% sequence homology shared between human BBOX (hBBOX) and psBBOX.[19] Through the development of recombinant psBBOX production using *E.coli* BL21 (DE3) competent cells and the 'cold-shock' protein-inducing vector, pCOLDI, high levels of protein production were observed (80 mg psBBOX per 1 L of bacterial culture).[19] Notably, recombinant hBBOX is comparatively difficult to produce in bacteria with relatively lower yields being observed.[18,19] Given the high similarity of psBBOX to hBBOX and its relatively high yield

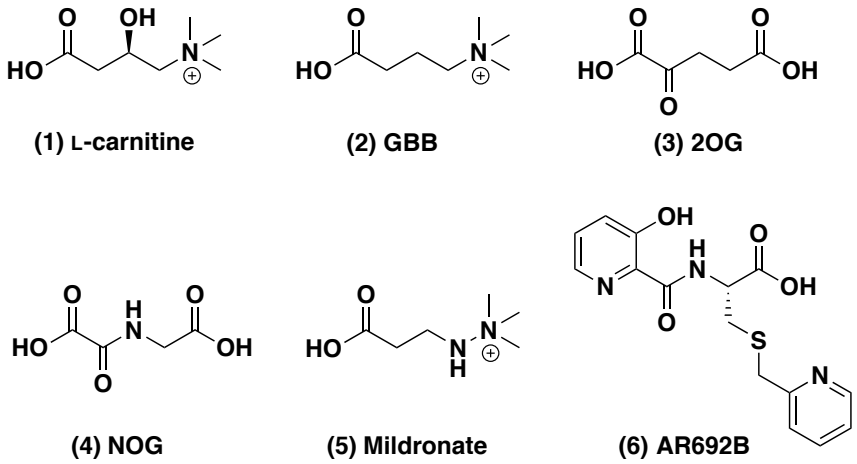


Figure 1 Chemical structures of BBOX co/substrates and inhibitors such as GBB mimic Mildronate and the potent iron-chelating AR692B.

of production, psBBOX was used as a model system to study the dynamics of BBOX enzymes. Unfortunately, attempts within the Schofield lab to crystallise psBBOX have so far failed; however, a homology model of psBBOX using the SWISS-MODEL[20-22] server was successfully obtained, based on a crystal structure of hBBOX containing bound $Zn^{(II)}$, GBB (**2**), and *N*-oxalylglycine (NOG) (**4**) (PDB id: 3O2G) (Figure 2).[18] Sequence alignment and overlays of the psBBOX model with hBBOX reveal that the overall folds and 2OG and $Fe^{(II)}$ binding residues are likely conserved between psBBOX and hBBOX with some

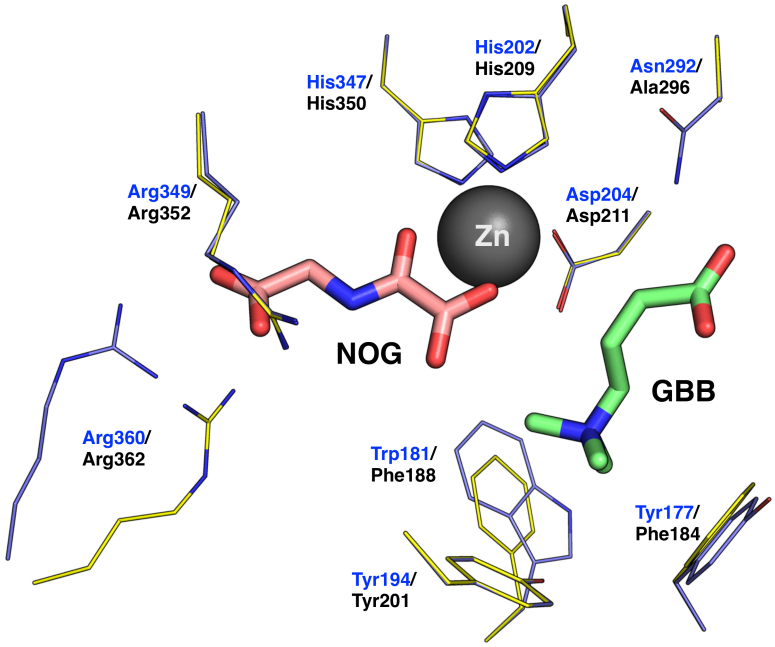


Figure 2 Overlaid GBB (green sticks) and NOG (red sticks) binding residues of hBBOX (blue lines, PDB id: 3O2G) and the psBBOX model (yellow lines).

differences in the GBB binding residues (Figure 2).[19] As observed with the TMLH homology model described in Chapter 2, differences exist in the 'aromatic cage', which is responsible for quaternary ammonium recognition. Given crystallographic data is yet to be obtained for psBBOX and the high sequence similarity to hBBOX, homology modelling enables a good estimation of key structural differences between the active sites of psBBOX and hBBOX. Thus, in order to further explore the BBOX system and support X-ray crystallographic discoveries with hBBOX, it was envisaged that various nuclear magnetic resonance (NMR) techniques may visualise the behaviour of psBBOX in solution. Given the requirement for large amounts of enzyme for such studies, psBBOX presented a viable option with which to design and explore various NMR experiments.

3.1.2 Mildronate and BBOX inhibition

One of the proposed therapeutic targets of the drug Mildronate (**5**) (Figure 1) (Meldonium, THP, Met-88)[23,24] is hBBOX (IC_{50} = 60 μM[25] / 12 μM[26]). Mildronate is clinically used in eastern Europe; it is given to patients as a cardioprotective agent (Chapter 1). Mildronate has recently received considerable attention given its proposed performance enhancing abilities leading to its abuse in the sporting community.[27-29] Mildronate inhibits hBBOX and therefore carnitine production; it is also a competitive substrate for hBBOX producing several products.[18,30] Mildronate's small size (147 Da) and structural similarity to the natural substrate of hBBOX, GBB, and product L-carnitine (Figure 1) may cause compromised selectivity over other carnitine/GBB binding proteins such as carnitine transporters.[31-34] Nevertheless, studies have shown the efficacy of GBB analogues as hBBOX and psBBOX inhibitors *in vitro*.[9,35-38] 2-Oxoglutarate (2OG) mimics are also effective inhibitors of psBBOX and hBBOX (see Appendix I); recently the discovery of a cell-active hBBOX inhibitor was reported.[39] AR692B (**6**) (Figure 1) (IC_{50} = 153 nM)[39] is based on a 3-hydroxy pyridine scaffold and a crystal structure of AR692B in complex with hBBOX (Figure 5),[39]

revealed two possible binding modes and a different enzyme conformation to that seen with GBB[18] and Midronate.[40] The distinct differences in the 'flexible-loop', located in the catalytic domain of each BBOX monomer observed with GBB and AR692B, suggest a dynamic protein fold in solution.

3.1.3 Previous NMR Studies on psBBOX

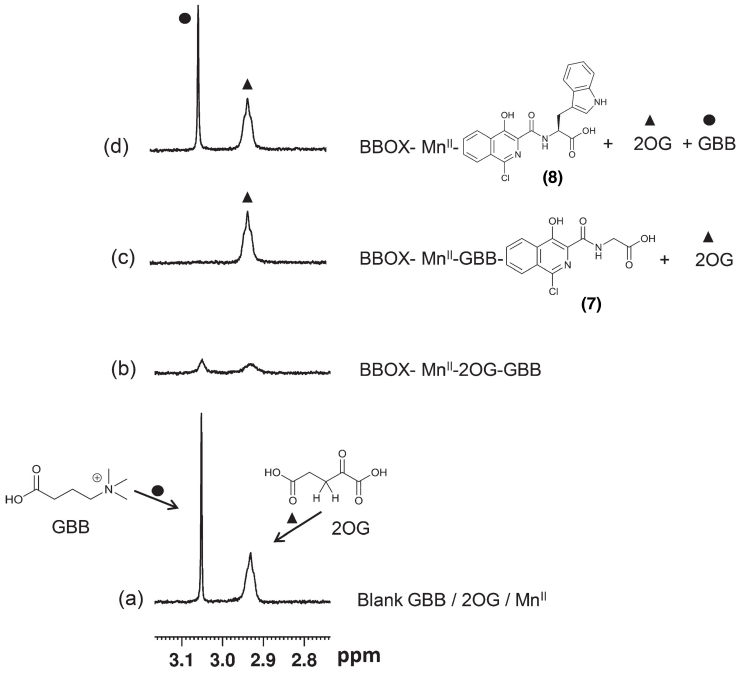


Figure 3 Example spectra obtained using the CPMG edited ^{1}H NMR GBB/2OG reporter assay with psBBOX. **A**) A solution containing the reporter ligands GBB and 2OG in the presence of catalytically inert $Mn^{(II)}$. **B**) psBBOX is added to the ligand solution. **C**) Addition of isoquinoline ligand (**7**) to (**b**). **D**) After addition of isoquinoline **(8)** to (**c**). Symbols (●, ▲) indicate GBB and 2OG signals, respectively. The assay mixture contained 15 μM psBBOX, 150 μM $Mn^{(II)}$, 25 μM GBB, 300 μM 2OG, 80 mM KCl and 25 μM isoquinoline ligand. Incubation solution: 50 mM Tris-D_{11}, pH 7.5, 100% D_2O. (*Figure adapted from ref no. 41)*.

The use of a ^{1}H NMR GBB/2OG reporter based assay was recently reported,[41] making use of paramagnetic relaxation enhancement, using either $Zn^{(II)}$ or $Mn^{(II)}$, to observe ligand binding to the psBBOX active site. The psBBOX ^{1}H NMR reporter assay enables monitoring of co/substrates and inhibitors binding to psBBOX (Figure 3), and provides information on the binding mode of the inhibitor of interest *i.e.* whether it displaces GBB, 2OG or both (Figure 3). Isoquinoline (**7**), for example, displaces 2OG almost entirely from the psBBOX active site, whereas the bulkier inhibitor (**8**) is able to displace both GBB and

2OG (Figure 3). Following from this work, it was possible to observe binding of Mildronate (**5**) (Figure 4), which is a structural analogue of GBB (**2**), and a competitive substrate for hBBOX (Section 3.1.2).[30] It was found that displacement of GBB by Mildronate from the psBBOX-$Zn^{(II)}$-2OG-GBB complex (and vice versa) does not proceed to more than 50 % *i.e.* at 1:1, Mildronate:GBB, under the experimental conditions (Figure 4).

In contrast with the results obtained with co/substrates, when potent hBBOX inhibitors are titrated into the psBBOX-$Zn^{(II)}$-2OG-GBB complex, near complete displacement of GBB is observed (Figure 3 and Figure 4). The experiments shown in Figures 3 and 4 demonstrate that full attenuation of GBB can be achieved; however, Mildronate only displaces ~ 50% of bound GBB. With the addition of a 2OG-mimic, *i.e.* a metal-chelating ligand such as hBBOX inhibitor AMG-1957661 (**9**) (IC_{50} = 2.7 µM) (Figure 3), near-complete displacement is observed. Interestingly, incubation of the assay mixture first with Mildronate (**5**) (1.5 mM Mildronate, 700 µM 2OG, 250 µM $Zn^{(II)}$, 25 µM psBBOX) for 10 minutes, followed by titration with GBB (**2**) (5 µM) displayed a GBB

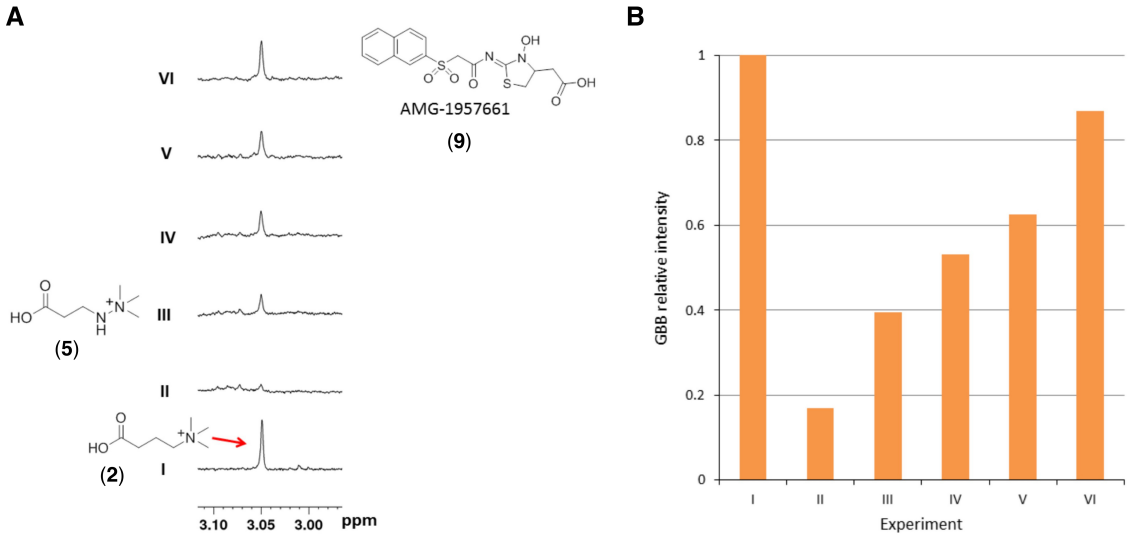


Figure 4 Titration of Mildronate only displaced ~ 50% of bound GBB. Metal chelating, 2OG-mimic AMG-1957661 is able to displace ~ 90% bound GBB. **A**) (**I**) 250 µM $Zn^{(II)}$, 5 µM GBB, 700 µM 2OG, 50 mM Tris-D_{11}, pH 7.5, D_2O. (**II**) 25 µM psBBOX added. (**III**) 500 µM Mildronate. (**IV**) 1 mM Mildronate, (**V**) 1.5 mM Midonrate. (**VI**) 500 µM AMG-1957661. ^1H NMR spectra displaying only the $-NMe_3^+$ signal arising from GBB is displayed. **B**) Gaphical representation of integration data obtained from (**A**). (*Figure adapted from the D. Phil thesis of Amjad Kahn.*)

signal indicating that only ~50% of total GBB was bound to the enzyme. Since psBBOX is a homodimer, these results led to the proposal that binding of a second molecule of GBB to the psBBOX-$Zn^{(II)}$-2OG-GBB complex could potentially strengthen binding of the first. Thus there may be cooperativity between the dimers of the psBBOX system. To explore this hypothesis it was proposed that monitoring of ligand binding to psBBOX could be achieved through the use of ^{19}F NMR. In contrast to the reported ^{1}H NMR reporter assay which focused on observing changes in ligand ^{1}H signals upon its binding to psBBOX, incorporation of a ^{19}F nucleus at a position of interest on psBBOX, such as the flexible loop, could provide a valuable insight into conformational changes induced by ligand binding.

3.1.4 Protein-observed ^{19}F NMR spectroscopy

The potential of ^{19}F NMR spectroscopy for the study of biological systems has been intensely studied with a number of applications reported such as small fragment screening for drug discovery,[42,43] imaging of tumor biomarkers,[44] and MRI contrast agents.[45] ^{19}F-labelling of proteins with the aim to monitor conformational changes upon ligand binding has proved fruitful in many cases.[43] Notable studies include, but are by no means limited to, the New Dehli metallo-β-lactamase (NDM-1)[46] and BET bromodomain drug discovery[47] efforts whereby ligand-induced conformational changes on ^{19}F-labelled proteins were monitored upon binding of known inhibitors. The quantitative data, gathered from these studies using ^{19}F NMR spectroscopy in many cases would be otherwise unobtainable by traditional methods such as CD and UV spectroscopy. Traditional NMR spectroscopy methods for monitoring proteins in solution namely ^{15}N or ^{13}C-labelling can provide equally useful information; however, the speed and ease with which one can gather experimental data and interpret spectra using ^{19}F NMR, provides an attractive alternative.[48-50] The efficacy of ^{19}F NMR spectroscopy in visualising biological systems, can be largely attributed to characteristics of the ^{19}F nucleus itself, having a 100% natural abundance (the ^{13}C isotope

having an abundance of 1.07%),[51] spin quantum number *I* of ½, and 83% signal sensitivity relative to ^{1}H.[43] Given the electronic properties of the ^{19}F nucleus, incorporated fluorinated amino acids and fluorine labels are relatively sensitive to changes in their chemical environment with a chemical shift range of >300 ppm.[43] In addition, traditional NMR methods, such as ^{1}H, ^{13}C and ^{15}N NMR, to monitor protein dynamics in solution are hampered by overlaps due to intrinsic H, C and N atoms present in biological systems; an issue not encountered with ^{19}F given the scarcity of organofluorine compounds in nature.[43]

3.1.5 ^{19}F labelling of proteins

In cases where obtaining structural data on a protein therapeutic target *via* X-ray crystallography is not available, designing novel chemical probes can be challenging. NMR spectroscopy presents an alternative to define the 3D structure of the target protein and also visualise binding of novel ligands. Even in cases where crystallography proves successful, this data only provides a static view and may not necessarily reflect the conformation(s) of a highly dynamic protein in solution. Various methods currently exist in order to introduce ^{19}F into proteins and they largely fall into two categories: chemical modification[49] and biosynthetic incorporation by microoganisms.[52] From recent advances in the synthesis of various fluorinated amino acids, incorporation of ^{19}F *via* biosynthesis has become widespread. Utilising auxotrophic bacterial strains for a particular amino acid and supplementing growth media with a fluorinated analogue can consequently provide uniformly ^{19}F labelled proteins in positions of the protein sequence normally occupied by the natural amino acid.[53] Occasionally this method can cause a number of issues including; fractional labelling, perturbations in protein folding, stability problems, and convoluted spectra for large proteins. In some cases site-specific ^{19}F labeling is more desirable. This can be achieved in two ways: incorporation of fluorinated amino acids using orthogonal amber suppressor tRNA paired with a aminoacyl-tRNA synthetase[54] and by chemical

modification, often of nucleophilic residues, typically cysteine.[49] Certain bio-incorporation methods can result in low yields of labelled protein due to toxic organofluorine supplementation, and inefficient expression.[43] Thus, *in vitro* chemical modifications of nucleophilic residues such as cysteine, the free thiol of which is highly nucleophilic, can provide an attractive option. Cysteine residues have been successfully labelled *via* chemical reactions such as thioester exchange, disulphide bond formation, and alkylation.[43] An alkylating reagent which has been developed for labelling cysteine residues is 3-bromo-1,1,1-trifluoroacetone (BFA).[55]

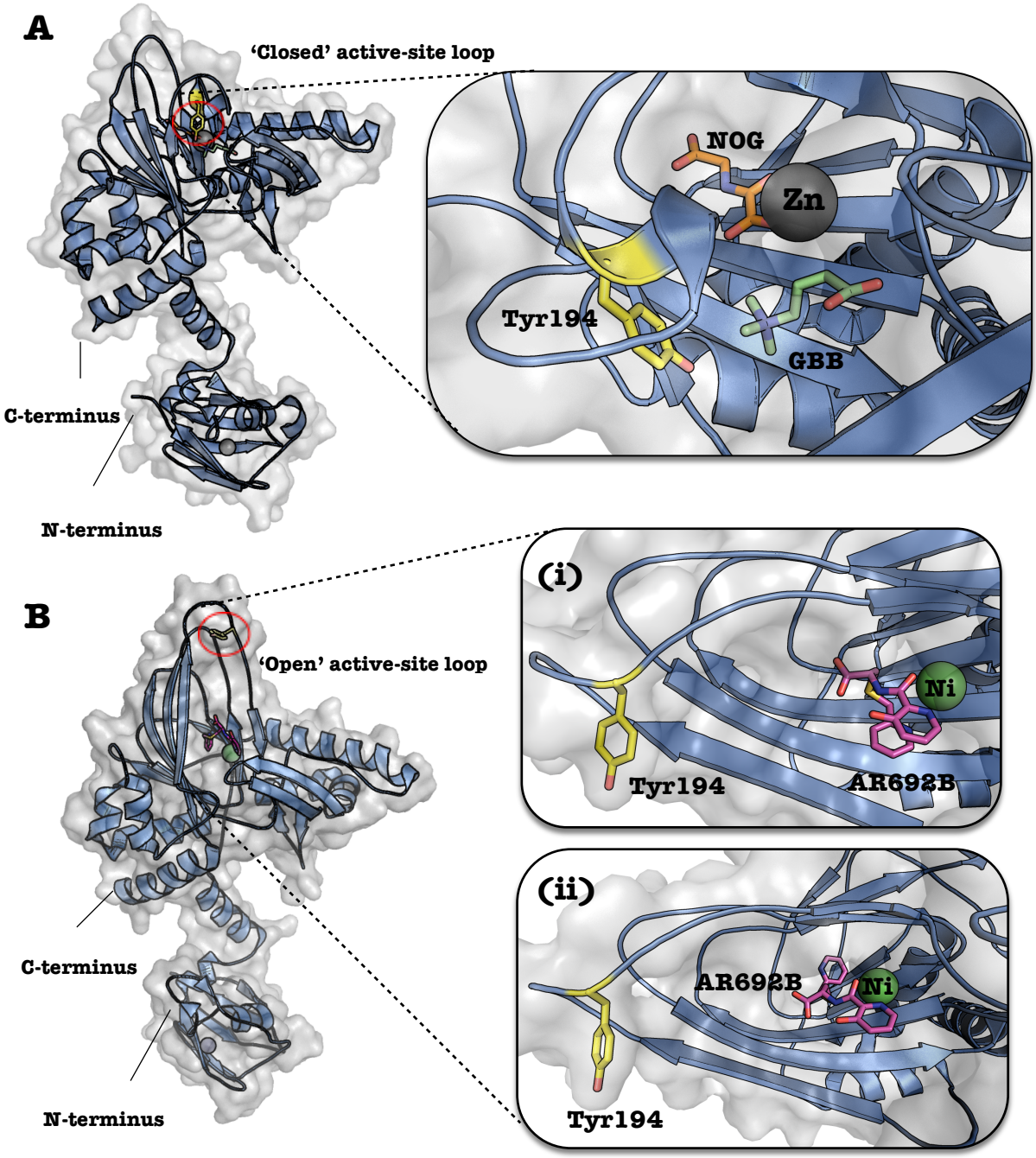
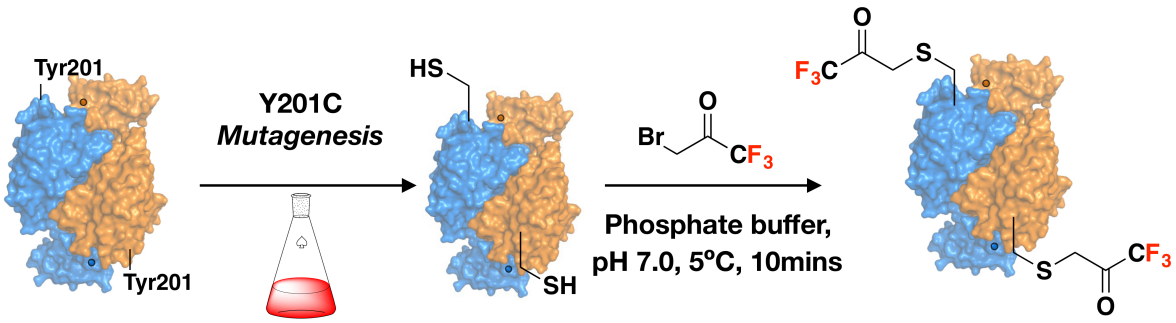


Figure 5 Crystallographically observed conformations of the "flexible-loop' region of hBBOX. **A**) One monomer of hBBOX (blue cartoon, light grey surface) with the substrate GBB, un-reactive 2OG, NOG (**4**) and Zn bound. With co/substrates bound the "flexible-loop" region of hBBOX adopts a closed configuration. Consequently Tyr194 (yellow sticks) is in close contact with the quaternary ammonium moiety of GBB. GBB is shown as green sticks and NOG as orange sticks (PDB id: 3O2G). **B**) One monomer of hBBOX (blue cartoon, light grey surface) with potent inhibitor AR692B ((**6**), Figure 1)(purple sticks) chelating Ni in the active site. With an inhibitor bound, the flexible-loop adopts an open conformation, exposing the active site. AR692B has been observed to adopt two conformations when bound to hBBOX; (**i**) with the pyridine ring folding over underneath the metal-chelating 3-hydroxy-pyridine moiety, perhaps gaining stability through π-stacking, and (**ii**) with the pyridine ring extending into the enzyme towards a small non-polar pocket. (PDB id: 4C8R).

3.2 ^{19}F labeling of psBBOX



Scheme 1 Generation of the Y201C psBBOX mutant *via* mutagenesis, followed by labeling of the mutant psBBOX with BFA.

Given the lack of structural data for psBBOX, ^{19}F labeling of psBBOX was used to further understand the dimeric psBBOX system in relation to hBBOX, and test the applicability of using an ^{19}F-labelled enzyme for chemical probe discovery. As described in Section 3.1, one key structural motif shared by both psBBOX and hBBOX is the 'flexible-loop' region, which is thought to be dynamic and involved in GBB recognition and binding.[18] Crystal structure data of hBBOX suggest the loop allows the enzyme to adopt a 'closed' (PDB id: 3O2G[18]) conformation during catalysis and an 'open' (PDB id : 4C8R[39]) conformation during inhibition (Figure 5). Tyr194, a residue present on the 'flexible-loop', is also a GBB binding residue, taking part in substrate binding. By aligning sequences of hBBOX and psBBOX, Tyr201 was identified as the corresponding residue on psBBOX and this residue was therefore targeted for mutation and labelling. To study psBBOX using ^{19}F NMR spectroscopy, a site-specific cysteine mutation of the enzyme at Tyr201 (Y201C) was introduced. This subsequently allowed for selective introduction of a trifluoromethyl ^{19}F moiety, using the sulfhydryl selective reagent BFA (Scheme 1). Prior to labeling psBBOX-Y201C, wild-type psBBOX was reacted with 100 equivalents of BFA; no reaction was observed by mass spectrometry (Figure 6). Treatment of psBBOX-Y201C with BFA and monitoring by mass-spectrometry showed labelling was selective for Cys201, regardless of the length of incubation time and amount of reagent used (Figure 7). This observation was

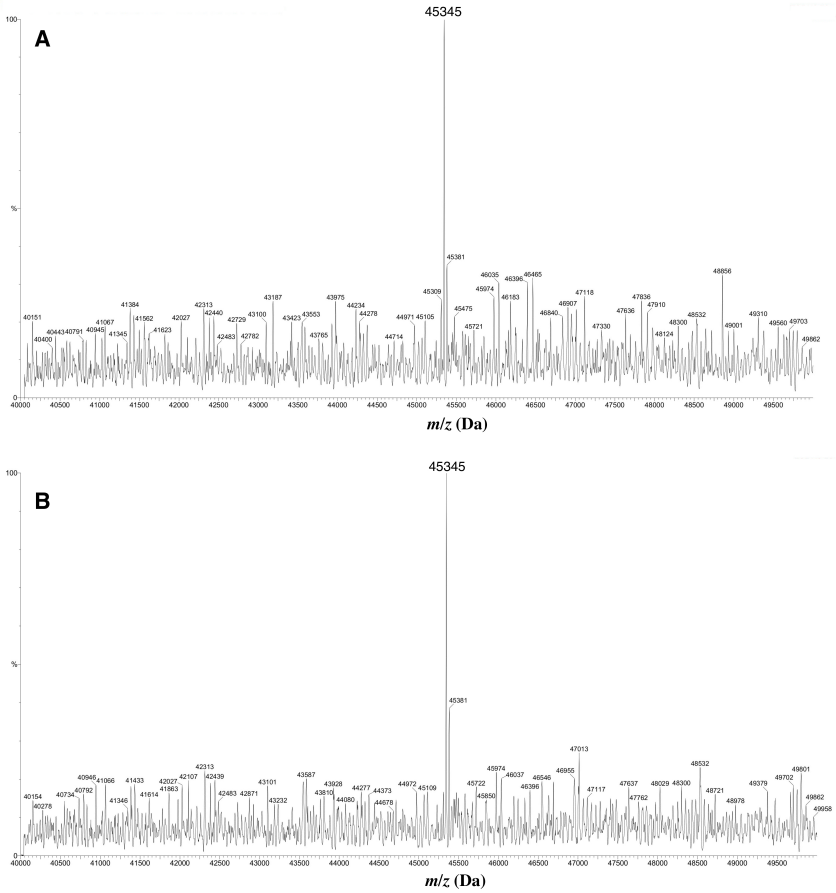


Figure 6 MS spectrum of wild-type psBBOX (M = 45345) (top) and MS spectrum of wild-type psBBOX incubated with 100 equivalents of BFA (M = 45345) (bottom).

pleasing, but a little surprising given the presence of several cysteine residues (8 in total) in the psBBOX sequence. However, this observed site-selective labelling is consistent with the highly dynamic 'flexible-loop' region (where the Y201C resides) being solvent exposed. The mass spectrometry result however revealed a mass of 45413 Da and not 45395 Da, for the labeled psBBOX-Y201C protein. This observation indicated a + 128 Da mass difference (not + 110 Da for BFA) which would suggest hydration of the ketone of BFA to the diol is observed *via* mass spectrometry. Whether the hydrated form of the BFA label is always present will require further MS and structural studies. As a control iodoacetamide (IA) was also used to label psBBOX-Y201C (Figure 8); this reagent usually ensures complete labelling of cysteine residues in a protein, regardless of their accessibility.[56] In contrast to

the BFA incubated sample, IA labelling resulted in masses corresponding to psBBOX with multiple labelled cysteines; at least one (45344 Da) but not more than 6 (45642 Da) cysteine residues were labelled (Figure 8).

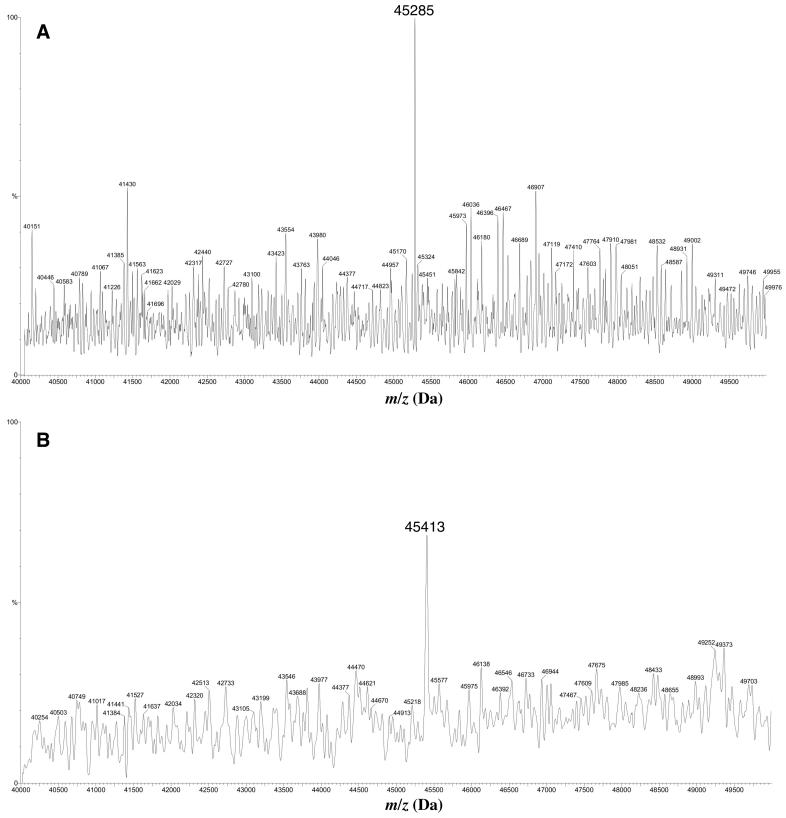


Figure 7 MS spectra of psBBOX Y201C mutant labeling. **A**) psBBOX Y201C mutant (M = 45285 Da). **B**) psBBOX Y201C, after being incubated with 100 equivalents of BFA (M = 45413 Da).

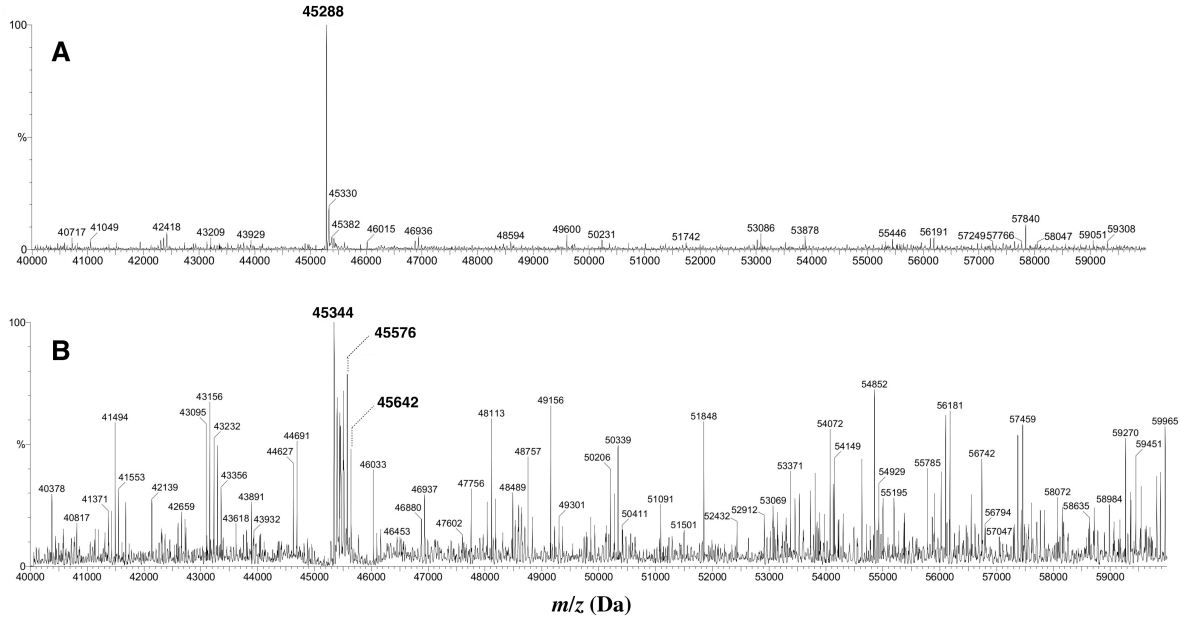


Figure 8 A) MS spectrum of psBBOX Y201C mutant (M = 45288). **B**) MS spectrum of psBBOX Y201C mutant incubated with 100 equivalents of IA. With IA multiple cysteines of psBBOX-Y201C are labelled (M = 45344, 45576, 45642).

3.3 Initial NMR experiments on psBBOX*

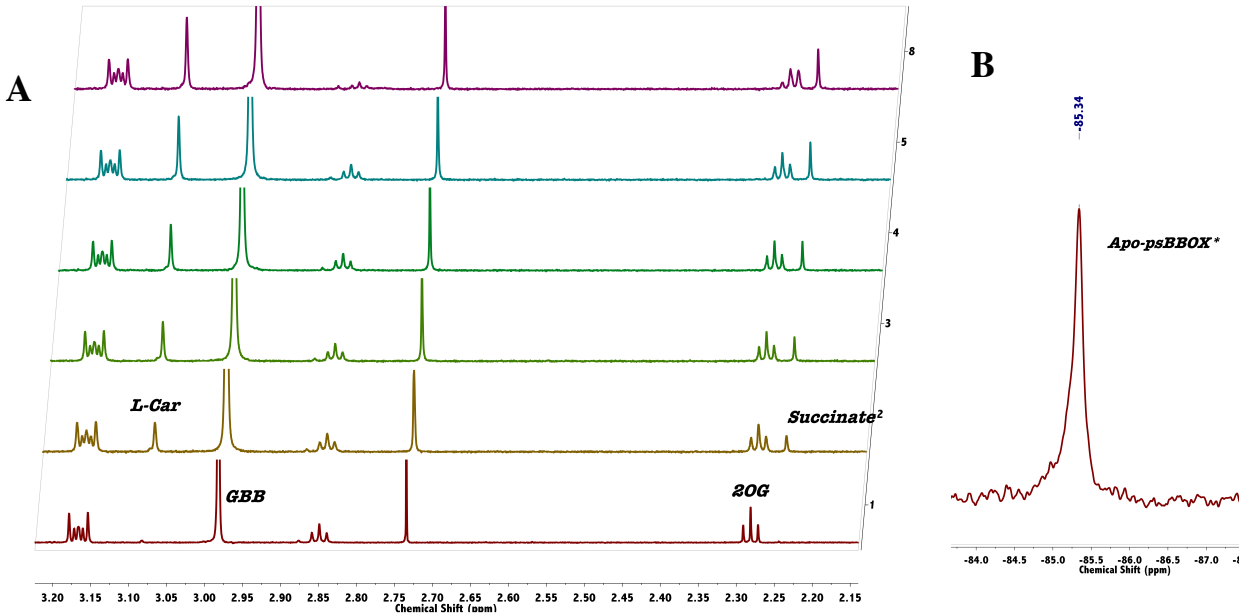


Figure 9 Initial 1D NMR spectra of the psBBOX* system. **A**) A ^{1}H NMR timecourse experiment. The first spectrum (*bottom, red*) was acquired without the presence of $Fe^{(II)}$ and psBBOX*. Experiment conditions: 1 mM psBBOX*, 500 µM $Fe^{(II)}$, 500 µM GBB, 250 µM 2OG, 250 µM L-ascorbate (di-sodium salt) in 50 mM Tris-D_{11}, pH 7.5 supplemented with 200 mM NaCl. **B**) ^{19}F NMR spectrum of *apo*-psBBOX* (100 µM). A sharp singlet is observed at -85.34 ppm relative to TFA (-76.55 ppm).

Prior to acquiring ^{19}F NMR spectral data, the effect of labelling on the catalytic activity was assessed by using ^{1}H NMR (Figure 9 (**A**)). BFA-labelled psBBOX-Y201C (referred to hereafter as psBBOX* for simplicity) was observed to retain catalytic activity by ^{1}H NMR, turning over both 2OG to succinate and GBB to carnitine. Thus, ligand binding experiments using ^{19}F NMR were conducted. Initial ^{19}F spectral acquisitions of the *apo*-psBBOX* enzyme (no active site metal or co-factors), using trifluoroacetic acid (TFA, -76.55 ppm) as a standard, yielded a single sharp singlet in the ^{19}F NMR spectrum at -85.34 ppm (Figure 9 (**B**)), indicating either; psBBOX* exists as a single distinct conformer in solution, or the loop movement is fast on the NMR timescale (fast exchange),[57] and a time-averaged shift is observed (exchange rates are described using NMR time scales[57] in the text).

Having observed efficient enzyme labelling and satisfactory activity a suitable transition metal ion was required for use with psBBOX*. Monitoring conformational

changes of psBBOX* on an NMR timescale upon binding of ligands without psBBOX* catalysed turnover was desired, thus a non-reactive transition metal alternative to $Fe^{(II)}$ was required. Given psBBOX* proved to be active (as observed by ^{1}H NMR), it is assumed that BFA labeling has not prevented the psBBOX enzyme from adopting a catalytically active conformation. However, further biophysical studies are needed to quantify the effect of BFA labelling on the enzyme conformation.

3.3.1 Metal screening

3.3.1.1 T_m Shift - psBBOX

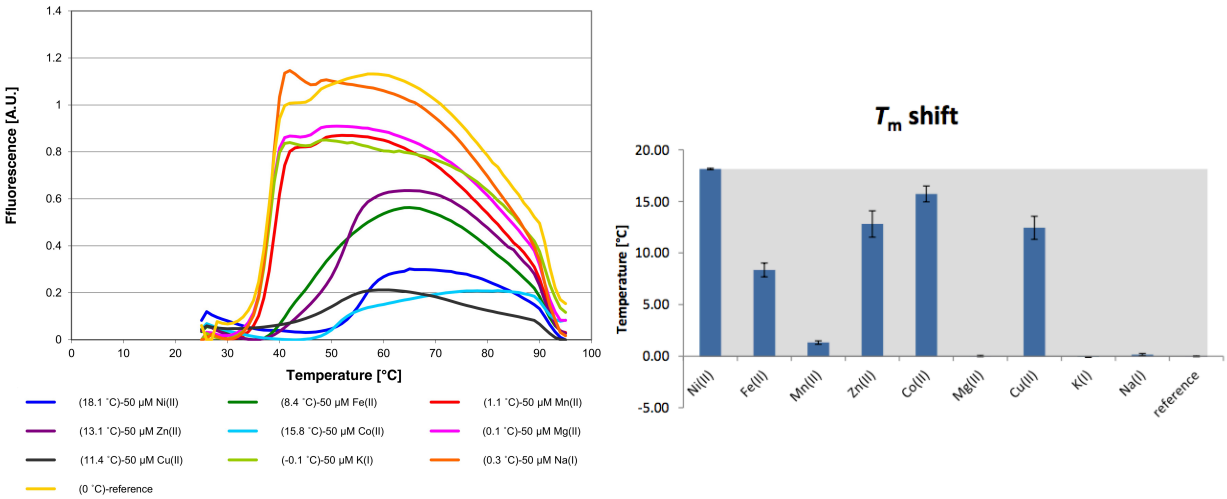


Figure 10 T_m shift data for psBBOX and a number of metal ions. Fluorescence spectra are displayed on the left, and transformed T_m shift data on the right. Non-reactive transition metal alternatives to $Fe^{(II)}$; $Ni^{(II)}$, $Zn^{(II)}$ and $Co^{(II)}$ display the most stabilisation.

Although psBBOX is an $Fe^{(II)}$ dependent oxygenase, the use of ferrous iron in NMR may lead to significant line-broadening due to its paramagnetic nature and consequently a decrease in spin-spin relaxation time.[41] Previous NMR and crystallographic studies on hBBOX, utilising $Zn^{(II)}$, $Ni^{(II)}$ and other transition metals as non-reactive $Fe^{(II)}$ alternatives have been reported.[18,26,39-41] Consequently a T_m screen of wild-type psBBOX with metal ions was carried out; addition of $Ni^{(II)}$, $Zn^{(II)}$ or $Co^{(II)}$ ions manifested the highest stability (Figure 10). Given $Ni^{(II)}$ is a known psBBOX and hBBOX inhibitor the observed increase in thermal stability is perhaps unsurprising. [9,58]

3.3.1.2 ^{19}F NMR spectra of psBBOX*-Metal complexes: $Zn^{(II)}$ and $Ni^{(II)}$

**A fresh sample of psBBOX* was used per ligand or co/factor studied. Stacked spectra represent a titration of a particular ligand to the same sample of psBBOX* (See Section 3.9.2).*

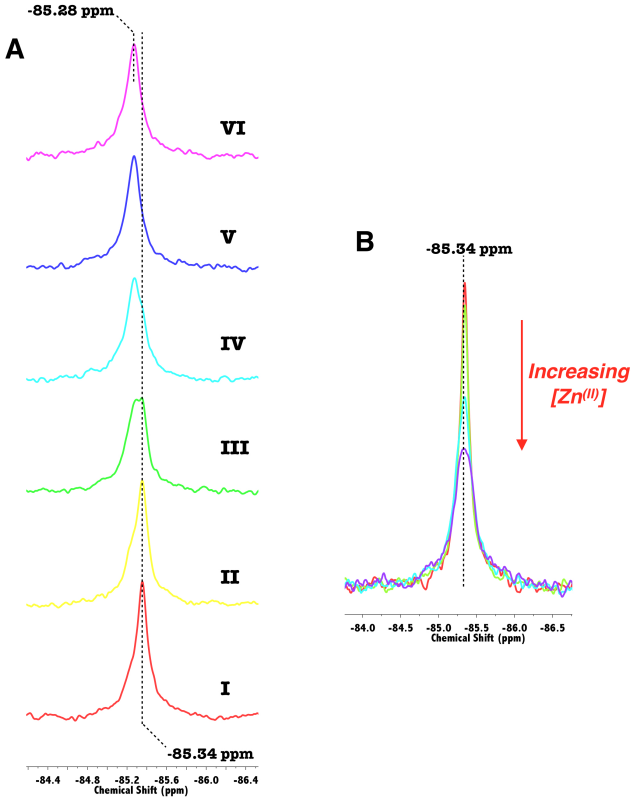


Figure 11 ^{19}F NMR spectra displaying effects of $Ni^{(II)}$ and $Zn^{(II)}$ on psBBOX*. **A**) (**I**) *apo*-psBBOX*. (**II**) 25 µM $NiSO_4$. (**III**) 50 µM $NiSO_4$ (**IV**) 75 µM $NiSO_4$ (**V**) 100 µM $NiSO_4$ (**VI**) 125 µM $NiSO_4$ **B**) Addition of up to 1.2 equivalents of or $ZnCl_2$ induces line broadening.

Titrating $Zn^{(II)}$ with psBBOX* gave no change in chemical shift with some line-broadening until the 1:1 metal/enzyme ratio was exceeded (Figure 11 (**B**)); a greater than 2:1, $Zn^{(II)}$:enzyme ratio caused severe precipitation of the enzyme. Titration of $Ni^{(II)}$ into psBBOX* led to the appearance of a signal at -85.28 ppm ($\Delta\delta_F$ = 0.06 ppm, relative to the *apo*-psBBOX* signal) with an increasing peak area upon titration of $Ni^{(II)}$ (Figure 11 (**A**)). This observation is typical of slow exchanging systems,[57] indicating that $Ni^{(II)}$ is a strong binder of psBBOX.

Unfortunately, the small chemical shift following titration of $Ni^{(II)}$ to psBBOX* ($\Delta\delta_F$ = 0.06 ppm) resulted in a signal overlapping with *apo*-psBBOX* (-85.34 ppm), which hindered accurate quantification of the effect of $Ni^{(II)}$ on psBBOX*. Nevertheless, approximate $Ni^{(II)}$ ion saturation of psBBOX* was observed at a 1:1.25 ratio of

metal:enzyme. The apparent slow exchange nature of the psBBOX*-$Ni^{(II)}$ signal would suggest $Ni^{(II)}$ to be a tight binder, in support of the reported inhibitory activity of $Ni^{(II)}$ towards psBBOX.[9] The small $\Delta\delta_F$ of psBBOX*-$Ni^{(II)}$ would suggest $Ni^{(II)}$ induces a small change in the local chemical environment of the -CF_3 label. Therefore, inhibition of psBBOX by $Ni^{(II)}$ may include slight changes in the flexible-loop. By contrast with $Ni^{(II)}$, $Zn^{(II)}$ titration did not yield an observable chemical shift, but led to broadening of the signal, which is typical of an intermediate exchange system.[57] Given that no chemical shift was observed relative to *apo*-psBBOX* during $Zn^{(II)}$ titration, $Zn^{(II)}$ binding seemingly has little or no effect on the chemical environment of the –CF_3 label.

Interestingly, the psBBOX*-$Zn^{(II)}$ and psBBOX*-$Ni^{(II)}$ complexes displayed different behaviour when the natural substrate, GBB, was titrated to the metal-protein complex (Section 3.2).

3.3.1.3 psBBOX-Metal complexes: $Fe^{(II)}$, $Co^{(II)}$ and $Mn^{(II)}$*

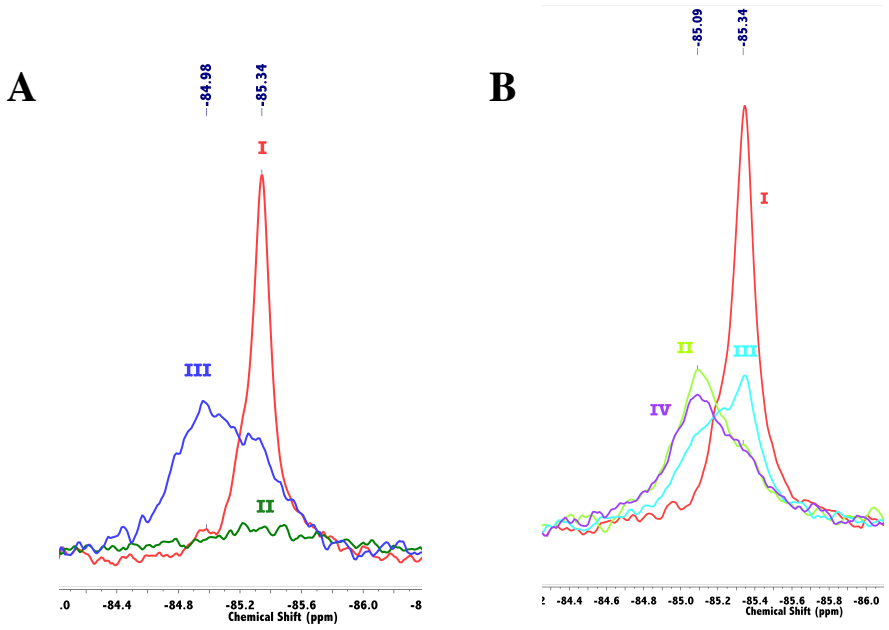


Figure 12 ^{19}F NMR spectra displaying effects of 1.2 equivalents of various transition metals on psBBOX* (**I**). **A**) Resulting ^{19}F signals arising from formation of (**II**) psBBOX*-$Mn^{(II)}$ and (**III**) psBBOX*-$Co^{(II)}$ **B**) Resulting ^{19}F NMR signals arising from formation of: (**I**) psBBOX* (**II**) psBBOX*-$Fe^{(II)}$ immediately after addition of metal (**III**) psBBOX*-$Fe^{(II)}$ + 2 hrs left at room temperature (**IV**) psBBOX*-$Fe^{(II)}$ + ascorbate (di-sodium salt).

Titration of other transition metals, yielded contrasting results to those described in Section 3.3.1.2 with $Zn^{(II)}$ and $Ni^{(II)}$ (Figure 11). Line broadening was observed with all three of the transition metal ions $Co^{(II)}$, $Mn^{(II)}$ and $Fe^{(II)}$ (Figure 12). This is perhaps unsurprising given the paramagnetic nature of $Co^{(II)}$, $Mn^{(II)}$ and $Fe^{(II)}$. From the spectra shown in Figure 12, $Mn^{(II)}$ is able to fully attenuate the original apo-psBBOX* signal, with $Co^{(II)}$ and $Fe^{(II)}$ doing so to a lesser extent. Interestingly, although $Fe^{(II)}$ displayed similar line broadening to that observed with $Co^{(II)}$ and $Mn^{(II)}$, when the titration mixture was left for 2 hours at room temperature a shift was observed (Figure 12). Repeating the titration of $Fe^{(II)}$ to psBBOX* in the presence of ascorbate, a known organic reducing agent, stablilisation of the signal representing the putative psBBOX*-$Fe^{(II)}$ (Figure 12) complex was observed. The signal shift observed following long incubation times thus likely results from the oxidation of $Fe^{(II)}$ to $Fe^{(III)}$.

3.4 Effects on psBBOX* ^{19}F signal with co/substrates

For reference purposes a summary table is provided in Section 3.7 (Table 1).

3.4.1 Effects of GBB

On titrating GBB with the psBBOX*-$Zn^{(II)}$ complex, a second signal was observed at -82.19 ppm, which grew with increasing GBB concentration (Figure 13). When peak areas were examined it was observed that saturation of the enzyme with GBB beyond 50% was not attainable (Figure 17), reaching a GBB concentration of 7 mM before precipitation of the protein was observed. Interestingly, in contrast to the observed signals with GBB and psBBOX*-$Zn^{(II)}$, no new signal was observed when GBB was titrated to the psBBOX*-$Ni^{(II)}$ complex.

The relatively large chemical shift ($\Delta\delta_F$ = 3.15 ppm) represents a significant change in chemical environment for the $-CF_3$ label, likely representing a GBB binding event which induces a conformational change in the flexible-loop of the psBBOX*-$Zn^{(II)}$ complex

(Figure 13). Furthermore, this observation suggests the aforementioned signals at -85.34 and -82.19 ppm potentially represent psBBOX*-$Zn^{(II)}$ and psBBOX*-$Zn^{(II)}$-GBB complexes, respectively. Further evidence for such complexes can be obtained from Figure 13; the putative psBBOX*-$Zn^{(II)}$-GBB signal exists in a slow exchange regime, as evident from the GBB concentration-dependent increase in the second signal at -82.19 ppm, coupled to an attenuation of the first signal at -85.34 ppm. However, it should also be noted, GBB can inhibit psBBOX at high concentrations (K_i = 125 µM)[19]. Therefore, given the high concentration of GBB required to attain a second signal at -82.19 ppm, this signal may also represent substrate inhibition of psBBOX*. Additionally, the relatively low affinity of psBBOX for GBB (K_m = 2.5 mM (163 uM, within Michaelis-Menten range))[19] can explain

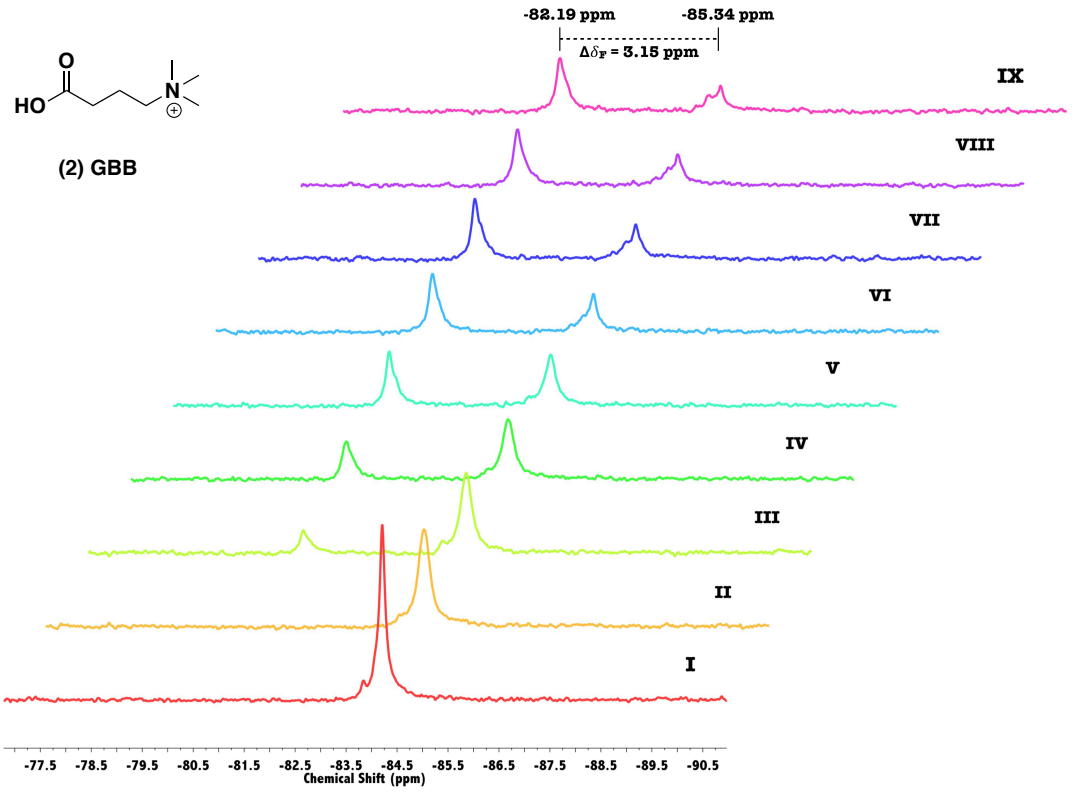


Figure 13 ^{19}F NMR spectra of titrations of $Zn^{(II)}$ and GBB to psBBOX*. Following addition of GBB to the psBBOX*-$Zn^{(II)}$ complex a new slow-exchaning peak is observed at 3.15 ppm higher, representing a large conformational change in the enzyme complex; binding of GBB may trigger closure of a likely 'flexible-loop'. (**I**) 100 µM psBBOX* (**II**) 100 µM $ZnCl_2$ (**III**) 1 mM GBB (**IV**) 2.5 mM GBB (**V**) 4 mM GBB (**VI**) 6 mM GBB (**VII**) 110 µM $ZnCl_2$ 6 mM GBB (**VIII**) 120 µM $ZnCl_2$ 6 mM GBB (**IX**) 120 µM $ZnCl_2$ 7 mM GBB.

the lack of appearance of a signal at -82.19 ppm at low concentrations of GBB; low concentrations of GBB in the ^{19}F NMR psBBOX* experiments likely display a fast exchange between psBBOX*-$Zn^{(II)}$ and psBBOX*-$Zn^{(II)}$-GBB. Hence, no changes are observed on the NMR chemical shift timescale; slow exchange is seemingly not observed until the point of GBB saturation of the psBBOX*-$Zn^{(II)}$ complex.

As mentioned in Section 3.1.3, ligand-observed ^{1}H NMR studies have previously shown that more than 50% of bound GBB cannot be displaced with substrate analogues such as Mildronate (Figure 4). The results disclosed above suggest GBB binds to only half of the psBBOX dimer. Moreover, the combined observations indicate that the binding of $Ni^{(II)}$ may inhibit psBBOX *via* stabilising the enzyme in a conformation, which does not bind GBB.

3.4.2 Effects of 2OG

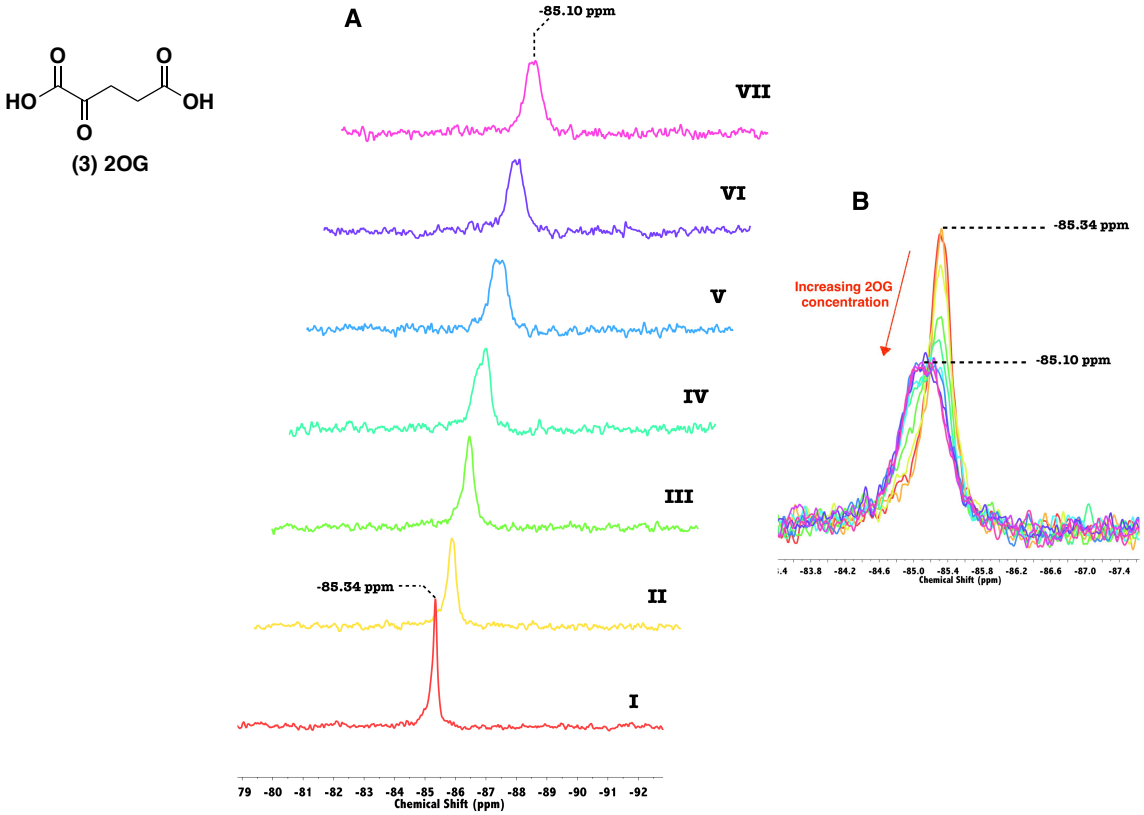


Figure 14 ^{19}F NMR spectra of titrations of $Zn^{(II)}$ and 2OG to psBBOX*. **A**) (**I**) 100 µM psBBOX* (**II**) 100 µM $ZnCl_2$ (**III**) 100 µM 2OG (**IV**) 1 mM 2OG (**V**) 2 mM 2OG (**VI**) 3.5 mM 2OG (**VII**) 4.5 mM 2OG. **B**) Increasing 2OG concentration induces signal broadening. **B**) An overlaid view of (**A**).

Titration of 2OG to psBBOX*-$Zn^{(II)}$ induces signal broadening at high concentrations (Figure 14) and an overlapping signal is initially formed at around -85.10 ppm (Figure 14 **A**(IV) and **B**).

Signal broadening as observed with 2OG and psBBOX*-$Zn^{(II)}$ (Figure 14), is typical of an intermediate NMR exchange regime,[57] suggesting 2OG is a weak binder. Indeed, psBBOX has a low affinity for 2OG (K_m = 532 μM)[19], therefore the observed signal broadening may reflect this intermediate protein-ligand exchange regime. As with GBB titrations described in Section 3.2.1, little change in the ^{19}F NMR sepctra of psBBOX* is seen at low 2OG concentrations, reflecting the low affinity of psBBOX for 2OG and likely due to the fast exchange of the psBBOX*-$Zn^{(II)}$ and psBBOX*-$Zn^{(II)}$-2OG complexes. The locality of the $–CF_3$ label in the active-site should also be considered when analysing effects of substrates and ligands on protein-observed NMR spectra. Given the $–CF_3$ label is positioned close to the GBB binding site, the sensitivity towards 2OG binding may be limited and hence the resulting signal is not clearly resolved. Further mutations and labelling at alternate positions within the BBOX active site could elucidate the scale of 2OG-induced conformational changes in solution. However, what can be deduced from the results described above is that 2OG has a significantly smaller effect on the 'flexible-loop' when compared to the observed effect of GBB on psBBOX* (Figure 13).

3.4.3 Effects of 2OG on psBBOX*-$Zn^{(II)}$-GBB

Addition of 2OG (5mM) to a psBBOX*-$Zn^{(II)}$-GBB assay mixture (50:1, 2OG:psBBOX*), caused a 0.21 ppm shift higher than the signal corresponding to psBBOX*-$Zn^{(II)}$-GBB *i.e.* from -82.19 ppm (Figure 15 (**II**)) to -82.40 ppm (Figure 15(**III**), Figure 16). In addition to a 2OG-induced signal shift, the -85.34 ppm signal broadened almost into the baseline (Figure 15 (**III**)).

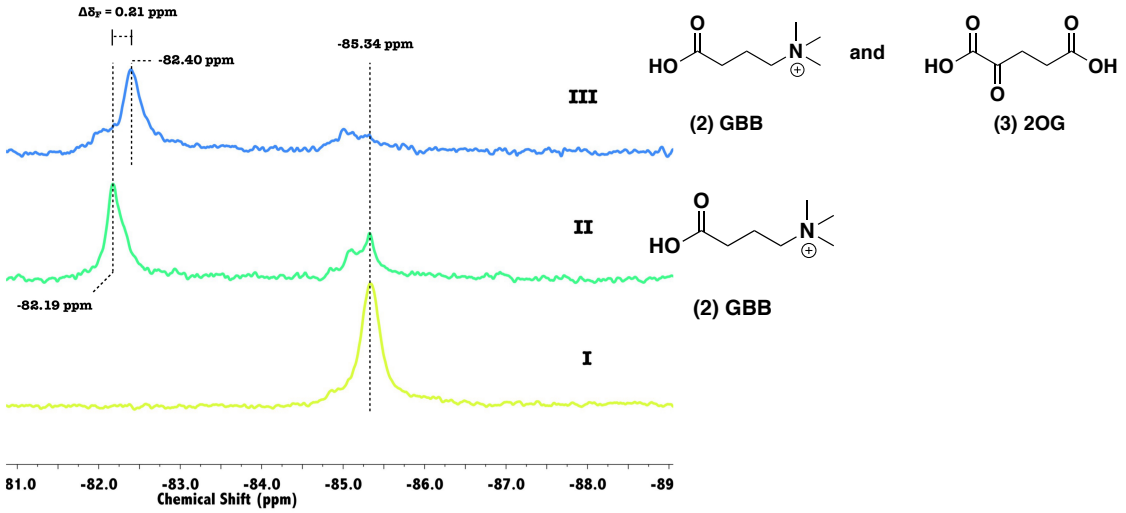


Figure 15 ^{19}F NMR sepctra resulting from addition of GBB followed by 2OG to the psBBOX*-$Zn^{(II)}$ complex. An upfield shift of 0.21 ppm is observed, possibly reflecting the formation of a psBBOX*-$Zn^{(II)}$-GBB-2OG complex. (**I**) psBBOX*-$Zn^{(II)}$ (100 μM psBBOX*, 100 μM $ZnCl_2$) (**II**) 7 mM GBB (**III**) 7 mM GBB, 5 mM 2OG.

To examine whether co/substrates could bind without the presence of $Zn^{(II)}$, titrations using *apo*-psBBOX*, GBB, and 2OG were carried out. No binding of GBB or 2OG was observed to *apo*-psBBOX*; the ^{19}F signal at -82.40 likely corresponding to bound GBB and 2OG, appeared after the addition of $Zn^{(II)}$ only. This observation indicated that metal binding is important for the binding of co/substrates.

Given the location of the $-CF_3$ label in the hydrophobic pocket of psBBOX* (Figure 5), the relatively small shift observed upon 2OG titration to psBBOX*-$Zn^{(II)}$-GBB can be

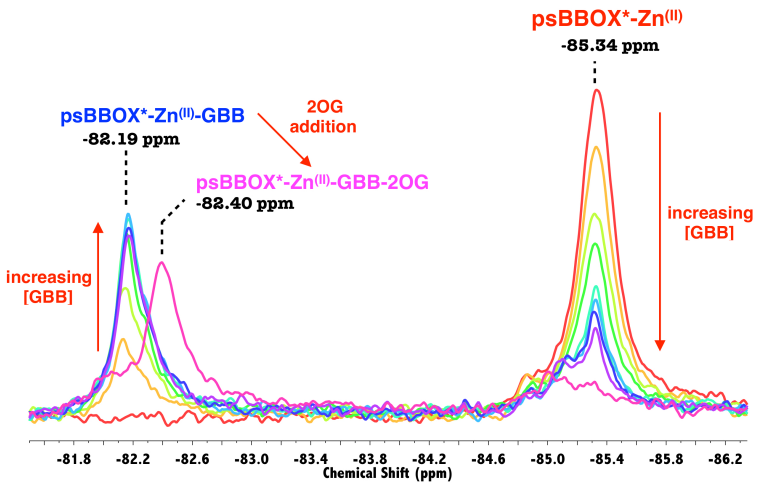


Figure 16 Overview of the effects of the psBBOX co/substrates, GBB and 2OG, on the psBBOX* ^{19}F NMR signal shape and chemical shift.

explained at least in part by the distance between the $-CF_3$ group and 2OG (Figure 16). Nevertheless, a chemical shift of 0.21 ppm potentially represents an observable conformational change of the psBBOX*-$Zn^{(II)}$-GBB complex and the resulting signal at -82.40 ppm may represent a psBBOX* complex in which both GBB and 2OG are bound. The changes in chemical shift and line broadening, seen on addition of 2OG to psBBOX*-$Zn^{(II)}$-GBB (Figure 16), are characteristic features of intermediate exchange regimes.[57] Therefore, the observed signal for psBBOX*-$Zn^{(II)}$-GBB-2OG at -82.40 ppm may represent an average of bound and unbound 2OG, *i.e.* psBBOX*-$Zn^{(II)}$-GBB and psBBOX*-$Zn^{(II)}$-GBB-2OG. The small change in chemical shift and attenuation of the putative psBBOX*-$Zn^{(II)}$ signal at -85.34 ppm (Figure 15, Figure 16) following the addition of 2OG, may suggest 2OG promotes further binding of GBB. This effect can also be observed in the relative peak areas of both signals (Figure 17); addition of 2OG further attenuates the signal at -85.34 ppm, whilst increasing the intensity of the signal at -82.40 ppm. The effect of 2OG on the psBBOX*-$Zn^{(II)}$-GBB ^{19}F spectrum is perhaps unsurprising, as GBB was observed to have a relatively high binding affinity for psBBOX in the presence of 2OG and Zn (K_D= 5 μM[41]), using the ^{1}H NMR reporter assay (Section 3.1.3).

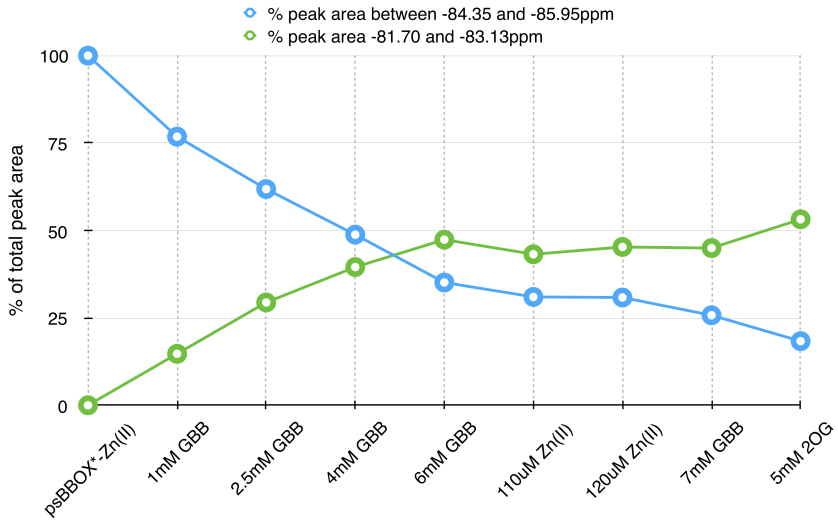


Figure 17 Effect of ^{19}F NMR signal peak area upon titration of co/substrates, GBB, 2OG and Mildronate. Increasing GBB concentration results in a second ^{19}F NMR signal at -82.19 ppm, the intensity of which cannot be further increased past 50% without de-stabilising the protein NMR sample. Addition of 2OG however can promote a slight increase in intensity along with a 0.21 ppm signal shift.

3.4.4 Effect of NOG on psBBOX*-$Zn^{(II)}$

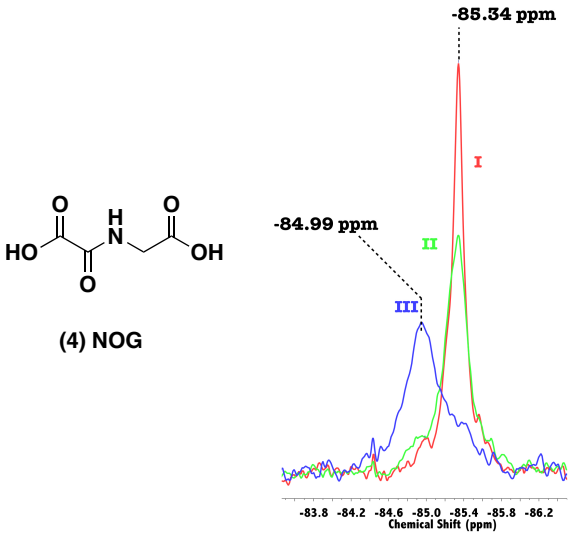


Figure 18 Titration of NOG to the psBBOX*-$Zn^{(II)}$ complex yields a new slow exchanging peak at -84.99 ppm, reflective of the formation of a psBBOX*-$Zn^{(II)}$-NOG complex. (**I**) 100 μM apo psBBOX* (**II**) 100 μM $ZnCl_2$ (**III**) 1.5 mM NOG.

Titration of the inactive 2OG analogue, *N*-oxalyl glycine (NOG), often used as a 2OG analogue in crystallographic studies concerning 2OG oxygenases,[59] displayed formation of a signal (-84.99 ppm, $\Delta\delta_F = 0.35$ ppm) with psBBOX*-$Zn^{(II)}$ (Figure 18, Figure 19). The new signal increased in a dose-dependent manner, whilst also attenuating the initial signal at -85.34 ppm (Figure 19 (**I**-**III**)).

NOG is a known inhibitor of BBOX ($IC_{50\ (hBBOX)}$ = 390 μM (fluoride release)[25], 124 μM (NMR assay)[25]) and other oxygenases. In support of these findings, the results from ^{19}F NMR suggest NOG to be a tighter binder of psBBOX* compared to 2OG, given the signal characteristics are typical of an intermediate/slow exchanging system. Moreover, in contrast to the large concentration of 2OG (>1 mM, Section 3.2.2) required to induce an observable change in the ^{19}F signal, significantly lower concentrations of NOG (~100μM) were required. However, high concentrations of NOG (>750 μM) induced signal broadening and protein precipitation.

3.4.4.1 Effect of GBB on psBBOX*-Zn$^{(II)}$-NOG

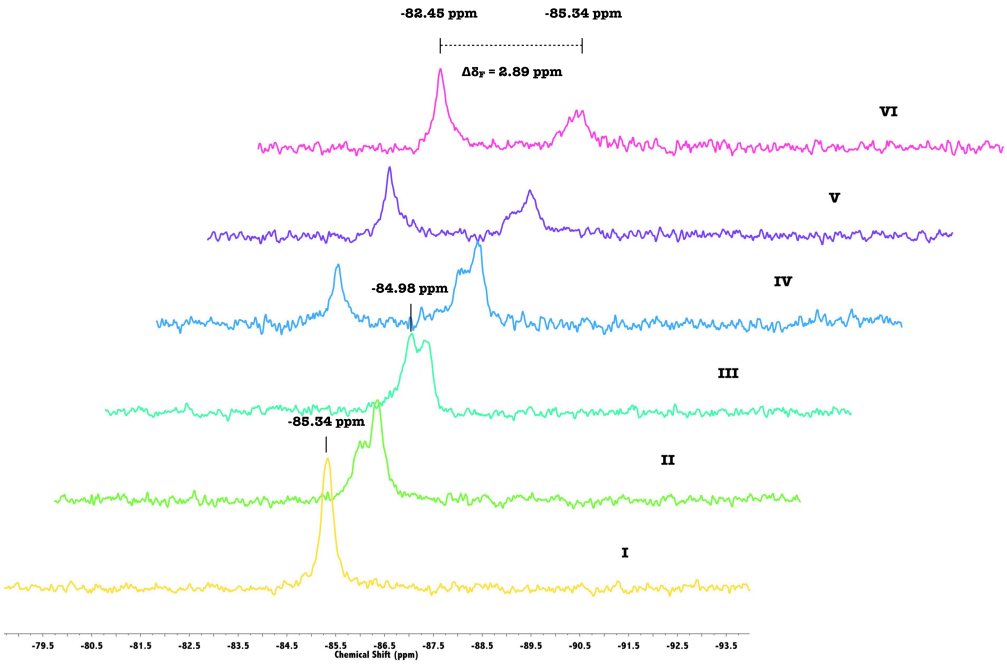


Figure 19 Titration of NOG followed by GBB, to the psBBOX*-Zn$^{(II)}$ complex. An overlapping slow exchanging signal can be observed at -84.98 ppm, after addition of NOG. Addition of GBB to the psBBOX*-Zn$^{(II)}$-NOG complex yields a slow-exchanging signal at -82.45 ppm indicating formation of a psBBOX*-Zn$^{(II)}$-NOG-GBB complex. (**I**) psBBOX*-Zn$^{(II)}$ (100 µM psBBOX*, 100 µM $ZnCl_2$ (**II**) 250 µM NOG (**III**) 500 µM NOG (**IV**) 500 µM NOG, 500 µM GBB (**V**) 500 µM NOG, 1500 µM GBB (**VI**) 500 µM NOG, 2500 µM GBB.

Titration of GBB to a psBBOX-Zn$^{(II)}$-NOG assay mixture enabled observation of a new signal as observed with psBBOX-Zn$^{(II)}$-GBB-2OG (Section 3.2.3), at -82.45 ppm ($\Delta\delta_F$ = 2.89 ppm) (Figure 19). Furthermore, addition of GBB resulted in attenuation of the signals at -85.34 ppm and -84.98 ppm (Figure 19 (**VI**).

The chemical shift change relative to the psBBOX*-Zn$^{(II)}$ signal, displayed in Figure 19 ($\Delta\delta_F$ = 2.89 ppm) coupled with slight signal broadening, is indeed similar to the 2OG-induced chemical shift observed on the psBBOX-Zn$^{(II)}$-GBB complex ($\Delta\delta_F$ = 2.94ppm, Section 3.2.3) and likely represents a conformational change in the flexible loop region of psBBOX*. The resulting signal at -82.45 ppm (psBBOX-Zn$^{(II)}$-NOG-GBB) is likely indicative of a slower exchange regime, compared to the psBBOX-Zn$^{(II)}$-GBB-2OG, which likely reflects the aforementioned inhibitory action of NOG on BBOX which may stabilise the psBBOX-Zn$^{(II)}$-NOG-GBB complex.

3.5 Effects of other substrates on psBBOX*-$Zn^{(II)}$

3.5.1 L/D-Carnitine

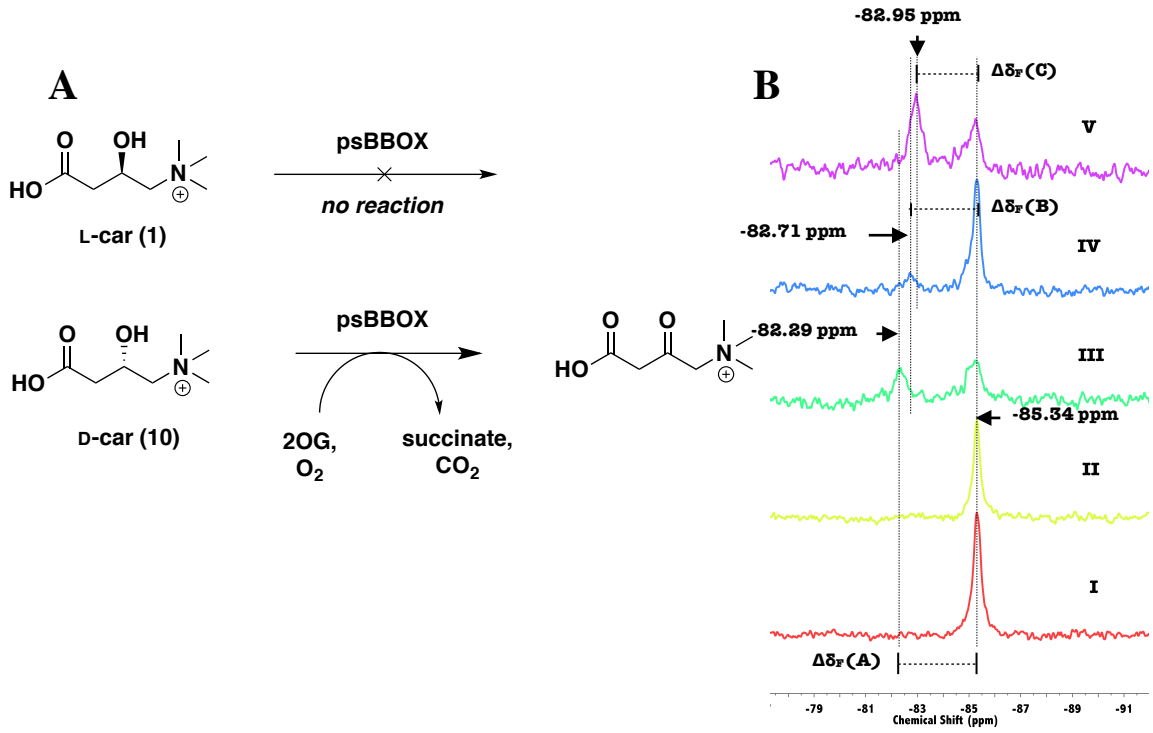


Figure 20 A) D-car but not L-car was observed to be a substrate for psBBOX.[19] **B)** Stacked ^{19}F NMR spectra of additions of L- and D-carnitine to psBBOX*. L-car was (**I**) 100 µM psBBOX*, 100 µM $ZnCl_2$ (**II**) 5 mM L-car (**III**) 5 mM L-car, 5 mM 2OG (**IV**) 5 mM D-car (**V**) 5 mM D-car, 5 mM 2OG.

Interestingly, different signals were observed with the product of BBOX catalysis L-carnitine (L-car)(**1**), and its enantiomer D-carnitine (D-car) (**10**) (Figure 20). Titration of L-car to the psBBOX*-$Zn^{(II)}$ complex displayed no new signal even at high concentrations (5mM) (Figure 20 (**II**)). Titration of D-car to psBBOX*-$Zn^{(II)}$ yielded a broad signal at -82.71 ppm ($\Delta\delta_F$ (B) = 2.63 ppm, Figure 20 (**IV**)) typical of intermediate/slow exchange. This observation indicates that D-car is a better binder to psBBOX* than L-car (within detection limits). As observed with GBB, high concentrations of (**10**) (~ 5 mM) were required to observe a second signal, which suggests a fast exchange regime exists at low concentrations.

Further differences are observed between L- and D-car when 2OG is added. Addition of 2OG to a psBBOX*-$Zn^{(II)}$-L-car titration yielded a new signal typical of intermediate exchange at -82.29 ppm ($\Delta\delta_F$ (A) = 3.05 ppm, Figure 20 (**III**)), as evident from significant line broadening. On titrating 2OG to the psBBOX*-$Zn^{(II)}$-D-car, a third new signal was observed at -82.95 ppm. The intermediate exchanging nature of the psBBOX*-$Zn^{(II)}$-D-car-2OG signal supports previous findings,[19] where D-car, but not L-car, was found to be a substrate for psBBOX. Interestingly, these findings with psBBOX* suggest L-car does bind to the enzyme complex in the presence of 2OG, even though it has been reported to not be a substrate (within limits of detection);[19] information not obtained from typical turnover experiments.

3.5.2 P-GBB

The quaternary phosphorus analogue of GBB (P-GBB, (**11**), synthesised by Jos Kamps) was recently reported as a substrate for psBBOX (Figure 21 (**A**)).[60] Titration of P-GBB to psBBOX*-$Zn^{(II)}$ displayed a signal at -82.04 ppm (Figure 21 (**II**-**III**)), with a chemical shift change ($\Delta\delta_F$(A) = 3.30 ppm) similar to that observed with psBBOX*-$Zn^{(II)}$-GBB (Section 3.2.1, Figure 13). This resonance at -82.04 ppm appeared in a slow/intermediate exchange regime at high concentrations, increasing proportionately with P-GBB concentration whilst also attenuating the signal at -85.34 ppm. Thus, the two resonances may represent psBBOX*-$Zn^{(II)}$-P-GBB and psBBOX*-$Zn^{(II)}$ complexes, respectively. Moreover, in contrast with GBB, signal intensity of the putative psBBOX*-$Zn^{(II)}$-P-GBB at -82.04 ppm, could not be increased with high P-GBB concentrations (Figure 21 (**B**, **III**).

The slightly lower shift of the P-GBB-induced signal at -82.04 ppm, when compared to psBBOX*-$Zn^{(II)}$-GBB (-82.19 ppm) may reflect, at least in part, the difference in electronics between the $–NMe_3^+$ and $–PMe_3^+$ moieties of GBB and P-GBB respectively,

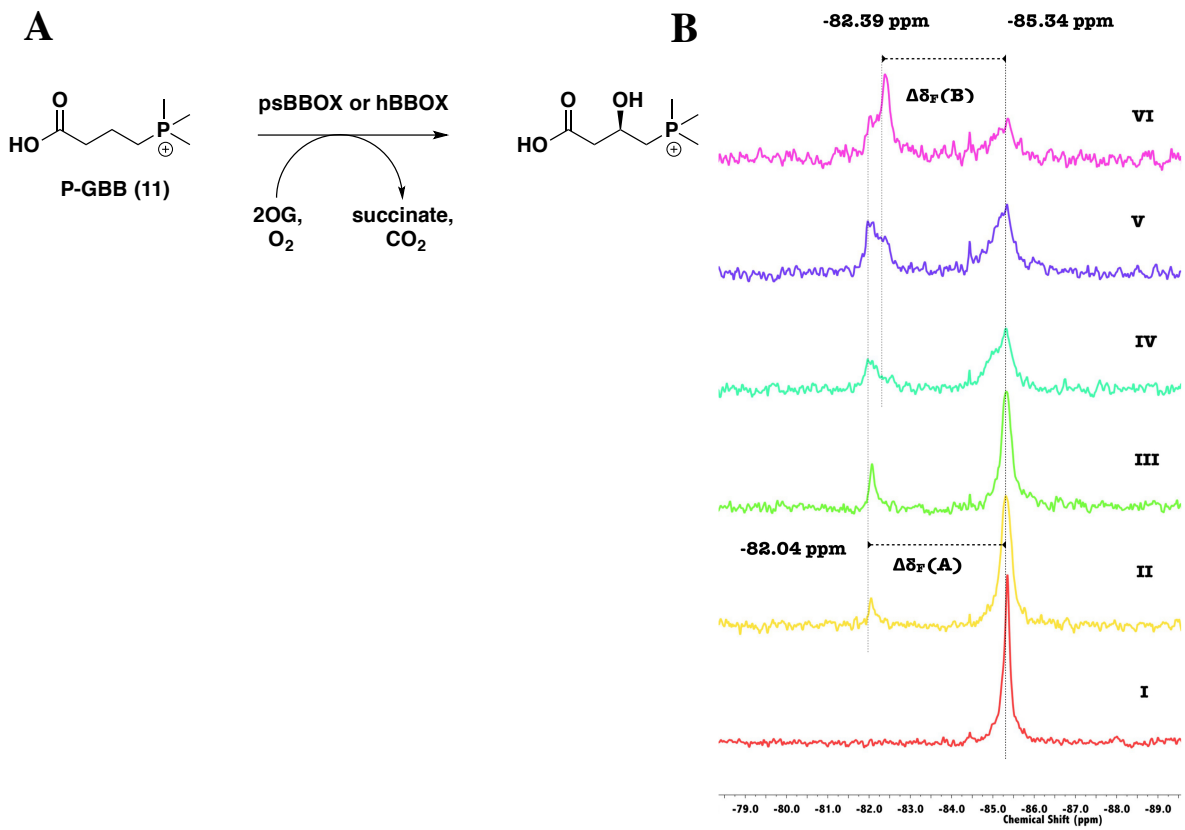


Figure 21 A) Chemical structures of the synthetic GBB analogue, P-GBB. Both psBBOX and hBBOX are capable of pro-*R*, C-3 hydroxylations of P-GBB. **B)** ^{19}F NMR spectra of a titration of P-GBB to the psBBOX*-$Zn^{(II)}$ complex. (**I**) 100 μM psBBOX* 100 μM $ZnCl_2$ (**II**) 1 mM P-GBB (**III**) 2.5 mM P-GBB (**IV**) 2.5 mM P-GBB, 5 mM 2OG (**V**) 5 mM P-GBB, 5 mM 2OG (**VI**) 5 mM P-GBB, 5 mM 2OG, 3 mM GBB.

reflecting the hypersensitivity of the ^{19}F nucleus to changes in local chemical environment. Furthermore, the inability of P-GBB to increase the signal intensity at -82.04 ppm may be attributed to the lower affinity of psBBOX for P-GBB compared to GBB (K_m = 1.2 mM[60] and 1.0 mM[60] respectively).

Addition of 2OG to the psBBOX*-$Zn^{(II)}$-P-GBB titration, enabled observation of a new signal at -82.39 ppm (Figure 21 (**B**, **IV**-**V**)) accompanied by significant broadening. Interestingly, addition of GBB to the psBBOX*-$Zn^{(II)}$-P-GBB-2OG mixture, gave rise to a signal at -82.40 ppm (Figure 21 (**B**, **VI**)), a chemical shift previously associated with formation of the psBBOX*-$Zn^{(II)}$-GBB-2OG complex.

Although chemical shift changes with psBBOX*-$Zn^{(II)}$-P-GBB-2OG were comparable to those observed with psBBOX*-GBB titrations (Section 3.2.2), significant

signal attenuation and broadening was observed, indicative of a fast/intermediate exchanging regime. Furthermore, this coalescence of the fast/intermediate exchanging signal at ~ -82.30 ppm could not be resolved with an increased number of scans. The formation of a signal at -82.40 ppm following the addition of GBB to the psBBOX*-$Zn^{(II)}$-P-GBB-2OG may suggest GBB competes with P-GBB for an active site (Figure 21).

3.5.3 GBBNF

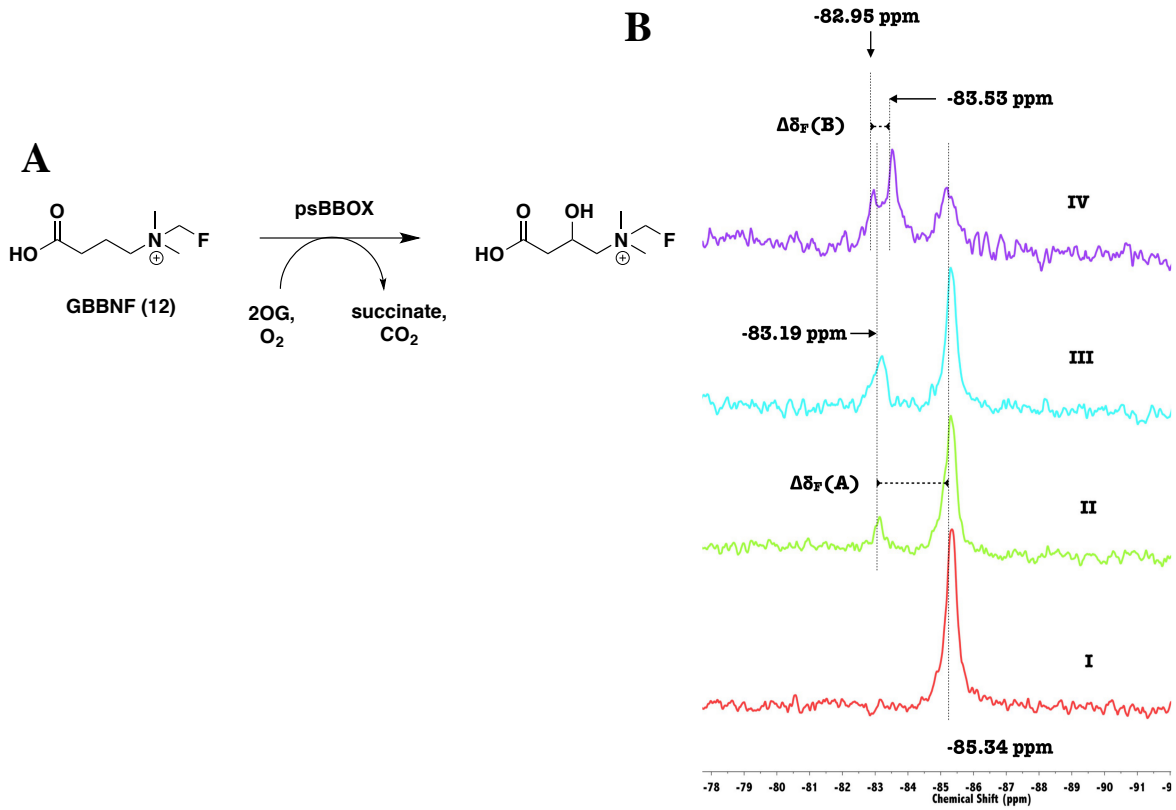


Figure 22 A) Chemical structure of the synthetic GBB analogue, GBBNF. Both psBBOX and hBBOX are capable of C-3 hydroxylations of GBBNF. **B)** ^{19}F NMR spectra of a titration of GBBNF to the psBBOX*-$Zn^{(II)}$ complex. (**I**) 100 µM psBBOX*, 100 µM $ZnCl_2$ (**II**) 1 mM GBBNF (**III**) 1.5 mM GBBNF (**IV**) 1.5 mM GBBNF, 7 mM 2OG.

The effects of the reported *N*-fluorinated psBBOX substrate, GBBNF[61] (**12**)(Figure 22 (**A**), synthesised by Dr. Anna Rydzik), on psBBOX*-$Zn^{(II)}$ were then examined by ^{19}F NMR. GBBNF was observed to form a signal at -83.19 ppm upon titration to psBBOX*-$Zn^{(II)}$, representing chemical shift difference from the psBBOX*-$Zn^{(II)}$ signal of $\Delta\delta_F(A) = 2.15$ ppm (Figure 22 (**B**, (**II**-**III**)).

This representative psBBOX*-$Zn^{(II)}$-GBBNF signal at -83.19 ppm, is 1.0 ppm lower when compared to psBBOX*-$Zn^{(II)}$-GBB (-82.19 ppm) and P-GBB (-82.04 ppm) assay mixtures. This is surprising given psBBOX can hydroxylate GBBNF almost as fast as GBB; the initial rate of hydroxylation was observed to be 0.29 vs 0.21 $\mu M.s^{-1}$ for GBB and GBBNF, respectively.[19] However, in contrast to GBB, GBBNF was not found to inhibit psBBOX at high concentrations[19] suggesting GBBNF is a weaker binder. Furthermore, this 1.0 ppm difference would suggest a relatively different conformation of the $–CF_3$ label in the presence of GBBNF compared to GBB and other substrates. One explanation for this observed phenomenon is the difference between GBB and GBBNF's quaternary amines. The location of the $–CF_3$ label in psBBOX* means, although the difference between the C-F bond of GBBNF versus the C-H of GBB is small, the electronic difference is observable with psBBOX* and ^{19}F NMR.

As observed with GBB, the GBBNF-induced signal at -82.95 ppm was only observed to form at high GBBNF concentrations (>10:1, GBBNF:psBBOX*) and increased in intensity in a dose-dependent manner (Figure 22 (**B**, **II**-**III**)). The peak shape at -82.95 ppm is broader in comparison to those observed with GBB; and therefore the combined observations suggest this signal may represent a slow/intermediate exchange regime, suggesting GBBNF to be a weaker binder than GBB.

Upon 2OG addition to the psBBOX*-$Zn^{(II)}$-GBBNF assay mixture (70:1, 2OG:psBBOX*), two overlapping signals were observed at -82.95 and -83.53 ppm (Figure 22, (**B**, **IV**)), either side of the previous psBBOX*-$Zn^{(II)}$-GBBNF signal at -83.19 ppm (Figure 22 (**B**, **III**)). Notably the signal at -83.53 ppm increased in intensity and was coupled to a decrease of the signal intensity at -85.34 ppm.

Similar to observations with GBB and 2OG titrations to psBBOX* (Section 3.2.1), the signal at -83.53 ppm may represent a complex where both 2OG and GBBNF are bound,

i.e. psBBOX*-$Zn^{(II)}$-GBBNF-2OG. The increase in broadening and chemical shift change, is typical of intermediate exchange which may be expected, following the addition of a weak binding ligand such as 2OG.

3.6 Effect of Inhibitors on the psBBOX*-$Zn^{(II)}$ complex

For reference purposes, a summary table is provided in Section 3.7 (Table 2).

3.6.1 Effect of substrate analogues

3.6.1.1 Mildronate

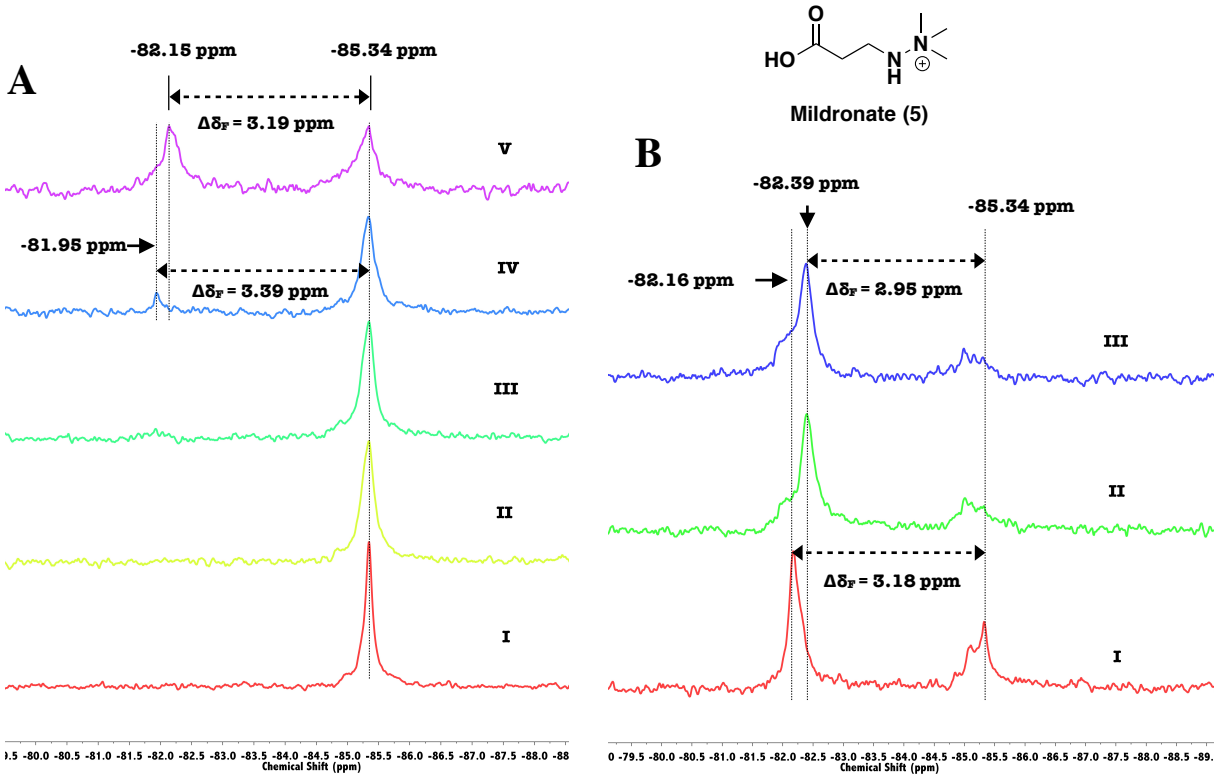


Figure 23 **A)** Resulting ^{19}F NMR spectra from a titration of Mildronate (**5**) to the psBBOX* enzyme. (**I**) 100 µM apo psBBOX* (**II**) 100 µM $ZnCl_2$, 1 mM (**5**) (**III**) 3 mM (**5**) (**IV**) 7 mM (**5**) (**V**) 7 mM (**5**), 2 mM 2OG. **B)** ^{19}F NMR spectra acquired during titration of (**5**) to the psBBOX*-$Zn^{(II)}$-GBB-2OG complex. (**I**) 100 µM psBBOX*, 100 µM $ZnCl_2$, 7 mM GBB (**II**) 7 mM GBB, 5 mM 2OG (**III**) 7 mM GBB, 5 mM 2OG, 2 mM (**5**).

Mildronate (**5**) is a weak inhibitor of human BBOX (IC_{50} = 34[26] and 62 μM[18]) and has been shown to be a competitive substrate.[18,30] A new signal was observed upon titration of 7 mM of (**5**) to the psBBOX*-$Zn^{(II)}$ complex at -81.95 ppm (Figure 23 (**A**, **IV**)); this represents a chemical shift change ($\Delta\delta_F$) of 3.39 ppm relative to the psBBOX*-$Zn^{(II)}$ complex. Adding

2OG to the psBBOX*-$Zn^{(II)}$-(**5**) titration induced a lower shift whilst also reducing the $\Delta\delta_F$ to 3.19 ppm (Figure 23 (**A**, **V**)). (**5**) was then added to a psBBOX*-$Zn^{(II)}$-GBB-2OG mixture (Figure 23 (**B**)); the representative psBBOX*-$Zn^{(II)}$-GBB-2OG ^{19}F signal at -82.40 ppm (Section 3.2.3) remained unchanged by the addition of Mildronate (Figure 23 (**B**, **III**)).

The signal at -81.95 ppm may represent a psBBOX*-$Zn^{(II)}$-(**5**) complex and is slightly higher (0.19 ppm) when compared to the GBB-induced chemical shifts observed with GBB titrations (-82.19 ppm, $\Delta\delta_F$ = 3.15 ppm) to psBBOX* (Section 3.2.1). However, concentrations >7 mM are required to observe a second signal with (**5**), as evident in Figure 23 (**A**). Although the new signal at -81.95 ppm likely represents a slow-exchange regime at high concentrations, at low concentrations, a fast regime likely exists with (**5**) and psBBOX*-$Zn^{(II)}$. This observation is typical of weak binding ligands. Furthermore, addition of 2OG induces a small chemical shift as seen with GBB-2OG titrations to psBBOX*, although with significant line broadening, typical of an intermediate exchange regime.[57] Nevertheless, the signal at -82.15 ppm may represent a psBBOX*-$Zn^{(II)}$-(**5**)-2OG complex. Given this chemical shift is relatively similar to the representative psBBOX*-$Zn^{(II)}$-GBB-2OG signal at -82.39 ppm, the observed inability of (**5**) to induce a substantial change in the ^{19}F spectrum can be due to a redundant signal which is not resolved. This observation is however in agreement with crystallographic studies on Mildronate and GBB; the two ligands bind in near-identical conformations in the BBOX active site. Another possibility is that with the inactive psBBOX*-$Zn^{(II)}$ complex initial binding of GBB may close the active site loop and prevent competitive binding of (**5**) although further studies are required to elucidate whether this is indeed the case.

3.6.1.2 AR758

The unsaturated GBB analogue AR758 (**13**)(Figure 24) is a known inhibitor of hBBOX and psBBOX ($IC_{50\ (hBBOX)}$ = 8.7 μM,[62] $IC_{50\ (psBBOX)}$= 11.4 mM[9]) and reduces carnitine levels in cells

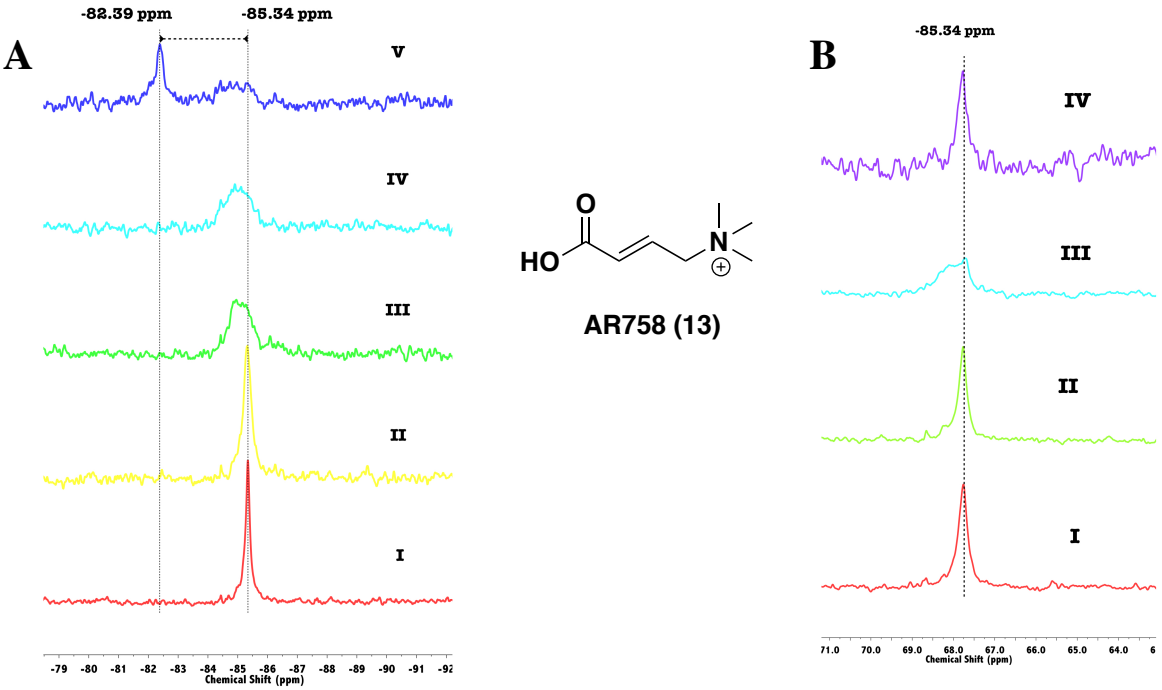


Figure 24 A) ^{19}F NMR spectra of a titration of AR758 to psBBOX*. (**I**) 100 µM apo psBBOX* (**II**) 100 µM $ZnCl_2$, 5 mM AR758 (**III**) 5 mM AR758, 10 mM 2OG (**IV**) 10 mM AR758, 10 mM 2OG (**V**) 10 mM AR758, 10 mM 2OG, 2.5 mM GBB. **B)** Buffer exchanging the reaction mixture containing AR758 and 2OG, restores the psBBOX* signal at -85.34 ppm. **B**) (**I**) 100 µM psBBOX*, 100 µM $ZnCl_2$ (**II**) 5 mM AR758 (**III**) 5 mM AR758, 5 mM 2OG (**IV**) After buffer exchange (1024 scans).

by a similar amount to Mildronate.[62] Titration of (**13**) to psBBOX*-$Zn^{(II)}$ (50:1, (**13**):psBBOX*) did not yield a typical second signal (Figure 24 (**A**, **II**)), as observed with psBBOX substrates (Section 3.2 and 3.3). Addition of 2OG to a psBBOX*-$Zn^{(II)}$-(**13**) assay mixture led to line broadening almost to baseline levels (Figure 24 (**A**, **III**-**IV**)). Addition of GBB provided a signal at -82.39 ppm. In a separate experiment, following addition of (**13**) and 2OG to a psBBOX*-$Zn^{(II)}$ mixture, it was found that after buffer exchanging the NMR sample, the *apo*-psBBOX* signal (-85.34 ppm) could be restored (Figure 24 (**B**, **IV**)).

The lack of appearance of a typical second signal with (**13**) may be attributed to the fact that (**13**) is not a psBBOX substrate and therefore, this phenomenon may be characteristic of psBBOX substrates. Even high concentrations of (**13**) (5 mM), had little observable effect on the ^{19}F NMR spectrum on psBBOX*-$Zn^{(II)}$ (Figure 24 (**A**, **II**)); only slight broadening was observed, which likely reflects an intermediate exchange regime, typical of weak binding ligands. Upon addition of an excess of 2OG (10 mM) significant

line broadening was observed along with a slight chemical shift, typical of intermediate exchange (Figure 24 (**A**, **III**-**IV**)). Addition of GBB to the psBBOX*-$Zn^{(II)}$-(**13**)-2OG sample led to observation of a typical signal corresponding to formation of psBBOX*-$Zn^{(II)}$-GBB-2OG complex at -82.39 ppm (Figure 24 (**A**, **V**)). This is important as this result suggests (**13**) binds to psBBOX* in an alternate way to substrates which does not induce a conformational change to the flexible-loop of psBBOX* or is not measurable by ^{19}F NMR. Given that (**13**) is an unreactive substrate analogue, it may not cause 'loop closure' of psBBOX* which occurs with GBB and other substrates (Figure 5). The signal at -82.39 ppm, appearing after GBB addition, is only observed in the presence of GBB and 2OG as described in Section 3.2.1 and may represent a putative psBBOX*-$Zn^{(II)}$-GBB-2OG complex. Should a psBBOX*-$Zn^{(II)}$-GBB-2OG complex be able to form in the presence of (**13**), the NMR result would support previous findings that (**13**) is indeed a weak inhibitor of psBBOX (IC_{50} = 11.4 mM[9]). After buffer exchanging the NMR sample containing the psBBOX*-$Zn^{(II)}$-AR758-2OG, assay mixture we were able to restore the psBBOX* signal at -85.34 ppm (Figure 24 (**B**, **IV**)).

3.6.2 Effect of FG2216 analogues on psBBOX*

3.6.2.1 FG2216

FG2216 (**14**)(Figure 25) is an orally active hypoxia-inducible factor prolyl-hydroxylase inhibitor,[63] reported for its ability to inhibit hBBOX (IC_{50} = 30 μM[39]) and psBBOX (IC_{50} = 1.2 μM[41]). Utilising the aforementioned ^{1}H NMR GBB/2OG reporter assay,[41] it was possible to observe inhibition of psBBOX by (**14**) involving competition with 2OG. ^{19}F-labelled psBBOX was used to investigate binding of (**14**). When titrated with psBBOX*, (**14**) causes formation of a singlet, slightly lower than the psBBOX*-$Zn^{(II)}$ signal at -85.60 ppm (Figure 25 (**III**-**IX**)).

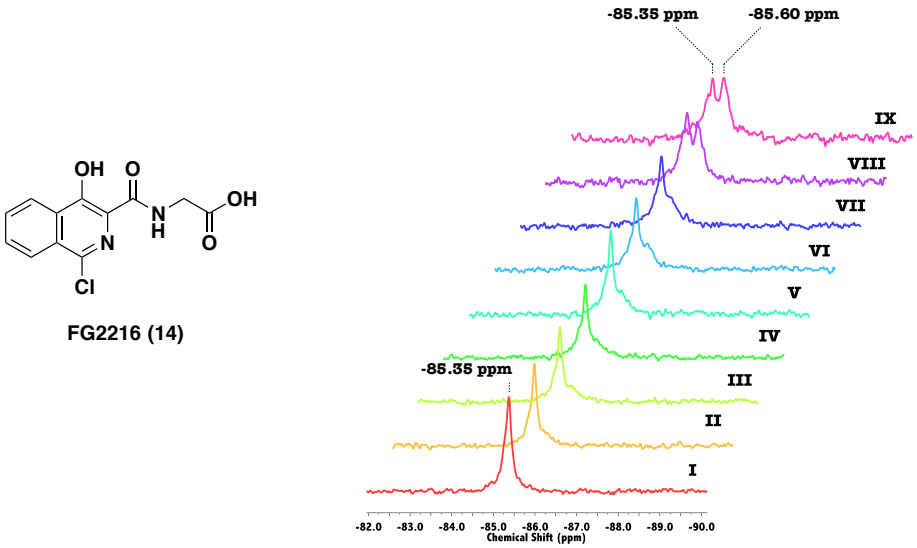


Figure 25 Monitoring binding of FG2216 to psBBOX* *via* ^{19}F NMR. Upfield signal appears in slow-exchange at -85.60 ppm representing a $\Delta\delta_F = 0.25$ ppm. Titration of 2OG mimicking inhibitors seemingly have a significantly smaller effect on the active site ^{19}F label. (**I**) 100 µM psBBOX* (**II**) 100 µM $ZnCl_2$ (**III**) 20 µM FG2216 (**IV**) 100 µM FG2216 (**V**) 200 µM FG2216 (**VI**) 400 µM FG2216 (**VII**) 600 µM FG2216 (**VIII**) 1 mM FG2216 (**IX**) 1 mM FG2216, left for1hr incubation 5°C.

Titration of up to 10 equivalents of (**14**) yielded no substantial changes to the signals (Figure 25 (**IX**)). (**14**) is a relatively efficient inhibitor of psBBOX, and the dose-dependent increase in the signal at -85.60 ppm is typical of a slow exchange regime which supports the reported inhibition data.[41] The small $\Delta\delta_F$ value of 0.25 ppm may indicate that a large conformational change is not induced on the 'flexible-loop', as contrast with GBB and other substrates ($\Delta\delta_F \sim 3.0$ ppm, Section 3.2, 3.3). This observation supports the results obtained from manual docking and energy minimization of (**14**) with psBBOX (Figure 29),[41] *i.e.* there is minimal interaction with the GBB binding residues.

3.6.2.2 FG-L-Ala

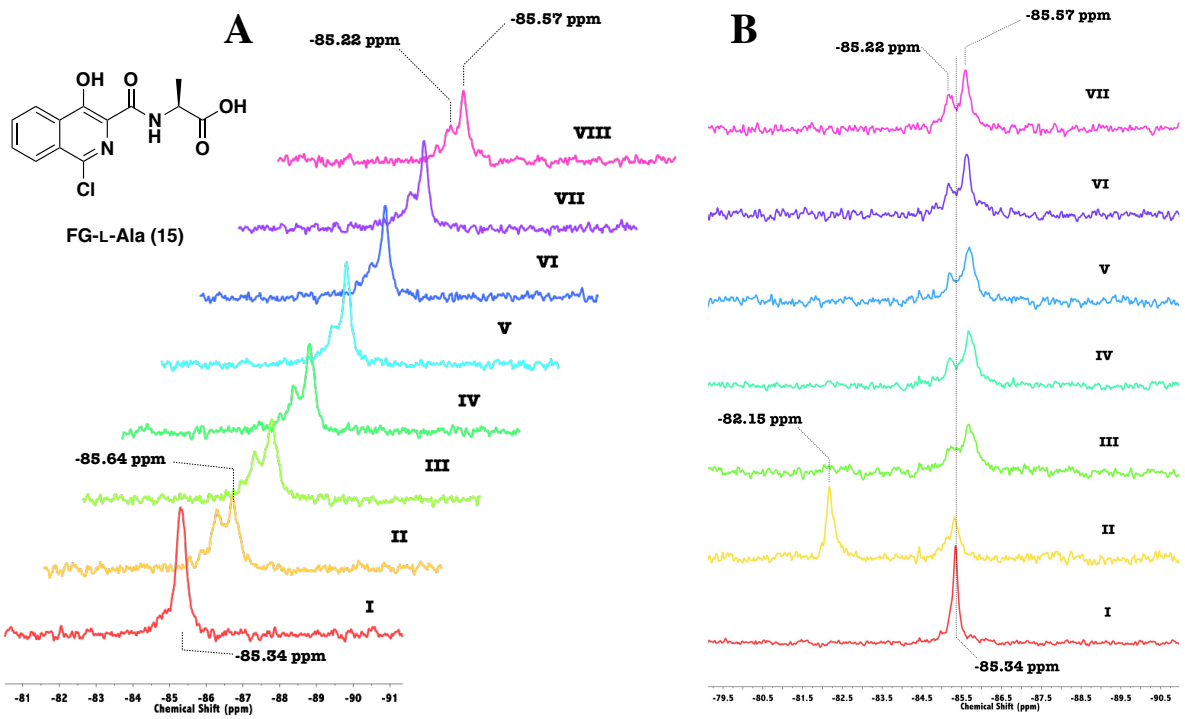


Figure 26 A) ^{19}F NMR spectra of a titration of (**15**) to psBBOX*. (**I**) 100 µM psBBOX*, 100 µM $ZnCl_2$ (**II**) 100 µM (**15**) (**III**) 200 µM (**15**) (**IV**) 800 µM (**15**) (**V**) 1500 µM (**15**) (**VI**) 2000 µM (**15**) (**VII**) 2 mM (**15**), 1.5 mM GBB (**VIII**) 2 mM (**15**), 7 mM GBB 5 mM 2OG. **B**) ^{19}F NMR spectra of a titration of (**15**) to the psBBOX*-$Zn^{(II)}$-GBB complex. (**I**) 100 µM psBBOX* (**II**) 100 µM $ZnCl_2$, 6 mM GBB (**III**) 200 µM (**15**), 6 mM GBB (**IV**) 400 µM (**15**), 6 mM GBB (**V**) 600 µM (**15**), 6 mM GBB (**VI**) 1.2 mM (**15**), 6 mM GBB (**VII**) 2.0 mM (**15**), 6 mM GBB.

Titration of the potent hBBOX and psBBOX inhibitor FG-L-ala (**15**) (IC_{50} = 0.22 µM[41] (psBBOX) IC_{50} = 5.8 µM[39] (hBBOX) to the psBBOX-$Zn^{(II)}$ complex, yielded a signal at -85.64 ppm. The signal continued to grow proportionately with the concentration of (**15**) up to 2 mM of (**15**). Adding GBB (Figure 26 (**VII**)) followed by 2OG (Figure 26 (**VIII**)) to the psBBOX*-$Zn^{(II)}$-(**15**) experiment caused the formation of a small broad signal at -85.22 ppm and a singlet at -85.57 ppm.

At low concentrations of (**15**) the signal observed at -85.64 ppm represents a slow exchange regime, typical of strong binding ligands. At 2 mM of (**15**) a distinct singlet can be seen at -85.64 ppm, which may represent a single conformation of the flexible loop of psBBOX*, caused as a result of (near) stoichiometric (**15**) binding. The small $\Delta\delta_F$ of 0.3 ppm suggests the binding of (**15**) may not induce a large conformational change in the

flexible loop. Addition of GBB and 2OG, revealed only small changes in the signal chemical shift. A small shift of the singlet in Figure 26 (**VI**) to -85.57 ppm ($\Delta\delta_F$ = 0.07 ppm) and the formation of a small, broad signal at -85.22 ppm upon GBB and 2OG addition suggest the co/substrates have a relatively insignificant effect on the psBBOX*-$Zn^{(II)}$-(**15**) complex. However, although the results following co/substrate addition suggest they have some effect, no signal typically observed with GBB was observed at -82.40 ppm, indicating GBB may not be able to bind.

3.6.2.3 FG-D-Ala

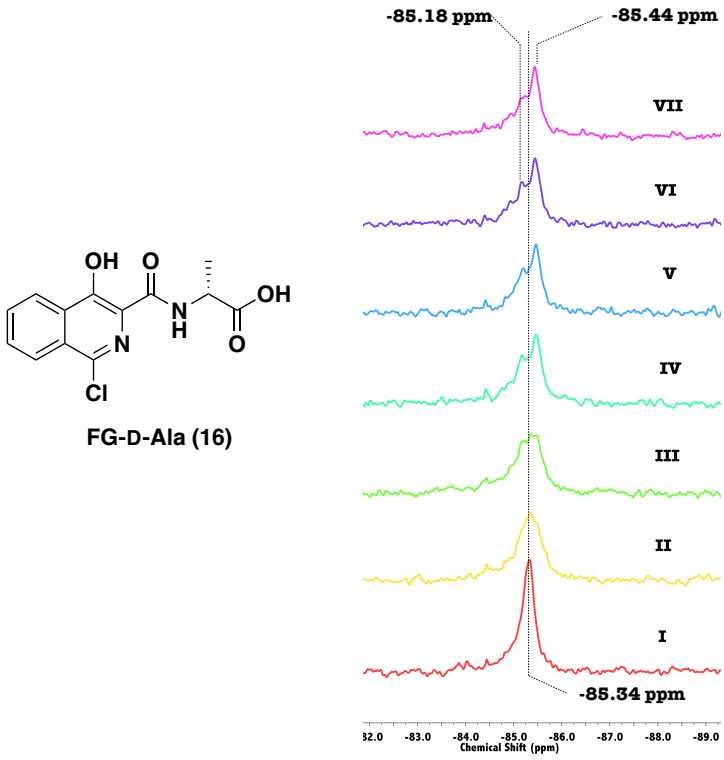


Figure 27 ^{19} F NMR spectra of a titration of the inhibitor FG-D-ala (**16**) to psBBOX*. (**I**) 100 µM psBBOX*, 100 µM $ZnCl_2$ (**II**) 100 µM (**16**). (**III**) 200 µM (**16**). (**IV**) 400 µM (**16**). (**V**) 800 µM (**16**). (**VI**) 1600 µM (**16**). (**VII**) 2000 µM (**16**).

Titration of FG-D-ala (**16**) (Figure 27) ($IC_{50\ (psBBOX)}$ = 0.20 µM) with psBBOX-$Zn^{(II)}$ resulted in broadening at low concentrations Figure 27 (**II**)) before two redundant signals emerged in a dose-dependent manner at -85.18 ppm and -85.44 ppm (Figure 27 (**VII**)).

The observed signals following titration of (**16**) to psBBOX* are comparable to that of structurally related compounds (**14**) and (**15**). The resulting ^{19}F signals observed on titrating (**15**) with psBBOX* are typical of strong binding ligands, and this is reflected by the slow exchange regime displayed by (**16**)(Figure 27). (**16**) is an enantiomer of (**15**) and the two share almost identical IC_{50} values of 0.20 and 0.22 μM respectively. Therefore, the observed similarity of the ^{19}F NMR spectra of (**15**) and (**16**) titrations with psBBOX* was anticipated.

3.6.2.4 FG-L/D-Trp

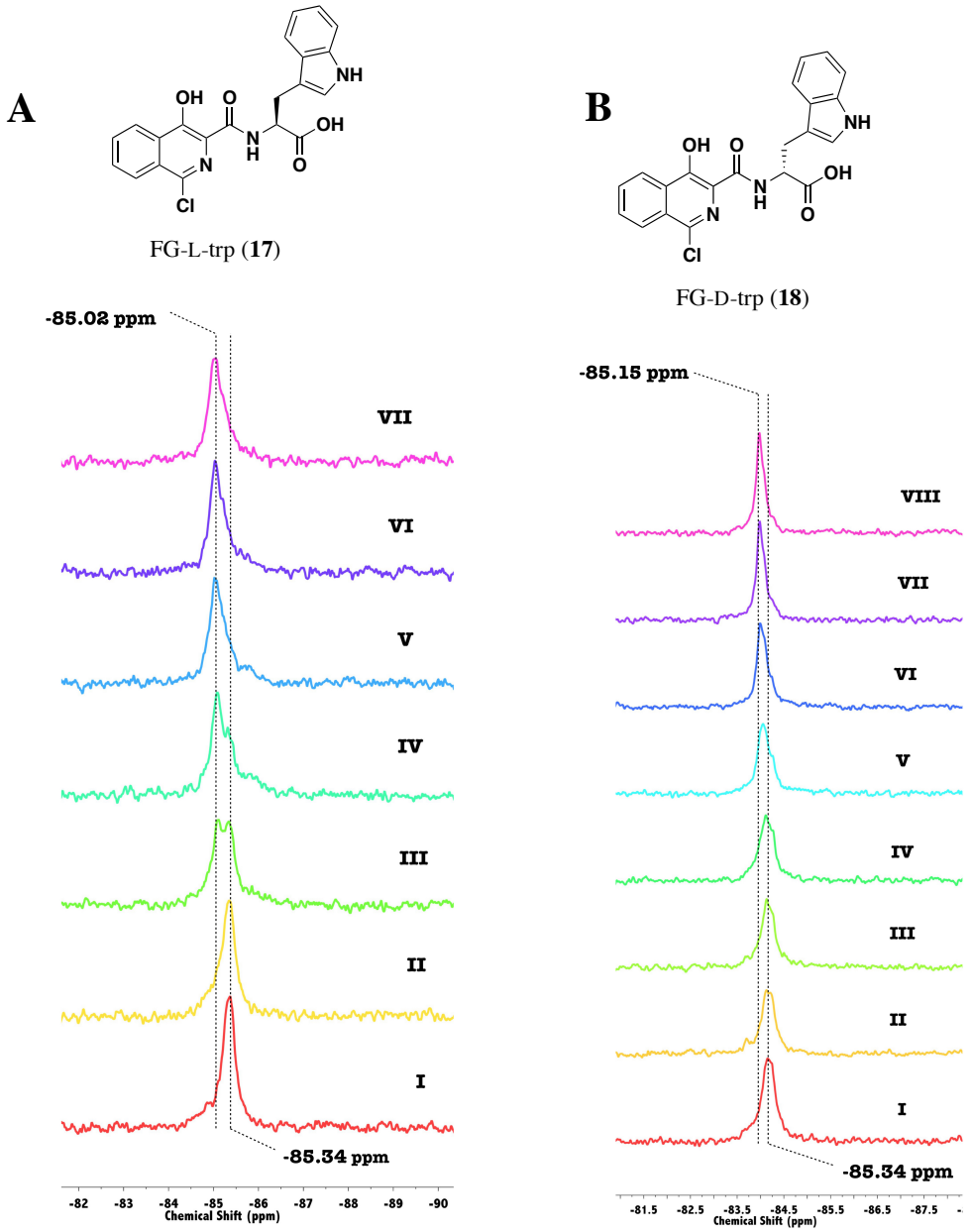


Figure 28 A) Titration of FG-L-Trp (**17**) to psBBOX* (**I**) 100 µM psBBOX*, 100 µM $ZnCl_2$ (**II**) 20 µM (**17**) (**III**) 100 µM (**17**) (**IV**) 200 µM (**17**) (**V**) 400 µM (**17**) (**VI**) 600 µM (**17**) (**VII**) 1mM (**17**). **B**) Titration of FG-D-Trp (**17**) to psBBOX* (**I**) 100 µM psBBOX*, 100 µM $ZnCl_2$ (**II**) 20 µM (**18**) (**III**) 100 µM (**18**). (**IV**) 200 µM (**18**) (**V**) 400 µM (**18**) (**VI**) 600 µM (**18**). (**VII**) 1 mM (**18**). (**VIII**) 1.4 mM (**18**).

FG-L-Trp (**17**) (Figure 28 (**A**)) was shown to be a good inhibitor of psBBOX (IC_{50} = 0.9 µM, K_D = 29 µM),[41] and using the ^{1}H NMR reporter assay[41] (Section 3.1.3) it was possible to observe its ability to displace both GBB and 2OG from the psBBOX*. Titration of (**17**) with the psBBOX*-$Zn^{(II)}$ complex caused formation of a singlet increasing in a dose-dependent manner at -85.02ppm (Figure 28 (**A**)).

In contrast to the less bulky analogues (**15**) and (**16**), titration of (**17**) induced formation of a signal (-85.02 ppm) with a higher shift ($\Delta\delta_F$ = 0.32 ppm) relative to the psBBOX*-$Zn^{(II)}$ complex (-85.34 ppm). Moreover, the induced signal is typical of a slow exchange regime as exhibited by strongly binding ligands. As observed with compounds (**14**), (**15**), and (**16**), (**17**) does not cause a large chemical shift as observed with GBB and other substrates ($\Delta\delta_F$ = ~ 3 ppm, Figure 28 (**A**)) suggesting minimal interactions with the flexible loop of psBBOX*. This observation is in support of docking simulations of (**17**) with psBBOX, that show minimal changes in Tyr201, *i.e.* the location of the $-CF_3$ label (Figure 29). The docking studies also propose that the indole of (**17**) may extend into the hydrophobic pocket, adjacent to the 2OG binding site rather than the GBB binding site. Previous crystallographic studies of the potent hBBOX inhibitor AR692B (**6**) (Figure 5) show this inhibitor adopts a similar conformation to that proposed for (**17**). Thus, the observed ability of (**17**) to eject both 2OG and GBB form psBBOX may stem from more significant movements in the hydrophobic pocket adjacent to the 2OG binding site, which as a result induces sufficient changes elsewhere in the protein to cumulatively prevent GBB binding.

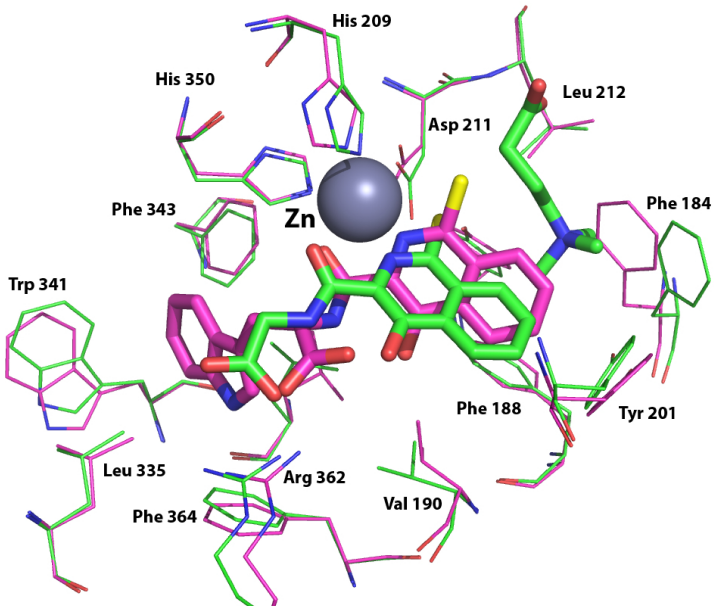


Figure 29 Inhibitors FG2216 (**14**) (green sticks, Cl in yellow) or FG-L-trp (**17**) (pink sticks, Cl in yellow) bound to a model psBBOX active site (based on hBBOX PDB ID: 3O2G) *via* docking simulation. *Figure adapted from Ref no. 41.*

Titration of FG-D-trp (**18**) (Figure 28 (**B**)) to psBBOX* caused formation of a signal at -85.15 ppm which increased in a dose-dependent manner.

As with the enantiomeric compound (**17**), the ^{19}F NMR signal observed with titration of (**18**) to psBBOX* is representative of a slow exchange regime (Figure 28 (**B**)), and reflects the affinity exhibited by (**18**)((IC_{50} = 18 μM, K_D = 168 μM)[41]) towards psBBOX.

3.6.3 Effect of AR92B on psBBOX*

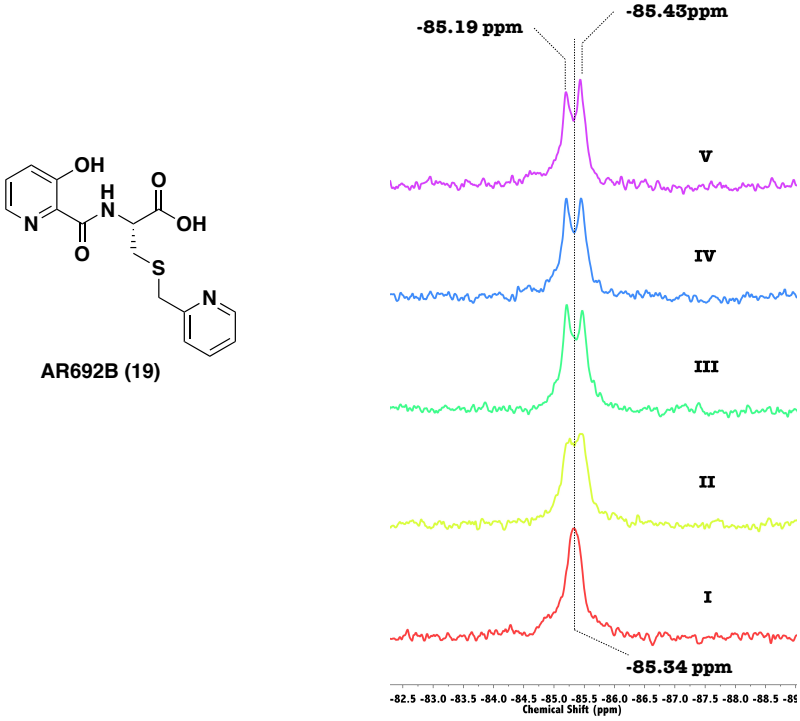


Figure 30 ^{19}F NMR spectra of a titration of AR692B (**19**) to the psBBOX*-$Zn^{(II)}$ complex. (**I**) 100 μM psBBOX*, 100 μM $ZnCl_2$ (**II**) 100 μM (**19**) (**III**) 200 μM (**19**) (**IV**) 600 μM (**19**) (**V**) 1 mM (**19**).

Titration of the potent hBBOX inhibitor AR692B (**19**)(IC_{50} = 0.15 μm[39]), to the psBBOX*-$Zn^{(II)}$ complex caused formation of two redundant signals at -85.19 ppm and -85.43 ppm, either side of the psBBOX*-$Zn^{(II)}$ signal at -85.34 (Figure 30).

The strong binding ability of (**19**) is reflected in the slow exchange regime exhibited by the resulting psBBOX* ^{19}F NMR signals following addition of (**19**) to psBBOX*. As observed with the FG2216 analogues (Section 3.3.2.1-3.3.2.4) the induced chemical shift following titration of (**19**) to psBBOX* is minimal in comparison to that observed with

substrates ($\Delta\delta_F$ = ~ 3.0 ppm)(Section 3.2). The small $\Delta\delta_F$ (0.15 and 0.09 ppm) of both signals suggest the conformation of the flexible loop is largely indifferent following binding of (**19**) to the psBBOX*. However, in contrast to the FG2216 analogues, the ^{19}F spectra suggest addition of (**19**) to psBBOX* may represent two different conformations of the flexible loop; this effect may be due to two conformations of the inhibitor itself, which has been observed in X-ray crystallographic studies on (**19**) bound to hBBOX (Section 3.2, Figure 5).[39]

3.6.4 Effect of RL190B on psBBOX*

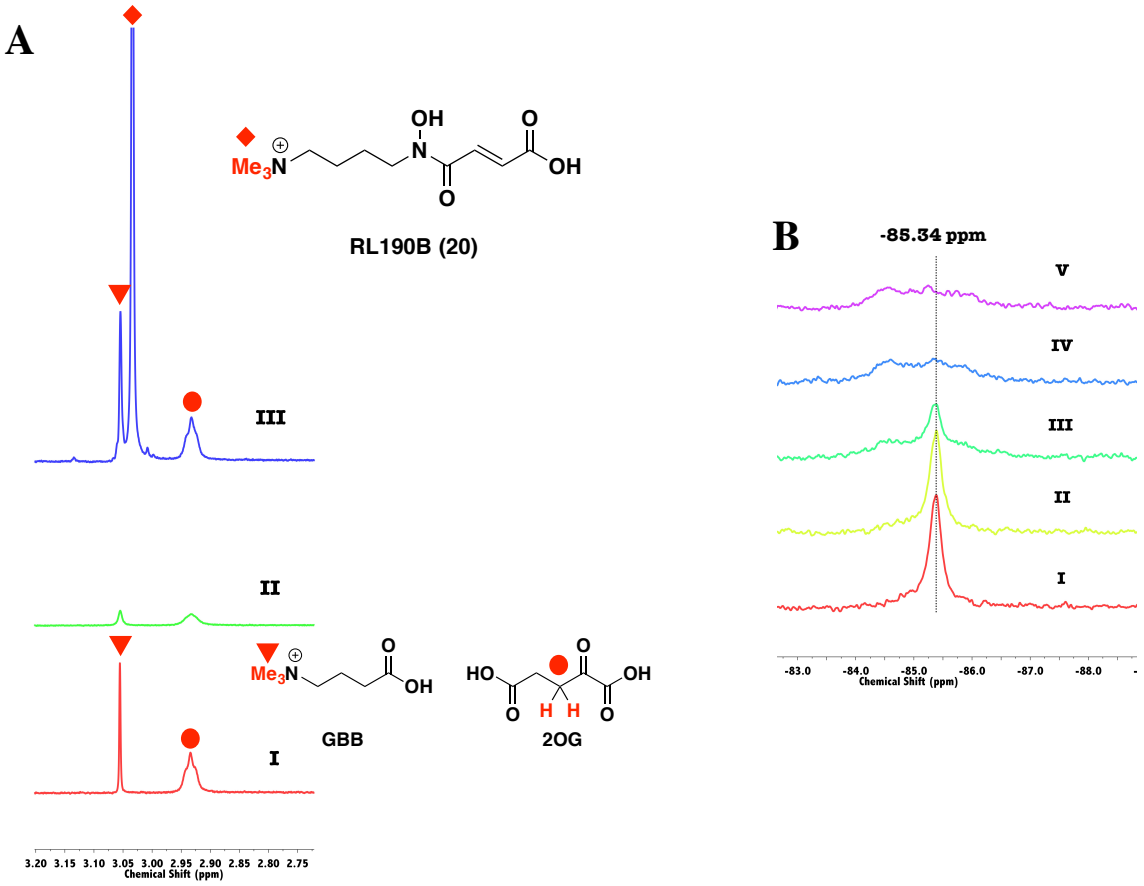


Figure 31 A) ^{1}H NMR spectra displaying displacement effect of RL190B (**20**)(red squares) on the psBBOX co/substrates GBB (red triangles) and 2OG (red circles). Near complete attenuation of the reporter signals is observed upon addition of psBBOX. (**20**) seemingly displaces both reporter ligands from wild-type psBBOX. (**I**) 20 μM GBB, 300 μM 2OG, 150 μM $Mn^{(II)}$. (**II**) + 20 μM psBBOX. (**III**) + 500 μM (**20**). Final assay mixture: 20 μM GBB, 300 μM 2OG, 150 μM $Mn^{(II)}$, 20 μM psBBOX, 500 μM (**20**), 80 mM KCl, 50 mM Tris-d_{11}, pH 7.5 in D_2O. Total assay volume 160 μL. **B**) ^{19}F NMR spectra acquired during titration of (**20**) to psBBOX*. (**I**) 100 μM psBBOX*, 100 μM $ZnCl_2$ (**II**) 20 μM (**20**) (**III**) 100 μM (**20**) (**IV**) 200 μM (**20**) (**V**) 400 μM (**20**).

RL190B (**20**), which was designed to include both GBB and 2OG binding motifs to act as a 'dual-substrate' mimic (Appendix I), (Figure 31 (**A**)) showed relatively good inhibitory activity against psBBOX (IC_{50} = 5 μM (Appendix I)). Furthermore, using the ^{1}H NMR GBB/2OG reporter assay,[41] it was observed that (**20**) fully displaced both bound substrates from wild-type psBBOX ((**20**)/2OG/GBB/$Mn^{(II)}$/psBBOX, 50:30:15:2:2) (Figure 31 (**A**)). Titration of (**20**) with psBBOX* yielded line-broadening, typical of an intermediate

exchange regime (Figure 31 (**B**)). Protein precipitation was observed above 400 μM of (**20**); therefore further titrations above this concentration were not attempted.

One possibility is, given the metal chelating ability of (**20**), the inhibitory mode may be partially *via* the denaturing of psBBOX* which would also explain the observed precipitation. However, further studies are needed to validate this proposal. What is evident from titration of RL190B to psBBOX* and the ^{1}H NMR reporter assay, is that although (**20**) can bind to the enzyme and remove co/substrates from the active site, it likely does not stabilise the 'flexible-loop' in contrast to other metal chelating inhibitors (Section 3.3.2). A similar effect was observed with the substrate mimic inhibitor AR758 (**13**) (Section 3.3.3). These observations are interesting as active site mimic inhibitors such as (**20**) have previously not been examined as inhibitors of BBOX enzymes. Therefore (**20**) and further analogues may provide novel BBOX inhibitors (Appendix I).

3.6.5 Effect of DMSO

Utilising small organic solvent molecules to investigate binding sites of a protein in solution is a known technique employing the use of ^{1}H and 2D techniques.[64] Titrating DMSO to psBBOX*, showed a change in the ^{19}F chemical shift of about 0.11 ppm at 6% DMSO

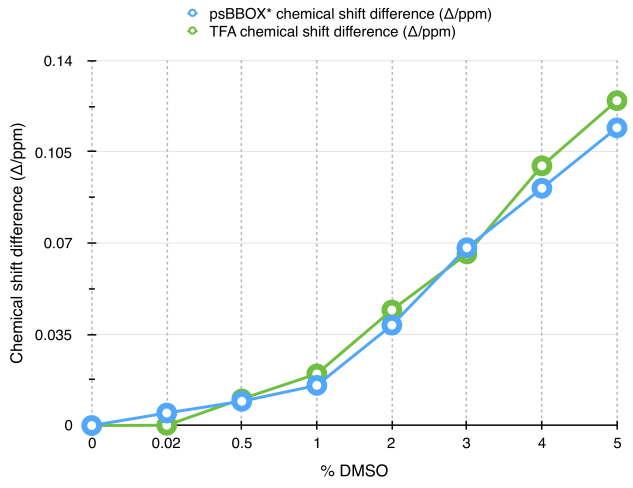


Figure 32 Graphical representation of the effect of increasing DMSO concentration on the ^{19}F signal of TFA and psBBOX*. DMSO appears to have a near identical effect on the CF_3 label as with TFA.

(Figure 32) (1-2% maximum DMSO present in inhibitor titrations to psBBOX*). This however was near identical to the chemical shift change of the TFA ^{19}F signal, suggesting the $-CF_3$ label is as exposed to the solvent as the TFA present in the sample tube. Thus, titration of DMSO inhibitor solutions to psBBOX* solutions have a minimal effect.

3.7 Summary and future perspectives

Table 1 ^{19}F NMR chemical shifts observed with various metals, 2OG, and substrates. $\Delta\delta_F$ is given as a difference in ppm between the observed signal following ligand titration and the signal observed with *apo*-psBBOX*.

Ligand(s) present	Chemical shift of resultant signal / ppm	Chemical shift difference $\Delta\delta_F$ / ppm	Figure in text	Exchange regime	Comments
apo*-psBBOX	-85.34	0.00	**8, 10-(I)**	fast	A single conformer is observed or rapid exchange between multiple conformers.
$Ni^{(II)}$	-85.28	0.06	**10-(II)**	slow	$Ni^{(II)}$ is a strong binder of BBOX enzymes.
$Zn^{(II)}$	-85.34	0.00	**10-(III)**	intermediate	Signal broadening observed.
$Mn^{(II)}$	~ -85.34	0.00	**11-A-(II)**	intermediate	$Mn^{(II)}$ paramagnetic. Signal broadens into baseline.
$Co^{(II)}$	~ -84.98	0.36	**11-A-(III)**	intermediate	$Co^{(II)}$ paramagnetic. Broadening and a small chemical shift observed.
$Fe^{(II)}$	~ -85.09	0.25	**11-A-(I-IV)**	intermediate	$Fe^{(II)}$ paramagnetic. Broadening and a small chemical shift observed.
GBB	-82.19	3.15	**12**	slow	GBB is likely in fast exchange at concentrations <1mM. Binding of second GBB, may promote loop closure.
2OG	~ -85.10	0.24	**13**	intermediate	Signal broadening, coupled with a small chemical shift is observed.
GBB + 2OG	-82.40	2.94	**14, 15**	intermediate	2OG induces broadening and a small chemical shift. Weak binder, therefore intermediate exchange observed.
NOG	-84.99	0.35	**17, 18**	slow	NOG can inhibit psBBOX, and is a significantly stronger binder than 2OG therefore see slow exchange.
NOG+GBB	-82.45	2.89	**18-(IV-VI)**	slow	May reflect GBB binding to the psBBOX*-NOG complex.
L-carnitine	-85.34	0.00	**19-B-(II)**	fast	L-Carnitine is not a psBBOX substrate. No second signal at a higher ppm is observed with psBBOX*.
L-carnitine + 2OG	-82.29	3.05	**19-B-(III)**	slow/ intermediate	2OG induces a broad, slow exchange signal. This may represent a higher requirement for 2OG than other substrates.
D-carnitine	-82.71	2.63	**19-B-(IV)**	slow/ intermediate	D-Carnitine is a psBBOX substrate. A broad signal at a higher ppm is observed, although >50:1 D-car:psBBOX* is required.
D-carnitine +2OG	-82.95	2.39	**19-B-(V)**	slow	2OG and D-car induce formation of a signal in a slower exchange regime than *L*-car.
P-GBB	-82.04	3.30	**20-B-(II-III)**	slow	P-GBB interacts in a similar manner to GBB. Quaternary phosphorus, induces slightly higher shift compared to GBB.
P-GBB + 2OG	~ -82.10	3.24	**20-B-(IV-V)**	intermediate	2OG, induces broadening of signals.
GBBNF	-83.19	2.15	**21-B-(II-III)**	slow/ intermediate	As with P-GBB and GBB, slow exchange is observed at >1 mM.
GBBNF + 2OG	-82.95, -83.53	2.39, 1.81	**21-B-(IV)**	intermediate	Broadening and a slight chemical shift is observed with the addition of 2OG.

Table 2 ^{19}F NMR chemical shifts observed with various inhibitors. $\Delta\delta_F$ is given as a difference in ppm between the observed signal following ligand titration and the signal observed with *apo*-psBBOX*.

Ligand(s) present	Chemical shift of resultant signal / ppm(ppm)	Chemical shift difference $\Delta\delta_F$ / ppm	Figure in text	Exchange regime	Comments
Zn(II)	-85.34	0.00	**8, 10-(I)**	intermediate	Signal broadening observed.
Mildronate (5)	-81.95	3.39	**22-A-(IV)**	slow	Slow exchange is only observed at significantly higher concentrations than with GBB (70:1, (**5**):psBBOX* *vs* 10:1, GBB:psBBOX*)
Mildronate + 2OG	-82.15	3.19	**22-A-(V)**	intermediate	2OG induces signal broadening coupled to a lower chemical shift.
AR758 (13)	~ -85.34	0.00	**23-A-(II)**	fast	(**13**) did not enable formation of a new signal. Addition of 2OG induced signal broadening.
FG2216 (14)	-85.60	0.26	**24**	slow	Strong binder (IC_{50} = 1.20 μM).
FG-L-ala (15)	-85.64	0.30	**25-A**	slow	Strong binder (IC_{50} = 0.22 μM).
FG-D-ala (16)	-85.18, -85.44	0.16, 0.10	**26**	slow	Strong binder (IC_{50} = 0.20 μM).
FG-L-trp (17)	-85.02	0.32	**27-A**	slow	Strong binder (IC_{50} = 0.90 μM).
FG-D-trp (18)	-85.15	0.20	**27-B**	slow	Good binder (IC_{50} = 18 μM).
AR692B (19)	-85.19, -85.43	0.15, 0.09	**29**	slow	Strong binder ($IC_{50\ (hBBOX)}$ = 0.15 μM). May reflect two conformations adopted by (**19**) in hBBOX active site.
RL190B (20)	~ -85.34	0.00	**30-B**	intermediate	Good binder (IC50 = 5.0 μM). May represent new inhibitor class.

A summay of ^{19}F NMR signals resulting from titration of various metals and co/substrates to psBBOX* is presented in Table 1. The largest chemical shift change relative to the psBBOX* signal at -85.34 ppm ($\Delta\delta_F$) was observed with GBB and other substrates (D-carnitine, P-GBB, GBBNF) (Table 1). Although a signal typical of a slow exchange regime was observed with all substrates at high concentrations (> 1 mM), all substrates other than GBB displayed either signal broadening or low intensity of the second signal or both, and therefore reflect more intermediate exchange regimes with psBBOX*-$Zn^{(II)}$; this can be typical of weak binding ligands (Section 3.3.1). In all ^{19}F NMR experiments with psBBOX* and substrates, the addition of 2OG induced a small chemical shift together with some line broadening, typical of intermediate exchange regimes in support of the poor binding affinity reported for 2OG and wild-type psBBOX (K_M = 532 μM)[19] in the presence of GBB.

In Section 3.2.3, % peak areas following GBB titrations to psBBOX*-$Zn^{(II)}$ were examined (Figure 17). Interestingly, saturating conditions of GBB (70:1, GBB:psBBOX*)

were not able to fully attenuate the psBBOX*-$Zn^{(II)}$ signal at -85.34 ppm. Moreover, the % peak area of the GBB-induced signal at -82.19 ppm did not increase to more than 50% of its original value, with the addition of 2OG (Figure 17). This result is important as the formation of the second signal at -82.19 upon GBB titration may represent a psBBOX*-$Zn^{(II)}$-GBB complex; this situation may also be occurring with other substrates where a second signal was observed. A further possibility is that the slow exchanging second signal observed at high GBB concentrations reflects a psBBOX*-dimer complex in which two GBB molecules are bound. At low concentrations of GBB there may exist a fast exchange regime and upon an increase in GBB concentration, binding of a second GBB molecule may strengthen binding of the first. Thus, binding of a second molecule of GBB may induce closure of the 'flexible-loop', which may be the reason for the observed slow exchange at high concentrations of GBB. The observed phenomena with GBB and psBBOX* may also be a result of GBB inhibition, which is known to occur for psBBOX at high concentrations of GBB (K_i = 125 uM).[19] Whether or not the formation of a second signal observed with GBB and other substrates is caused by closure of the flexible loop will require further structural studies.

Interestingly, Mildronate (**5**), which is a putative inhibitor and competitive substrate for BBOX, was able to cause formation of a second signal, although much less effectively than GBB, with only high concentrations of (**5**) (7 mM) yielding an observable signal 3.39 ppm downfield to psBBOX* (Table 2). Furthermore, GBB was able to induce a slow exchange signal without 2OG with psBBOX*-$Zn^{(II)}$; this is in contrast to titrations with (**5**) and psBBOX*, where an increase in the second signal was seemingly, correlated to the presence of 2OG.

As presented in Table 2, treatment of psBBOX* with metal chelating ligands presented in Section 3.3.2 and 3.3.3, caused formation of signals at small chemical shifts

relative to the psBBOX* signal at -85.34 ppm. Although mostly representing slow exchange regimes, the signals produced are largely non-redundant making quantification of binding *via* integration difficult. Nevertheless, interesting results were observed for ligands such as AR692B (**19**), where formation of two signals of equal intensity was observed upon titration to psBBOX*-$Zn^{(II)}$. This result potentially represents two bound conformations of (**19**), as observed in crystallographic studies of AR692B and hBBOX,[39] or it may represent two conformations of the 'flexible-loop'

Inhibitors AR758 (**13**) and RL190B (**20**) provided contrasting results to the other ligands discussed above (Section 3.3.1.2 and Section 3.3.4). Upon addition of (**13**) no effect on the psBBOX* signal was observed suggesting (**13**) may have little effect on the 'flexible-loop' of psBBOX*. Inhibitor (**20**) on the other hand caused formation of an extremely broad signal, typical of intermediate exchange and may reflect its weaker inhibition ($IC_{50\ (psBBOX)}$ = 5 μM) compared to the slow exchanging signals caused by FG2216 analogues and (**19**).

Figure 33 displays some possible conformations of the psBBOX* 'flexible-loop', which were proposed from the results of the protein-observed NMR experiments discussed above. However, further structural and biophysical studies are required to elucidate whether these proposed situations are accurate.

Overall, the results suggest that whereas the 'flexible-loop' $–CF_3$ label is highly sensitive to substrate binding events, it seemingly lacks sufficient sensitivity to allow for the observation of non-redundant signals following the binding of 2OG, and inhibitors binding in the 2OG binding site. Given the non-redundant ^{19}F NMR signals following the binding of multiple ligands, accurate quantification *via* integration is difficult. Therefore, further substitutions and labelling of the BBOX active site closer to the 2OG binding site may aid in defining the induced conformational changes upon binding of such ligands. Although

more difficult to produce, comparison to a similarly ^{19}F-labelled hBBOX mutant would also prove useful.

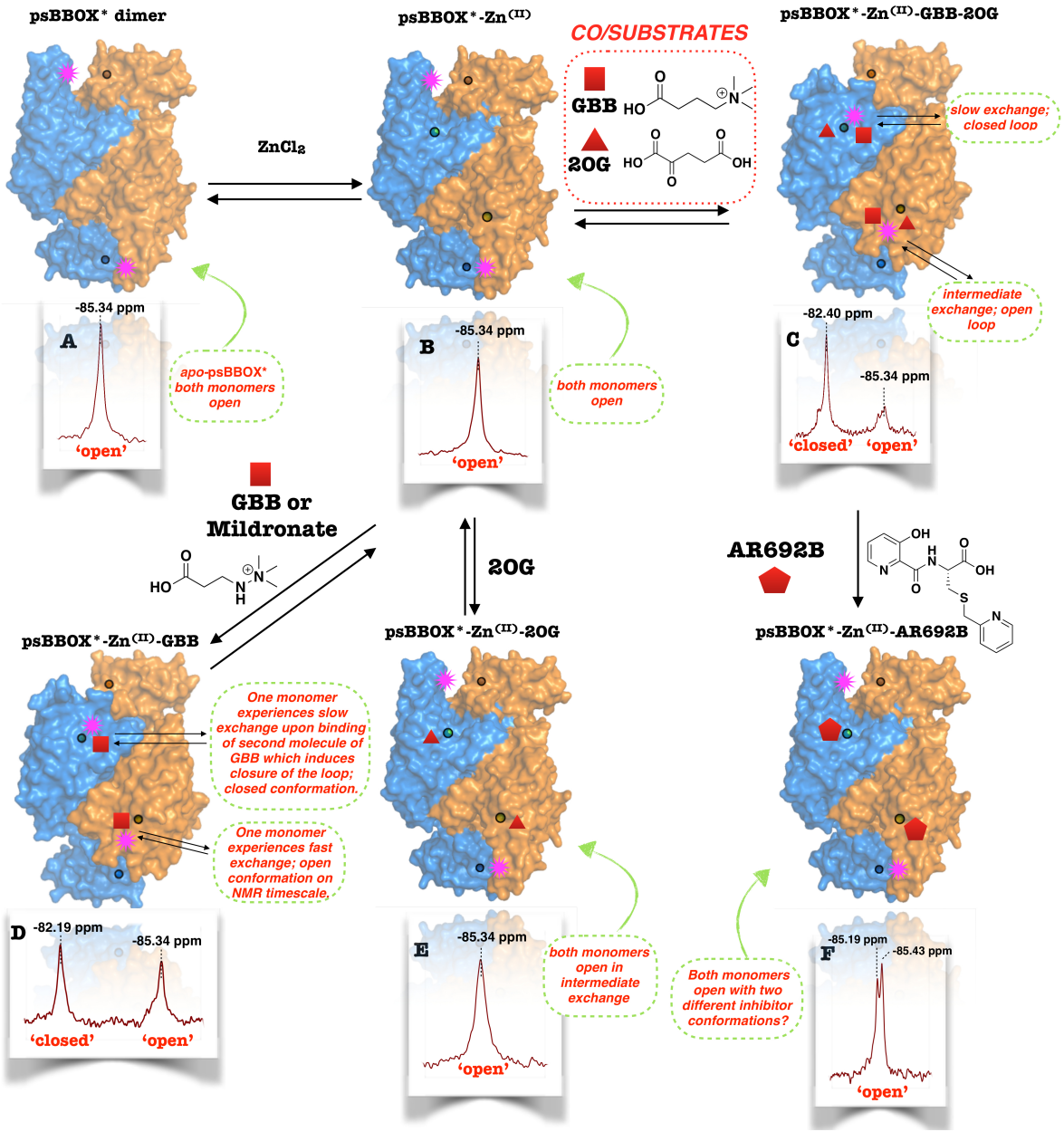


Figure 33 Possible scenarios which may explain the observed ^{19}F NMR signals arising from titrations of co/substrates and inhibitors to psBBOX*. Pink stars represent locations of the $-CF_3$ label. Each monomer of dimeric psBBOX* is coloured as either a blue or orange surface. Human BBOX structural data have been used to generate the images; 'closed' conformation PDB id: 3O2G, 'open' conformation PDB id: 4C8R. **A**) A single stable conformer or a fast exchange regime (more likely) is observed in the ^{19}F NMR spectrum of apo-psBBOX*. **B**) Addition of $Zn^{(II)}$ to psBBOX* causes slight line broadening. **C**) Addition of GBB and 2OG causes formation of a signal at a higher shift to psBBOX*-$Zn^{(II)}$, which may represent a 'closed' conformation. **D**) GBB may induce a 'closed' conformation of psBBOX*without 2OG. **E**) Addition of 2OG to psBBOX*-$Zn^{(II)}$ results in broadening of the ^{19}F signal;. this may reflect minimal changes in the 'flexible-loop'. **F**) As with 2OG, titration of inhibitors causes minimal changes to the psBBOX* signal, which may reflect minimal conformational changes in the flexible loop. The observed inhibitor-induced signals may represent different binding modes.

3.8 Acknowledgements

Mutagenesis and mass spectrometric monitoring of the BFA labelling of psBBOX-Y201C protein variant was carried out by Dr Anna Rydzik (Department of Chemistry, University of Oxford), who also kindly provided metal T_m shift data for wild-type psBBOX. ^{1}H NMR dual reporter assay titrations were carried out by Dr. Amjad Kahn (Department of Chemistry, University of Oxford). Dr Anna Rydzik and Dr Jürgen Brem deserve a huge thanks for many discussions and guidance along with Prof Timothy Claridge (Department of Chemistry, University of Oxford) for interpretation of NMR data. Compounds (**12**)-(**19**) were provided by Dr Anna Rydzik.[39,62] Compound (**11**) was synthesized by Mr. Jos Kamps.[60]

3.9 Materials and methods

3.9.1 NMR - instrumentation

NMR measurements were conducted using a Bruker AVIII HD 600 spectrometer equipped with a BB-^{19}F/^{1}H Prodigy N_2 cryoprobe operating at 298 K using 5 mm diameter NMR tubes (Norell). ^{19}F[^{1}H] decoupled spectra were recorded using inverse-gated Waltz-16 ^{1}H decoupling with rf field of 3.125 kHz. ^{19}F 90^o pulse lengths were 11 μs and spectra were typically obtained using 256 scans (unless otherwise stated). Line broadening of 20 Hz wa applied using MestReNova version 11.0 and all spectra were referenced to a trifluoroacetic acid (TFA) standard (-76.55 ppm).

3.9.2 NMR – Sample preparation and data aquisition

A typical NMR sample totaled 500 μL and was made up in 5 mm NMR tubes. Each sample contained 100 μM psBBOX* in Tris buffer (50 mM, pH 7.5) supplemented with 200 mM NaCl in 90% H_2O and 10% D_2O (50 μL). An internal standard of TFA (50 μM) was used.

Before every substrate/inhibitor titration experiment, an apo-psBBOX* ^{19}F NMR spectra was acquired without any co/factors or ligands. Co/factors and/or ligands were subsequently titrated to the same sample of psBBOX* and a spectral acquisition was made after each addition unless otherwise stated. Chemical exchange rates are referred to on an NMR timescale in the text.[57] In the context of this thesis chemical exchange rates are in reference to the intermolecular exchange rates between psBBOX* and various co/factors and/or ligands. Exchange between two signals is assigned as slow, medium or fast depending on the type of effect seen upon changing concentration of the ligand or co/factor in question. When the exchange between two chemical entities is slow, signal intensity is concentration dependent and the two signals possess two different chemical shifts. This is a direct result of the rate of exchange between the two entities being slow enough to observe on an NMR timescale. In an analogous fashion a fast exchanging system can be seen in NMR spectroscopy when two chemical entities are exchanging rapidly; where two signals are typically observed in a slow exchange system, when the rate of exchange is too fast on an NMR timescale, individual signals for both entities are not observed but rather a single signal along with a chemical shift is observed. An intermediate exchanging system is observed in NMR when the rate of exchange between two entities is roughly equal to the difference in chemical shift of the two individual entities and hence line broadening or "coalescence" of the two signals is often observed.

3.9.3 Enzyme production and purification

3.9.3.1 Reagents for molecular biology

All materials and reagents used were from New England Biolabs, Invitrogen, Bio-Rad, Roche or Simga-Aldrich unless otherwise stated. Water used was purified using a Millipore Elix® Reverse Osmosis system which was purified again by a Millipore Milli-Q® Synthesis

system with a 0.22 μm filter. IPTG and ampicillin solutions were sterilized before use with a 0.2 μm filter from Minisart®, Sartorius Stedim.

3.9.3.2 Expression

DNA encoding for psBBOX-Y201C variant together with a *N*-terminal hexa his-tag in a pCOLDI construct (provided by Dr. Anna Rydzik) was transformed into BL21 (DE3) competent cells before being frozen as a glycerol stock in liquid nitrogen and stored at -80°C. Glycerol stocks of bacterial cell cultures were made up using a 3:1 ratio of glycerol to cell culture. From this an overnight starter culture was prepared and large-scale protein expression and purification was carried out according to the protocol for wild-type psBBOX.[19] 12 flasks containing 2TY media (600 ml) were supplemented with ampicillin (50μg/ml) before 6ml of the overnight starter culture was added. The flasks were then incubated at 37°C with shaking (180 rpm) until $O.D_{600}$ reached 0.6. Following this observation the incubation temperature was reduced to 15°C and the shaking stopped. The flasks remained at this temperature for 30 mins before IPTG (ispropyl β–galactopyranoside) was added (0.2 mM final concentration of IPTG). The flasks were then incubated overnight at 15°C with shaking. The following morning the bacterial cultures were carefully dispensed into centrifuge tubes and pelleted via centrifugation (10 min, 7000 rpm). The resulting cell pellet was transferred into plastic sealable bags, weighed and frozen at -80°C and left overnight.

3.9.3.3 Cell lysis and protein purification[19]

The frozen cell pellet was quickly removed from the freezer and placed in a glass beaker equipped with a stirrer bar. The beaker containing frozen cell pellet was cooled with ice. His column binding buffer was added to the cell pellet (5 x weight of frozen cells) followed 1mg of DNAse I and a protease inhibitor tablet (Roche). The beaker (in an ice box) was

placed on a stirrer plate and allowed to stir until cell pellets had sufficiently thawed. The resulting suspension was subjected to sonication using a 10 second on 10 second off pulse sequence for a total of 10 minutes. A Vibra Cell VCX 500 sonicator equipped with 13 mm probe was used for this purpose. The resulting suspension was centrifuged at 14,000 rpm for 20 minutes at 4 °C and the supernatant was collected, filtered using a 0.4 µM Omnipore™ filter (Millipore U.K.).

The filtered protein was then purified using an Amersham Pharmacia Biotech Äkta FPLC System (P920 pump system, IPC900 UV detector, Frac900 fraction collector and Unicorn Sotware) and 5 ml nickel affinity column (His-Trap®, Novagen). The His column was equilibrated with 10 CV of binding buffer and the filtered cell lysate was loaded onto the column using the FPLC pump. The loaded column was then washed with 5 CV of binding buffer. The column was then washed with 5-10 CV (until UV absorbance reached base line levels) of wash buffer. Wash flow-through was kept aside as high expression level of protein usually resulted in a saturated his-column. The bound protein was then eluted with 5CV's of elution buffer using the FPLC fraction collector. UV absorbing fractions were then analysed by SDS-PAGE. Fractions containing protein were then supplemented with EDTA (final concentration 1mM) and left overnight at 4°C. The next day the fractions were concentrated using Amicon® Ultra-4 Ultracel® PL filtration devices (Millipore) with 30 kDa molecular weight limit membranes and an Allegra™ 21R centrifuge (Beckman Coulter, S4180 rotor, 3500 rpm at 4°C). The resulting protein solutions were then buffer exchanged into Tris buffer using PD10 desalting columns (GE Healthcare) following the gravity protocol supplied by the manufacturer. On average 85 mg of protein per L of culture media was obtained from 12 flasks of media.

3.9.3.4 BFA labelling of psBBOX-Y201C

A psBBOX-Y201C solution was incubated at 5°C and buffer exchanged into PBS buffer. A fresh solution of 3-bromo-1,1,1-trifluoroacetone (BFA) was made up in PBS buffer (100mM). The BFA PBS solution was added to the psBBOX-Y201C solution to give a 12.5 : 1 ratio of BFA : Y201C. The resulting mixture was left at room temperature for 10 minutes before being buffer exchanged into Tris buffer using a PD-10 desalting column. The resulting protein in tris buffer was concentrated, aliquoted and frozen and stored at -80°C.

Buffers used during His-column purification:

Binding buffer: 50mM HEPES, pH 7.6, 0.5M NaCl, 5mM imidazole

Wash buffer: 50mM HEPES, pH 7.6, 0.5M NaCl, 30mM imidazole

Elution buffer: 50mM HEPES, pH 7.6, 0.5M NaCl, 500mM imidazole

Strip buffer: 50mM HEPES, pH 7.6, 0.5M NaCl, 100mM imidazole

Tris buffer: 50mM Tris, pH 7.5, 0.2M NaCl

3.9.3.5 Expression materials

2TY (2X Tryptone/Yeast) medium used for bacterial cell expression was made up of: 16g Bacto typtone, 10g Yeast extracts, 5g NaCl. Media was autoclaved at 121°C for 20 minutes before use. *E.coli* strain used: *BL21 (DE3)*: F^- *ompT hsdS*$_B$ ($r_B^- m_B^-$) *gal dcm* (DE3).

3.9.3.6 T_m Measurements on psBBOX

T_m shift measurements were carried out by Dr. Anna Rydzik. 10 µl of 250 µM stock (5×) of metal in 50 mM HEPES pH 7.5 was added to well (final conc 50 µM). Iron solution was prepared freshly before start of the experiment and used before color of solution changed to yellow (corresponding to oxidation of Fe(II) to Fe(III)). A control contained 10 µl of buffer instead of metal solution. 2 ml of master mix was prepared by mixing 1.25 ml stock of sypro orange (made by diluting 1 µl of sypro orange in 2.5 ml of 50 mM HEPES pH 7.5), 11 µl of

460 uM psBBOX (final conc 2 μM) and 739 μl of 50 mM HEPES pH 7.5. 40 μl of mix was added to wells, to get final volume of 50 μl. Experiment was carried out in triplicates.

DSF was performed using a MiniOpticon Real-Time PCR Detection System (Bio-Rad), monitoringprotein unfolding using SYPRO orange (Invitrogen) according to reported method. FAM (492 nm) and ROX (610 nm) filters were used for excitation and emission, respectively. Reaction mixes contained 2 μM protein, 50 μM metal and 1× SYPRO orange in a final volume of 50 μL. Reagents were prepared in 50 mM HEPES buffer pH 7.5. Iron solution was prepared shortly before experiment. Fluorescence readings were taken every 1 °C in the range 25–95 °C, with the temperature increased linearly by 1 °C per minute. The software provided was used to perform global minimum subtraction.

The inflection point, representing T_m, was calculated by fitting the Boltzmann equation to the sigmoidal curves obtained; data were processed using GraphPad Prism 5.0. The T_m shift caused by the addition of small molecules/fragments was determined by subtraction of the "reference" T_m (protein without metal) from the T_m obtained in the presence of the metal. Conditions were tested in triplicate, with standard deviations typically <1 °C.

3.10 References

1. C. Alves and R. V. Lima, Dietary supplement use by adolescents, *J. Pediatr. (Rio J)*, 2009, **85**, 287-294.
2. E. P. Brass, Supplemental carnitine and exercise, *Am. J. Clin. Nutr.*, 2000, **72**, 618s-623s.
3. P. L. Magoulas and A. W. El-Hattab, Systemic primary carnitine deficiency: an overview of clinical manifestations, diagnosis, and management, *Orphanet. J. Rare Dis.*, 2012, **7**, 68.
4. K. K. Witte and A. L. Clark, Micronutrients and their supplementation in chronic cardiac failure. An update beyond theoretical perspectives, *Heart Fail. Rev.*, 2006, **11**, 65-74.
5. R. Lango, R. T. Smolenski, M. Narkiewicz, J. Suchorzewska and W. Lysiak-Szydlowska, Influence of L-carnitine and its derivatives on myocardial metabolism and function in ischemic heart disease and during cardiopulmonary bypass, *Cardiovasc. Res.*, 2001, **51**, 21-29.
6. V. Bernal, A. Sevilla, M. Canovas and J. L. Iborra, Production of L-carnitine by secondary metabolism of bacteria, *Microb. Cell. Fact.*, 2007, **6**, 1-17.
7. P. Arense, V. Bernal, D. Charlier, J. L. Iborra, M. R. Foulquie-Moreno and M. Canovas, Metabolic engineering for high yielding L(-)-carnitine production in Escherichia coli, *Microb. Cell. Fact.*, 2013, **12**.
8. G. Lindstedt, Lindstedt, S., Midtvedt, T., Tofft, M., The Formation and Degradation of Carnitine in Pseudomonas*, *Biochemistry*, 1967, **6**, 1262-1270.
9. G. Lindstedt, S. Lindstedt and M. Tofft, Gamma-butyrobetaine hydroxylase from Pseudomonas sp AK 1, *Biochemistry*, 1970, **9**, 4336-4342.
10. G. Lindstedt, S. Lindstedt and I. Nordin, Purification and properties of gamma-butyrobetaine hydroxylase from Pseudomonas sp AK 1, *Biochemistry*, 1977, **16**, 2181-2188.
11. U. Ruetschi, I. Nordin, B. Odelhog, H. Jornvall and S. Lindstedt, gamma-Butyrobetaine hydroxylase. Structural characterization of the Pseudomonas enzyme, *Eur. J. Biochem.*, 1993, **213**, 1075-1080.
12. C. J. Rebouche and H. Seim, Carnitine metabolism and its regulation in microorganisms and mammals, *Annu. Rev. Nutr.*, 1998, **18**, 39-61.
13. H. P. Kleber, Bacterial carnitine metabolism, *FEMS Microbiol. Lett.*, 1997, **147**, 1-9.

14. H. Jung, K. Jung and H. P. Kleber, L-carnitine metabolization and osmotic stress response in Escherichia coli, *J. Basic Microbiol.*, 1990, **30**, 409-413.
15. R. K. Emaus and L. L. Bieber, A biosynthetic role for carnitine in the yeast Torulopsis bovina, *J. Biol. Chem.*, 1983, **258**, 13160-13165.
16. F. M. Vaz and R. J. Wanders, Carnitine biosynthesis in mammals, *Biochem. J.*, 2002, **361**, 417-429.
17. K. Strijbis, F. M. Vaz and B. Distel, Enzymology of the carnitine biosynthesis pathway, *IUBMB Life*, 2010, **62**, 357-362.
18. I. K. Leung, T. J. Krojer, G. T. Kochan, L. Henry, F. von Delft, T. D. Claridge, U. Oppermann, M. A. McDonough and C. J. Schofield, Structural and mechanistic studies on gamma-butyrobetaine hydroxylase, *Chem. Biol.*, 2010, **17**, 1316-1324.
19. A. M. Rydzik, I. K. Leung, G. T. Kochan, N. D. Loik, L. Henry, M. A. McDonough, T. D. Claridge and C. J. Schofield, Comparison of the substrate selectivity and biochemical properties of human and bacterial gamma-butyrobetaine hydroxylase, *Org. Biomol. Chem.*, 2014, **12**, 6354-6358.
20. K. Arnold, L. Bordoli, J. Kopp and T. Schwede, The SWISS-MODEL workspace: a web-based environment for protein structure homology modelling, *Bioinformatics*, 2006, **22**, 195-201.
21. F. Kiefer, K. Arnold, M. Kunzli, L. Bordoli and T. Schwede, The SWISS-MODEL Repository and associated resources, *Nucleic Acids Res.*, 2009, **37**, D387-392.
22. M. C. Peitsch and J. Tschopp, Comparative molecular modelling of the Fas-ligand and other members of the TNF family, *Mol. Immunol.*, 1995, **32**, 761-772.
23. E. Liepinsh, R. Vilskersts, D. Loca, O. Kirjanova, O. Pugovichs, I. Kalvinsh and M. Dambrova, Mildronate, an inhibitor of carnitine biosynthesis, induces an increase in gamma-butyrobetaine contents and cardioprotection in isolated rat heart infarction, *J. Cardiovasc. Pharmacol.*, 2006, **48**, 314-319.
24. E. Liepinsh, I. Konrade, E. Skapare, O. Pugovics, S. Grinberga, J. Kuka, I. Kalvinsh and M. Dambrova, Mildronate treatment alters gamma-butyrobetaine and l-carnitine concentrations in healthy volunteers, *J. Pharm. Pharmacol.*, 2011, **63**, 1195-1201.
25. A. M. Rydzik, I. K. Leung, G. T. Kochan, A. Thalhammer, U. Oppermann, T. D. Claridge and C. J. Schofield, Development and application of a fluoride-detection-based fluorescence assay for gamma-butyrobetaine hydroxylase, *Chem. Bio. Chem*, 2012, **13**, 1559-1563.

26. K. Tars, J. Rumnieks, A. Zeltins, A. Kazaks, S. Kotelovica, A. Leonciks, J. Sharipo, A. Viksna, J. Kuka, E. Liepinsh and M. Dambrova, Crystal structure of human gamma-butyrobetaine hydroxylase, *Biochem. Biophys. Res. Commun.*, 2010, **398**, 634-639.
27. C. Gorgens, S. Guddat, J. Dib, H. Geyer, W. Schanzer and M. Thevis, Mildronate (Meldonium) in professional sports - monitoring doping control urine samples using hydrophilic interaction liquid chromatography - high resolution/high accuracy mass spectrometry, *Drug. Test. Anal.*, 2015, **7**, 973-979.
28. H. K. Greenblatt and D. J. Greenblatt, Meldonium (Mildronate): A Performance-Enhancing Drug?, *Clin. Pharm. Drug Dev.*, 2016, **5**, 167-169.
29. V. Dzerve and M. I. S. Group, A dose-dependent improvement in exercise tolerance in patients with stable angina treated with mildronate: a clinical trial "MILSS I", *Medicina (Kaunas)*, 2011, **47**, 544-551.
30. L. Henry, I. K. Leung, T. D. Claridge and C. J. Schofield, gamma-Butyrobetaine hydroxylase catalyses a Stevens type rearrangement, *Bioorg. Med. Chem. Lett.*, 2012, **22**, 4975-4978.
31. E. Liepinsh, M. Makrecka, J. Kuka, H. Cirule, E. Makarova, E. Sevostjanovs, S. Grinberga, R. Vilskersts, D. Lola, E. Loza, I. Stonans, O. Pugovics and M. Dambrova, Selective inhibition of OCTN2 is more effective than inhibition of gamma-butyrobetaine dioxygenase to decrease the availability of l-carnitine and to reduce myocardial infarct size, *Pharmacol. Res.*, 2014, **85**, 33-38.
32. E. Liepinsh, M. Makrecka-Kuka, J. Kuka, R. Vilskersts, E. Makarova, H. Cirule, E. Loza, D. Lola, S. Grinberga, O. Pugovics, I. Kalvins and M. Dambrova, Inhibition of L-carnitine biosynthesis and transport by methyl-gamma-butyrobetaine decreases fatty acid oxidation and protects against myocardial infarction, *Br. J. Pharmacol.*, 2015, **172**, 1319-1332.
33. N. Longo, M. Frigeni and M. Pasquali, Carnitine transport and fatty acid oxidation, *Biochim. Biophys. Acta*, 2016, **1863**, 2422-2435.
34. K. Jaudzems, J. Kuka, A. Gutsaits, K. Zinovjevs, I. Kalvinsh, E. Liepinsh, E. Liepinsh and M. Dambrova, Inhibition of carnitine acetyltransferase by mildronate, a regulator of energy metabolism, *J. Enzyme Inhib. Med. Chem.*, 2009, **24**, 1269-1275.
35. D. L. Ziering and R. A. Pascal, Mechanism-Based Inhibition of Bacterial Gamma-Butyrobetaine Hydroxylase, *J. Am. Chem. Soc.*, 1990, **112**, 834-838.

36. R. C. Petter, S. Banerjee and S. Englard, Inhibition of Gamma-Butyrobetaine Hydroxylase by Cyclopropyl-Substituted Gamma-Butyrobetaines, *J. Org. Chem.*, 1990, **55**, 3088-3097.
37. K. Tars, J. Leitans, A. Kazaks, D. Zelencova, E. Liepinsh, J. Kuka, M. Makrecka, D. Lola, V. Andrianovs, D. Gustina, S. Grinberga, E. Liepinsh, I. Kalvinsh, M. Dambrova, E. Loza and O. Pugovics, Targeting Carnitine Biosynthesis: Discovery of New Inhibitors against gamma-Butyrobetaine Hydroxylase, *J. Med. Chem.*, 2014, **57**, 2213-2236.
38. S. F. Ng, H. M. Hanauskeabel and S. Englard, Cosubstrate Binding-Site of Pseudomonas Sp Ak1 Gamma-Butyrobetaine Hydroxylase - Interactions with Structural Analogs of Alpha-Ketoglutarate, *J. Biol. Chem.*, 1991, **266**, 1526-1533.
39. A. M. Rydzik, R. Chowdhury, G. T. Kochan, S. T. Williams, M. A. McDonough, A. Kawamura and C. J. Schofield, Modulating carnitine levels by targeting its biosynthesis pathway - selective inhibition of gamma-butyrobetaine hydroxylase, *Chem. Sci.*, 2014, **5**, 1765-1771.
40. K. Tars, J. Leitans, A. Kazaks, D. Zelencova, E. Liepinsh, J. Kuka, M. Makrecka, D. Lola, V. Andrianovs, D. Gustina, S. Grinberga, E. Liepinsh, I. Kalvinsh, M. Dambrova, E. Loza and O. Pugovics, Targeting carnitine biosynthesis: discovery of new inhibitors against gamma-butyrobetaine hydroxylase, *J. Med. Chem.*, 2014, **57**, 2213-2236.
41. A. Khan, R. K. Lesniak, J. Brem, A. M. Rydzik, H. Choi, I. K. H. Leung, M. A. McDonough, C. J. Schofield and T. D. W. Claridge, Development and application of ligand-based NMR screening assays for gamma-butyrobetaine hydroxylase, *Med. Chem. Comm*, 2016, **7**, 873-880.
42. C. Dalvit, Ligand- and substrate-based F-19 NMR screening: Principles and applications to drug discovery, *Prog. Nucl. Magn. Reson. Spectrosc.*, 2007, **51**, 243-I.
43. K. E. Arntson and W. C. Pomerantz, Protein-Observed Fluorine NMR: A Bioorthogonal Approach for Small Molecule Discovery, *J. Med. Chem.*, 2016, **59**, 5158-5171.
44. J. Ruiz-Cabello, B. P. Barnett, P. A. Bottomley and J. W. Bulte, Fluorine (19F) MRS and MRI in biomedicine, *NMR Biomed.*, 2011, **24**, 114-129.
45. E. T. Ahrens and J. Zhong, In vivo MRI cell tracking using perfluorocarbon probes and fluorine-19 detection, *NMR Biomed.*, 2013, **26**, 860-871.

46. A. M. Rydzik, J. Brem, S. S. van Berkel, I. Pfeffer, A. Makena, T. D. Claridge and C. J. Schofield, Monitoring conformational changes in the NDM-1 metallo-beta-lactamase by 19F NMR spectroscopy, *Angew. Chem. Int. Ed. Engl.*, 2014, **53**, 3129-3133.
47. A. K. Urick, L. M. L. Hawk, M. K. Cassel, N. K. Mishra, S. Liu, N. Adhikari, W. Zhang, C. O. dos Santos, J. L. Hall and W. C. K. Pomerantz, Dual Screening of BPTF and Brd4 Using Protein-Observed Fluorine NMR Uncovers New Bromodomain Probe Molecules, *ACS Chem. Biol.*, 2015, **10**, 2246-2256.
48. C. T. Gee, K. E. Arntson, A. K. Urick, N. K. Mishra, L. M. L. Hawk, A. J. Wisniewski and W. C. K. Pomerantz, Protein-observed F-19-NMR for fragment screening, affinity quantification and druggability assessment, *Nat. Protoc.*, 2016, **11**, 1414-1427.
49. J. L. Kitevski-LeBlanc and R. S. Prosser, Current applications of F-19 NMR to studies of protein structure and dynamics, *Prog. Nucl. Magn. Reson. Spectrosc.*, 2012, **62**, 1-33.
50. H. Chen, S. Viel, F. Ziarelli and L. Peng, F-19 NMR: a valuable tool for studying biological events, *Chem. Soc. Rev.*, 2013, **42**, 7971-7982.
51. J. T. Gerig, Fluorine NMR, 2001, DOI: http://www.biophysics.org/Portals/1/PDFs/Education/gerig.pdf.
52. C. Frieden, S. D. Hoeltzli and J. G. Bann, The preparation of F-19-labeled proteins for NMR studies, *Methods Enzymol.*, 2004, **380**, 400-415.
53. H. W. Kim, J. A. Perez, S. J. Ferguson and I. D. Campbell, The specific incorporation of labelled aromatic amino acids into proteins through growth of bacteria in the presence of glyphosate. Application to fluorotryptophan labelling to the H(+)-ATPase of Escherichia coli and NMR studies, *FEBS Lett.*, 1990, **272**, 34-36.
54. L. Wang, A. Brock, B. Herberich and P. G. Schultz, Expanding the genetic code of Escherichia coli, *Science*, 2001, **292**, 498-500.
55. T. H. Kim, K. Y. Chung, A. Manglik, A. L. Hansen, R. O. Dror, T. J. Mildorf, D. E. Shaw, B. K. Kobilka and R. S. Prosser, The Role of Ligands on the Equilibria Between Functional States of a G Protein-Coupled Receptor, *J. Am. Chem. Soc.*, 2013, **135**, 9465-9474.
56. S. Sechi and B. T. Chait, Modification of cysteine residues by alkylation. A tool in peptide mapping and protein identification, *Anal. Chem.*, 1998, **70**, 5150-5158.
57. A. D. Bain, Chemical exchange in NMR, *Prog. Nucl. Magn. Reson. Spectrosc.*, 2003, **43**, 63-103.

58. G. Lindstedt, Effect of metal ions on the hydroxylation of gamma-butyrobetaine to carnitine in rat liver homogenages, *Biochim. Biophys. Acta*, 1967, **141**, 492-498.
59. M. A. McDonough, C. Loenarz, R. Chowdhury, I. J. Clifton and C. J. Schofield, Structural studies on human 2-oxoglutarate dependent oxygenases, *Curr. Opin. Struct. Biol.*, 2010, **20**, 659-672.
60. J. J. Kamps, A. Khan, H. Choi, R. K. Lesniak, J. Brem, A. M. Rydzik, M. A. McDonough, C. J. Schofield, T. D. Claridge and J. Mecinovic, Cation-pi Interactions Contribute to Substrate Recognition in gamma-Butyrobetaine Hydroxylase Catalysis, *J. Eur. Chem.*, 2016, **22**, 1270-1276.
61. A. M. Rydzik, I. K. H. Leung, A. Thalhammer, G. T. Kochan, T. D. W. Claridge and C. J. Schofield, Fluoromethylated derivatives of carnitine biosynthesis intermediates - synthesis and applications, *Chem. Commun.*, 2014, **50**, 1175-1177.
62. A. M. Rydzik, Dphil, University of Oxford, 2014.
63. W. M. Bernhardt, M. S. Wiesener, P. Scigalla, J. Chou, R. E. Schmieder, V. Gunzler and K. U. Eckardt, Inhibition of Prolyl Hydroxylases Increases Erythropoietin Production in ESRD, *J. Am. Soc. Nephrol.*, 2010, **21**, 2151-2156.
64. C. Dalvit, P. Floersheim, M. Zurini and A. Widmer, Use of organic solvents and small molecules for locating binding sites on proteins in solution, *J. Biomol. NMR*, 1999, **14**, 23-32.

Chapter 4

Novel metallo-β-lactamase inhibitors

Contents

4.0 NOVEL METALLO-β-LACTAMASE INHIBITORS 173

4.1 INTRODUCTION 173

4.2 METALLO-β-LACTAMASE MEDIATED RESISTANCE 174

4.2 BBOX INHIBITORS: BROAD SPECTRUM MBL INHIBITORS? 176

4.3 *IN SILICO* VIM INHIBITOR DESIGN 179

4.4 DISCOVERY OF CAPTOPRIL ANALOGUES 180

4.4.1 Inhibition data for (15) and (16) 181

4.4.2 Crystallographic studies of (15) and (16) 183

4.4 CELLULAR SCREENING 184

4.5 SUMMARY AND FUTURE PERSPECTIVES 185

4.6 ACKNOWLEDGEMENTS 186

4.7 MATERIALS AND METHODS 186

4.7.1 Modelling of RL331 (3) 186

4.8 SYNTHESIS 187

Methyl ((S)-3-(acetylthio)-2-methylpropanoyl)-D-tryptophanate (13) 187

Methyl ((S)-3-(acetylthio)-2-methylpropanoyl)-L-tryptophanate (14) 188

((S)-3-Mercapto-2-methylpropanoyl)-D-tryptophan RL368 (15) 189

((S)-3-Mercapto-2-methylpropanoyl)-L-tryptophan RL369 (16) 190

4.8.1 Compounds from modeling 191

4-((1-Chloro-4-hydroxyisoquinoline-3-carboxamido)methyl)benzoic acid (6) 191

Methyl (4-((1-chloro-4-hydroxyisoquinoline-3-carboxamido)methyl)benzoyl)-D-tryptophanate (7) 192

(4-((1-Chloro-4-hydroxyisoquinoline-3-carboxamido)methyl)benzoyl)-D-tryptophan (3) 193

4.9 REFERENCES 194

4.0 Novel metallo-β-lactamase inhibitors

4.1 Introduction

Antibiotic resistance is a major worldwide concern with several million cases being reported annually of patients who are infected with antibiotic-resistant bacteria by the World Health Organisation (WHO) and the European Centre for Disease and Prevention and Control (ECDPC).[1,2] The clinically prevalent β-lactam containing antibiotics constitute a diverse family of compounds that are key to antimicrobial chemotherapy[3] (Figure 1). β-Lactam antibiotics function as pseudosubstrates for penicillin binding proteins (PBPs), preventing the ability of PBPs to produce cross-linked peptidoglycan polymers, leading to lysis of the bacterial cell wall.[3-6] β-Lactam mediated inhibition of PBPs is near irreversible[7] and is achieved through acylation,[6,8] following PBP mediated cleavage of the β-lactam ring.[9] Indeed, such is the global importance of β-lactam antibiotics that many are considered by the WHO as some of the most important medicines required by a basic health system

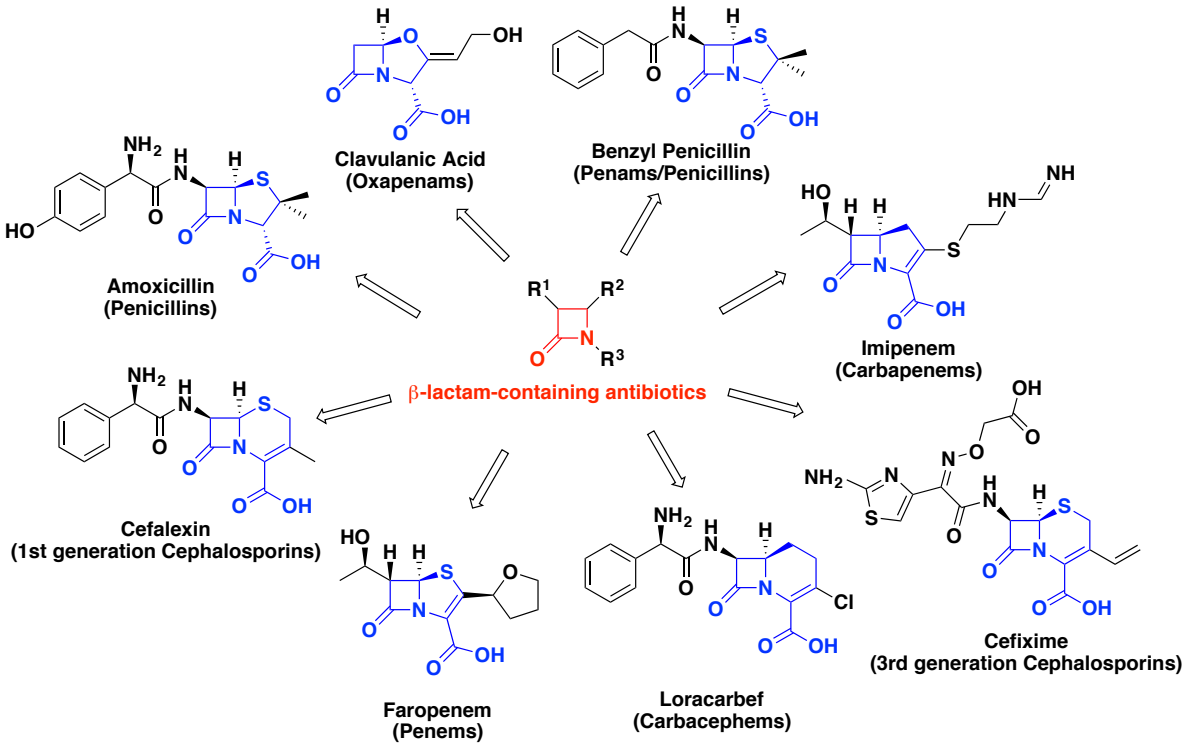


Figure 1 Chemical structures of relevant clinically used β-lactam antibiotics along with some of those listed by the World Health Organisation (WHO) as medications for a basic health system.

(Figure 1).[10]

Bacterial resistance to the most prevalent form of clinically used antibiotics (including β-lactam containing compounds), has manifested itself in three major ways: a reduction of drug permeability across the cell membrane, mutation of the PBP binding site and production of serine- and metallo-β-lactamases (SBLs and MBLs respectively). The work in this chapter concerns the zinc-dependent MBL family of enzymes.

4.2 Metallo-β-lactamase mediated resistance

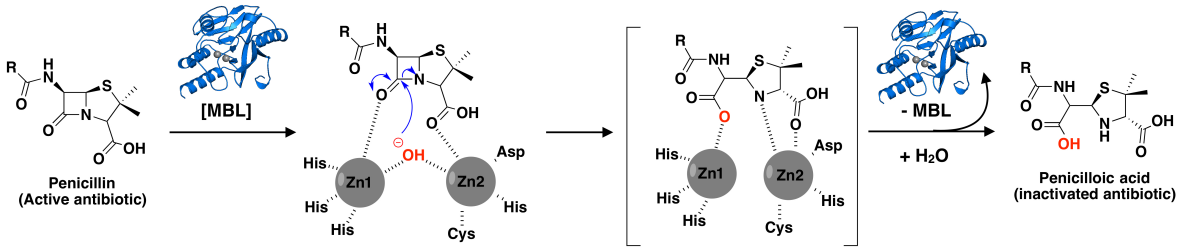


Figure 2 Outline mechanism of MBL-catalysed hydrolysis of a generic penicillin antibiotic. MBL mediated hydrolysis of the β-lactam inactivates β-lactam containing antibiotics towards PBP inhibition.

MBLs are capable of hydrolysing the amide bond of the four membered β-lactam ring, which is present in all β-lactam containing antibiotics (Figure 2).[11] MBLs have been known to the scientific community since their discovery in the 1960s.[12] The first MBL discovered was the metallo-β-lactamase from *Bacillus cereus*, BcII,[13] 20 years before the first clinical application of carbapenems,[14] which are known as the 'last resort' β-lactam containing antibiotics, often used against infections caused by multiresistant pathogens.[15] In the 1980s the importance of MBLs changed from biochemical phenomena to clinical threat when zinc(II)-dependent β-lactamases were discovered to be coded in multiple clinical strains of bacteria such as *Bacteroides fragilis*[16] and *Stenotrophomonas maltophilia*[17] and others.[14,18] Further cause for concern arose following the discovery of genes coding for MBLs in transferable plasmids in multiple Gram-negative pathogens.[15] *Via* horizontal gene transfer, MBL genetic material can be transferred between bacteria of the same species and between

different species.[19] It is through this way MBLs have become widespread amongst prevalent pathogens and now present a serious threat in the clinic.[14]

The largest and most clinically relevant MBL enzymes are members of the Impenemase (IMP), Verona integrin-encoded (VIM) and New Delhi (NDM) MBL families, which have spread across the globe creating a major health problem.[3,20] MBLs can be subdivided into the B1, B2 and B3 subclasses depending on sequence homology and coordination of zinc;[21-23] MBLs are known to bind two (B1 and B3), or less commonly one (B2), zinc ions in their active-sites.[24] Of the three subclasses of MBL, the B1 class binds two zinc ions in its active site and is the most clinically relevant.[20,25] Cause for concern over MBL mediated antibiotic resistance arises because: (1) clinically useful SBL inhibitors are available whereas no such compounds exist for MBLs, moreover MBLs can hydrolyse all clinically used SBL inhibitors, including avibactam; (2) MBLs have been shown to not only hydrolyse recent generation of carbapenems,[26] but nearly all β-lactam antibiotics, including those shown in Figure 1;[27] (3) the identification of DNA encoding for MBLs in transferable plasmids.[20]

No clinically useful MBL inhibitors are reported and almost all MBL inhibitors reported to-date work *via* active site metal chelation.[28,29] The lack of useful MBL inhibitors is understandable given, structural variations in the active-site loops of clinically related class B1 MBLs, including the Verona integrin-encoded MBL (VIM), Impenemase (IMP) and New Delhi MBL (NDM). Such variations mean developing potent and broad-spectrum inhibition across the B1 MBL subclass, which is likely required for a clinically useful MBL inhibitor, is challenging.[19,30,31] An additional challenge with designing broad-spectrum MBL inhibitors is selectivity for bacterial MBLs over structurally related human MBL-fold enzymes.[29] Regardless of the scientific challenge in achieving MBL inhibition, MBL

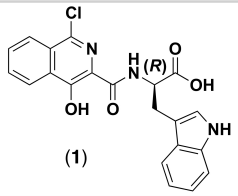
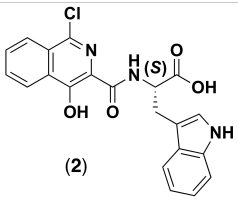
inhibitors have been described in the literature, including tirazoles,[32] carboxylic acids,[33] trifluoromethyl ketones,[34] and thiols[35] and recently cyclic boronates.[36]

4.2 BBOX inhibitors: broad spectrum MBL inhibitors?

The VIM MBL enzymes are probably the most widely distributed MBL family with more than 40 variants being reported.[37] The large number of VIM proteins likely reflects the rapid evolution of MBL variants; a constant challenge impairing successful MBL inhibitor generation.

The Schofield group has recently reported that multiple variants of the VIM family of MBLs are inhibited by the BBOX inhibitors (FG-D-Trp, (**1**)) and (FG-L-Trp, (**2**)) (Table 1).[19,37] Interestingly, although little variation in kinetic characteristics and protein folding was observed between the VIM variants, (**1**) and (**2**) displayed different inhibitory profiles. The (*R)*-stereoisomer of (**1**) is not only a more potent inhibitor of all the VIM variants examined (VIM-2, -4, -5 and -38) than its enantiomer (**2**), but also manifested apparent selectivity towards VIM variants 5 and 38. However, when compounds (**1**) and (**2**) were screened against other class B MBLs it was found that modest levels of inhibition could be obtained for IMP-1, NDM-1, VIM-2 and the B1/B2 São Paolo metallo-β-lactamase (SPM)-

Table 1 Comparing the inhibitory effects of BBOX inhibitors (**1**) and (**2**) against five different VIM protein variants.

	IC_{50} (μM)								
Inhibitor	VIM-1	VIM-2	VIM-4	VIM-5	VIM-38	Bc II	SPM-1	IMP-1	NDM-1
 (**1**)	>1000	90	200	2	2	132	47	74	47
 (**2**)	60	300	600	50	80	61	23	76	61

1. These observations suggest that derivatives of (**1**) and (**2**), may be able to act as broad-spectrum MBL inhibitors. In order to investigate how isoquinoline compounds bind to MBL proteins, crystallographic studies were undertaken, with the aim of obtaining structural data for (**1**) and (**2**) in complex with VIM-5. Given the ~25-fold difference in inhibition between (**1**) and (**2**) against VIM-5 (Table 1), different binding modes for the two compounds were envisaged.

A crystal structure of VIM-5 complexed with (**1**) (di-$Zn^{(II)}$:VIM-5:**1**) was obtained (Figure 3); analysis of the active site residues revealed that (**1**) binds to residues in the VIM-5 active site that are crucial for catalysis. Apparently tight electrostatic interactions were observed to occur between Arg228 and Thr229 and the carboxylate moiety of (**1**) along with hydrophobic π-π stacking interactions between the isoquinoline moiety of (**1**) and the Tyr67 sidechain (Figure 3). Notably, (**1**) did not bind in a manner involving $Zn^{(II)}$ chelation. This is interesting given the metal chelating binding mode of the isoquinoline pharmacophores with PHD2, and thus a metal binding mode was predicted for their interaction with BBOX (Chapter 3).

Unfortunately a crystal structure of VIM-5:**2** (di-$Zn^{(II)}$:VIM-5:**2**) could not be obtained; however, a crystal structure of (**2**) was obtained in complex with oxidised VIM-5 (oxidised at Cys221 and therefore only one zinc ion present) (Figure 3). Surprisingly, the crystal structure of (**2**) in complex with oxidised VIM-5 presented a very different binding mode to that of (**1**) (Figure 3). The (*S*)-stereochemistry of (**2**), apparently forces (**2**) further towards the active site opening, than in the case for (**1**). In order to predict the binding mode of (**2**) to di-$Zn^{(II)}$-VIM-5, an oxidised VIM-5:**1** crystal structure was obtained and compared with the di-$Zn^{(II)}$-VIM-5:**1** structure. Pleasingly, with oxidised VIM-5, (**1**) binds in a near identical position to its conformation found in the di-$Zn^{(II)}$-VIM-5 complex (Figure 3). Thus, although a di-$Zn^{(II)}$-VIM-5 structure in complex with (**2**) was not obtained a near-identical

orientation of ligands and residues can be assumed. The oxidised VIM-5:**2** structure identifies electrostatic interactions between the carboxylate of (**2**) and residues Arg228 and Asn233. Hydrophobic interactions occur between Tyr67 and with the indole ring of (**2**), in contrast to (**1**). In addition the isoquinoline of (**2**) is positioned to form hydrophobic interactions with Phe61.

The binding mode differences of (**1**), and (**2**), as observed in the VIM-5 complexes (Figure 3) provide an explanation for the difference in inhibition potencies for (**1**) and (**2**) (Table 1). To further investigate the absence of active site zinc chelation for (**1**) and (**2**), solution phase NMR spectroscopy was used to monitor binding of (**1**) and (**2**) to *apo*-VIM-5. *Apo*-VIM-5 was prepared *via* treatment of the di-$Zn^{(II)}$-VIM-5 complex with ethylenediaminetetraacetic acid (EDTA) to remove the active-site zinc ions. The inactivity of the *apo*-VIM-5 protein was confirmed by its failure to hydrolyse β-lactams such as meropenem, using ^{1}H NMR spectroscopy.

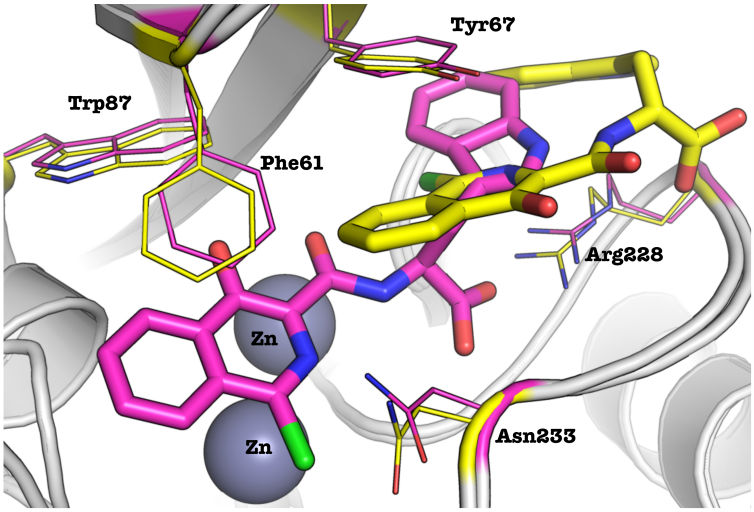


Figure 3 View from crystal structures of **(1)** (yellow sticks) overlaid with that of **(2)** (magenta sticks) bound to the active site of VIM-5. Inhibitors are not observed to chelate the active site Zn ions. Although different binding modes can be observed for the two inhibitors, little change is observed in the conformation of the active site residues.

4.3 *In silico* VIM inhibitor design

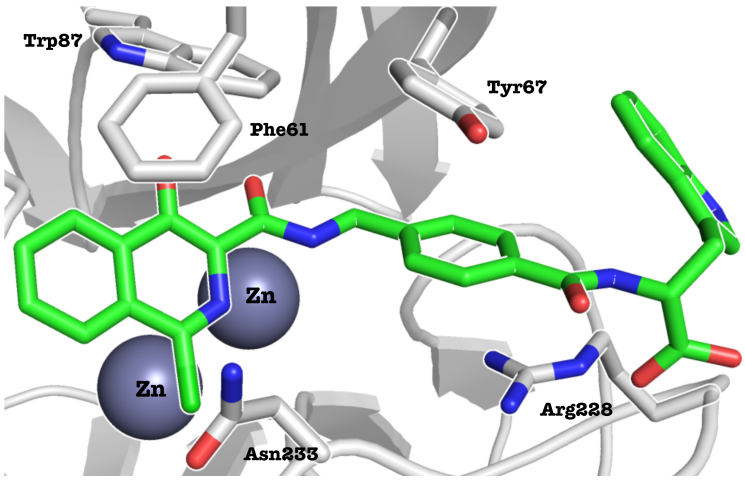
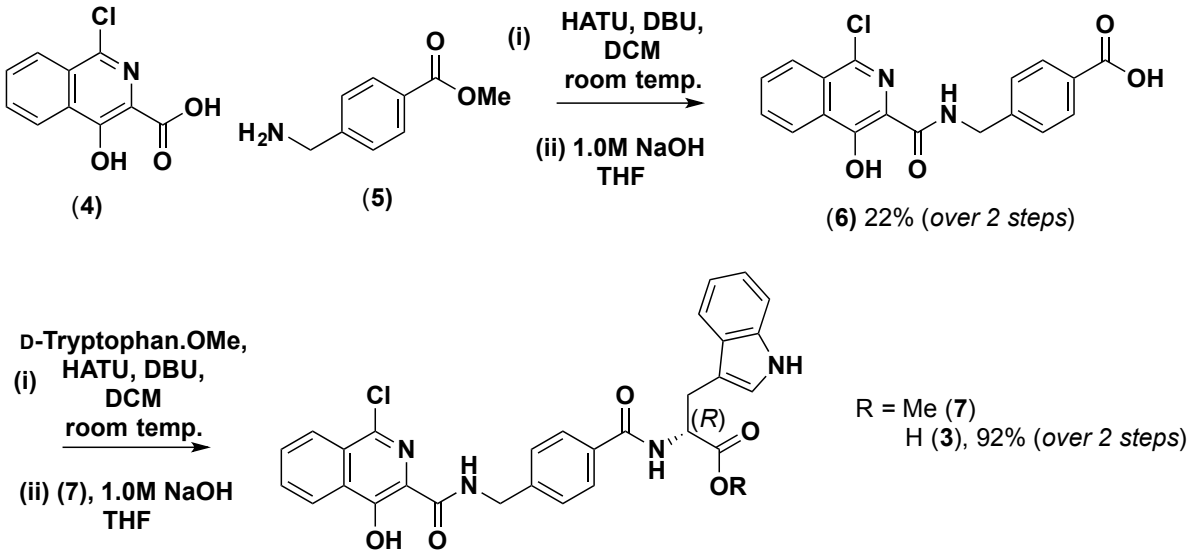


Figure 4 Predicted binding mode of RL331 (3, green sticks) with VIM-5 (grey cartoon). Key binding residues represented as grey sticks.

From the X-ray crystallographic studies of VIM-5 in complex with isoquinolines (**1**) or (**2**), (Figure 3) it was envisaged that an inhibitor may be able to occupy the same chemical space as (**1**) and (**2**) combined, as a means to improve inhibition. From molecular modelling experiements (Section 4.7.1) it was proposed that compound (**3**) (Scheme 1) may bind effectively (Figure 4). (**3**) maintains an isoquinoline positioned in a similar way to (**2**), which is linked to a D-try ptophan moiety positioned similar to that in (**1**) *via* a phenyl

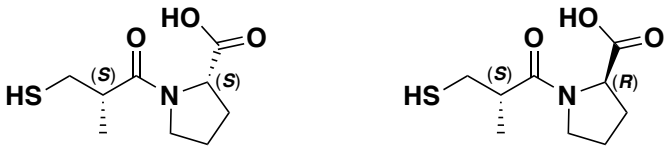


Scheme 1 Synthetic route used to obtain compound (**3**), which was designed *in silico* (Section 4.7.1) as a potential MBL inhibitor.

group linker (Scheme 1).

Synthesis of (**3**) began from the commercially available isoquinoline (**4**) and amine (**5**), which were coupled using 1-[bis(dimethylamino)methylene]-1*H*-1,2,3-triazolo[4,5-b]pyridinium 3-oxid hexafluorophosphate (HATU), and following hydroxide treatment gave carboxylic acid (**6**) (Scheme 1). (**6**) was subjected to amide coupling with D-tryptophan methyl ester to yield (**7**), which was hydrolysed using 1.0M NaOH to give (**3**) in 92% yield. Unfortunately (**3**) was found to be a relatively poor inhibitor of VIM-5 (IC_{50} = 41 μM), being only marginally better than (**2**) (IC_{50} = 50 μM), suggesting the binding modes of (**1**) and (**2**) may be overlapping and attempting to include binding interactions of both compounds into one molecule may be difficult.

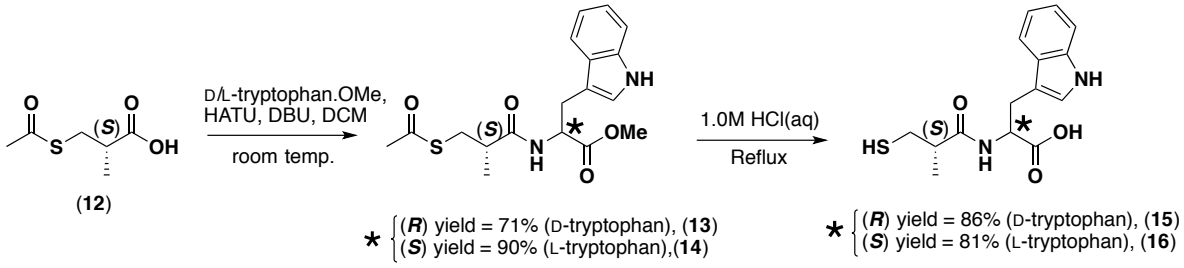
4.4 Discovery of Captopril analogues



L-captopril (**8**) D-captopril (**9**)

Figure 5 Structures of the ACE II inhibitor (2*S*,2*S*)-L-captopril (**8**) and stereoisomer (2*S*,2*R*)-D-captopril (**9**). Both inhibit multiple MBLs across all subclasses, with (**9**) being the more potent against most MBLs.[31, 40, 41]

L-Captopril (**8**) has been used since its discovery in the 1970s as a treatment for high blood pressure.[38,39] This is achieved *via* the ability of (**8**) to target the human angiotensin-converting enzyme (ACE) and bind to the active-site $Zn^{(II)}$ ion.[38] (**8**) has also been reported to inhibit multiple MBLs, also binding to the active site $Zn^{(II)}$ ions.[31,40,41] D-Captopril (**9**), *i.e.* the (2*S*,2*R*) stereoisomer of captopril, is reported as the more potent of the two isomers against most MBLs.[39,41,42] The zinc-chelating ability of (**8**) and (**9**) is in contrast to the non-requirement for active-site zinc chelation observed with the isoquinoline MBL inhibtors (**1**) and (**2**). However, similarly to (**1**) and (**2**), (**8**) and (**9**) binding involved the catalytically important Arg228 residue for both VIM-2 and VIM-5.[39] Moreover, the carboxylates of (**8**) and (**9**) are known to interact with Lys224 of IMP-1 and BcII (Lys224 is analogous to



Scheme 2 Synthetic strategy used to obtain captopril derivatives **15** and **16**.

Arg228 in VIM-2 and -5). β-Lactam antibiotics, in fact also utilise these carboxylate interactions. Thus, comp ounds RL368 (**15)** and RL369 (**16) (**Scheme 2**)** were designed in order to maintain the hydrophobic interactions displayed by (**1)** and (**2)** in the active-site, whilst additionally possessing a mercapto-propanal moiety present in D- and L-captopril enabling chelation to the active-site zinc.

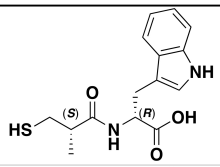
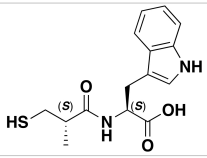
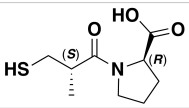
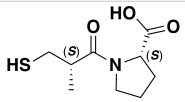
Hence, commercially available (*S*)-3-(acetylthio)-2-methylpropionic acid (**12)** was reacted *via* amide coupling with HATU with either D- or L-tryptophan methylesters to give (**13**) or (**14**), respectively (Scheme 2). Refluxing esters (**13**) or (**14**) in aqueous HCl removed the acetylthio- and methyl ester protecting groups in a one-pot process to yield thiols (**15**) and (**16**) in 86% and 81% yield, respectively.

4.4.1 Inhibition data for (15) and (16)

Compounds (**15**) and (**16**) were screened against class B1 MBLs using a fluorogenic assay developed for MBLs[19] to determine their inhibitory ability (Table 2). The clinically relevant class B1 enzymes screened were VIM-1, VIM-2, VIM-5, IMP-1, NDM-1 and SPM-1. To investigate the selectivity (**15**) and (**16**) for other class B MBLs, the class B2 MBL CphA[43] and class B3 enzyme L1[44] were also tested. For comparison, the known broad-spectrum MBL inhibtors L-captopril (**8**) and D-captopril (**9**) were also screened (Table 2).[19,31] The results reveal, both (**15**) and (**16**) as broad spectrum class B MBL inhibitors. Notably (**15**) showed increased activity with the class B3 MBL, L1, when compared to (**8**) and (**9**). Thiol

(**15**) displayed superior inhibition potency and was also more selective for class B1 MBLs, with sub-micromolar inhibition observed for most of the class B1 enzymes screened; (**15**) displayed strong inhibition with VIM-2 and IMP-1 (IC_{50} = 55 nM and 41 nM respectively) (Table 2). In contrast (**16**) did not show a significant improvement from L/D-captopril; compared to (**15**), (**16**) had a sub-micromolar inhibitory effect on only one of the class B MBLs screened, SPM-1.

Table 2 Comparing inhibition of the captoril diastereomers (**8**) and (**9**) with novel analogues (**15**) and (**16**).

		IC_{50} values (μM)								
No.	**Structure**	**Class B1**							**Class B2**	**Class B3**
		VIM-1	**VIM-2**	**VIM-5**	**NDM-1**	**SPM-1**	**BcII**	**IMP-1**	**CphA**	**L1**
RL368 (15)		0.526	0.055	0.175	24.8	0.890	1.63	0.041	~400	16.2
RL369 (16)		33.7	1.06	2.19	64.8	0.260	30.4	3.98	>400	97.3
D-captopril (9)		7.45	4.54	14.9	62.1	1.16	12.03	6.75	>400	67.08
L-captopril (8)		42.8	2.47	10.5	197	1.65	47.8	2.50	>400	73.7

4.4.2 Crystallographic studies of (15) and (16)

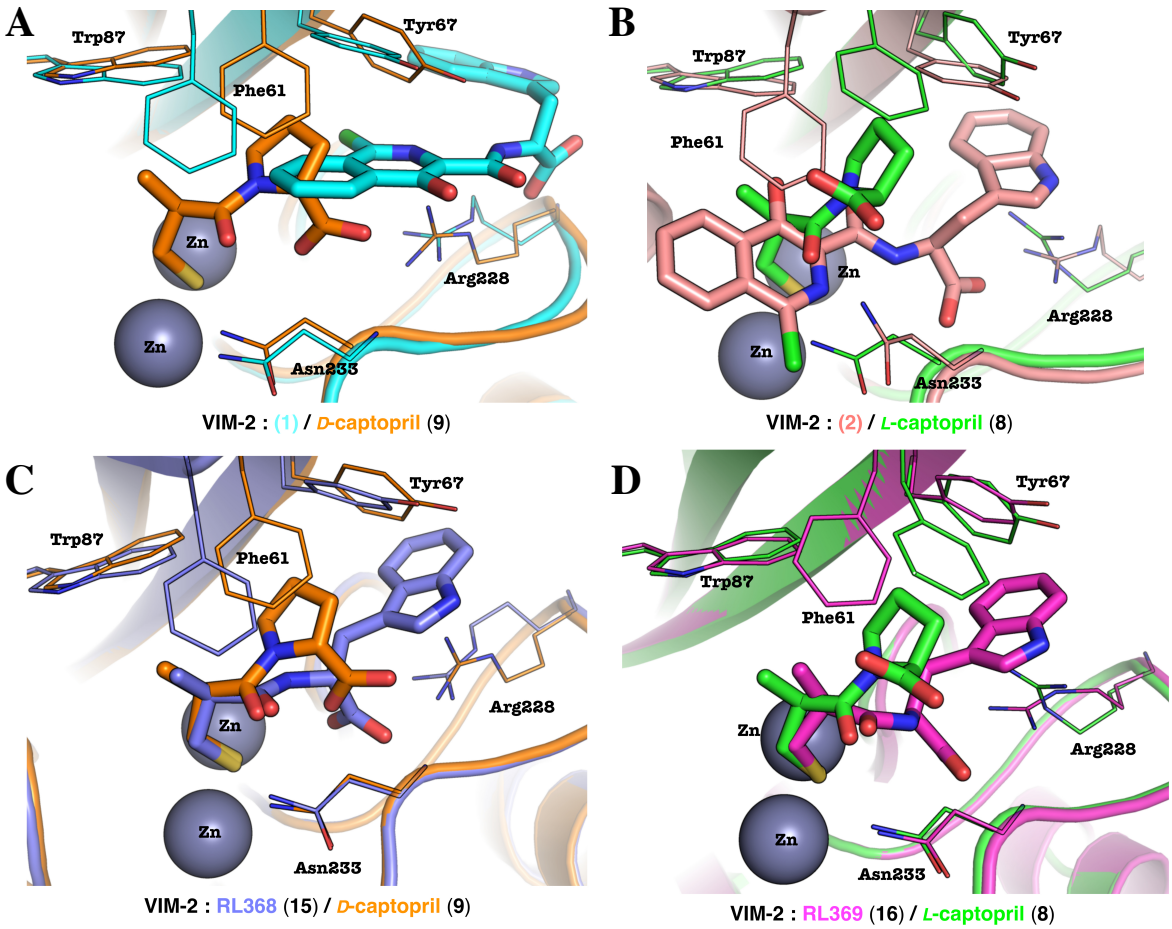


Figure 6 Views from overlaid crystal structures of **A**) (**1**) (cyan sticks) and (**9**) (orange sticks) with VIM-2, **B**) (**2**) (peach sticks) and (**8**) (green sticks) with VIM-2, **C**) (**15**) (lilac sticks) and (**9**) (orange sticks) with VIM-2, **D**) (**16**) (magenta sticks) and (**8**) (green sticks) with VIM-2. (1) and (2) do not chelate the active-site $Zn^{(II)}$ ions. All four compounds in (**C**) and (**D**) bind the two active-site zinc ions of VIM-2. Captopril isomers (**8**) and (**9**) in complex with VIM-2 generated from PDB id: 4C1E. (**15**) and (**16**) interact with aromatic residues in the active-site differently, compared to the captopril isomers (**8**) and (**9**).

X-ray crystal structures of (**15**) (Figure 6 (**C**)) and (**16**) (Figure 6 (**D**)) in complex with VIM-2 provided information on their binding modes. (**15**) and (**16**) bind in a similar mode to that observed for (**2**), (**8**) and (**9**); *i.e. via* electrostatic interactions with carboxylates of (**15**) and (**16**) and Arg228, hydrogen bonding between the carbonyl oxygen of the amide of (**15**), (**16**) and Asn233 and hydrophobic interactions between Tyr67 and the indole ring of (**15**) and (**16**) (Figure 6). Moreover, zinc chelation was observed for both (**15**) and (**16**). One key difference that can be seen from Figure 6 is that the D- and L-captopril induce a more significant change in the conformation of Phe61, which resides on the L3 loop of

VIM-2. This is most obvious from the VIM-2:L-captopril structure (Figure 6). Little overall difference is observed in the orientations of (**15**) and (**16**). Although one clear difference in the two binding modes is in the orientation of the amide; a *trans*-amide is observed with (**15**), and (**16**) adopts a less commonly observed *cis*-conformation (Figure 7). The energetically unfavourable *cis*-conformation of the amide of (**16**) may reflect its less potent inhibition compared to (**15**).

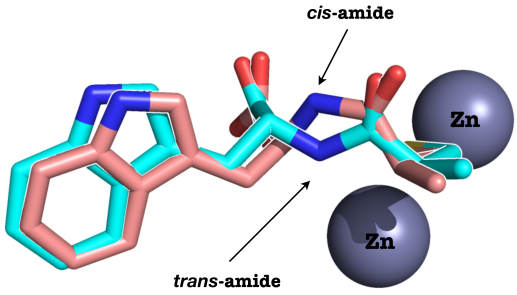


Figure 7 Overlay of the thiols (**15**) (cyan sticks) and (**16**) (peach sticks) bound to VIM-2. The reduced potency of inhibitor (**16**) compared to (**15**) may be a result of the unfavoured *cis*-amide conformation.

4.4 Cellular screening

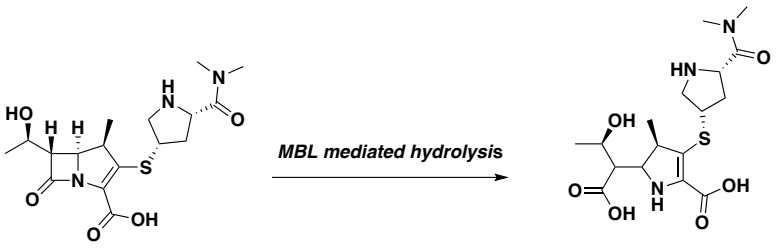
Table 3 Comparing the activity of (**15**) and (**16**) against clinically relevant bacterial cells expressing IMP-1 and VIM-1. A clinically relevant MIC of meropenem is classed as ≤ 1mg.L^{-1}.[39]

	Meropenem MIC (mg l-1)					
Compound (conc.)	*E.coli* +IMP-1	*E. aerogenes* + IMP-1	*K. pneumoniae* + IMP-1	*E.coli* +VIM-1	*E. aerogenes* +VIM-1	*K. pneumoniae* +VIM-1
DMSO	32	32	32	16	16	16
RL368 (10 mg/L)	32	16	8	8	8	16
RL368 (25 mg/L)	8	0.5	1	4	8	4
RL368 (50 mg/L)	0.5	0.5	0.125	0.25	0.5	0.5
RL369 (10 mg/L)	32	32	32	16	16	16
RL369 (25 mg/L)	32	16	8	16	16	16
RL369 (50 mg/L)	32	8	8	8	16	16

The ability of (**15**) and (**16**) to inhibit MBLs in cells was then assessed by testing them against multidrug-resistant strains expressing class B1 MBL proteins IMP-1 and VIM-1, using an antimicrobial susceptibility assay (Table 3). The activities of (**15**) and (**16**) were assessed against three Gram-negative pathogens of clinical origin, *Escherichia coli*,

Enterobacter aerogenes, and *Klebsiella pneumonia*. In this assay the *in vitro* activity of MBL inhibitors is measured by their capacity to potentiate the activity of meropenem (Figure 8) (a broad-spectrum, clinically used, β-lactam antibiotic of the carbapenem class)[45] in well-characterised and clinically derived bacterial strains.[31,39]

(**16**) showed little cellular activity compared to the DMSO standard, with some activity seen at 50 mg/L. Pleasingly, 50 mg/L of (**15**) provided a clinically sensitive MIC (≤ 1mg/L in this assay) of mereopenem, across all bacterial species (Table 3).



Meropenem (**17**) Hydrolysed Meropenem (**18**)

Figure 8 Chemical structure of the broad-spectrum β-lactam antibiotic Meropenem (**17**) and the resulting structure of the product of the reaction of (**18**) with an MBL protein

4.5 Summary and future perspectives

X-ray crystallographic data of (**1**) and (**2**) bound to VIM-5 revealed differences in the binding modes of the two diastereomers (Figure 6), identifying them as non-metal chelating inhibitors. Compounds (**1**) and (**2**) bind forming interactions with key residues on the L3 and L10 loops which are critical for catalysis (Figure 6). This mode appears sufficiently strong to outcompete (potentially) the metal chelating ability of the isoquinoline core as seen with 2OG-oxygenase enzyme systems. In support of this proposal, NMR experiments identified a non-requirement for zinc with respect to binding of isoquinolines (**1**) and (**2**) to VIM-5.

Potent MBL inhibitors chelating to the active site zinc ions have been reported;[39] including the captopril diastereomers (**8**) and (**9**). Hence, it was envisaged that thiols (**15**) and (**16**), may display potent inhibition of class B1 MBLs and so potentiate the activity of

meropenem, in Gram-negative pathogens producing MBLs. (**15**) and (**16**) were found to be potent inhibitors of the class B1 MBLs screened (Table 2). Following the resolution of X-ray crystal structures of (**15**) and (**16**) in complex with VIM-2 (Figure 6), it was possible to suggest a reason for the observed inhibition difference between the two compounds. It was observed that that (**16**) adopts a *cis*-conformation of its amide bond, whereas the amide of (**15**) adopts a *trans*-conformation. Currently there are no clinically used MBL inhibtors, and it is hoped that the efforts described in this chapter, will enable future drug discovery efforts in the field of β-lactam antibacterial resistance.

4.6 Acknowledgements

Dr. Jürgen Brem deserves huge thanks for providing compounds (**1**) and (**2**), discussions and advice. Modelling of (**3**), MBL fluorogenic inhibitory assays and X-ray crystallography were carried out by Dr. Guobo Li (Department of Chemistry, University of Oxford). *In vitro* cell-based screening of compounds (**15**) and (**16**) was carried out by Dr. Matthew Avison (School of Cellular & Molecular Medicine, University of Bristol).

4.7 Materials and methods

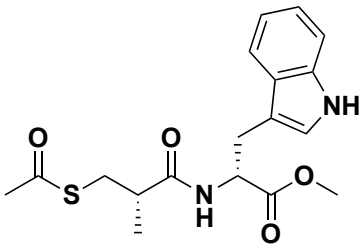
4.7.1 Modelling of RL331 (3)

Molecular docking experiments were carried out by Dr. Guo-Bo Li. From overlaying crystal structures of VIM-5:(**1**) and VIM-5:(**2**), it was envisioned a linker such as a phenyl, may connect the isoquinoline of (**1**) and tryptophan of (**2**). Thus compound RL331 (**3**), was designed. The binding of (**3**) was predicted using molecular docking simulations using the GOLD docking program. The di-zinc catalytic binding site was set as the docking site, and all the involved residues kept as rigid. The number of generated docking poses was set as 20. The scoring function is goldscore. Other parameters were set as default.

4.8 Synthesis

All general synthetic materials and methods are identical to those described in Chapter 2.

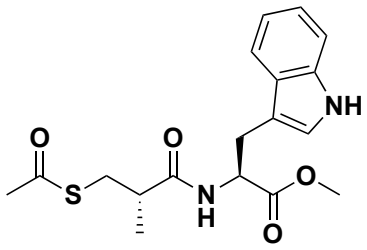
***Methyl ((S)-3-(acetylthio)-2-methylpropanoyl)-D-tryptophanate* (13)**



D-Tryptophan methylester hydrochloride (500 mg, 1.96 mmol) and 1-[bis(dimethylamino)methylene]-1H-1,2,3-triazolo[4,5-b]pyridinium-3-oxide hexafluorophosphate (HATU) (1.49 g, 3.92 mmol) were dissolved in CH_2Cl_2 (19.6 ml). To this solution (*S*)-3-(acetylthio)-2-methylpropionic acid (Chem-Impex)(0.33 ml, 2.36 mmol) was added followed by a dropwise addition of 1,8-diazabicyclo[5.4.0]undec-7-ene (DBU) (1.17 ml, 7.84 mmol). The mixture was stirred at room temperature, until complete conversion of the starting amine was observed by TLC (9:1, CH_2Cl_2/MeOH). The reaction mixture was evaporated to dryness before being purified by flash column chromatography (0 to 45% EtOAc in cyclohexane, over 10 column volumes (CVs)). Collection and evaporation of the appropriate fractions yielded (**13**) as an orange oil (504 mg, 1.39 mmol, 71%). **^{1}H NMR** ($CDCl_3$, 400 MHz) δ = 9.07 (1H, s, indole N*H*), 7.49 (1H, d, *J* = 8.0 Hz, *Ar*), 7.31 (1H, d, *J* = 8.0 Hz, *Ar*), 7.16 – 7.10 (1H, m, *Ar*), 7.09 – 7.02 (1H, m, *Ar*), 6.94 (1H, d, *J* = 2.5 Hz, *Ar*), 6.34 (1H, d, *J* = 8.0 Hz, -CON*H*), 4.90 (1H, dt, *J* = 8.0, 5.5 Hz, -NHC*H*CH_2-), 3.64 (3H, s, -OCH_3), 3.34 – 3.23 (2H, m, -NHCHCH_2-), 3.04 (1H, dd, *J* = 13.5, 7.5 Hz, -SC($H_A$$H_B$)CH-), 2.90 (1H, dd, *J* = 13.5, 6.0 Hz, -SC($H_A$$H_B$)CH-), 2.38 (1H, h, *J* = 6.5 Hz, -SCH_2C*H*-), 2.23 (3H, s, -SCOCH_3), 1.10 (3H, d, *J* = 7.0 Hz, -SCH_2CHCH_3) ppm. **^{13}C NMR** ($CDCl_3$, 101 MHz) δ = 196.0, 174.1, 172.3, 136.2, 127.5, 123.1, 121.9, 119.3, 118.4, 111.4, 109.4, 53.0, 52.3, 41.1, 32.3, 30.5, 27.5, 17.1 ppm. **FT-IR** ν_{max} (film)

3313, 1740, 1687, 1655, 1524, 1457, 1437, 1215, 744 cm^{-1}. $[\alpha]_D^{25}$ = -40.7° (c = 0.39 in MeOH). **HRMS** (ESI-TOF) calcd for $C_{18}H_{23}N_2O_4S$ $[M+H]^+$: 363.1373, found: 363.1376.

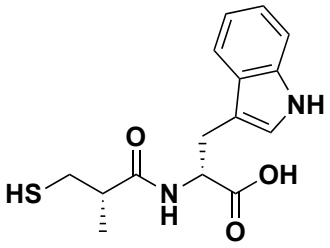
Methyl ((S)-3-(acetylthio)-2-methylpropanoyl)-L-tryptophanate (14)



L-Tryptophan methylester hydrochloride (250 mg, 0.98 mmol), HATU (745 mg, 1.96 mmol) and (*S*)-3-(acetylthio)-2-methylpropionic acid (Chem-Impex)(0.16 ml, 1.18 mmol) were dissolved in CH_2Cl_2 (10 ml). Following a dropwise addition of DBU (0.59 ml, 3.92 mmol), the mixture was stirred at room temperature until complete conversion was observed by TLC (9:1, CH_2Cl_2/MeOH). The mixture was then evaporated to dryness, then purified by flash column chromatography (0 to 50% EtOAc in cyclohexane over 10 CVs). The appropriate fractions were collected and dried to yield a orange/brown oil (320 mg, 0.88 mmol, 90%). **^{1}H NMR** ($CDCl_3$, 400 MHz) δ = 9.65 (1H, d, *J* = 2.5 Hz, indole N*H*), 7.53 (1H, d, *J* = 8.0 Hz, *Ar*), 7.31 (1H, d, *J* = 8.0 Hz, *Ar*), 7.15 – 7.08 (1H, m, *Ar*), 7.07 – 7.02 (1H, m, *Ar*), 7.01 (1H, d, *J* = 2.5 Hz, *Ar*), 6.63 (1H, d, *J* = 8.0 Hz, -CON*H*), 4.91 (1H, dt, *J* = 8.0, 6.0 Hz, -NHC*H*CH_2-), 3.60 (3H, s, -OCH_3), 3.28 (2H, d, *J* = 6.0 Hz, -NHCHCH_2-), 3.02 (1H, dd, *J* = 13.5, 8.0 Hz, -SC($H_A$$H_B$)CH-), 2.92 (1H, dd, *J* = 13.5, 6.0 Hz, -SC($H_A$$H_B$)CH-), 2.49 – 2.39 (1H, m, -SCH_2C*H*-), 2.23 (3H, s, -SCOCH_3), 1.13 (3H, d, *J* = 7.0 Hz, -SCH_2CHCH_3) ppm. **^{13}C NMR** ($CDCl_3$, 101 MHz) δ = 195.5, 174.1, 172.1, 136.2, 127.3, 123.1, 121.4, 118.9, 118.1, 111.3, 108.9, 52.7, 51.9, 40.8, 32.0, 30.2, 27.4, 17.1 ppm. **FT-IR** ν_{max} (film) 3305, 1740, 1656, 1519, 1382, 1251, 1149, 955, 743 cm^{-1}. $[\alpha]_D^{25}$ = -48.5° (c =

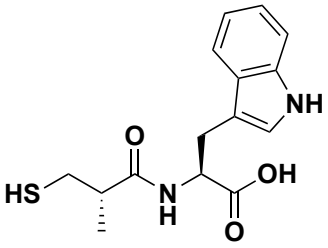
0.43 in MeOH). **HRMS** (ESI-TOF) calcd for $C_{18}H_{23}N_2O_4S$ $[M+H]^+$: 363.1373, found: 363.1375.

((S)-3-Mercapto-2-methylpropanoyl)-D-tryptophan RL368 (15)



Methyl ((*S*)-3-(acetylthio)-2-methylpropanoyl)-D-tryptophanate (**13**) (250 mg, 0.69 mmol) was dissolved in 1.0M aqueous HCl (2.7 ml) before the mixture was stirred at reflux overnight. The reaction mixture was allowed to cool to room temperature before being diluted with H_2O (10 ml). The mixture was then extracted with EtOAc (3 x 15 ml), after which all organic fractions were collected, dried over $MgSO_4$, filtered, concentrated, and purified by flash column chromatography (95:5, CH_2Cl_2 / (MeOH + 0.1% AcOH)). The appropriate fractions were collected and concentrated to give a slightly yellow, viscous oil (181mg, 0.59mmol, 86%). **^{1}H NMR** (CD_3OD, 400 MHz) δ = 7.57 (1H, dt, *J* = 8.0, 1.1 Hz, *Ar*), 7.32 (1H, dt, *J* = 8.0, 1.0 Hz, *Ar*), 7.11 – 7.05 (2H, m, 14, *Ar*), 7.03 – 6.98 (1H, m, *Ar*), 4.75 (1H, dd, *J* = 8.5, 5.0 Hz, -NHC*H*CH_2-), 3.37 (1H, ddd, *J* = 14.5, 5.0, 1.0 Hz, -NHCHC($H_A$$H_B$)-), 3.17 (1H, dd, *J* = 14.5, 8.5 Hz, -NHCHC($H_A$$H_B$)-), 2.68 (1H, dd, *J* = 13.0, 8.0 Hz, HSC($H_A$$H_B$)CH-), 2.52 – 2.43 (1H, m, HSCH_2C*H*-), 2.38 (1H, ddt, *J* = 13.0, 6.0, 1.3 Hz, HSC($H_A$$H_B$)CH-), 1.00 (3H, d, *J* = 7.0 Hz, HSCH_2CHCH_3) ppm. **^{13}C NMR** (CD_3OD, 101 MHz) δ = 177.4, 175.2, 138.0, 128.8, 124.3, 122.4, 119.7, 119.3, 112.2, 111.1, 54.5, 45.7, 28.5, 28.4, 17.3 ppm. **FT-IR** ν_{max} (film) 1680, 1578, 1518, 1454, 1348, 1288, 1202, 739 cm^{-1}. $[\alpha]_D^{25}$ = -30.0° (c = 0.13 in MeOH). **HRMS** (ESI-TOF) calcd for $C_{15}H_{18}N_2O_3NaS$ $[M+Na]^+$: 329.0930, found: 329.0925.

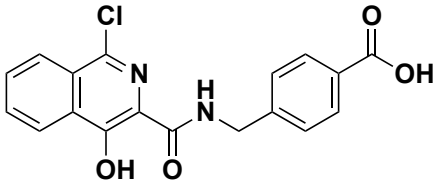
((S)-3-Mercapto-2-methylpropanoyl)-L-tryptophan RL369 (16)



Methyl ((*S*)-3-(acetylthio)-2-methylpropanoyl)-L-tryptophanate (**14**) (250 mg, 0.82 mmol) was dissolved in 1.0M aqueous HCl (2.7 ml) before the mixture was stirred at reflux overnight. The reaction mixture was diluted with H_2O (10 ml) and extracted with EtOAc (3 x 15 ml) before the organic layers were combined, dried over $MgSO_4$, filtered and concentrated before being purified by flash column chromatography (95:5, CH_2Cl_2/(MeOH+0.1% AcOH)). The appropriate fractions were collected and evaporated to yield a clear, slightly yellow oil (171 mg, 0.56 mmol, 81%). **^{1}H NMR** (CD_3OD, 400 MHz) δ = 7.60 (1H, dt, *J* = 8.0, 1.1 Hz, *Ar*), 7.31 (1H, dt, *J* = 8.0, 1.0 Hz, *Ar*), 7.14 (1H, s, *Ar*), 7.11 – 7.05 (1H, m, *Ar*), 7.03 – 6.98 (1H, m, *Ar*), 4.79 (1H, dd, *J* = 9.0, 5.0 Hz, -NHC*H*CH_2-), 3.37 (1H, ddd, *J* = 15.0, 5.0, 1.0 Hz, -NHCHC(H_AH_B)-), 3.17 (1H, ddd, *J* = 15.0, 9.0, 1.0 Hz, -NHCHC(H_AH_B)-), 2.33 (1H, ddt, *J* = 12.5, 5.0, 1.0 Hz, HSC(H_AH_B)CH-), 2.58 – 2.43 (2H, m, HSC(H_AH_B)CH-, $HSCH_2CH$-), 1.11 (3H, d, *J* = 6.5 Hz, $HSCH_2CHCH_3$) ppm. **^{13}C NMR** (CD_3OD, 101 MHz) δ = 177.3, 175.3, 138.0, 128.8, 124.5, 122.4, 119.8, 119.3, 112.2, 111.1, 54.3, 45.8, 28.6, 28.4, 17.5 ppm. **FT-IR** ν_{max} (film) 1694, 1587, 1520, 1487, 1385, 1346, 1165, 964, 943, 785, 741 cm^{-1}. $[\alpha]_D^{25}$ = -18.5° (c = 0.18 in MeOH). **HRMS** (ESI-TOF) calcd for $C_{15}H_{18}N_2O_3NaS$ $[M+Na]^+$: 329.0930, found: 329.0930.

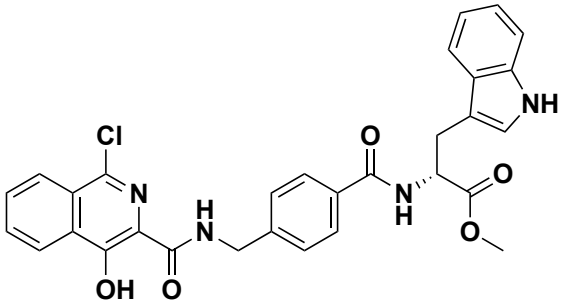
4.8.1 Compounds from modeling

***4-((1-Chloro-4-hydroxyisoquinoline-3-carboxamido)methyl)benzoic acid* (6)**



1-Chloro-4-hydroxyisoquinoline-3-carboxylic acid (**4**) (667 mg, 2.98 mmol), methyl-4-(aminomethyl)-benzoate hydrochloride (**5**) (500 mg, 2.48 mmol) and HATU (1.89 g, 4.96 mmol) were dissolved in CH_2Cl_2 (25 ml). DBU (1.85 ml, 12.40 mmol) was then added dropwise, after which the mixture was allowed to stir at room temperature until complete consumption of the starting amine (**5**) was observed by TLC (85:15, CH_2Cl_2/MeOH). The reaction mixture was passed through a pad of silica, eluting with cyclohexane/EtOAc (3:7). The filtrate was concentrated and dissolved in THF (6 ml) before 1.0M aqueous NaOH (1.2 ml) was added. The resulting mixture was stirred at room temperature overnight before the reaction was neutralized with 1.0M aqueous HCl. The resulting white precipitate was isolated using büchner filtration and washed with cold EtOAc, collected and dried *in vacuo* overnight to give a white amorphous solid (197mg, 0.55 mmol, 22% over two steps). **m.p.** 190-192°C. **^{1}H NMR** (DMSO-d_6, 400 MHz) δ = 9.70 (1H, s, -N*H*), 8.37 – 8.21 (2H, m, *Ar*), 8.01 – 7.95 (2H, m, *Ar*), 7.93 – 7.90 (2H, m, *Ar*), 7.48 (2H, d, *J* = 8.0 Hz, *Ar*), 4.61 (2H, d, *J* = 6.5 Hz, -NHC*H*$_2$-) ppm. **^{13}C NMR** (DMSO-d_6, 101 MHz) δ = 168.8, 167.2, 154.4, 143.9, 138.5, 131.7, 129.6, 129.5, 128.5, 127.5, 126.1, 126.0, 123.0, 120.7, 42.2 ppm. **FT-IR** ν_{max} (film) 3391, 3071, 2835, 1699, 1651, 1615, 1537, 1363, 1318, 1300, 765, 750, 625 cm^{-1}. **HRMS** (ESI-TOF) calcd for $C_{18}H_{13}ClN_2O_4$ $[M+H]^+$: 357.0637, found: 357.0640.

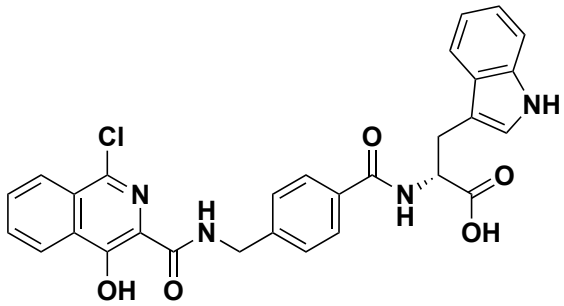
***Methyl (4-((1-chloro-4-hydroxyisoquinoline-3-carboxamido)methyl)benzoyl)-D-tryptophanate* (7)**



4-((1-Chloro-4-hydroxyisoquinoline-3-carboxamido)methyl)benzoic acid (**6**) (114 mg, 0.32 mmol), D-tryptophan methylester hydrochloride (82 mg, 0.32 mmol) and HATU (243 mg, 0.64 mmol) were dissolved in CH_2Cl_2 (3.2 ml). DBU (0.19 ml, 1.28 mmol) was added dropwise after which the resulting solution was stirred at room temperature until complete converstion of the starting amine was observed by TLC (90:10, CH_2Cl_2/MeOH). The mixture was then concentrated and purified by flash column chromatography (0 to 50% EtOAc in cyclohexane over 10 CVs). The appropriate fractions were collected and concentrated to give (**7**) as an orange oil (86.9 mg, 0.16 mmol, 49%). **^{1}H NMR** ($CDCl_3$, 400 MHz) δ = 13.10 (1H, s, -O*H*), 8.40 – 8.35 (2H, m, *Ar, indole*-N*H* 33), 8.26 – 8.16 (2H, m, *Ar*, -CON*H*CH_2-), 7.83 – 7.74 (2H, m, *Ar*), 7.64 (2H, d, *J* = 8.0 Hz, *Ar*), 7.53 (1H, d, *J* = 8.0 Hz, *Ar*), 7.32 (3H, dd, *J*=8.5, 2.5 Hz, *Ar*), 7.18 – 7.13 (1H, m, *Ar*), 7.10 – 7.03 (1H, m, *Ar*), 6.96 (1H, s, -C=C*H*NH-), 6.70 (1H, d, *J* = 7.5 Hz, -CON*H*CH-), 5.13 (1H, dt, *J* = 7.5, 5.0 Hz, -NHC*H*CH_2-), 4.65 (1H, d, *J* = 6.0 Hz, -NHCH_2-), 3.70 (2H, s, -OCH_3), 3.46 (1H, dd, *J* = 13.0, 5.5 Hz, -CHC(H_A,H_B)-), 3.41 (1H, dd, *J* = 15.0, 3.5 Hz, -CHC(H_A,H_B)-) ppm. **^{13}C NMR** ($CDCl_3$, 101 MHz) δ = 172.5, 169.0, 166.6, 155.0, 141.5, 139.6, 136.3, 133.3, 130.98, 130.94, 130.4, 129.5, 127.8, 127.7, 127.7, 126.5, 123.5, 123.0, 122.4, 120.7, 119.8, 118.7, 111.5, 110.0, 53.6, 52.6, 27.7, 14.3 ppm. **FT-IR** ν_{max} (film) 3383, 1738, 1640, 1535,

1354, 1319, 1219, 1010, 748 cm^{-1}. $[\alpha]_D^{25}$ = -55.3° (c = 0.85 in $CHCl_3$). **HRMS** (ESI-TOF) calcd for $C_{30}H_{26}ClN_4O_5$ $[M+H]^+$: 557.1586, found: 557.1585.

(4-((1-Chloro-4-hydroxyisoquinoline-3-carboxamido)methyl)benzoyl)-D-tryptophan (3)



Methyl (4- ((1 - chloro - 4 - hydroxyisoquinoline - 3 - carboxamido) methyl) benzoyl) - *D* - tryptophanate (**7**) (86.9 mg, 0.16 mmol) was dissolved in THF (2 ml) before 1.0M aqueous NaOH (0.47 ml) was added. The mixture was then stirred overnight at room temperature before being neutralized with 1.0M aqueous HCl. The resulting solution was extracted with EtOAc (3 x 5 ml) and the organic layers combined, dried over $MgSO_4$, filtered and concentrated before being purified by flash column chromatography (95:5, CH_2Cl_2/MeOH +0.1% AcOH)) to give the desired compound (79.5 mg, 0.15 mmol, 92%). **^{1}H NMR** (CD_3OD, 400 MHz) δ = 9.01 (1H, s, -CON*H*CH_2-), 8.18 – 8.12 (1H, m, *Ar*), 8.09 – 8.04 (1H, m, *Ar*), 7.70 (2H, p, *J* = 3.5 Hz, *Ar*), 7.64 – 7.60 (2H, m, *Ar*), 7.57 (1H, dt, *J* = 8.0, 0.9 Hz, *Ar*), 7.32 (2H, dt, *J* = 8.0, 2.0 Hz, *Ar*), 7.30 – 7.26 (1H, m, *Ar*), 7.10 (1H, s, -C=C*H*NH-), 7.03 (1H, ddd, *J* = 8.0, 7.0, 1.0 Hz, *Ar*), 6.95 (1H, ddd, *J* = 8.0, 7.0, 1.0 Hz, *Ar*), 4.95 – 4.91 (10H, m, -CON*H*CH-), 4.54 (2H, s, -NHCH_2-), 3.47 (1H, dd, *J* = 14.7, 5.0 Hz, -CHC(H_A,H_B)-), 3.36 – 3.26 (1H, m, -CHC(H_A,H_B)-) ppm. **^{13}C NMR** (CD_3OD, 101 MHz) δ = 175.3, 175.2, 170.3, 169.7, 155.5, 143.7, 140.3, 138.0, 134.1, 132.0, 131.0, 130.2, 128.8, 128.6, 128.5, 127.1, 124.4, 124.0, 122.4, 119.9, 119.2, 112.3, 111.1, 43.3, 28.3, 20.7 ppm. **FT-IR** ν_{max} (film) 1719, 1620, 1483, 1437, 1319, 969, 744 cm^{-1}. $[\alpha]_D^{25}$ = +25.7° (c = 0.98 in MeOH). **HRMS** (ESI-TOF) calcd for $C_{29}H_{24}ClN_4O_5$ $[M+H]^+$: 543.1430, found: 543.1428.

4.9 References

1. T. U. Berendonk, C. M. Manaia, C. Merlin, D. Fatta-Kassinos, E. Cytryn, F. Walsh, H. Burgmann, H. Sorum, M. Norstrom, M. N. Pons, N. Kreuzinger, P. Huovinen, S. Stefani, T. Schwartz, V. Kisand, F. Baquero and J. L. Martinez, Tackling antibiotic resistance: the environmental framework, *Nat. Rev. Microbiol.*, 2015, **13**, 310-317.
2. The antibiotic alarm, *Nature*, 2013, **495**, 141.
3. A. I. Karsisiotis, C. F. Damblon and G. C. Roberts, A variety of roles for versatile zinc in metallo-beta-lactamases, *Metallomics*, 2014, **6**, 1181-1197.
4. G. R. Donowitz and G. L. Mandell, Drug therapy. Beta-lactam antibiotics (2), *N. Engl. J. Med.*, 1988, **318**, 490-500.
5. E. M. Wise, Jr. and J. T. Park, Penicillin: its basic site of action as an inhibitor of a peptide cross-linking reaction in cell wall mucopeptide synthesis, *Proc. Natl. Acad. Sci. U. S. A.*, 1965, **54**, 75-81.
6. D. J. Tipper and J. L. Strominger, Mechanism of action of penicillins: a proposal based on their structural similarity to acyl-D-alanyl-D-alanine, *Proc. Natl. Acad. Sci. U. S. A.*, 1965, **54**, 1133-1141.
7. P. D. Cooper, Site of action of radiopenicillin, *Bacteriol. Rev.*, 1956, **20**, 28-48.
8. P. M. Blumberg and J. L. Strominger, Interaction of penicillin with the bacterial cell: penicillin-binding proteins and penicillin-sensitive enzymes, *Bacteriol. Rev.*, 1974, **38**, 291-335.
9. B. G. Spratt, Properties of the penicillin-binding proteins of Escherichia coli K12, *Eur. J. Biochem.*, 1977, **72**, 341-352.
10. W. H. Organization, WHO Model List of Essential Medicines, 2015.
11. M. S. Helfand and R. A. Bonomo, Beta-lactamases: a survey of protein diversity, *Curr. Drug Targets Infect. Disord.*, 2003, **3**, 9-23.
12. L. D. Sabath and E. P. Abraham, Zinc as a cofactor for cephalosporinase from Bacillus cereus 569, *Biochem. J.*, 1966, **98**, 11C-13C.
13. L. D. Sabath and E. P. Abraham, Zinc as a Cofactor for Cephalosporinase from Bacillus Cereus 569, *Biochem. J.*, 1966, **98**, C11-&.
14. M. R. Meini, L. I. Llarrull and A. J. Vila, Overcoming differences: The catalytic mechanism of metallo-beta-lactamases, *FEBS Lett.*, 2015, **589**, 3419-3432.

15. T. R. Walsh, M. A. Toleman, L. Poirel and P. Nordmann, Metallo-beta-lactamases: the quiet before the storm?, *Clin. Microbiol. Rev.*, 2005, **18**, 306-+.
16. G. J. Cuchural, M. H. Malamy and F. P. Tally, Beta-Lactamase-Mediated Imipenem Resistance in Bacteroides-Fragilis, *Antimicrob. Agents Chemother.*, 1986, **30**, 645-648.
17. T. R. Walsh, L. Hall, S. J. Assinder, W. W. Nichols, S. J. Cartwright, A. P. Macgowan and P. M. Bennett, Sequence-Analysis of the L1 Metallo-Beta-Lactamase from Xanthomonas-Maltophilia, *BBA-Gene Struct. Expr.*, 1994, **1218**, 199-201.
18. K. Shannon, A. King and I. Phillips, Beta-Lactamases with High-Activity against Imipenem and Sch 34343 from Aeromonas-Hydrophila, *J. Antimicrob. Chemother.*, 1986, **17**, 45-50.
19. S. S. van Berkel, J. Brem, A. M. Rydzik, R. Salimraj, R. Cain, A. Verma, R. J. Owens, C. W. Fishwick, J. Spencer and C. J. Schofield, Assay platform for clinically relevant metallo-beta-lactamases, *J. Med. Chem.*, 2013, **56**, 6945-6953.
20. G. Cornaglia, H. Giamarellou and G. M. Rossolini, Metallo-beta-lactamases: a last frontier for beta-lactams?, *Lancet Infect. Dis.*, 2011, **11**, 381-393.
21. C. Bebrone, Metallo-beta-lactamases (classification, activity, genetic organization, structure, zinc coordination) and their superfamily, *Biochem. Pharmacol.*, 2007, **74**, 1686-1701.
22. M. Widmann, J. Pleiss and P. Oelschlaeger, Systematic analysis of metallo-beta-lactamases using an automated database, *Antimicrob. Agents Chemother.*, 2012, **56**, 3481-3491.
23. M. Galleni, J. Lamotte-Brasseur, G. M. Rossolini, J. Spencer, O. Dideberg, J. M. Frere and G. Metallo-beta-lactamases Working, Standard numbering scheme for class B beta-lactamases, *Antimicrob. Agents Chemother.*, 2001, **45**, 660-663.
24. K. Bush and G. A. Jacoby, Updated functional classification of beta-lactamases, *Antimicrob. Agents Chemother.*, 2010, **54**, 969-976.
25. M. F. Mojica, R. A. Bonomo and W. Fast, B1-Metallo-beta-Lactamases: Where Do We Stand?, *Curr. Drug Targets.*, 2016, **17**, 1029-1050.
26. T. R. Walsh, Emerging carbapenemases: a global perspective, *Int. J. Antimicrob. Agents*, 2010, **36**, S8-14.
27. D. T. King and N. C. J. Strynadka, Targeting metallo-beta-lactamase enzymes in antibiotic resistance, *Future Med. Chem.*, 2013, **5**, 1243-1263.

28. S. M. Drawz and R. A. Bonomo, Three Decades of beta-Lactamase Inhibitors, *Clin. Microbiol. Rev.*, 2010, **23**, 160-+.
29. J. Brem, S. S. van Berkel, W. Aik, A. M. Rydzik, M. B. Avison, I. Pettinati, K. D. Umland, A. Kawamura, J. Spencer, T. D. Claridge, M. A. McDonough and C. J. Schofield, Rhodanine hydrolysis leads to potent thioenolate mediated metallo-beta-lactamase inhibition, *Nat. Chem.*, 2014, **6**, 1084-1090.
30. J. F. Wang and K. C. Chou, Metallo-beta-Lactamases: Structural Features, Antibiotic Recognition, Inhibition, and Inhibitor Design, *Curr. Top. Med. Chem.*, 2013, **13**, 1242-1253.
31. J. Brem, S. S. van Berkel, D. Zollman, S. Y. Lee, O. Gileadi, P. J. McHugh, T. R. Walsh, M. A. McDonough and C. J. Schofield, Structural Basis of Metallo-beta-Lactamase Inhibition by Captopril Stereoisomers, *Antimicrob. Agents Chemother.*, 2016, **60**, 142-150.
32. T. Weide, S. A. Saldanha, D. Minond, T. P. Spicer, J. R. Fotsing, M. Spaargaren, J. M. Frere, C. Bebrone, K. B. Sharpless, P. S. Hodder and V. V. Fokin, NH-1,2,3-Triazole-based Inhibitors of the VIM-2 Metallo-beta-Lactamase: Synthesis and Structure-Activity Studies, *ACS Med. Chem. Lett.*, 2010, **1**, 150-154.
33. P. Chen, L. B. Horton, R. L. Mikulski, L. Deng, S. Sundriyal, T. Palzkill and Y. Song, 2-Substituted 4,5-dihydrothiazole-4-carboxylic acids are novel inhibitors of metallo-beta-lactamases, *Bioorg. Med. Chem. Lett.*, 2012, **22**, 6229-6232.
34. M. W. Walter, A. Felici, M. Galleni, R. P. Soto, R. M. Adlington, J. E. Baldwin, J. M. Frere, M. Gololobov and C. J. Schofield, Trifluoromethyl alcohol and ketone inhibitors of metallo-beta-lactamases, *Bioorg. Med. Chem. Lett.*, 1996, **6**, 2455-2458.
35. B. M. Lienard, G. Garau, L. Horsfall, A. I. Karsisiotis, C. Damblon, P. Lassaux, C. Papamicael, G. C. Roberts, M. Galleni, O. Dideberg, J. M. Frere and C. J. Schofield, Structural basis for the broad-spectrum inhibition of metallo-beta-lactamases by thiols, *Org. Biomol. Chem.*, 2008, **6**, 2282-2294.
36. J. Brem, R. Cain, S. Cahill, M. A. McDonough, I. J. Clifton, J. C. Jimenez-Castellanos, M. B. Avison, J. Spencer, C. W. G. Fishwick and C. J. Schofield, Structural basis of metallo-beta-lactamase, serine-beta-lactamase and penicillin-binding protein inhibition by cyclic boronates, *Nat. Commun.*, 2016, **7**.
37. A. Makena, A. O. Duzgun, J. Brem, M. A. McDonough, A. M. Rydzik, M. I. Abboud, A. Saral, A. C. Cicek, C. Sandalli and C. J. Schofield, Comparison of Verona Integron-

Borne Metallo-beta-Lactamase (VIM) Variants Reveals Differences in Stability and Inhibition Profiles, *Antimicrob. Agents Chemother.*, 2016, **60**, 1377-1384.

38. J. A. Day and S. M. Cohen, Investigating the Selectivity of Metalloenzyme Inhibitors, *J. Med. Chem.*, 2013, **56**, 7997-8007.
39. J. Brem, S. S. van Berkel, D. Zollman, S. Y. Lee, O. Gileadi, P. J. McHugh, T. R. Walsh, M. A. McDonough and C. J. Schofield, Structural Basis of Metallo-beta-Lactamase Inhibition by Captopril Stereoisomers, *Antimicrob. Agents Chemother.*, 2015, **60**, 142-150.
40. B. M. R. Lienard, G. Garau, L. Horsfall, A. I. Karsisiotis, C. Damblon, P. Lassaux, C. Papamicael, G. C. K. Roberts, M. Galleni, O. Dideberg, J. M. Frere and C. J. Schofield, Structural basis for the broad-spectrum inhibition of metallo-beta-lactamases by thiols, *Org. Biomol. Chem.*, 2008, **6**, 2282-2294.
41. U. Heinz, R. Bauer, S. Wommer, W. Meyer-Klaucke, C. Papamichaels, J. Bateson and H. W. Adolph, Coordination geometries of metal ions in D- or L-captopril-inhibited metallo-beta-lactamases, *J. Biol. Chem.*, 2003, **278**, 20659-20666.
42. A. M. Rydzik, J. Brem, S. S. van Berkel, I. Pfeffer, A. Makena, T. D. Claridge and C. J. Schofield, Monitoring conformational changes in the NDM-1 metallo-beta-lactamase by 19F NMR spectroscopy, *Angew. Chem. Int. Ed. Engl.*, 2014, **53**, 3129-3133.
43. C. Bebrone, H. Delbruck, M. B. Kupper, P. Schlomer, C. Willmann, J. M. Frere, R. Fischer, M. Galleni and K. M. Hoffmann, The structure of the dizinc subclass B2 metallo-beta-lactamase CphA reveals that the second inhibitory zinc ion binds in the histidine site, *Antimicrob. Agents Chemother.*, 2009, **53**, 4464-4471.
44. T. R. Walsh, L. Hall, S. J. Assinder, W. W. Nichols, S. J. Cartwright, A. P. MacGowan and P. M. Bennett, Sequence analysis of the L1 metallo-beta-lactamase from Xanthomonas maltophilia, *Biochim. Biophys. Acta*, 1994, **1218**, 199-201.
45. J. R. Edwards, P. J. Turner, C. Wannop, E. S. Withnell, A. J. Grindey and K. Nairn, In vitro antibacterial activity of SM-7338, a carbapenem antibiotic with stability to dehydropeptidase I, *Antimicrob. Agents Chemother.*, 1989, **33**, 215-222.

Chapter 5

Design of a multi-functional chemical probe for PHD2

Contents

5.0 DESIGN OF A MULTI-FUNCTIONAL CHEMICAL PROBE FOR PHD2 201

5.1 INTRODUCTION – PHD2 201

5.2 COVALENT CAPTURE OF PHD2 203

5.2.1 Previous work on covalent inhibitors of PHD2 204

5.2.2 Design and synthesis of RL409 (18) 207

5.3 CONJUGATION OF PHD2 WITH RL409 (18) 210

5.3.1 Initial experiments 210

5.3.2 Photo-activation of PHD2-(18) 211

5.4 SUMMARY AND FUTURE PERSPECTIVES 212

5.5 ACKNOWLEDGEMENTS 214

5.6 SYNTHESIS 214

5-Bromo-2-hydroxy-3-nitrobenzoic acid (11)[42] 214

5-Azido-2-hydroxy-3-nitrobenzoic acid (16) 215

Ethyl (5-azido-2-hydroxy-3-nitrobenzoyl)glycinate (13) 215

(5-Azido-2-hydroxy-3-nitrobenzoyl)glycine (17) 216

(3-Acrylamido-5-azido-2-hydroxybenzoyl)glycine (18) 217

Methyl (3-acrylamido-5-azido-2-hydroxybenzoyl)glycinate (19) 218

5.7 REFERENCES 219

5.0 Design of a multi-functional chemical probe for PHD2

5.1 Introduction – PHD2

In animals, adaptations to changes in oxygen concentrations are mediated at the cellular level by the α-subunit of the αβ-heterodimeric hypoxia-inducible factors (HIFs).[1] The HIFs enable regulation of the transcription in response to changes in oxygen levels.[2,3] Although the HIF-α subunit is transcribed and translated constantly under regular oxygen levels (normoxia),[4] its degradation is efficient. HIF-α degradation is promoted by the hydroxylation of prolyl residues in the *N*- and *C*-terminal oxygen dependent degradation domains (NODD and CODD) (Figure 1). The prolyl hydroxylase domain containing enzymes 1, 2 and 3 (PHD1, 2 and 3) are members of the $Fe^{(II)}$ and 2OG dependent oxygenase family and catalyse *trans*-4-prolyl hydroxylations on both CODD and NODD (Figure 1),[5-8] resulting in binding of both to the von Hippel-Landau tumor suppressor. In turn this signals for ubiquitination and degradation of HIF-α via the proteasomal pathway.[9-11] Under low oxygen conditions (hypoxia) HIF-α degradation is slowed as a result of reduced PHD2 activity (Figure 1). HIF-α dimerises with HIF-β, following translocation into the nucleus. The resulting dimeric HIF complex activates gene arrays involved in the

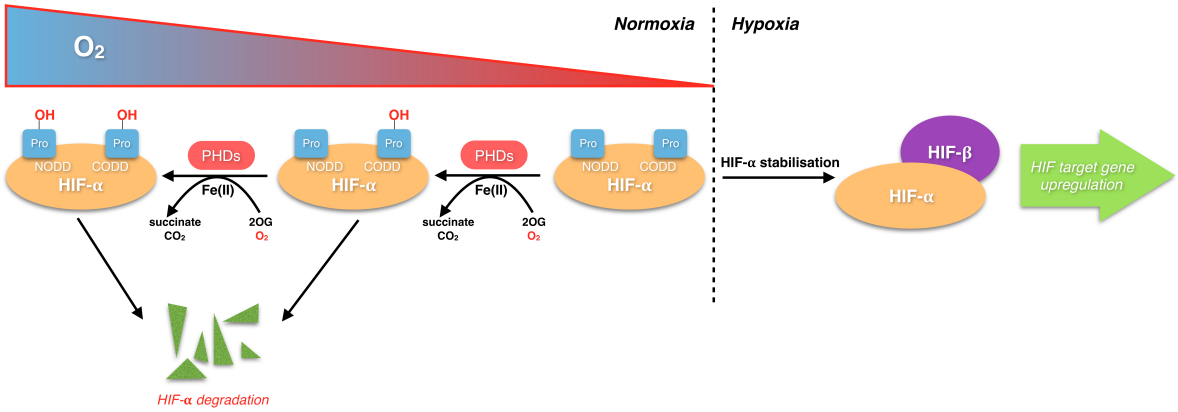


Figure 1 Under normoxic conditions hydroxylation of NODD/CODD, increases with increasing O_2 concentration, which in turn increases HIF-α affinity for VHL, signaling for degradation of HIF-α. Under hypoxic conditions, HIF-α combines with HIF-β in the nucleus to form the functional heterodimeric HIF complex.

hypoxic response. Genetic and biochemical studies have identified the PHDs as one of the most important sensors of oxygen,[1] with stabilisation of HIF-α occurring under hypoxic conditions, as a result of impaired PHD activity. Indeed, activity of the PHDs has been shown to be strongly affected by changes in oxygen concentration.[12] Given that the functional HIF complex targets numerous therapeutically important genes such as those encoding for erythropoietin and vascular endolethial growth factor, inhibition of PHDs as a means to regulate the HIF system, is the objective of drug discovery efforts.[13] Notably, PHD inhibitors are currently being assessed through clinical trials as to their efficacy for the treatment of anaemia *via* HIF-mediated erythropoietin upregulation.[13,14] Of the three PHD isoforms in higher animals, PHD2 may be most clinically relevant, because deletion of PHD2, but not PHD1 and 3, were shown to be lethal in mouse models.[15-17] Clinically relevant mutations of PHD2 have been shown to stabilise HIF-α and correlate with familial erythrocytosis and have been associated with cancer.[18,19]

Currently all inhibitors of PHD2, and other $Fe^{(II)}$, 2OG oxygenases are reversible and non-covalent binders, competing for 2OG or substrate binding sites, and ususally chelating the active site $Fe^{(II)}$.[5,6,20] Irreversibly binding, or covalent but reversible PHD2 inhibitors have not been reported, but would be useful in analysis of 2OG-oxygenases in cells. In the context of the PHDs, a PHD selective probe could also enable functional analysis of alternate (*i.e.* non-HIF-α) substrates of PHD2. Many alternative PHD substrates have been reported, but their physiological relevance and roles if any in hypoxic response have yet to be determined.[21] In other contexts, such probe compounds have been used for activity-based profiling (ABP) of proteins of interest in cells *e.g.* to determine inhibitor specificity and for protein identification.[22-24] The work described in this Chapter, describes the design, synthesis and implementation of a PHD2-selective activity based probe aimed at capturing PHD2 from cell lysates.

5.2 Covalent capture of PHD2

Effective activity-based profiling (ABP) makes use of chemical probes that (normally) capture proteins of interest *via* covalent interactions with its target protein. Moreover, covalent inhibition can be achieved *via* 'mechanism-based' inhibitor design. Chemical probes and are therefore similar in design to covalent inhibitors, and are usually functionalised (or can be functionalised) with a moiety capable of linking to an affinity tag such as biotin. Subsequently, the labeled protein of interest can be captured from cell lysates using a solid support possessing bound streptavidin to which biotin possesses high affinity.[25,26] Visualisation of the target protein is then possible after gel electrophoresis, Western blotting or mass spectrometry. Notably, the serine proteases have been extensively explored using such methodology. Serine proteases form covalent intermediates with substrates; irreversible covalent inhibition of them has been achieved through the synthesis of substrate analogues.[27,28]

In contrast to the serine proteases, PHD2 forms non-covalent complexes with its substrates, therefore the design of a substrate analogue inhibitor, capable of trapping PHD2, is challenging. Careful positioning of the electrophilic function on the chemical probe is therefore required, allowing for crosslinking only when a nucleophilic residue of the protein of interest is at an appropriate distance for a crosslinking reaction to occur. Alternative strategies to study proteins that do not pass through a covalent protein-substrate intermediate have been reported, notably through the use of photoaffinity probes. As initially proposed by Westheimer *et al*. in the 1960s,[29] a photoaffinity probe should possess three characteristics: selectivity for the target protein, a photoreactive component, and an affinity tag or 'handle' such as biotin.[30,31] Photoaffinity probes can be constructed from already existing reversible inhibitors of the protein of interest, thus providing the element of selectivity in cell lysates. In 1969 Fleet *et al*. described a more stable aryl azide

photoreactive group, which after irradiation allows for a covalent linkage to occur between the photoaffinity probe and protein of interest, likely *via* a radical mediated reaction.[32] Following irradiation, the 'handle' moiety, conjugated to the probe, allows for isolation and/or visualisation of the captured proteins *via* western blotting or mass spectrometry, following isolation using streptavidin beads.

As mentioned in Chapter 3, cysteine residues are often the targets for chemically modifying proteins, owing to the presence of a nucleophilic primary thiol.[33] Protein modification reagents often are designed to be cysteine specific, containing functionalities such as maleimides, vinyl sulphones and alpha-halo carbonyls (Chapter 3).[34-36] Methodologies also exist that make use of lysine residues, such as reacting deprotonated lysine with aptly activated carbonyl compounds such as *N*-hydroxysuccinimides, or with Michael acceptors, *e.g.* α, β-unsaturated ketones.[37]

Thus the initial aim was to synthesise a trifunctional chemical probe with the ability for irreversible covalent binding selective for PHD2, that would allow for ABP *via* conjugation to a handle such as biotin and subsequent visualisation/purification. A longer term objective was the capture of PHD substrates.

5.2.1 Previous work on covalent inhibitors of PHD2

Glycine derivatives of salicylic acids (**1**), 3-hydroxy pyridines (**2**) and isoquinolines (**3**) inhibit PHD2 (Figure 2).[38-40] By examining crystal structures of inhibitors in complex with PHD2 (Figure 3) it was possible to identify potential sites of functionalisation of reversible inhibitors. As seen in Figure 3, the crystallographic evidence implies that the aromatic group of FG2216 (**3**) is partially solvent exposed. Unfortunately crystal structure data of glycine coupled salicylic acid derivatives in complex with PHD2 have not been achieved, although a similar binding mode to that displayed by (**3**) can be proposed. Metal chelation most likely

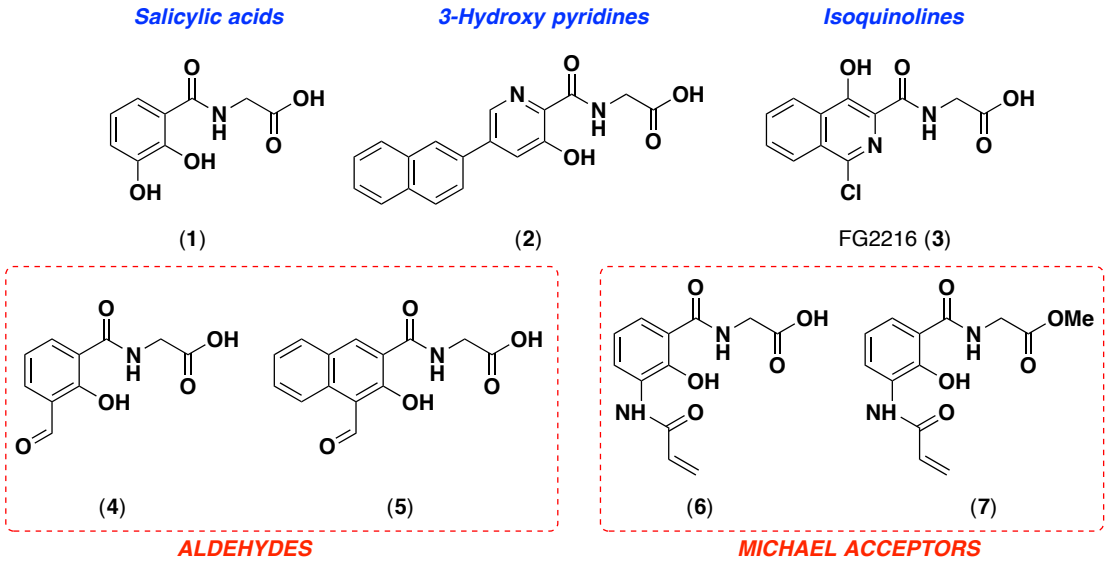


Figure 2 Chemical structures of reversible and covalent salicylic acid, 3-hydroxy pyridine and isoquinoline PHD2 inhibitors.

occurs through the amide carbonyl oxygen and *ortho*-hydroxy function; modelling of inhibitor (**3**) in a manner that also leaves the *meta*- and *para*-positions solvent exposed, thus providing three potential sites for modification that would most likely not clash with ligand binding. Glycine coupled salicylic derivatives such as (**1**), then seemed a good starting point from which to design functionalised inhibitors, covalently binding to PHD2.

The metal binding region of PHD2, does not harbor nucleophilic residues that are appropriately positioned for reaction with an electrophile. However, nucleophilic residues

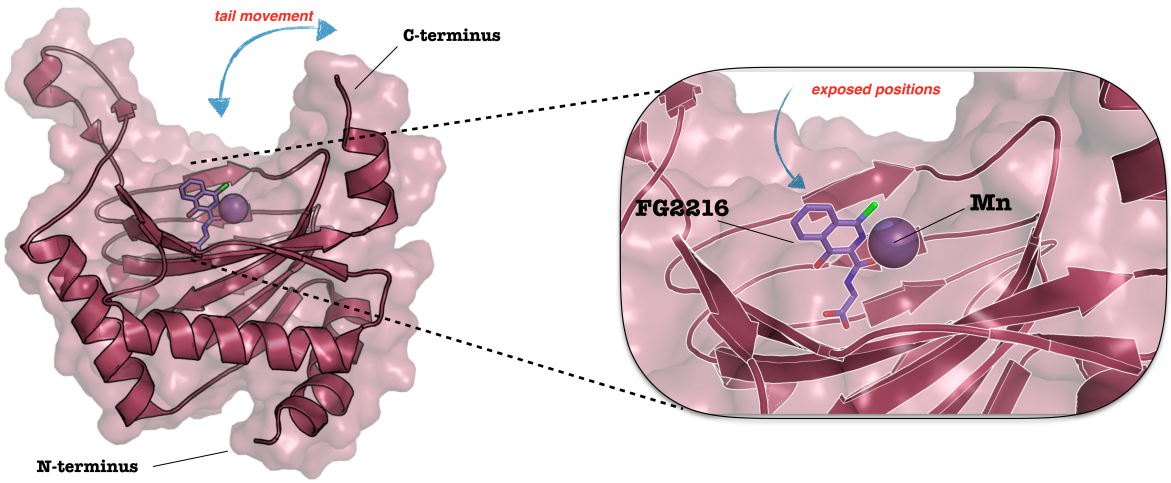


Figure 3 Crystal structure of FG2216 (**3**) (purple sticks) complexed with $Mn^{(II)}$(grey sphere) and PHD2 (red surface/cartoon)(PDB id = 4UWD). Previous irreversible inhibitors (*main text*) were found to bind *via* the flexible *C*-terminal tail located adjacent to the active site. Functionalising the solvent exposed regions of reversible inhibitors enabled covalent linking to PHD2 *via* K408 located on the *C*-terminus tail.

do exist on the flexible PHD2 *C*-terminus tail, which is adjacent to the active site. In previous work by Dr. Jasmin Mecinovic and Dr. Jacob Bush, aldehydes, (**4**) and (**5**), along with α, β-unsaturated amide (**6**), were shown to react covalently with PHD2.[41] Using liquid chromatography coupled with tandem mass spectroscopy (LC-MS/MS) it was possible to identify the residue that was covalently modified on PHD2. Amide (**6**) was identified to covalently link to PHD2 via Lys408 which (as predicted) is located on the *C*-terminal tail. Aldehydes (**4**) and (**5**), were also shown to bind to K408 using denaturing MS/MS. This result is interesting given the flexible *C*-terminal tail has many lysyl residues. Although covalent binding was observed with aldehydes (**4**) and (**5**), the resulting PHD2-adducts proved unstable under standard acidic reverse phase chromatography typically used in denaturing LC-MS/MS analysis. From these observations, it was concluded that an unsaturated amide would prove a more stable modification to use for the design of a multifunctional chemical probe for PHD2.

Futher work by Dr. Jacob Bush showed PHD2 crosslinked with amide (**6**), was still capable of catalysing the hydroxylation of CODD, at a rate not too dissimilar from unmodified PHD2.[41] (**6**) was found to have an IC_{50} of >2 mM confirming its weak inhibitory ability. Moreover, the ester derivative (**7**) was observed to upregulate HIF-1α in cells *via* western blot analysis (Figure 4); upregulation of HIF-1α by (**7**) was induced at all concentrations of (**7**). This observation was expected, given the concentrations of (**7**) at all measured doses was in excess, thus it is likely all the PHD2 present was crosslinked. Moreover, (**6**) was assessed for its selectivity against other 2OG oxygenases, possessing a lysine residue close to the active site. PHD isoforms PHD 1 and PHD3, along with *N*-methyl lysine demethylase JMJD2A, were found to not covalently bind (**6**) by denaturing mass spectrometry.

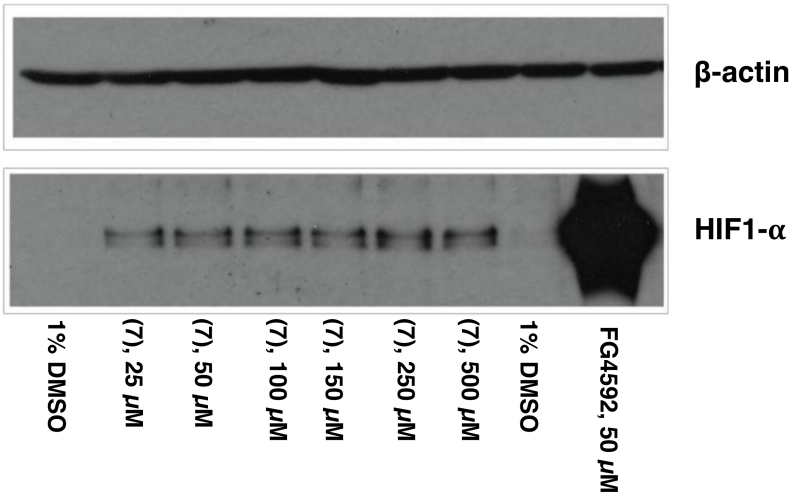
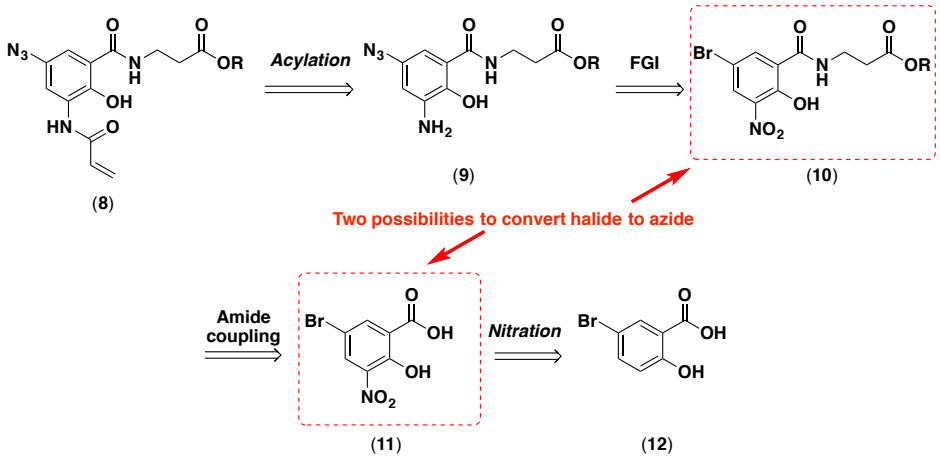


Figure 4 Western blot analysis following treatment of HeLa cells with ester (**7**). Cell lysis was carried out after treatment with (**7**). HIF1-α is upregulated at all concentrations of (**7**). The potent, cell permeable inhibitor of PHD2, FG4592 was used as a control. (*Figure modified from the DPhil thesis of Dr. Jacob Bush, analysis performed by Dr. Tzu-Lan Yeh.*

Having observed PHD2 selectivity and excellent crosslinking ability with (**6**), modification of (**6**) was attempted in order to include photoreactivity; thus, enabling activity-based profiling and photo-capture of PHD2 substrate complexes.

5.2.2 Design and synthesis of RL409 (18)

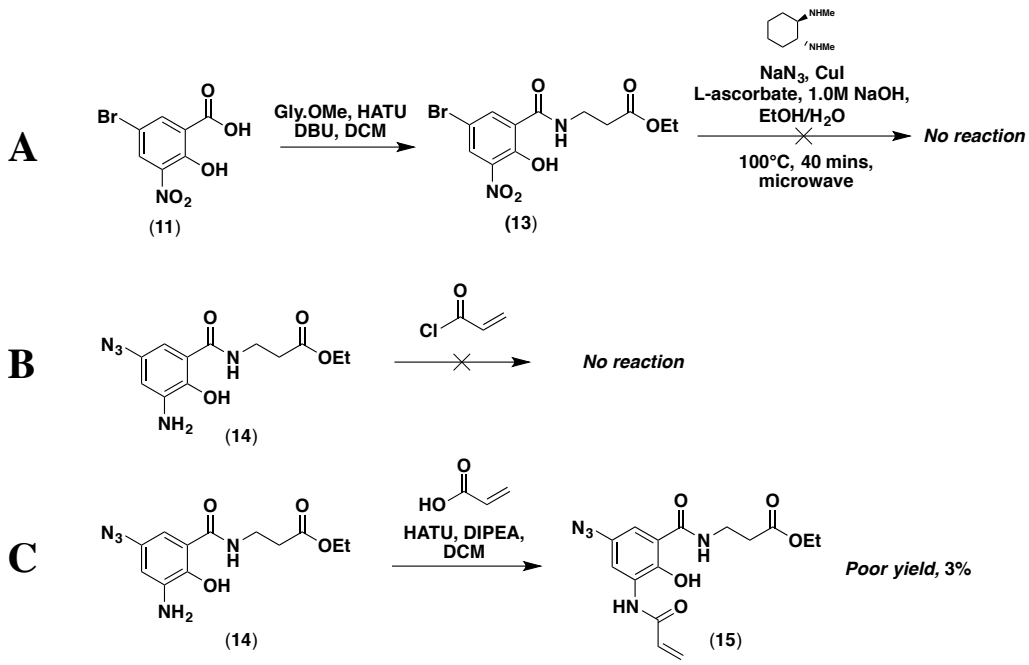


Scheme 1 Reterosynthetic analysis of the designed PHD2 probe compound.

It was envisaged that the final *N*-acylation of the aryl amine (**9**) to give (**8**) could be carried out as the final step (Scheme 1). Amine (**9**) could be obtained via a reduction of the nitro group of (**10**), following amide coupling to install the glycine ester moiety of compound (**9**). Nitration of 5-bromo-salycilic acid[42] (**12**) is reported and so synthesis towards (**8**) was

initiated with nitration of (**12**). It was decided that installation of the azide would be carried out after nitration to increase the reactivity of the bromine towards nucleophilic aromatic substitution and given the harsh nitration conditions may cause decomposition of the azide.

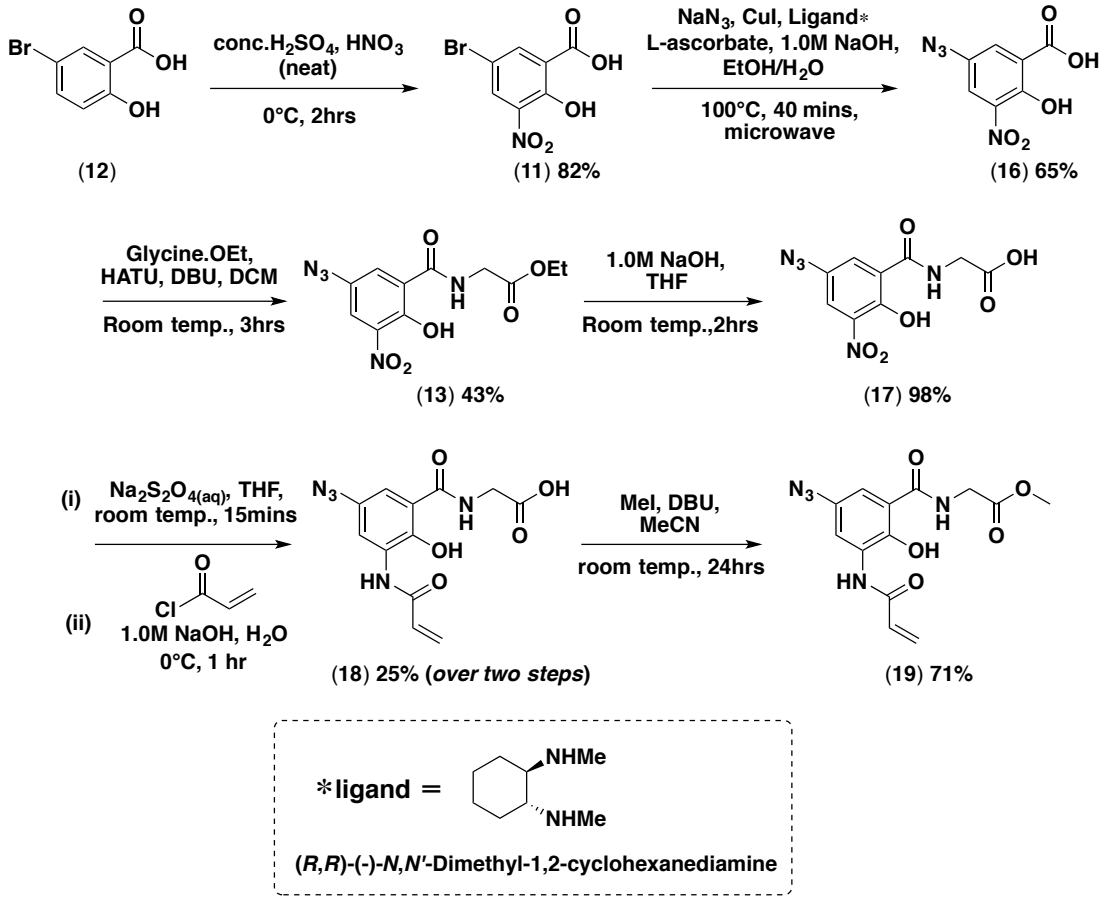
Thus, synthesis of nitro (**11**) was accomplished in an excellent yield (82%), similar



Scheme 2 Initial attempts to introduce the azide function and early attempts to acylate amine (**14**).

to that reported.[42] From this point an amide coupling with glycine ethylester employing HATU was carried out. Although the coupling reaction proceeded well to give (**13**), subsequent attempted conversion of (**13**) to the desired azide yielded multiple products (Scheme 2 (**A**)). Thus, the aryl halide to azide conversion was carried out before the amide coupling. Pleasingly, azide (**16**) was obtained in good yield (65%) (Scheme 3). HATU coupling of (**16**) with glycine ethyl ester to give (**13**) was successful (Scheme 3). Reduction of the nitro function with typical palladium on carbon hydrogenation could not be used, given the azide would likely be reduced under such conditions. Therefore aqueous sodium dithionite ($Na_2S_2O_4$) was employed as a chemoselective reducing agent for the nitro group. Pleasingly, reduction of nitro (**13**) to aryl amine (**14**) was rapid (~ 20 minutes). However, subsequent acylation attempts with acrylic acid/HATU or acryloyl chloride/NaOH gave

little or none of the desired compound (**15**) (Scheme 2 (**B**, **C**)). The solubility of ester (**14**) was thought to be a possible issue during acylations of (**14**). Thus, hydrolysis of the ester group of (**14**) was carried out followed by nitro reduction with $Na_2S_2O_4$. Thus from (**17**), carboxylic acid (**18**) was obtained in 25% yield over two steps (Scheme 3). The methyl ester of (**17**) was obtained in good yield (**19**, 71%) *via* methylation of the carboxylic acid under mild conditions (Scheme 3).



Scheme 3 Final synthetic route followed to obtain PHD2 probe (**18**) and its prodrug form (**19**) used for cellular studies.

5.3 Conjugation of PHD2 with RL409 (18)

5.3.1 Initial experiments

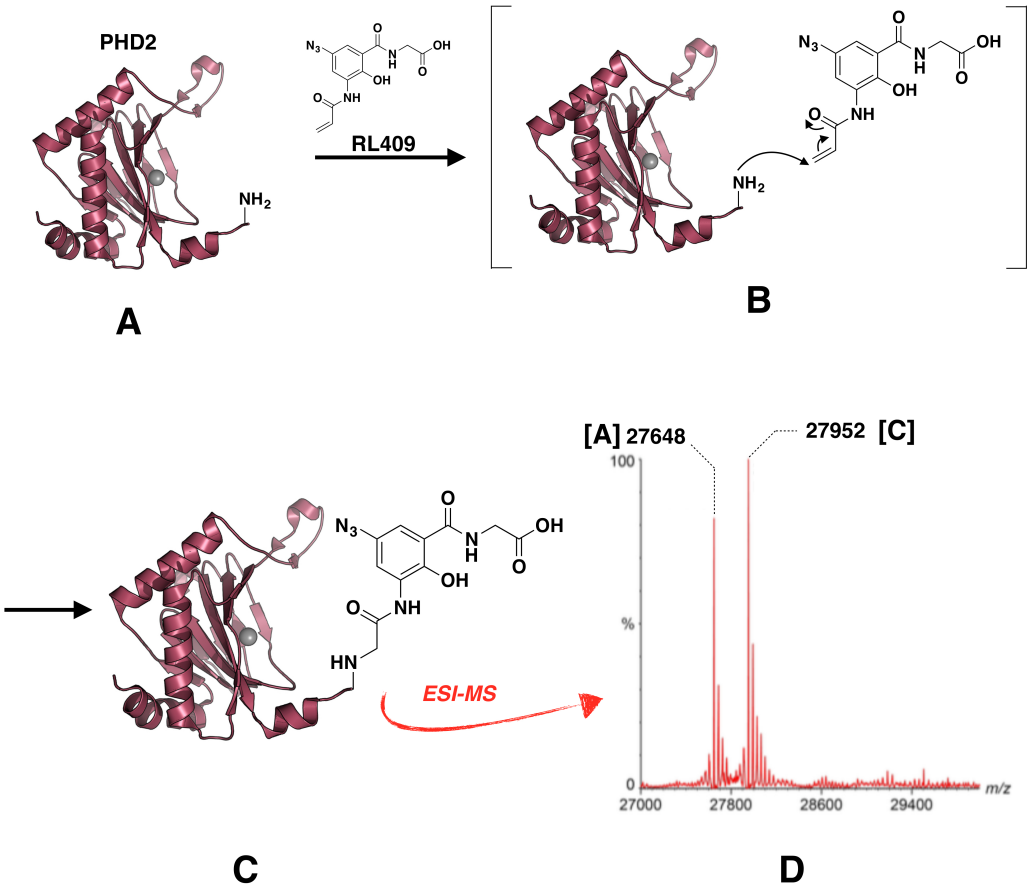


Figure 5 A) Unmodified PHD2-Fe (27648 Da). **B)** [PHD2-Fe-(**18**)] Non-covalent adduct. **C)** PHD2-Fe-(**18**) covalent complex (27952 Da). **D)** Resulting ESI mass-spectrum of the reaction between PHD2 and (**18**). Near complete reaction was observed after the 2.5 hour incubation period. Reaction conditions: (**18**) (20 μM), PHD2 (20 μM) and Fe (20 μM) was incubated at 37°C for 2.5 hours. (*ESI-MS spectrum obtained from the D. Phil thesis of Dr Jacob Bush*).

Upon reaction of RL409 (**18**) with PHD2 *in vitro*, a new peak at 27,952 Da was observed by electrospray ionisation mass-spectrometry (MS). The MS results implied successful crosslinking between (**18**) and PHD2 (Figure 5). MS analysis was carried out after incubation of PHD2 with (**18**) and $Fe^{(II)}$ at 37°C over the course of 2.5 hours. As a control, binding of inhibitor (**6**) (which does not posess an azide moiety) to PHD2 was also carried out to assess any affect the azide may have on the extent of crosslinking to PHD2. Pleasingly crosslinking of (**18**) with PHD2 was similar to (**6**), indicating the azide moiety likely yields little or no steric issues with the binding site of PHD2.

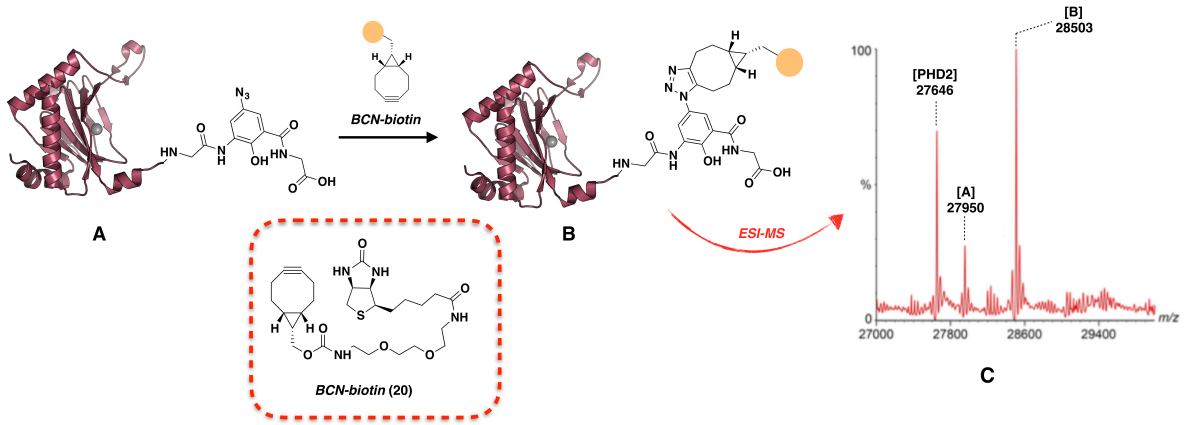


Figure 6 A) Covalent PHD2-Fe-(**18**) complex (27950 Da). **B)** Covalent complex formed after reaction of (A) with BCN-biotin (**20**). **C)** Resulting ESI mass spectrum of the copper-free 'click' reaction between PHD2-(**18**) and (**20**). Near complete conversion to the biotinylated protein complex (B, 28503 Da). Reaction conditions: (**18**) (20 μM), PHD2 (20 μM) and $Fe^{(II)}$(20 μM) were incubated at 37°C for 4 hours before (**20**) (100 μM) was added. The resulting mixture was incubated for a further 1 hour at 37°C. (*ESI-MS spectrum obtained from the D. Phil thesis of Dr Jacob Bush*).

To explore the use of (**18**) as an activity-based probe for the capture PHD2 in cells, the reaction between PHD2-(**18**) and BCN-biotin (**20**) was carried out and monitored by MS (Figure 6). Pleasingly, near complete reaction of PHD2-(**18**) with (**20**) was observed, when using the strained [2+3] cycloaddition reaction (by MS) (Figure 6, 28503 Da). Considering the results presented in Figure 5 and Figure 6, (**18**) seemingly provides a new method of crosslinking PHD2 with molecules possessing a cyclooctyne functionality, potentially enabling ABP of PHD2 in cells. Whether the PHD2-(**18**) covalent complex is catalytically active, however, was not examined, although given the PHD2-(**6**) covalent adduct was found to be still catalytically active (Section 5.2.1),[41] it may also be the case with (**18**).

5.3.2 Photo-activation of PHD2-(18)

The photo-activation of the PHD2-(**18**) was monitored using ESI mass-spectrometry. After forming the PHD2-(**18**) adduct, as previously described (Section 5.3.1), the sample was irradiated the complex with UV light (310nm) at 4°C for 12 minutes and analysed. Elimination of a molecule of N_2 was observed (27920 Da)(Figure 7 (**B**)) corresponding to conversion of the azide moieity of (**18**) to a nitrene followed by intramolecular insertion or abstraction of hydrogen *i.e.* [PHD2:(**18**) – N_2]. The observed MS results implied the cross-

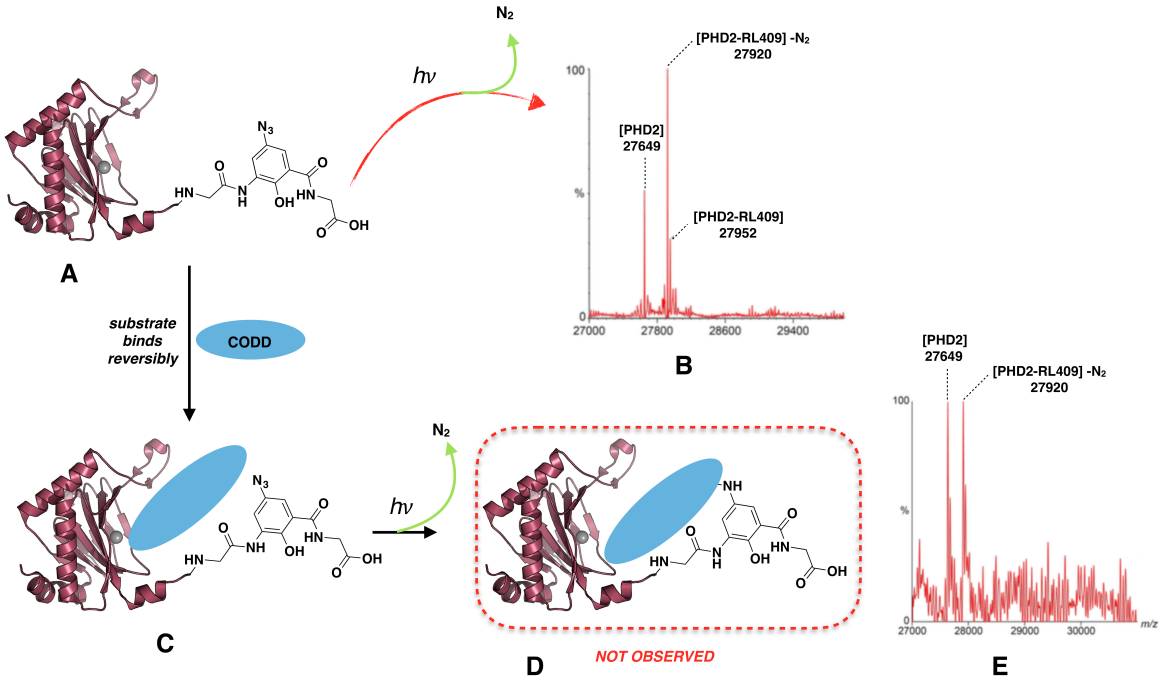


Figure 7 A) PHD2-Fe-RL409. **B)** Resulting mass spectrum after irradiation of (A) with UV light (310nm). RL409 is photoactive. **C)** CODD-PHD2-Fe-RL409 non-covalent adduct. D) Photocrosslinking to CODD not observed. **E)** Resulting mass spectrum after irradiation of a CODD PHD2-RL409 incubation. (*ESI-MS spectra were obtained from the D. Phil thesis of Dr Jacob Bush*).

linked PHD2-(**18**) was photo-active, indicating the aryl azide group of (**18**) reacted as predicted.[32,41] Having validated the photoreactivity of PHD2-(**18**) it was hoped to investigate its ability to photocrosslink to PHD2 substrates. Thus, after forming the PHD2-(**18**) as previously described (Section 5.3.1), 100 μM of CODD peptide was added before the mixture was irradiated with UV light at 310nm (4°C for 12 mins) and analysed. Unfortunately a mass of 30178 Da which would identify formation of a PHD2-(**18**)-CODD complex was not observed. This result may be partly due to the impurity of the CODD peptide used;[41] as seen in (Figure 7 (**E**)), the impurity of CODD peptide can be seen to contribute to a large amount of background noise.

5.4 Summary and future perspectives

Compound RL409 (**18**) presents the first compound of its class, *i.e.* a reversible covalent inhibitor of PHD2, with further conjugation capabilities. The ability of (**18**) to covalently

modify PHD2 was demonstrated. The PHD2-(**18**) covalent adduct was then able to further react with a biotin handle (**20**) providing the option for activity based profiling. An efficient synthesis of the free acid (**18**) and methyl ester (**19**) versions of RL409 was successfully designed and implemented for *in vitro* work. Unfortunately, photocrossinking of (**18**) to CODD was not conclusive and additional studies are required on this issue. Further studies are also required to elucidate whether RL409 will be suitable for the activity based profiling of PHD2 in cell lysates, and this work is ongoing.

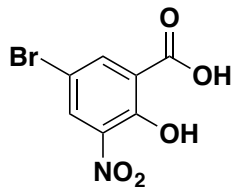
5.5 Acknowledgements

Compounds (**4**)-(**7**) were synthesised by Dr. Jasmin Mecinovic. ESI-MS reaction monitoring of PHD2 with compounds (**4**), (**6**), (**7**) (Section 5.2) and (**18**) (Section 5.3) were carried out by Dr. Jacob Bush.[41]

5.6 Synthesis

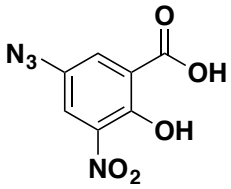
Synthetic materials and methods were identical to those discussed in Chapter 2.

***5-Bromo-2-hydroxy-3-nitrobenzoic acid* (11)**[42]



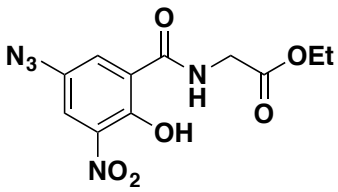
To a suspension of 5-bromosalicylic acid (**12**)(23 g, 105 mmol) in concentrated sulfuric acid (70 ml) at 0°C, a mixture of nitric acid (6.6 ml) and conc. sulfuric acid (15.4 ml) was added dropwise whilst maintaining a reaction temperature of < 10°C. The reaction was stirred on ice for 1 hour before the ice bath was removed and the reaction stirred at room temperature for 3 hours at which point the reaction was observed to be complete by LCMS. The resulting mixture was decanted into a conical flask containing crushed ice, which gave a bright yellow precipitate which was collected by büchner filtration, washed with cold water and dried to leave a yellow solid. After recrystallised from EtOAc, a crystalline bright yellow solid was obtained (22.4 g, 86.1 mmol, 82%). **m.p.** 168-170°C. **^{1}H NMR** (CD_3OD, 400 MHz) δ = 8.26 (1H, d, *J* = 2.5 Hz), 8.28 (1H, d, *J* = 2.5 Hz) ppm. **^{13}C NMR** (101 MHz, CD_3OD) δ = 110.1, 118.7, 126.6, 134.3, 138.8, 155.8, 171.4 ppm. **FT-IR** ν_{max} (neat) 2581, 1673, 1522, 1428, 1341, 1231, 1172, 1153, 954, 906, 895, 795, 709, 692 cm^{-1}. **HRMS** (ESI-TOF) calcd for $C_7H_4BrNO_5$ $[M+H]^+$: 259.9200 and 261.9180, found: 259.9198 and 261.9177.

5-Azido-2-hydroxy-3-nitrobenzoic acid (16)



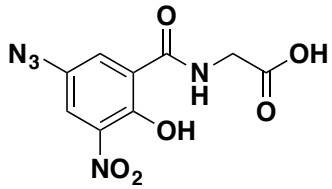
To a solution of 5-bromo-2-hydroxy-3-nitrobenzoic acid (**11**) (1.35 g, 5.15 mmol) in a 5:1 mixture of ethanol and distilled water (10.3 ml) was added sodium azide (670 mg, 10.3 mmol), sodium L-ascorbate (51.4 mg, 0.26 mmol), copper(I) iodide (98 mg, 0.52 mg) and (*R*,*R*)-(–)-*N*,*N*′-dimethyl-1,2-cyclohexanediamine. The reaction vessel was placed under an atmosphere of N_2 before being heated to 100°C with stirring using a microwave reactor, until complete consumption of the starting material was observed by LCMS (~ 45 mins). The reaction was cooled to room temperature before being quenched with 1.0M $HCl_{(aq)}$ (~ 10 ml). The resulting suspension was passed through a short pad of silica gel and the filtrate was extracted with EtOAc (3 x 20 ml). The organic layers were collected, dried over anhydrous $MgSO_4$, filtered and concentrated before being purified by flash column chromatography (99:1, EtOAc/AcOH). The appropriate fractions were collected and concentrated to give a dark yellow solid. (798 mg, 3.58 mmol, 65%). **m.p.** 154-156°C. **^{1}H NMR** (DMSO-d_6, 400 MHz) δ = 7.73 (1H, d, *J* = 3.0 Hz), 7.89 (1H, d, *J* = 3.0 Hz) ppm. **^{13}C NMR** (101 MHz, DMSO-d_6) δ = 120.9, 125.3, 129.1, 137.2, 138.6, 152.7, 169.8 ppm. **FT-IR** ν_{max} (neat) 3362, 3016, 2970, 2497, 1738, 1532, 1448, 1365, 1229, 1216, 1168, 889, 796 cm^{-1}. **HRMS** (ESI-TOF) calcd for $C_7H_3N_4O_5$ $[M-H]^-$: 223.0109, found: 223.0108.

Ethyl (5-azido-2-hydroxy-3-nitrobenzoyl)glycinate (13)



5-Azido-2-hydroxy-3-nitrobenzoic acid (**16**) (525 mg, 2.34 mmol), HATU (1.78 g, 4.69 mmol), glycine ethyl ester hydrochloride salt (359 mg, 2.57 mmol) and DBU (1.8 ml, 11.7 mmol) were dissolved in CH_2Cl_2 (23ml). The mixture was stirred at rom temperature untill the reaction was observed to be complete by TLC (17:1, CH_2Cl_2/MeOH). Following addition 1M $HCl_{(aq)}$ (30 ml) the organic materials were extracted with CH_2Cl_2 (3 x 30 ml), after which all organic layers were combined, dried over anhydrous $MgSO_4$, filtered and concentrated. The crude material was then purified by flash column chromatography (0 to 60% EtOAc in cyclohexane 10 CVs). The appropriate fractions were collected and concentrated to give a dark orange oil (310 mg, 1.0 mmol, 43% yield). **^{1}H NMR** (CD_3OD, 400 MHz) δ = 1.29 (3H, t, *J* = 7.0 Hz), 4.16 (2H, s), 4.22 (2H, q, *J* = 7.0 Hz), 7.81 (1H, d, *J* = 3.0 Hz), 7.90 (1H, d, *J* = 3.0 Hz) ppm. **^{13}C NMR** (101 MHz, CD_3OD) δ = 14.5, 40.1, 62.5, 120.4, 120.7, 124.5, 126.2, 132.9, 152.3, 167.5, 170.9 ppm. **FT-IR** ν_{max} (film) 3410, 2940, 2110, 1742, 1650, 1583, 1535, 1470, 1377, 1325, 1210, 838 cm^{-1}. **HRMS** (ESI-TOF) calcd for $C_{11}H_{12}N_5O_6$ $[M+H]^+$: 310.0782, found: 310.0783.

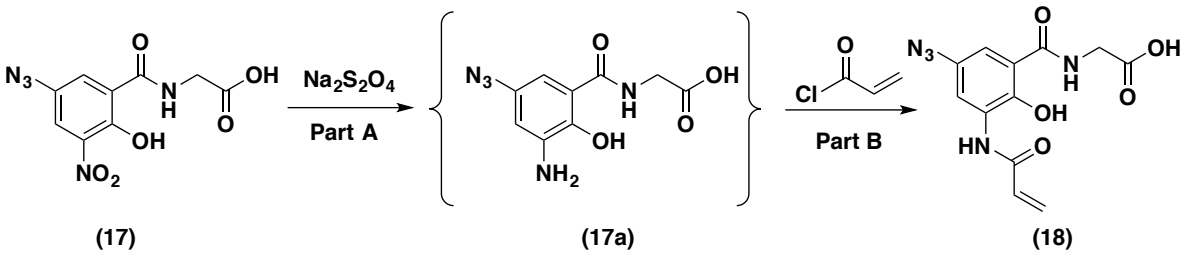
(5-Azido-2-hydroxy-3-nitrobenzoyl)glycine (17)



To a solution of (5-azido-2-hydroxy-3-nitrobenzoyl)glycinate (**13**) (883 mg, 2.86 mmol) in THF (5.72 ml), 1.0M $NaOH_{(aq)}$ was added and after 30 minutes a red precipitate had formed which was isolated by büchner filtration, washed several times with CH_2Cl_2 and dried under vacuum flow to yield the product as a red solid (801 mg, 2.85 mmol, 99%). **m.p.** 184-187°C. **^{1}H NMR** (DMSO-d_6, 400 MHz) δ = 3.59 (2H, d, *J* = 4.5 Hz), 7.45 (1H, d, *J* = 3.5 Hz), 7.71 (1H, d, *J* = 3.5 Hz) ppm. **^{13}C NMR** (101 MHz, DMSO-d_6) δ = 44.8, 118.8, 118.9, 126.6, 127.2, 136.2, 164.4, 172.2 ppm. **FT-IR** ν_{max} (film) 3415, 2126, 1651, 1586, 1537,

1509, 1406, 1334, 1285, 1248, 838, 794 cm^{-1}. **HRMS** (ESI-TOF) calcd for $C_9H_6N_5O_6$ [M-H]$^-$: 280.0324, found: 280.0321.

(3-Acrylamido-5-azido-2-hydroxybenzoyl)glycine (18)



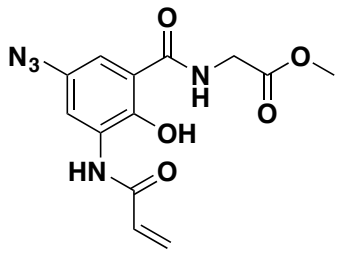
(17) (17a) (18)

Part A: To a solution of (5-azido-2-hydroxy-3-nitrobenzoyl)glycine (**17**) (200 mg, 0.71 mmol) in THF (5.46 ml), a solution of $Na_2S_2O_4$ (1.24 g, 7.1 mmol) in distilled water (10.6 ml) was added dropwise. After 15 minutes the reaction was observed to be complete by LCMS and the reaction was decanted into a saturated brine solution. The mixture was extracted with EtOAc (5 x 30 ml) and the organic fractions collected, dried over anhydrous Na_2SO_4, filtered and concentrated to give amine (**17a**) as a clear oil (100mg, 0.40 mmol, 56% yield), which was used without further purification for the next step.

Part B: (3-amino-5-azido-2-hydroxybenzoyl)glycine (**17a**) (100 mg, 0.40 mmol) was suspended in water (2 ml) and cooled with an ice bath. To this suspension was added 1.0M $NaOH_{(aq)}$ (400 µL) and acryloyl chloride (159 µL, 1.96 mmol). The mixture was then stirred for 1 hour after which a beige precipitate was observed to form which was isolated by Büchner filtration, dried over 48 hrs in a vacuum to give the product as a beige solid (55 mg, 0.18 mmol, 25% yield over two steps). **m.p.** (decomp.) 289-290°C. **^{1}H NMR** (CD_3OD, 400 MHz) δ = 4.10 (2H, s), 5.80 (1H, dd, *J* = 10.5, 1.5 Hz), 6.39 (1H, dd, *J* = 17.0, 1.5 Hz), 6.60 (1H, dd, *J* = 17.0, 10.5 Hz), 7.27 (1H, d, *J* = 2.5 Hz), 8.16 (1H, d, *J* = 2.5 Hz) ppm. **^{13}C NMR** (CD_3OD, 101 MHz) δ = 41.8, 113.1, 115.9, 116.9, 128.6, 129.9, 132.0, 132.1, 150.3, 166.4, 171.2, 172.8 ppm. **FT-IR** ν_{max} (film) 2928, 2496, 2115, 1728, 1643, 1595, 1538,

1475, 1447, 1247, 970, 792 cm^{-1}. **HRMS** (ESI-TOF) calcd for $C_{12}H_{12}N_5O_5$ $[M+H]^+$: 306.0833, found: 306.0835.

Methyl (3-acrylamido-5-azido-2-hydroxybenzoyl)glycinate (19)



To a solution of (3-acrylamido-5-azido-2-hydroxybenzoyl)glycine (**18**)(20 mg, 0.07 mmol) in acetonitrile (70 µL), methyl iodide (7.5 µL, 0.12 mmol) and DBU (10.5 µL, 0.07 mmol) were added. The reaction was allowed to stir at room temperature for 24 hrs before 1M $HCl_{(aq)}$ (15 µL) was added and the organic material extracted with CH_2Cl_2 (3 x 5 ml). The organic fractions were collected, dried over $MgSO_4$, filtered and concentrated before the crude material was purified by flash column chromatography (0 to 100% EtOAc in cyclohexane over 10 CVs). All appropriate fractions were collected and dried to give the product as a waxy solid (17 mg, 0.05 mmol, 71% yield). **m.p.** (decomp.) 160-163°C. **^{1}H NMR** ($CDCl_3$, 400 MHz) δ = 3.85 (3H, s, -OC*H*$_3$), 4.24 (2H, d, *J* = 5.5 Hz, -CONHC*H*$_2$-), 5.80 (1H, dd, *J* = 10.0, 1.5 Hz, -COCH=C*H*$_A$H$_B$), 6.29 (1H, dd, *J* = 17.0, 10.0 Hz, -COC*H*=CH$_2$), 6.42 (1H, dd, *J* = 17.0, 1.5 Hz, -COCH=CH$_A$*H*$_B$), 6.79 (1H, d, *J* = 2.5 Hz, *Ar*), 7.34 (1H, t, *J* = 4.5 Hz, -CON*H*CH$_2$-), 7.97 (1H, br. s, -N*H*COCH=CH$_2$), 8.43 (1H, d, *J* = 2.5 Hz, *Ar*) ppm. **^{13}C NMR** ($CDCl_3$, 101 MHz) δ = 41.4, 53.1, 109.7, 113.0, 114.7, 128.5, 129.4, 131.1, 131.3, 147.9, 163.8, 166.0, 169.5 ppm. **FT-IR** ν_{max} (film) 3351, 2926, 2114, 1732, 1676, 1532, 1438, 1229, 1188, 1029, 978, 731 cm^{-1}. **HRMS** (ESI-TOF) calcd for $C_{13}H_{13}N_5O_5$ $[M-H]^-$: 318.0844, found: 318.0843.

5.7 References

1. R. Chowdhury, I. K. Leung, Y. M. Tian, M. I. Abboud, W. Ge, C. Domene, F. X. Cantrelle, I. Landrieu, A. P. Hardy, C. W. Pugh, P. J. Ratcliffe, T. D. Claridge and C. J. Schofield, Structural basis for oxygen degradation domain selectivity of the HIF prolyl hydroxylases, *Nat. Commun.*, 2016, **7**, 12673.
2. C. J. Schofield and P. J. Ratcliffe, Oxygen sensing by HIF hydroxylases, *Nat. Rev. Mol. Cell Biol.*, 2004, **5**, 343-354.
3. G. L. Semenza, M. K. Nejfelt, S. M. Chi and S. E. Antonarakis, Hypoxia-inducible nuclear factors bind to an enhancer element located 3' to the human erythropoietin gene, *Proc. Natl. Acad. Sci. U. S. A.*, 1991, **88**, 5680-5684.
4. G. L. Wang, B. H. Jiang, E. A. Rue and G. L. Semenza, Hypoxia-inducible factor 1 is a basic-helix-loop-helix-PAS heterodimer regulated by cellular O2 tension, *Proc. Natl. Acad. Sci. U. S. A.*, 1995, **92**, 5510-5514.
5. N. R. Rose, M. A. McDonough, O. N. King, A. Kawamura and C. J. Schofield, Inhibition of 2-oxoglutarate dependent oxygenases, *Chem. Soc. Rev.*, 2011, **40**, 4364-4397.
6. M. A. McDonough, C. Loenarz, R. Chowdhury, I. J. Clifton and C. J. Schofield, Structural studies on human 2-oxoglutarate dependent oxygenases, *Curr. Opin. Struct. Biol.*, 2010, **20**, 659-672.
7. P. Jaakkola, D. R. Mole, Y. M. Tian, M. I. Wilson, J. Gielbert, S. J. Gaskell, A. von Kriegsheim, H. F. Hebestreit, M. Mukherji, C. J. Schofield, P. H. Maxwell, C. W. Pugh and P. J. Ratcliffe, Targeting of HIF-alpha to the von Hippel-Lindau ubiquitylation complex by O2-regulated prolyl hydroxylation, *Science*, 2001, **292**, 468-472.
8. A. C. Epstein, J. M. Gleadle, L. A. McNeill, K. S. Hewitson, J. O'Rourke, D. R. Mole, M. Mukherji, E. Metzen, M. I. Wilson, A. Dhanda, Y. M. Tian, N. Masson, D. L. Hamilton, P. Jaakkola, R. Barstead, J. Hodgkin, P. H. Maxwell, C. W. Pugh, C. J. Schofield and P. J. Ratcliffe, C. elegans EGL-9 and mammalian homologs define a family of dioxygenases that regulate HIF by prolyl hydroxylation, *Cell*, 2001, **107**, 43-54.
9. T. Bishop and P. J. Ratcliffe, HIF hydroxylase pathways in cardiovascular physiology and medicine, *Circ. Res.*, 2015, **117**, 65-79.
10. R. K. Bruick, Oxygen sensing in the hypoxic response pathway: regulation of the hypoxia-inducible transcription factor, *Genes Dev.*, 2003, **17**, 2614-2623.

11. W. G. Kaelin, Jr. and P. J. Ratcliffe, Oxygen sensing by metazoans: the central role of the HIF hydroxylase pathway, *Mol. Cell*, 2008, **30**, 393-402.
12. D. Ehrismann, E. Flashman, D. N. Genn, N. Mathioudakis, K. S. Hewitson, P. J. Ratcliffe and C. J. Schofield, Studies on the activity of the hypoxia-inducible-factor hydroxylases using an oxygen consumption assay, *Biochem. J.*, 2007, **401**, 227-234.
13. M. C. Chan, J. P. Holt-Martyn, C. J. Schofield and P. J. Ratcliffe, Pharmacological targeting of the HIF hydroxylases--A new field in medicine development, *Mol. Aspects Med.*, 2016, **47-48**, 54-75.
14. L. Yan, V. J. Colandrea and J. J. Hale, Prolyl hydroxylase domain-containing protein inhibitors as stabilizers of hypoxia-inducible factor: small molecule-based therapeutics for anemia, *Expert Opin. Ther. Pat.*, 2010, **20**, 1219-1245.
15. E. Berra, E. Benizri, A. Ginouves, V. Volmat, D. Roux and J. Pouyssegur, HIF prolyl-hydroxylase 2 is the key oxygen sensor setting low steady-state levels of HIF-1alpha in normoxia, *EMBO J.*, 2003, **22**, 4082-4090.
16. R. L. Chen, S. Nagel, M. Papadakis, T. Bishop, P. Pollard, P. J. Ratcliffe, C. W. Pugh and A. M. Buchan, Roles of individual prolyl-4-hydroxylase isoforms in the first 24 hours following transient focal cerebral ischaemia: insights from genetically modified mice, *J. Physiol.*, 2012, **590**, 4079-4091.
17. K. Takeda, V. C. Ho, H. Takeda, L. J. Duan, A. Nagy and G. H. Fong, Placental but not heart defects are associated with elevated hypoxia-inducible factor alpha levels in mice lacking prolyl hydroxylase domain protein 2, *Mol. Cell. Biol.*, 2006, **26**, 8336-8346.
18. F. S. Lee and M. J. Percy, The HIF pathway and erythrocytosis, *Annu. Rev. Pathol.*, 2011, **6**, 165-192.
19. H. Kato, T. Inoue, K. Asanoma, C. Nishimura, T. Matsuda and N. Wake, Induction of human endometrial cancer cell senescence through modulation of HIF-1alpha activity by EGLN1, *Int. J. Cancer.*, 2006, **118**, 1144-1153.
20. C. C. Thinnes, A. Tumber, C. Yapp, G. Scozzafava, T. Yeh, M. C. Chan, T. A. Tran, K. Hsu, H. Tarhonskaya, L. J. Walport, S. E. Wilkins, E. D. Martinez, S. Muller, C. W. Pugh, P. J. Ratcliffe, P. E. Brennan, A. Kawamura and C. J. Schofield, Betti reaction enables efficient synthesis of 8-hydroxyquinoline inhibitors of 2-oxoglutarate oxygenases, *Chem. Commun.*, 2015, **51**, 15458-15461.

21. B. W. Wong, A. Kuchnio, U. Bruning and P. Carmeliet, Emerging novel functions of the oxygen-sensing prolyl hydroxylase domain enzymes, *Trends Biochem. Sci*, 2013, **38**, 3-11.
22. H. Ovaa, P. F. van Swieten, B. M. Kessler, M. A. Leeuwenburgh, E. Fiebiger, A. M. van den Nieuwendijk, P. J. Galardy, G. A. van der Marel, H. L. Ploegh and H. S. Overkleeft, Chemistry in living cells: detection of active proteasomes by a two-step labeling strategy, *Angew. Chem. Int. Ed. Engl.*, 2003, **42**, 3626-3629.
23. C. Kocks, R. Maehr, H. S. Overkleeft, E. W. Wang, L. K. Iyer, A. M. Lennon-Dumenil, H. L. Ploegh and B. M. Kessler, Functional proteomics of the active cysteine protease content in Drosophila S2 cells, *Mol. Cell. Proteomics*, 2003, **2**, 1188-1197.
24. C. R. Berkers, M. Verdoes, E. Lichtman, E. Fiebiger, B. M. Kessler, K. C. Anderson, H. L. Ploegh, H. Ovaa and P. J. Galardy, Activity probe for in vivo profiling of the specificity of proteasome inhibitor bortezomib, *Nat. Methods*, 2005, **2**, 357-362.
25. R. E. Wang, C. R. Hunt, J. Chen and J. S. Taylor, Biotinylated quercetin as an intrinsic photoaffinity proteomics probe for the identification of quercetin target proteins, *Bioorg. Med. Chem.*, 2011, **19**, 4710-4720.
26. D. K. Nomura, M. M. Dix and B. F. Cravatt, Activity-based protein profiling for biochemical pathway discovery in cancer, *Nat. Rev. Cancer*, 2010, **10**, 630-638.
27. J. C. Powers, J. L. Asgian, O. D. Ekici and K. E. James, Irreversible inhibitors of serine, cysteine, and threonine proteases, *Chem. Rev.*, 2002, **102**, 4639-4750.
28. P. Haquette, M. Salmain, K. Svedlung, A. Martel, B. Rudolf, J. Zakrzewski, S. Cordier, T. Roisnel, C. Fosse and G. Jaouen, Cysteine-specific, covalent anchoring of transition organometallic complexes to the protein papain from Carica papaya, *Chem. Bio. Chem*, 2007, **8**, 224-231.
29. A. Singh, E. R. Thornton and F. H. Westheimer, The photolysis of diazoacetylchymotrypsin, *J. Biol. Chem.*, 1962, **237**, 3006-3008.
30. P. P. Geurink, L. M. Prely, G. A. van der Marel, R. Bischoff and H. S. Overkleeft, Photoaffinity labeling in activity-based protein profiling, *Top. Curr. Chem.*, 2012, **324**, 85-113.
31. T. Tomohiro, M. Hashimoto and Y. Hatanaka, Cross-linking chemistry and biology: development of multifunctional photoaffinity probes, *Chem. Rec.*, 2005, **5**, 385-395.
32. G. W. J. Fleet, R. R. Porter and J. R. Knowles, Affinity Labelling of Antibodies with Aryl Nitrene as Reactive Group, *Nature*, 1969, **224**, 511-&.

33. J. M. Chalker, G. J. Bernardes, Y. A. Lin and B. G. Davis, Chemical modification of proteins at cysteine: opportunities in chemistry and biology, *Chem. Asian. J.*, 2009, **4**, 630-640.
34. K. E. Arntson and W. C. Pomerantz, Protein-Observed Fluorine NMR: A Bioorthogonal Approach for Small Molecule Discovery, *J. Med. Chem.*, 2016, **59**, 5158-5171.
35. E. Weerapana, C. Wang, G. M. Simon, F. Richter, S. Khare, M. B. Dillon, D. A. Bachovchin, K. Mowen, D. Baker and B. F. Cravatt, Quantitative reactivity profiling predicts functional cysteines in proteomes, *Nature*, 2010, **468**, 790-795.
36. J. Hemelaar, A. Borodovsky, B. M. Kessler, D. Reverter, J. Cook, N. Kolli, T. Gan-Erdene, K. D. Wilkinson, G. Gill, C. D. Lima, H. L. Ploegh and H. Ovaa, Specific and covalent targeting of conjugating and deconjugating enzymes of ubiquitin-like proteins, *Mol. Cell. Biol.*, 2004, **24**, 84-95.
37. C. Dax, M. Coincon, J. Sygusch and C. Blonski, Hydroxynaphthaldehyde phosphate derivatives as potent covalent Schiff base inhibitors of fructose-1,6-bisphosphate aldolase, *Biochemistry*, 2005, **44**, 5430-5443.
38. N. C. Warshakoon, S. Wu, A. Boyer, R. Kawamoto, J. Sheville, R. T. Bhatt, S. Renock, K. Xu, M. Pokross, S. Zhou, R. Walter, M. Mekel, A. G. Evdokimov and S. East, Design and synthesis of substituted pyridine derivatives as HIF-1alpha prolyl hydroxylase inhibitors, *Bioorg. Med. Chem. Lett.*, 2006, **16**, 5616-5620.
39. B. M. Lienard, A. Conejo-Garcia, I. Stolze, C. Loenarz, N. J. Oldham, P. J. Ratcliffe and C. J. Schofield, Evaluation of aspirin metabolites as inhibitors of hypoxia-inducible factor hydroxylases, *Chem Commun*, 2008, 6393-6395.
40. M. Demetriades, I. K. H. Leung, R. Chowdhury, M. C. Chan, M. A. McDonough, K. K. Yeoh, Y. M. Tian, T. D. W. Claridge, P. J. Ratcliffe, E. C. Y. Woon and C. J. Schofield, Dynamic Combinatorial Chemistry Employing Boronic Acids/Boronate Esters Leads to Potent Oxygenase Inhibitors, *Angew. Chem. Int. Ed.*, 2012, **51**, 6672-6675.
41. J. T. Bush, Dphil, University of Oxford, 2015.
42. S. J. Taylor, A. K. Padyana, A. Abeywardane, S. Liang, M. H. Hao, S. De Lombaert, J. Proudfoot, B. S. Farmer, 3rd, X. Li, B. Collins, L. Martin, D. R. Albaugh, M. Hill-Drzewi, S. S. Pullen and H. Takahashi, Discovery of potent, selective chymase inhibitors via fragment linking strategies, *J. Med. Chem.*, 2013, **56**, 4465-4481.

Chapter 6

Summary

6.0 Summary

Chapter 1 introduced the $Fe^{(II)}$, 2-oxoglutarate dependent oxygenase enzymes, with a focus on the two members of the family involved in the biosynthesis of L-carnitine in mammals. These two oxygenases, N^{ε}-trimethyllysine hydroxylase (TMLH) and γ-butyrobetaine hydroxylase (BBOX), catalyse the first and final steps in carnitine biosynthesis,[1] respectively. Studies on them were the main overall focus of the work described in the thesis. An overview of the current literature regarding the biosynthesis of L-carnitine from a therapeutic perspective was provided. Mildronate (Meldonium, THP, Met-88) is an inhibitor of human BBOX and is used clinically in Eastern Europe and as a treatment for cardiovascular diseases and,[2] more widely as a performance enhancer.[3] A discussion of the literature concerning the biochemical modes of action and purported clinical outcomes of Mildronate was provided.

Chapter 2 described work concerning the first committed step of carnitine biosynthesis.[1] TMLH catalyses the C-3 hydroxylation of N^{ε}-trimethyllysine; however, the stereochemistry of the hydroxylated C-3 carbon of the TMLH product had not previously been assigned. Using ^{1}H NMR the outcome of TMLH catalysed hydroxylation was shown to be a single diastereomer. Through the use of an asymmetric silver(I)-catalysed aldol reaction, it was possible to synthesise stereochemically enriched (2*S*,3*R*)-3-hydroxy-N^{ε}-trimethyllysine.[4] This compound enabled the assignment of the enzyme catalysed reaction product as (2*S*,3*S*)-3-hydroxy-N^{ε}-trimethyllysine using 1D and 2D NMR spectroscopy. The assignment was further supported by amino acid analysis. As a result of synthetic work, a novel and efficient method of obtaining diastereochemically pure (2*S*,3*R*)-3-hydroxy-N^{ε}-trimethyllysine and (2*S*,3*R*)-3-hydroxy-lysine was presented. Moreover, (2*S*,3*R*)-3-hydroxy-lysine was used as a standard for amino acid analysis to elucidate the previously unknown,

stereochemistry of two, 2OG-dependent oxygenases involved in post-translational lysyl-hydroxylation.

The work described in Chapter 3 concerned the production and use of a ^{19}F labelled cysteine variant of bacterial BBOX from *Pseudomonas sp. AK1* (Y201C). It was envisaged that ^{19}F labelling of the cysteine mutation would enable the monitoring of conformational changes in the flexible loop region of psBBOX using ^{19}F NMR spectroscopy. Pleasingly, it was discovered that ^{19}F labelling using 1,1,1-trifluoro-3-bromoacetone (BFA) was site-selective for the site of substitution *i.e.* Cys201. Thus, using ^{19}F NMR it was possible to observe small-molecule induced chemical shift changes following titration of co/substrates and inhibitors. The results enabled an enhanced understanding of conformational changes involving the flexible loop regions of psBBOX. The largest chemical shift change was observed with GBB and other substrates whereas the available inhibitors displayed significantly smaller conformational changes. The results support currently available X-ray crystallographic data that suggest substrates, rather than the available inhibitors induce a closed flexible loop conformation. The results also validate the use of ^{19}F chemical labelling to monitor ligand binding to 2OG-dependent oxygenases and identify a potential new class of small molecule inhibitors of BBOX. A discussion of BBOX inhibition and synthetic work towards novel BBOX inhibitors is disclosed in Appendix I. Future work will include screening of these novel compounds with the intent to regulate carnitine levels in cells and hence cellular energy metabolism.

Chapter 4 introduced the topic of metallo β-lactamase (MBL) mediated antibiotic resistance and described the design and synthesis of novel, broad-spectrum class B metallo β-lactamase inhibitors. Known isoquinoline based inhibitors of BBOX, have previously been shown to be effective MBL inhibitors,[5,6] and as a result a novel MBL inhibitor was designed *in silico*. Following successful synthetic work, this modified isoquinoline proved a

relatively ineffective inhibitor of MBLs. Thus, mercaptopropionic acid derivatives RL368 and RL369 were targeted as metal chelating inhibitors of MBLs, analogous to the broad spectrum MBL inhibitors L- and D-captopril. Following successful synthesis of the target compounds, RL368, in particular, showed superior broad spectrum MBL inhibition. Moreover, RL368 displayed *in vitro* cell-based potential as an antibiotic potentiator, following an antimicrobial susceptibility assay against Gram negative bacteria of clinical origin (*E. coli*, *E. aerogenes* and *K. pneumonia*). The predicted binding modes of RL369/369 to VIM-2 were validated by X-ray crystallography. Overall the results should contribute towards the development of clinically useful broad spectrum MBL inhibitors.

Chapter 5 described the biological and therapeutic importance of the 2OG-oxygenase, prolyl hydroxylase domain containing enzyme 2 (PHD2), which is involved in oxygen sensing.[7] With the aim of studying PHD2 in cells, previous work within the Schofield lab has identified covalent PHD2 inhibitors. It was envisaged that through derivatisation of a covalent probe compound with appropriately positioned electrophilic and photo-active moieties, it may be possible to detect previously unknown PHD2 substrates. Through the design, synthesis and implementation of a such a covalent probe compound, RL409, it was possible to covalently bind PHD2 *in vitro*. Successful incorporation of the photo-active azide moiety in RL409 allowed for attachment of a biotin tag to the covalent PHD2-RL409 complex using a copper-free 'click' reaction. The results indicate that RL409 may prove a useful tool in PHD2-directed affinity based profiling and novel substrate detection in cells. Futher work will involve assessment of RL409 as a cellular ABP tool for PHD2 in cells.

Overall the work in the thesis has furthered our understanding of metallo-enzymes in a therapeutic context. This has been achieved through the use of small molecule tools to study the structure and function of 2OG-oxygenases and metallo-β-lactamases.

Furthermore the work has highlighted the potential value of targeting these enzymes as a means to combat global health concerns. Careful design and synthesis of chemical probes has contributed to the success of the projects disclosed in this thesis and therefore emphasises the importance of chemical synthesis in the study of biological systems.

References

1. K. Strijbis, F. M. Vaz and B. Distel, Enzymology of the Carnitine Biosynthesis Pathway, *IUBMB Life*, 2010, **62**, 357-362.
2. M. Dambrova, E. Liepinsh and I. Kalvinsh, Mildronate: cardioprotective action through carnitine-lowering effect, *Trends Cardiovasc. Med.*, 2002, **12**, 275-279.
3. H. K. Greenblatt and D. J. Greenblatt, Meldonium (Mildronate): A Performance-Enhancing Drug?, *Clin. Pharm. Drug Dev.*, 2016, **5**, 167-169.
4. R. K. Lesniak, S. Markolovic, K. Tars and C. J. Schofield, Human carnitine biosynthesis proceeds via (2S,3S)-3-hydroxy-Nepsilon-trimethyllysine, *Chem. Commun.*, 2016, **53**, 440-442.
5. S. S. van Berkel, J. Brem, A. M. Rydzik, R. Salimraj, R. Cain, A. Verma, R. J. Owens, C. W. Fishwick, J. Spencer and C. J. Schofield, Assay platform for clinically relevant metallo-beta-lactamases, *J. Med. Chem.*, 2013, **56**, 6945-6953.
6. A. Makena, A. O. Duzgun, J. Brem, M. A. McDonough, A. M. Rydzik, M. I. Abboud, A. Saral, A. C. Cicek, C. Sandalli and C. J. Schofield, Comparison of Verona Integron-Borne Metallo-beta-Lactamase (VIM) Variants Reveals Differences in Stability and Inhibition Profiles, *Antimicrob. Agents Chemother.*, 2016, **60**, 1377-1384.
7. R. Chowdhury, I. K. Leung, Y. M. Tian, M. I. Abboud, W. Ge, C. Domene, F. X. Cantrelle, I. Landrieu, A. P. Hardy, C. W. Pugh, P. J. Ratcliffe, T. D. Claridge and C. J. Schofield, Structural basis for oxygen degradation domain selectivity of the HIF prolyl hydroxylases, *Nat. Commun.*, 2016, **7**, 12673.

Appendix I

Synthesis of novel BBOX inhibitors

Contents

1.0 APPENDIX I – SYNTHESIS OF NOVEL BBOX INHIBITORS 231

1.1 BBOX INHIBITION 231

1.2 FLUORIDE RELEASE ASSAY 232

1.3 3-HYDROXY-PYRIDINES – AR692B 233

1.4 BBOX ACTIVE SITE MIMETICS 234

1.5 PYRROLO PYRIDINES 237

1.6 TRIAZOLYL PYRIDINES 238

1.7 'METATHESIS' COMPOUND 239

1.8 SUMMARY 240

1.9 EXPERIMENTAL 241

1.9.1 General remarks 241

1.9.2 Synthesis 241

(23) *Tert*-butyl (4-((benzoyloxy)amino)butyl)carbamate[12] 241

(24) Ethyl (*E*)-4-((benzoyloxy)(4-((tert-butoxycarbonyl)amino)butyl)amino)-4-oxobut-2-enoate 242

(25) Ethyl (*E*)-4-((4-aminobutyl)(benzoyloxy)amino)-4-oxobut-2-enoate 243

(26) (*E*)-4-(*N*-(benzoyloxy)-4-ethoxy-4-oxobut-2-enamido)-*N,N,N*-trimethylbutan-1-aminium 244

(21) (*E*)-4-(3-carboxy-*N*-hydroxyacrylamido)-*N,N,N*-trimethylbutan-1-aminium (RL190B) 245

(28) (*E*)-4-(hydroxy(4-(((1-methyl-1H-pyrazol-3-yl)methyl)amino)butyl)amino)-4-oxobut-2-enoic acid 246

1.9.3 General Procedure for synthesis of pyrrolo pyridinyl series compounds 247

Methyl (2*S*,3*S*)-2-(5,7-dioxo-5,7-dihydro-6H-pyrrolo[3,4-b]pyridin-6-yl)-3-methylpentanoate 247

Methyl (*S*)-2-(5,7-dioxo-5,7-dihydro-6H-pyrrolo[3,4-b]pyridin-6-yl)-4-methylpentanoate 248

Methyl 2-(5,7-dioxo-5,7-dihydro-6H-pyrrolo[3,4-b]pyridin-6-yl)acetate 248

Methyl (*S*)-2-(5,7-dioxo-5,7-dihydro-6H-pyrrolo[3,4-b]pyridin-6-yl)-3-methylbutanoate 249

Methyl (*S*)-2-(5,7-dioxo-5,7-dihydro-6H-pyrrolo[3,4-b]pyridin-6-yl)-3-phenylpropanoate 250

(34) Methyl (*R*)-2-(5,7-dioxo-5,7-dihydro-6H-pyrrolo[3,4-b]pyridin-6-yl)-3-((pyridin-2-ylmethyl)thio)propanoate 250

Methyl (*S*)-2-(5,7-dioxo-5,7-dihydro-6H-pyrrolo[3,4-b]pyridin-6-yl)-3-(1H-indol-3-yl)propanoate 251

(*S*)-2-(5,7-dioxo-5,7-dihydro-6H-pyrrolo[3,4-b]pyridin-6-yl)-4-methyl-*N*-(4-nitrophenyl)pentanamide 252

(*S*)-2-(5,7-dioxo-5,7-dihydro-6H-pyrrolo[3,4-b]pyridin-6-yl)-4-methylpentanoic acid 253

Methyl *N*-(tert-butoxycarbonyl)-*S*-(pyridin-2-ylmethyl)-L-cysteinate[2] 253

(34a) Methyl *S*-(pyridin-2-ylmethyl)-L-cysteinate[2] 254

(35) Methyl (*S*)-3-phenyl-2-(4-(pyridin-2-yl)-1H-1,2,3-triazol-1-yl)propanoate 255

Methyl *S*-(4-bromobenzyl)-*N*-(tert-butoxycarbonyl)-L-cysteinate (41) 256

Methyl *S*-(4-allylbenzyl)-*N*-(tert-butoxycarbonyl)-L-cysteinate (42) 256

Methyl *N*-(5-allyl-3-(benzyloxy)picolinoyl)-*S*-(4-allylbenzyl)-L-cysteinate (43) 257

1.10 REFERENCES 258

1.0 Appendix I – Synthesis of novel BBOX inhibitors

This section of the thesis outlines synthetic work carried out in order to identify novel inhibitor scaffolds of hBBOX as a means to therapeutically regulate carnitine biosynthesis and thus cellular energy metabolism. Following screening of the compounds disclosed herein, it is hoped more potent and selective inhibitors, compared to the clinically used compound Mildronate,[1,2] can be identified.

1.1 BBOX inhibition

As discussed in Chapters 1-3, Mildronate (**3**) (Figure 1) is currently the only human BBOX (hBBOX) inhibitor that is clinically used (in eastern Europe).[1,2] Whether its clinical effects are wholly BBOX-mediated remains the subject of debate (Chapter 1).[3,4] Nevertheless, Mildronate is a (weak) inhibitor and competitive substrate of BBOX *in vitro* (IC_{50} = 12 μM[5] / 60 μM[6]) and its success has resulted in the generation of novel GBB (**1**) analogues (*e.g.* (**4**) and (**5**)) (Figure 1) as inhibitors of BBOX.[7,8]

hBBOX/psBBOX inhibitor scaffolds other than GBB-mimics, have also been explored (predominantly 2OG-analogues) (Figure 1) such as pyridine carboxylic acids (**6**

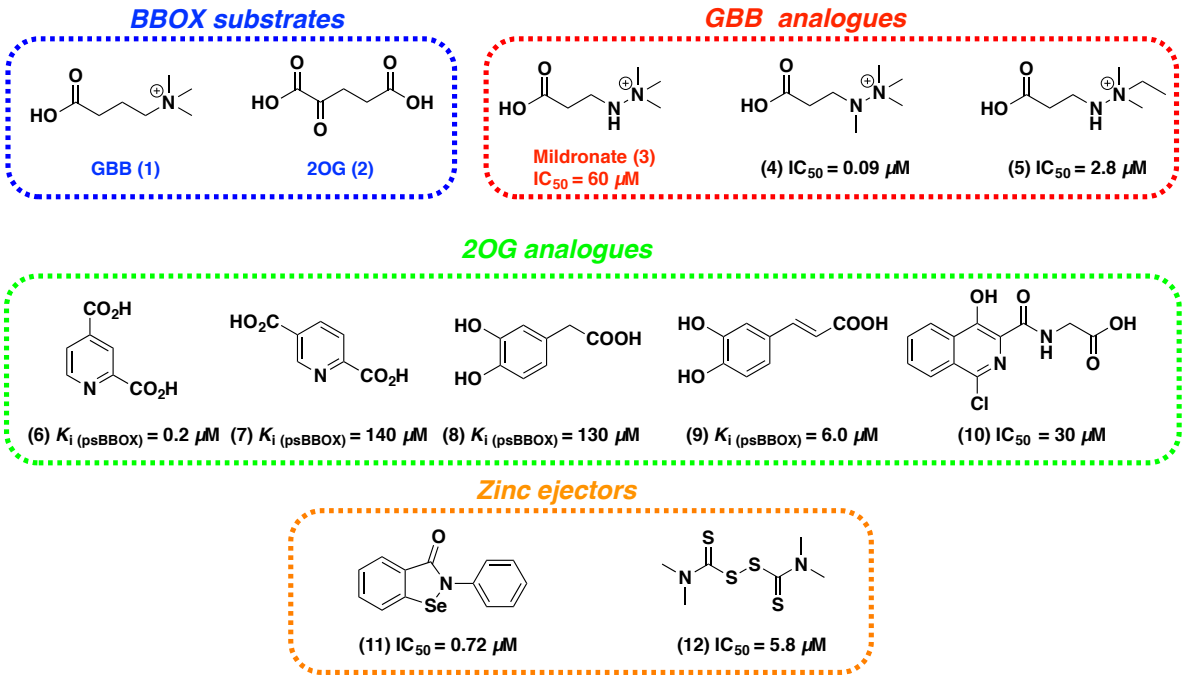


Figure 1 Chemical strucutres of various different types of previously reported BBOX inhibitors.[5-11]

and **7**),[9] benzoic acids (**8** and **9**),[9] isoquinolines (**10**),[2,10] and zinc ejectors (**11** and **12**).[11] Work within the Schofiled lab has led to the identification of potent BBOX inhibitors, in part as a result of the development of a BBOX-specific fluoride release assay.[2,6]

1.2 Fluoride release assay

A fluoride release assay specific to BBOX was developed in order to provide a medium-throughput fluorescence-based assay as a means to discover new BBOX inhibitors (Figure 2).[6] The reported method relies on the ability of hBBOX to catalyse C-3 hydroxylation of a C-3 fluorinated GBB analogue, GBBF (**13**).[6] BBOX mediated hydroxylation of GBBF, induces the departure of fluoride. TBS-protected fluorescein (**14**) is present in the incubation mixture and therefore BBOX-mediated fluoride-release triggers fluoride-mediated deprotection of (**14**) to give the highly fluorescent compound (**15**). The observed fluorescence in this assay is therefore proportional to the release of fluoride by BBOX. This fluorescence can be modulated with the use of inhibitors, and hence can be used as a measure of the inhibition caused by novel compounds competing with (**13**) for the active site of BBOX. Whilst (**13**) is relatively difficult to synthesise (8 steps), (**14**) can be obtained in a single step from a commercially available fluorescein (**14a**).[6]

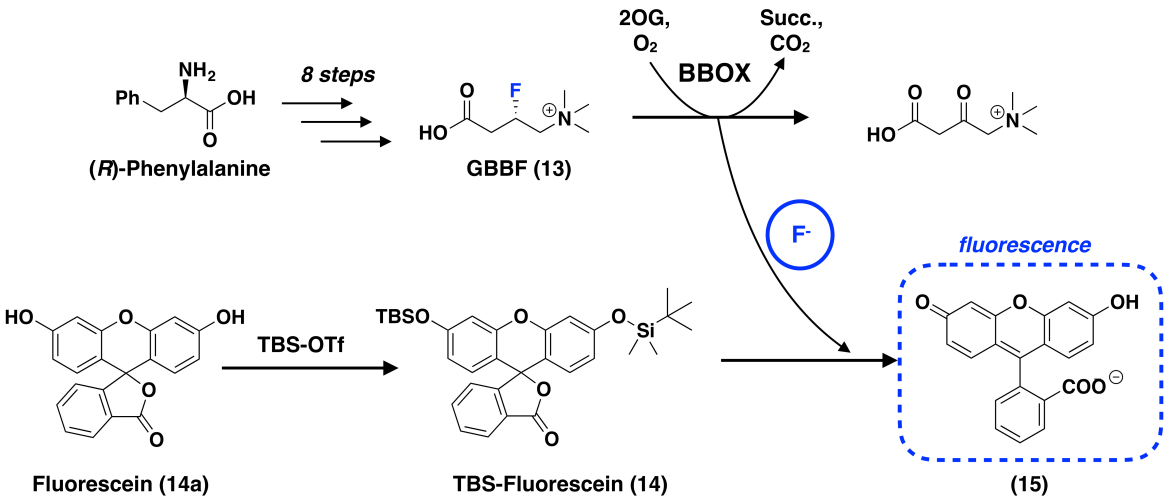


Figure 2 Chemical process involved in the BBOX specific fluoride release assay, developed by Dr. Anna Rydzik.[6]

1.3 3-hydroxy-pyridines – AR692B

Using the BBOX fluoride release assay,[6] a compound screen carried out by Dr. Anna Rydzik of 500 compounds revealed promising hits for BBOX inhibition.[2] The most potent of these were the 3-hydroxypyridine series (Figure 3 (**A**)).[2] These compounds are potent hBBOX inhibitors and, bind to the metal *via* the pyridine nitrogen and amide oxygen, so mimicking 2OG.[2] As discussed in detail in Chapter 3, a crystal structure of the most potent inhibitor of the 3-hydroxy pyridine series (**19**) (IC_{50} = 153 nM)[2] in complex with hBBOX revealed the molecule adopts either a 'horse-shoe' shape or 'open' conformation in the BBOX active site (Figure 3 (conformations I and II respectively)). The carboxylate of (**19**) interacts strongly with Arg-360 in a similar way to 2OG. In conformation I, The bulky side

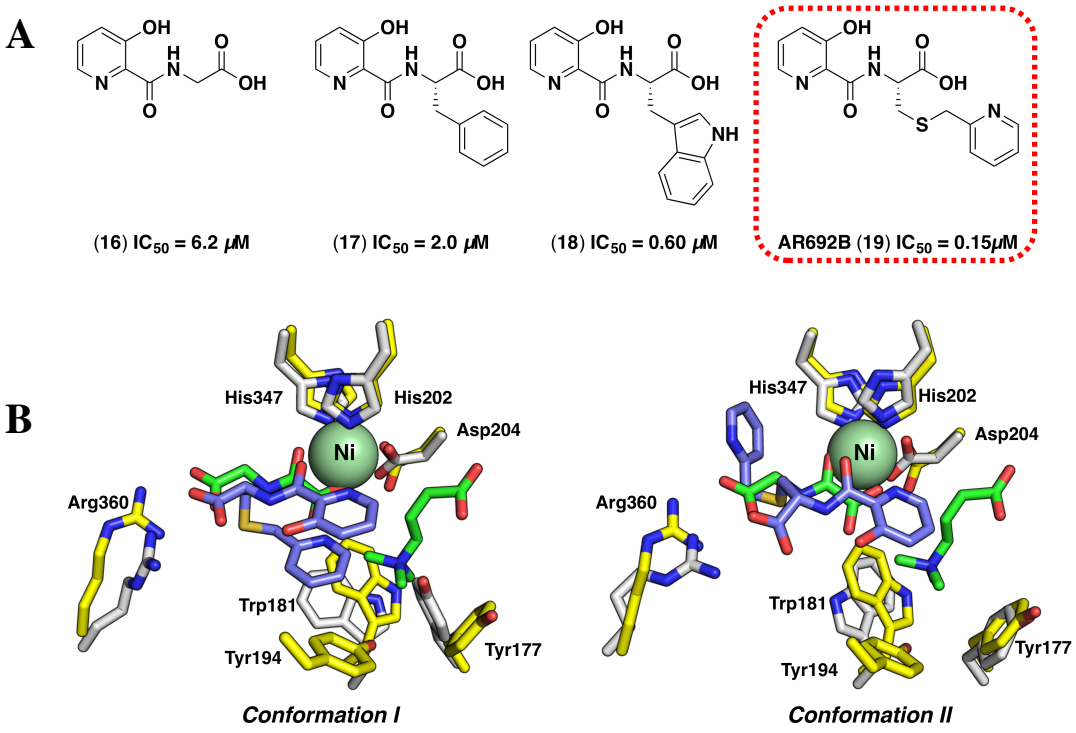


Figure 3 **A**) 3-Hydroxy pyridine inhibitors of hBBOX. **B**) A view from a crystal structure of AR692B (**19**)(blue sticks) with hBBOX (white sticks)(PDB id: 4C8R), overlaid with a structure of GBB (green sticks), NOG (green sticks) and hBBOX (yellow sticks)(PDB id: 3O2G). Catalytically inactive $Ni^{(II)}$ substitutes for $Fe^{(II)}$. Two conformations of (**19**) are observed.

chain folds underneath the pyridine ring, is stabilized by apparent π-stacking interactions (Figure 3). Conformation II on the other hand, shows the amino acid derived side chain of the inhibitor occupying a hydrophobic pocket adjacent to the 2OG binding site.

It was envisaged that the previous BBOX inihibition culminating in (**19**) could be extended further by: (1) designing novel cosubstrate/substrate mimics, that incorporate both GBB and 2OG 'binding motifs'; (2) synthesising fluorine analogues of (**19**), (3) preventing rotation about the 2-pyridine-carbonyl bond *i.e.* using pyrrolo derivatives; and (4) investigating an alternative metal chelation scaffold involving the use of triazolyl derivatives.

1.4 BBOX Active site mimetics

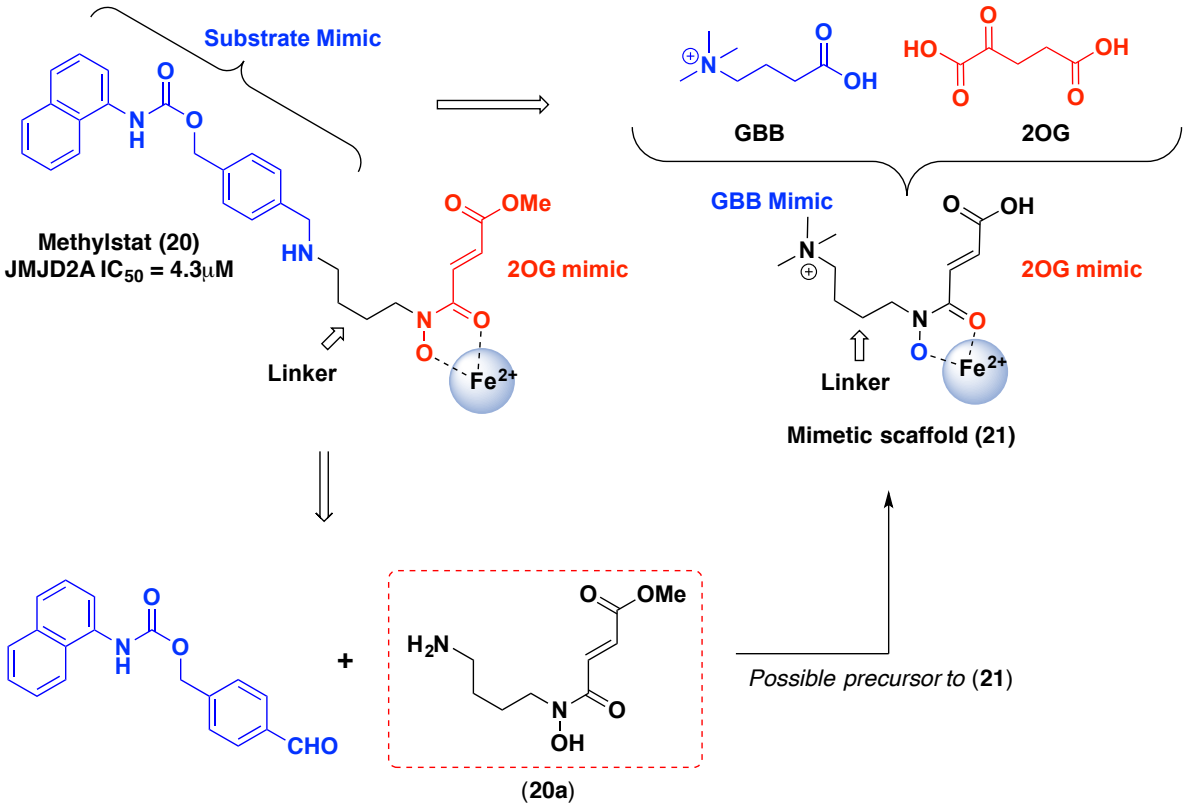
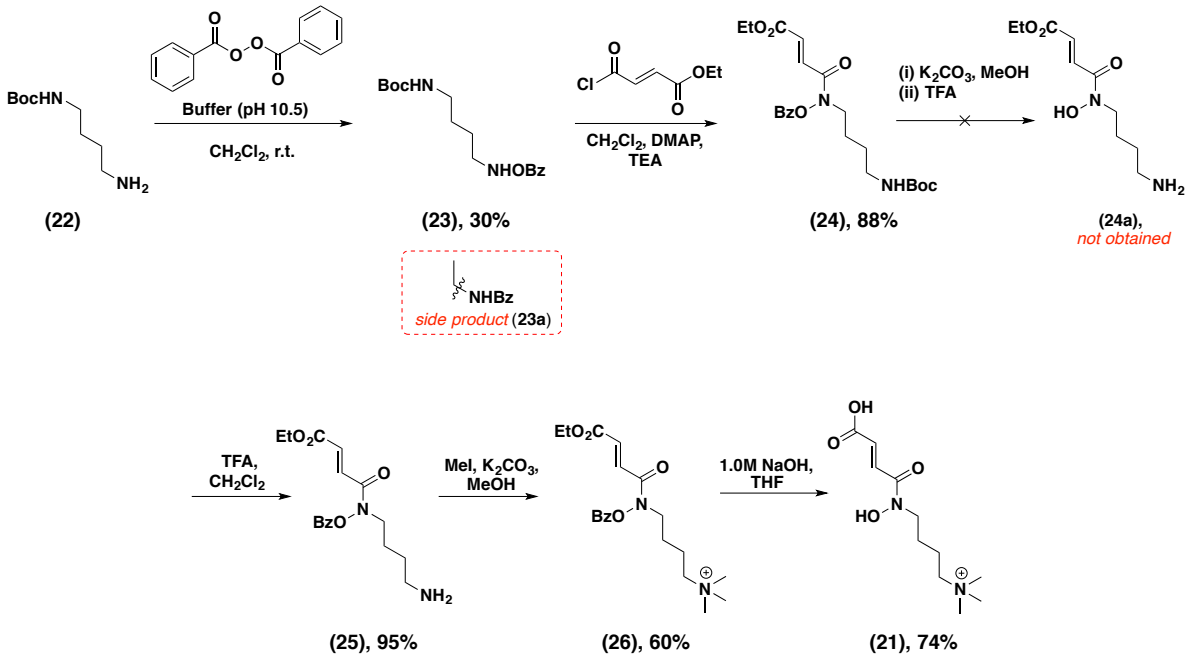


Figure 4 Left: Methylstat (**20**), with its substrate competing element highlighted in blue, and its 2OG mimic in red. (**20a**) is used as a precursor to Methylstat and was envisaged as a precursor to the proposed BBOX inhibitor RL190B (**21**)

Methylstat (**20**) is a jumonji-C domain containing histone demethylase (Jmjc KDM) inhibitor (Figure 4).[12] The Jmjc KDM enzymes are Fe^{2+}containing, 2OG oxygenases (Figure 4); mechanistic links have been established between BBOX and the Jmjc KDMs, including



Scheme 1 Synthetic route followed to obtain the active site mimetic RL190B (**21**).

the observation that formaldehyde (produced by lysine demethylases) is a product in the reaction of Mildronate and BBOX.[13] An initial scaffold (**21**) was envisaged as a potential new class of BBOX inhibitor (Figure 4). A 2OG mimic moiety identical to that in (**20**) linked to a trimethylamine moiety mimicking that of the quaternary amine of Mildronate/GBB was identified as a target. Amine (**20a**) is reported as a precursor towards the synthesis of Methylstat and it was envisaged that (**20a**) might also provide access to (**21**). First the reported procedure[12] for the synthesis of the amine (**20a**) was attempted towards the synthesis of (**21**) (Scheme 2). Thus, the commercially available amine (**22**), was reacted with benzoyl peroxide in CH_2Cl_2 and sodium carbonate buffer (pH = 10.5) to yield benzoyl protected carbamate (**23**). Benzoyl protection of (**22**) proceeded with a lower yield than reported (30% *vs* 75%[12]) (Scheme 1), largely due to the undesired formation of the *N*-Bz protected amine (**23a**). Acylation of (**23**) with ethyl fumaroyl chloride gave (**24**) in good yield (88%). Following the reported procedure, (**24**) was subjected to boc and benzoyl group deprotections in order to obtain amine (**24a**).[12] This method first employs a benzoyl deprotection using K_2CO_3 in methanol to give the free hydroxylamine, followed by a TFA

mediated deprotection to give the free amine. It was observed that K_2CO_3 mediated benzoyl deprotection of (**24**) was extremely fast (~5-10 mins) and led to side products as observed by LCMS. Thus, a modification of the literature protocol was employed whereby the benzoyl function was maintained whilst TFA mediated boc deprotection in CH_2Cl_2 was carried out to yield amine (**25**) in high yield (95%). Overall this modification allowed gave better yields and allowed the elimination of a step required to obtain (**21**) (5 *vs* 6 steps[12]), given both ester and benzoyl-protected hydroxylamine groups of (**26**) can be cleaved with mild aqueous hydroxide (Scheme 1). Thus, alkylation of (**25**) to give quaternary amine (**26**) with methyl iodide was followed by hydroxide mediated hydrolysis to give the target compound (**21**) in 74% yield from (**26**).

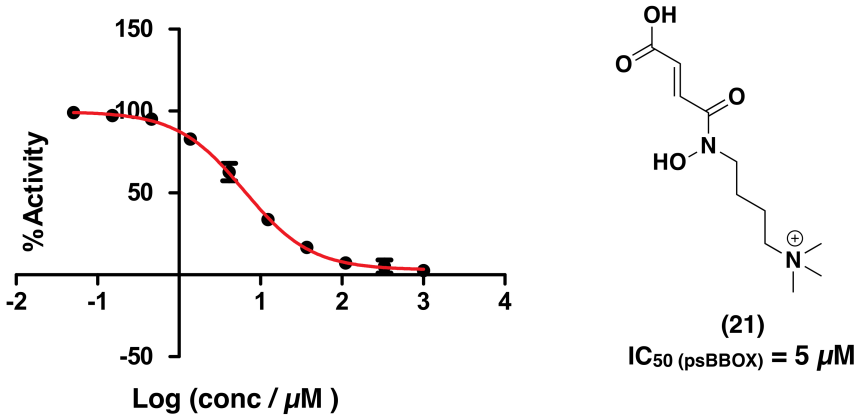
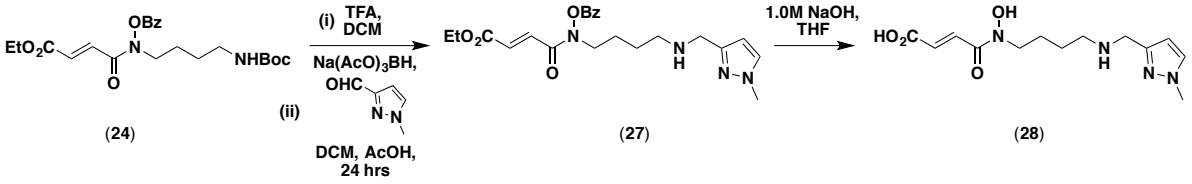


Figure 5 Curve used to obtain an IC_{50} value for the BBOX active site mimic (**21**). Raw data was obtained in triplicate, using the BBOX fluoride release assay, and the resulting data was analysed using Prism.

The IC_{50} of (**21**) (RL190B) was examined using the reported fluoride release assay[6] for hBBOX with a modification for psBBOX (1μM psBBOX vs. 400nM hBBOX). Given the high K_m values for co/substrates for psBBOX, a larger concentration of psBBOX was required to obtain adequate fluorescence sensitivity in order to obtain IC_{50} data. Recombinant human BBOX is significantly more difficult to produce (Chapter 3) and work

to obtain IC_{50} data for (**21**) against hBBOX is ongoing. The obtained IC_{50} value for psBBOX, 5 μM, indicated that (**21**) is a relatively potent inhibitor.

To investigate whether other moieties other than quaternary ammonium can be supported in the active site of BBOX, the active site mimic (**28**) was targeted (Scheme 2). Following a TFA-mediated Boc-group deprotection of (**24**) and a reductive amination using triacetoxy borohydride, (**27**) was then hydrolysed in aqueous hydroxide to give the target compound (**28**); assay work on (**28**) is ongoing. Should pyrazole (**28**) indicate suitable inhibitory activity against hBBOX, further active site mimics will be targeted. Although a

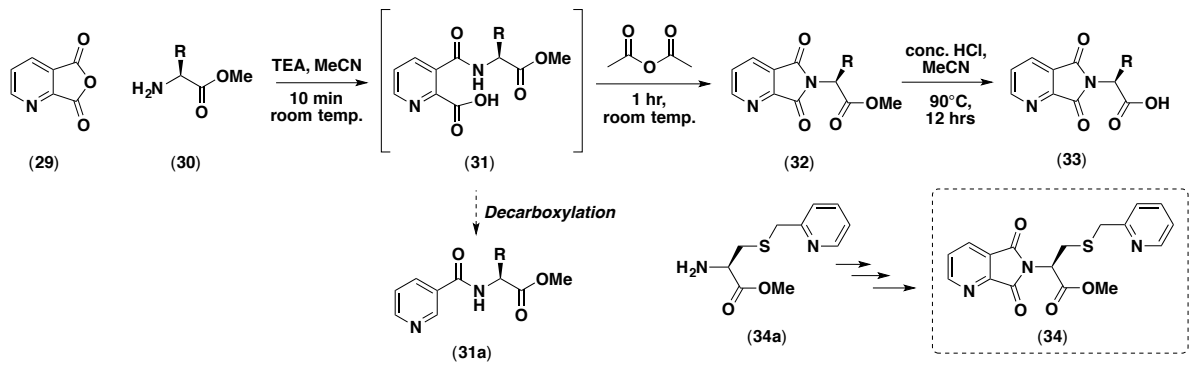


Scheme 2 Synthetic route followed to obtain active site mimic (**28**).

relatively low IC_{50} value for (**21**) was obtained (5 μM), given the NMR data presented in Chapter 3 for compound (**21**), it is likely that further exploration of active site mimetic compounds may prove to yield better inhibitors of hBBOX and psBBOX.

1.5 Pyrrolo pyridines

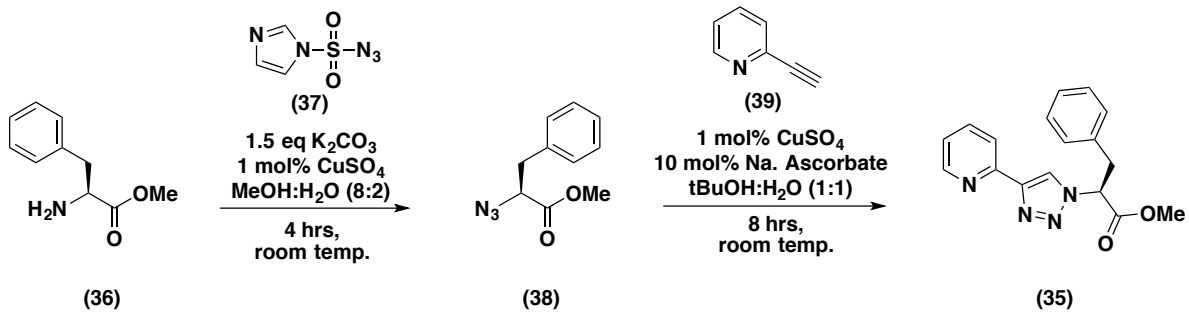
As a novel and alternate metal-chelating core to the 3-hydroxypyridine *e.g.* (**19**), pyrrolo pyridine analogues (**33**) were targeted (Scheme 3). It was envisaged that (**33**), may be able to create a more rigid inhibitor scaffold compared to (**19**). Initially, condensation of 2,3-



Scheme 3 Synthesis of amino acid-derived pyrrolo pyridines.

pyridine dicarboxylic anhydride (**29**) with amino acids in toluene, proved unsuccessful, probably due to the insolubility of (**29**). However, use of pyridine as a solvent enabled rapid production of the intermediate (**31**) in apparent quantitative yield as observed by LCMS. However, due to the issues of using hot pyridine other methods are preferable, and some alternatives were investigated. Heating in polar solvents enabled rapid dissolution of (**29**); however, heat and/or use of protic solvents promoted the pyridyl-nitrogen assisted decarboxylation to give the unwanted side product (**31a**). Nevertheless, it was found that use of acetonitrile and triethylamine, enabled rapid production of (**31**) at room temperature in quantitative yield. Following removal of volatiles, it was discovered that stirring crude acid (**31**) in acetic anhydride as solvent enabled rapid ring closure to obtain the pyrrolo pyridine (**32**). A number of substituted (**-R** (Scheme 3)) pyrrolo-pyridine esters, were synthesised and are disclosed in the experimental section. Synthesis of the free acid pyrrolo pyridines (**33**) can be obtained using concentrated HCl, and acetonitrile (Scheme 3). Notably, a pyrrolo pyridine analogous to (**19**) was successfully obtained following prior synthesis of amino acid (**34a**) according to the reported procedure.[2]

1.6 Triazolyl pyridines

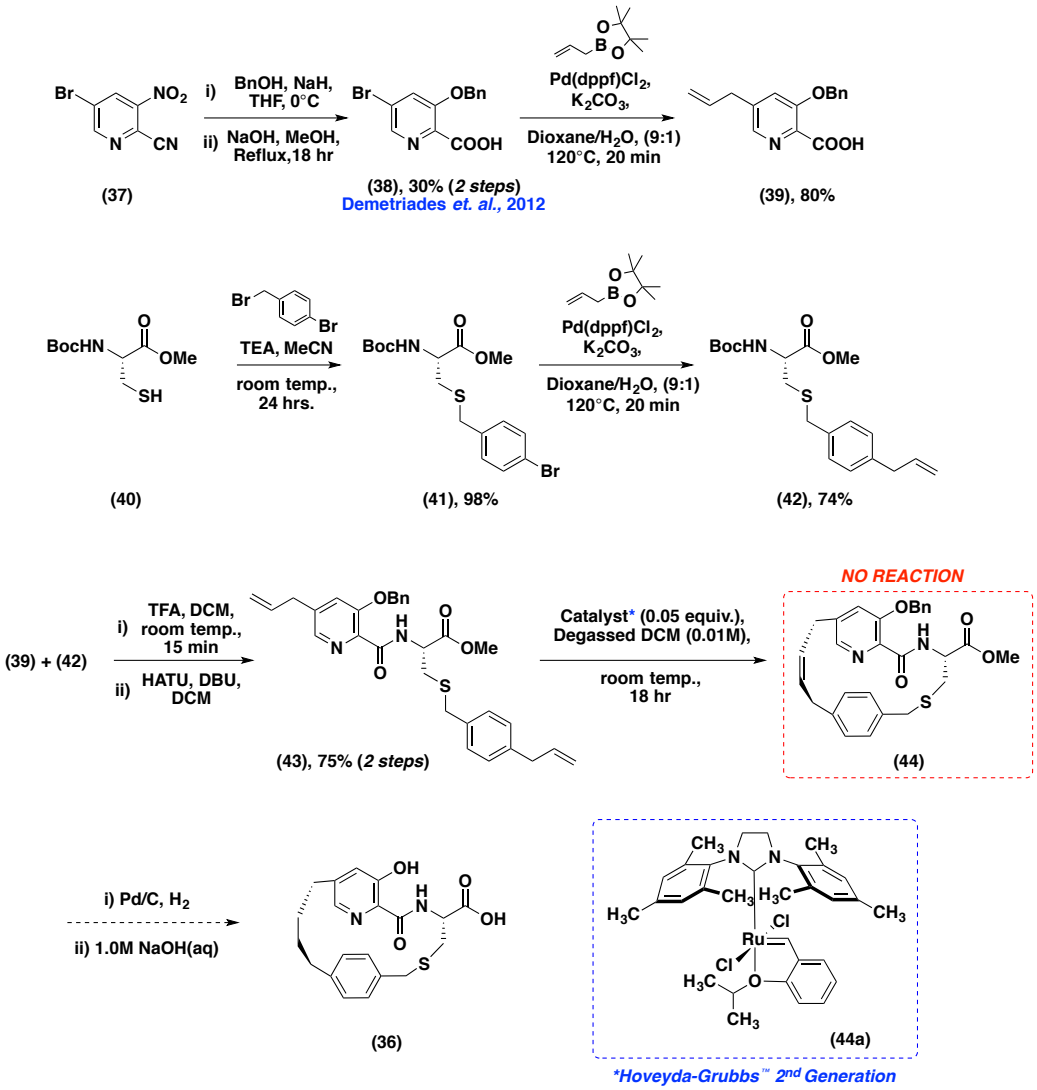


Scheme 4 Synthesis of triazolyl pyridines as alternate metal chelating BBOX inhibitors.

It was envisaged that triazolyl pyridine compounds such as (**35**), may provide improved metal chelation compared to the pyridine nitrogen/carbonyl oxygen chelation of 3-hydroxy pyridines such as (**19**). Thus, (**35**) was targeted for synthesis work. It was found that azide

(**38**) could be readily obtained *via* a diazo-transfer reaction involving L-phenylalanine methyl ester and diazo-transfer reagent (**37**), which was synthesised according to the reported procedure.[14] Pleasingly, triazole (**35**) could be rapidly obtained without purification of azide (**38**), *via* a copper-catalysed 'click' reaction. Given the rapid and efficient manner in which triazolyl pyridines can be obtained, synthetic work to obtain analogous scaffolds is currently being undertaken.

1.7 'Metathesis' compound



Scheme 5 Synthetic route used in an attempt to obtain potential cyclic BBOX inhibitor (44).

In other work carried out, attempts were made to make the cyclic compound (**36**) which had been identified as a potential BBOX inhibitor based on analysis of BBOX crystal structures

when complexed with the acyclic inhibitor AR692B (**19**) (Section 1.3, Figure 3 (**A**) and (**B**) *conformation II*). The planned synthetic route (Scheme 5) has not yet provided access to (**36**) due to apparent failure of the ring-closing metathesis (RCM) of compound (**43**). No ring-closing or cross-metathesis products were observed to form, and it is envisaged that the use of higher boiling, non-polar solvent, such as toluene, may allow access to higher reaction temperatures and thus enable formation of (**44**) *via* RCM. Compound (**38**) was successfully obtained using the reported procedure.[15] Preliminary experimental details are provided in this Appendix.

1.8 Summary

In this section, synthetic work towards a number of novel BBOX inhibitors scaffolds was described, and it is envisaged that the work disclosed here will direct future BBOX ligand design. Moreover, elucidation of the efficacy of these inhibitors against human BBOX *in vitro* is currently being undertaken and will hopefully aid in the discovery of potent BBOX inhibitors.

1.9 Experimental

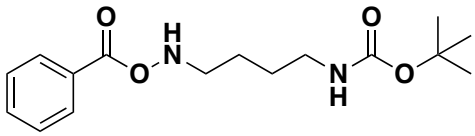
1.9.1 General remarks

IC_{50} data were obtained using the fluoride release assay[6] modified for psBBOX according to the reported procedure.[10] TBS-fluorescein (**14**) was provided by Dr. Anna Rydzik. GBBF (**13**) was synthesised according to the reported procedure.[6]

1.9.2 Synthesis

Materials and methods used for the synthesis of compounds described in this section are identical to those described in Chapter 2.

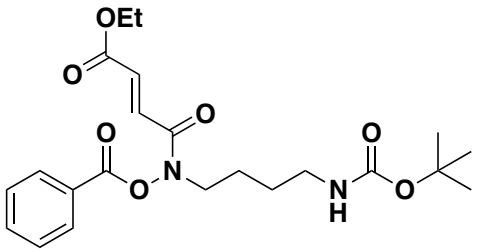
(23) ***Tert-butyl (4-((benzoyloxy)amino)butyl)carbamate***[12]



To a buffered (pH 10.5 $NaHCO_3$/NaOH) solution (10 ml) of *N*-boc-1,4-diaminobutane (0.94 g, 5.0 mmol) was added a solution of benzoyl peroxide (1.45 g, 6.0 mmol) in CH_2Cl_2 (20 ml). This mixture was then stirred for 2.5 hours at room temperature with monitoring by TLC (5:1, cyclohexane/EtOAc). The mixture was then separated and the aqueous layer extracted with CH_2Cl_2 (3 x 20 ml) before the organic fractions were washed with a 10% (aq) $Na_2S_2O_3$ solution, dried over Na_2SO_4, filtered and concentrated to dryness under *vacuo*. The resulting crude oil was purified using flash column chromatography (5:1, cyclohexane/EtOAc), after which a colourless oil was obtained (630 mg, 2.04 mmol, 40%). $\mathbf{R}_f$ 0.1 (5:1, cyclohexane/EtOAc). **^{1}H-NMR** ($CDCl_3$, 400 MHz) δ = **^{1}H NMR** ($CDCl_3$, 400 MHz) δ = 1.43 (9H, s, -^{t}Bu), 1.56 – 1.71 (4H, m, BocNHCH$_2$C*H*$_2$C*H*$_2$CH$_2$N-), 3.15 (4H, t, *J* = 6.5 Hz, BocNHC*H*$_2$CH$_2$CH$_2$C*H*$_2$N-), 4.62 (1H, br. t, *J* = 6.0 Hz, BocN*H*-), 7.43 – 7.48 (2H, m, *Ar*), 7.56 – 7.61 (1H, m, *Ar*), 8.01 (2H, dd, *J* = 8.5, 1.5 Hz, *Ar*) ppm. **^{13}C NMR**

($CDCl_3$, 101 MHz) δ = 24.6, 27.0, 27.7, 28.5, 40.4, 79.3, 128.4, 128.7, 129.5, 133.5, 156.1, 167.0 ppm. **FT-IR** ν_{max} (film) 3336, 2979, 2932, 1689, 1573, 1391, 1270, 1251, 1169, 709 cm^{-1}. **HRMS** (ESI-TOF) calcd for $C_{16}H_{25}N_2O_4$ $[M+H]^+$: 309.1809, found: 309.1811.

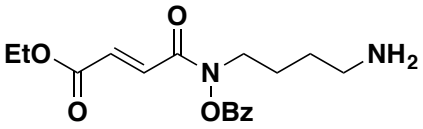
(24) *Ethyl (E)-4-((benzoyloxy)(4-((tert-butoxycarbonyl)amino)butyl)amino)-4-oxobut-2-enoate*



A solution of (**23**) (630 mg, 2.04 mmol) in CH_2Cl_2 (21 ml) was cooled using an ice bath, before triethylamine (0.6 ml, 4.08 mmol), DMAP (2 mg, 0.016 mmol) and ethylfumaroyl chloride (430 mg, 2.65 mmol) were sequentially added. The mixture was then allowed to warm to room temperature and after 2hrs the starting material was observed to be consumed by TLC (1:1, cyclohexane/EtOAc). Following addition of sat. (aq) NH_4Cl, the aqueous layer was extracted with EtOAc (3 x 20ml), the organic phase dried over anhydrous Na_2SO_4, filtered, concentrated and purified by flash column chromatography (10:1, cyclohexane: EtOAc), to give a yellow oil (777 mg, 1.79 mmol, 88%). $\mathbf{R}_f$ 0.55 (100% EtOAc). **^{1}H NMR** ($CDCl_3$, 400 MHz) δ = 1.29 (3H, t, *J* = 7.0 Hz, -$COCH_2CH_3$), 1.45 (9H, s, -^{t}Bu), 1.55 – 1.66 (3H, m, -$NCH_2CH_2CH_2CH_2NHBoc$), 1.69 – 1.79 (2H, m, -$NCH_2CH_2CH_2CH_2NHBoc$), 3.18 (2H, q, *J* = 6.5 Hz, -$NCH_2CH_2CH_2CH_2NHBoc$), 3.94 (2H, t, *J* = 7.0 Hz, -$NCH_2CH_2CH_2CH_2NHBoc$), 4.22 (2H, q, *J* = 7.0 Hz, -$COCH_2CH_3$), 4.60 (1H, br. s, BocN*H*-), 6.96 (1H, d, *J* = 15.5 Hz, -NCOC*H*=CHCO-),7.17 (1H, d, *J* = 15.5 Hz, -NCOCH=C*H*CO-), 7.56 (2H, t, *J* = 8.0 Hz, *Ar*), 7.70 – 7.76 (1H, m, *Ar*), 8.11 – 8.15 (2H, m, *Ar*) ppm. ^{13}C NMR (101 MHz, Chloroform-*d*) δ 14.2, 27.1, 27.5, 28.5, 61.4, 79.4, 129.0, 130.3, 131.1, 133.5, 134.9, 156.1, 160.1, 165.3, 171.5. **FT-IR** ν_{max} (film) 3369, 2977, 2934, 1768, 1716,

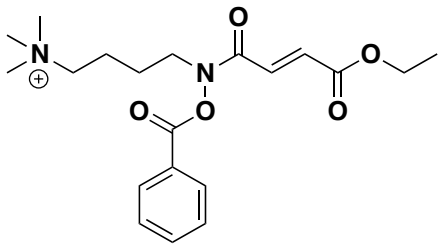
1668, 1517, 1301, 1240, 1174, 1035, 1006, 708 cm^{-1}. **HRMS** (ESI-TOF) calcd for $C_{22}H_{30}N_2O_7Na$ $[M+Na]^+$: 457.1945, found: 457.1939.

(25) *Ethyl (E)-4-((4-aminobutyl)(benzoyloxy)amino)-4-oxobut-2-enoate*



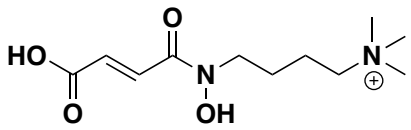
To a solution of (**24**) (2.05 g, 4.72 mmol) in CH_2Cl_2 (50 ml), was added trifluoroacetic acid (6.41 ml, 94.4 mmol) dropwise. The resulting mixture was allowed to stir at room temperature until complete consumption of the starting material was observed (TLC 100% EtOAc)(~ 50 mins). The reaction mixture was then dried under *vacuo* before distilled water (50 ml) and CH_2Cl_2 (50 ml) was added and the organic material extracted with CH_2Cl_2 (2 x 50 ml). The organic layers were combined, dried over Na_2SO_4 , filtered and concentrated to yield the desired amine (**25**) as a slightly yellow oil (1.50 g, 4.48 mmol, 95%) which was used without any further purification. **^{1}H NMR** ($CDCl_3$, 400 MHz) δ = 1.22 (3H, t, *J* = 7.0 Hz, -$COCH_2CH_3$), 1.71 – 1.89 (4H, m, -$NCH_2CH_2CH_2CH_2NH_2$), 3.00 – 3.15 (2H, m, -$NCH_2CH_2CH_2CH_2NH_2$), 3.91 (2H, t, *J* = 6.0 Hz, -$NCH_2CH_2CH_2CH_2NH_2$), 4.16 (2H, q, *J* = 7.0 Hz, -$COCH_2CH_3$), 6.84 (1H, d, *J* = 15.5 Hz, -NCOC*H*=CHCO-), 7.10 (1H, d, *J* = 15.5 Hz, -NCOCH=C*H*CO-), 7.49 – 7.56 (2H, m, *Ar*), 7.66 – 7.77 (3H, m, *Ar*), 8.04 – 8.10 (2H, m, *Ar*) ppm. **^{13}C NMR** (101 MHz, $CDCl_3$) δ = 13.9, 23.9, 24.4, 39.7, 53.4, 61.5, 125.6, 129.1, 130.2, 133.8, 135.1, 161.0, 161.3, 165.0 ppm. **FT-IR** ν_{max} (film) 2980, 1768, 1719, 1669, 1452, 1394, 1201, 1177, 1139, 710 cm^{-1}. **HRMS** (ESI-TOF) calcd for $C_{17}H_{22}N_2O_5$ $[M+H]^+$: 335.1602, found: 335.1601.

(26) *(E)-4-(N-(benzoyloxy)-4-ethoxy-4-oxobut-2-enamido)-N,N,N-trimethylbutan-1-aminium*



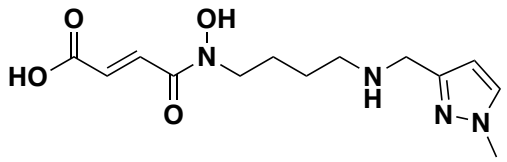
To a solution of (**25**) (1.50 g, 4.48 mmol) in dry acetonitrile (50 ml), methyliodide (1.76 ml, 28.3 mmol) and *N*,*N*-Diisopropylethylamine (4.21 ml, 23.6 mmol) were added. The reaction mixture was allowed to stir until complete consumption of the starting material was observed by LCMS. The reaction mixture was then concentrated, before distilled water (50 ml) and Et_2O (50 ml) were added. The aqueous phase was washed with Et_2O (5 x Et_2O) before being frozen in liquid nitrogen and lyophilised over 24hrs. The resulting crude mixture was purified by reverse-phase, flash column chromatography using a 50 g Biotage® SNAP Ultra C18 column (1:99 to 0:100 MeCN(+0.1% TFA) /H_2O(+0.1% TFA) with collection wavelength set to λ = 270 nm). Lyophilisation of the appropriate fractions gave quaternary amine (**26**) as a yellow oil (1.01 g, 2.69 mmol, 60%). **^{1}H NMR** (D_2O, 400 MHz) δ = 0.94 (3H, s, -$COCH_2CH_3$), 1.57 – 1.66 (2H, m, -$NCH_2CH_2CH_2CH_2NMe_3^+$), 1.69 – 1.78 (2H, m, -$NCH_2CH_2CH_2CH_2NMe_3^+$), 2.97 (9H, s, -NMe_3^+), 3.16 – 3.24 (2H, m, -$NCH_2CH_2CH_2CH_2NMe_3^+$), 3.76 – 3.94 (4H, m, -$COCH_2CH_3$, -$NCH_2CH_2CH_2CH_2NMe_3^+$), 6.60 (1H, d, *J* = 15.5 Hz, -NCOC*H*=CHCO-), 6.94 (1H, d, *J* = 15.5 Hz, -NCOCH=C*H*CO-), 7.38 (2H, t, *J* = 7.5 Hz, *Ar*), 7.57 (1H, t, *J* = 7.5 Hz, *Ar*), 7.90 (2H, d, *J* = 7.5 Hz, *Ar*) ppm. **^{13}C NMR** (101 MHz, D_2O) δ = 13.1, 19.6, 23.0, 47.7, 52.7, 62.0, 65.7, 129.1, 129.9, 130.3, 133.1, 135.4, 162.2, 162.5, 162.9 ppm. **FT-IR** ν_{max} (film) 2972, 1685, 1480, 1291, 1186, 1131, 720, 708 cm^{-1}. **HRMS** (ESI-TOF) calcd for $C_{20}H_{29}N_2O_5^+$ $[M]^+$: 377.2071, found: 377.2071.

(21) *(E)-4-(3-carboxy-N-hydroxyacrylamido)-N,N,N-trimethylbutan-1-aminium* (RL190B)



To a solution of (**26**) (500 mg, 1.33 mmol) in THF (13.3 ml) was added 1.0M $NaOH_{(aq)}$ (4.0 ml) and the resulting mixture was stirred at room temperature for 3 hours until complete removal of both benzoyl and ethyl ester moieties was observed by LCMS. The reaction mixture was concentrated under *vacuo*, before being lyophilised and purified by reverse phase flash column chromatography using a 50 g Biotage® SNAP Ultra C18 column (1:99 to 0:100 MeCN(+0.1% TFA) /H_2O(+0.1% TFA). Fractions containing the product were assessed by TLC and LCMS before being collected and lyophilised to yield the product as a pale yellow oil (293 mg, 1.12 mmol, 74%). **^{1}H NMR** (DMSO-d_6, 400 MHz) δ = 1.54 – 1.63 (2H, m, -$NCH_2CH_2CH_2CH_2NMe_3^+$), 1.63 – 1.74 (2H, m, -$NCH_2CH_2CH_2CH_2NMe_3^+$), 3.03 (9H, s, -NMe_3^+), 3.26 – 3.33 (2H, m, -$NCH_2CH_2CH_2CH_2NMe_3^+$), 3.64 (2H, t, *J* = 7.0 Hz, -$NCH_2CH_2CH_2CH_2NMe_3^+$), 6.56 (1H, d, *J* = 15.5 Hz, -NCOC*H*=CHCO-), 7.47 (1H, d, *J* = 15.5 Hz, -NCOCH=C*H*CO-). **^{13}C NMR** (101 MHz, DMSO-d_6) δ = 19.4, 23.1, 39.9, 46.9, 52.2, 64.9, 131.4, 132.7, 163.5, 166.4. **FT-IR** ν_{max} (film) 3437, 1659, 1436, 1407, 1311, 1020, 952, 932, 698, 668 cm^{-1}. **HRMS** (ESI-TOF) calcd for $C_{11}H_{21}N_2O_4^+$ $[M]^+$: 245.1496, found: 245.1496.

(28) (E)-4-(hydroxy(4-(((1-methyl-1H-pyrazol-3-yl)methyl)amino)butyl)amino)-4-oxobut-2-enoic acid

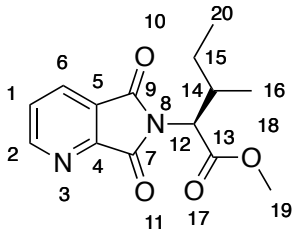


To a solution of amine (**25**) (307 mg, 0.92 mmol) in CH_2Cl_2 (9.2 ml) was added methyl-1*H*-pyrazole-5-carbaldehyde (109 mg, 1.10 mmol), $Na(AcO)_3BH$ (1.07 g, 5.07 mmol) and AcOH (105 µL, 1.84 mmol). The mixture was stirred at room temperature for 24 hrs before EtOH and 2N (aq) HCl were added. The mixture was then concentrated and purified using flash column chromatography (5:95, MeOH/CH_2Cl_2), after which a yellow oil was obtained. The crude oil (60 mg) was taken and dissolved in THF (1.4 ml) before 1.0 M (aq) NaOH (420 µL) was added and the mixture stirred overnight at room temperature. The reaction mixture was then neutralised with 1M (aq) HCl before being concentrated and purified by reverse-phase, flash column chromatography as described for compound (**21**), to give a pale yellow oil (35.5 mg, 0.12 mmol, 86%). **^{1}H NMR** (DMSO-d_6, 400 MHz) δ = 1.44 – 1.69 (4H, m, -$NCH_2CH_2CH_2CH_2NHCH_2$-), 2.74 (2H, t, J = 7.0 Hz, -$NCH_2CH_2CH_2CH_2NHCH_2$-), 3.59 (2H, t, J = 6.5 Hz, -$NCH_2CH_2CH_2CH_2NHCH_2$-), 3.80 (3H, s, -NCH_3), 3.97 (2H, s, -$NCH_2CH_2CH_2CH_2NHCH_2$-), 6.29 (1H, d, J = 2.0 Hz, *Ar*), 6.53 (1H, d, J = 15.5 Hz, HO_2CH=C*H*CON-), 7.28 – 7.35 (2H, m, HO_2CH=C*H*CON-, *Ar*) ppm. **^{13}C NMR** (DMSO-d_6, 101 MHz) δ = 23.7, 24.4, 36.3, 41.7, 47.0, 47.2, 106.6, 129.5, 135.8, 137.2, 137.4, 164.4, 168.5 ppm. **FT-IR** ν_{max} (film) 3345, 1754, 1423, 1415, 1298, 1055, 958, 925, 704, 658 cm^{-1}. **HRMS** (ESI-TOF) calcd for $C_{13}H_{21}N_4O_4$ $[M+H]^+$: 297.1563, found: 297.1561.

1.9.3 General Procedure for synthesis of pyrrolo pyridinyl series compounds

To a solution of the appropriate amino acid (1.0 equiv.), and 2,3 pyridine dicarboxylic anhydride (1.0 equiv.) in MeCN (0.3 M) was added TEA, dropwise. The mixture was then allowed to stir at room temperature until complete consumption of the starting material was observed by TLC (3:7, MeOH/CH_2Cl_2). Excess acetic anhydride was then added, and allowed to stir until complete comsumption of the starting material was observed by LCMS (~1 hr). The resulting mixture was concentrated to dryness before being purified *via* flash column chromatography. The appropriate fractions were then collected and solvents removed in *vacuo* to give the target compound.

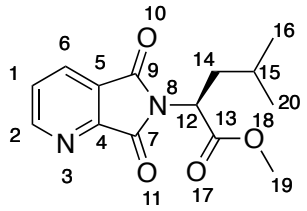
Methyl (2S,3S)-2-(5,7-dioxo-5,7-dihydro-6H-pyrrolo[3,4-b]pyridin-6-yl)-3-methylpentanoate



L-isoleucine methyl ester hydrochloride (100 mg, 0.55 mmol) and 2,3-pyridine dicarboxylic anhydride (82 mg, 0.55 mmol) were reacted with TEA (0.5 ml) in MeCN (3 ml) following the General Procedure. After 10 mins acetic anhydride was added (5 ml). After 1 hr, reaction solvents were removed and the residue was purified to give a clear oil (85 mg, 0.31 mmol, 56%). $\mathbf{R}_f$ 0.5 (100% EtOAc). **^{1}H-NMR** ($CDCl_3$, 400 MHz) δ = 0.87 (3H, t, *J* = 7.5 Hz, C(20)H_3), 1.02 - 1.10 (1H, m, C(15)H_A), 1.12 (3H, d, *J* = 6.5 Hz, C(16)H_3), 1.43 - 1.56 (m, 1H, C(15)H_B), 2.48 - 2.63 (1H, m, C(14)*H*), 3.71 (3H, s, C(19)H_3), 4.72 (1H, d, *J* = 8.0 Hz, C(12)*H*), 7.68 (1H, dd, *J* =7 .5, 5.0 Hz, C(1)*H*), 8.20 (1H, dd, *J* = 8.0, 1.5 Hz, C(6)*H*), 9.01 (1H, dd, *J* = 5.0 Hz, 1.5 Hz, C(2)*H*) ppm. **^{13}C-NMR** ($CDCl_3$, 101 MHz) δ = 10.9, 16.7, 25.7, 34.4, 52.4, 57.1, 126.9, 127.6, 131.4, 151.1, 155.5, 165.6, 165.6, 168.9 ppm. **FT-IR**

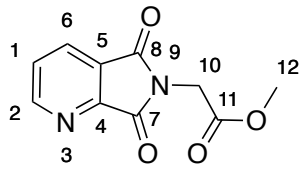
ν_{max} (film) 2967, 1720, 1595, 1376, 1079, 736 cm^{-1}. **HRMS** (ESI-TOF) calcd for $C_{14}H_{16}N_2O_4Na$ $[M+Na]^+$: 299.1002, found: 299.1003.

Methyl (S)-2-(5,7-dioxo-5,7-dihydro-6H-pyrrolo[3,4-b]pyridin-6-yl)-4-methylpentanoate



L-Leucine methyl ester hydrochloride (100 mg, 0.55 mmol) and 2,3-pyridine dicarboxylic anhydride (82 mg, 0.55 mmol) were reacted with TEA (0.5 ml) in MeCN (3 ml) according to the General Procedure. After 10mins acetic anhydride was added (5 ml). After 1 hr, reaction solvents were removed and the residue was purified to give a clear oil (93mg, 0.34 mmol, 61%); $\mathbf{R}_f$ 0.45 (100% EtOAc); **^{1}H-NMR** ($CDCl_3$, 400 MHz) δ = 0.79 (6 H, dd, *J* = 10.0, 6.5 Hz, C(16)H_3+C(20)H_3), 1.28 - 1.40 (1 H, m, C(15)*H*), 1.88 - 1.96 (1 H, m, C(14)H_A), 2.15 - 2.25 (1 H, m, C(14)H_B), 3.59 (3 H, s, C(19)H_3), 4.87 (1 H, dd, *J* = 11.5, 4.5 Hz, C(12)*H*), 7.52 (1 H, dd, *J* = 7.5, 5.0 Hz, C(1)*H*), 8.05 (1 H, dd, *J*=7.5, 1.5 Hz, C(6)*H*), 8.86 (1 H, dd, J = 5.0, 1.5 Hz, C(2)*H*) ppm. **^{13}C-NMR** ($CDCl_3$, 101 MHz) δ = 20.9, 23.1, 25.04, 37.1, 52.8, 126.8, 127.1, 127.6, 131.4, 151.3, 155.5, 165.6, 165.6 ppm. **HRMS** (ESI-TOF) calcd for $C_{14}H_{16}N_2O_4Na$ $[M+Na]^+$: 299.1002 found, 299.1004.

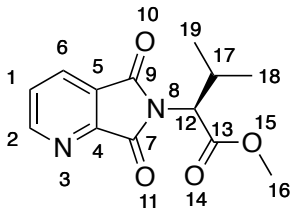
Methyl 2-(5,7-dioxo-5,7-dihydro-6H-pyrrolo[3,4-b]pyridin-6-yl)acetate



Glycine methyl ester hydrochloride (100 mg, 0.80 mmol) and 2,3-pyridine dicarboxylic anhydride (119 mg, 0.80 mmol) were reacted with TEA (0.5 ml) in MeCN (3 ml) according to the General Procedure. After 10 mins acetic anhydride was added (5 ml). After 1 hr, reaction solvents were removed and the residue was purified to give a clear oil (123 mg,

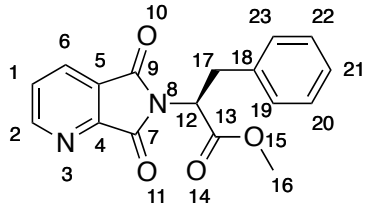
0.56 mmol, 70 %). $\mathbf{R}_f$ 0.55 (100% EtOAc). **^{1}H-NMR** ($CDCl_3$, 400 MHz) δ = 3.71 (3 H, s, C(12)H_3), 4.46 (2 H, s, C(10)H_2), 7.60 (1 H, dd, *J* = 7.5, 5.0 Hz, C(1)*H*), 8.15 (1 H, dd, *J* = 7.5, 1.5 Hz, C(6)*H*), 8.95 (1 H, dd, *J* = 5.0, 1.5 Hz, C(2)*H*) ppm. **^{13}C-NMR** ($CDCl_3$, 101 MHz) δ = 38.5, 52.5, 127.0, 127.1, 131.2, 151.4, 155.2, 164.9, 165.0, 166.9 ppm. **FT-IR** ν_{max} (film) 3001, 1751, 1717, 1597, 1216, 1082, 742 cm^{-1}. **HRMS** (ESI-TOF) calcd for $C_{10}H_8N_2O_4Na$ $[M+Na]^+$: 243.0376, found 243.0375.

Methyl (S)-2-(5,7-dioxo-5,7-dihydro-6H-pyrrolo[3,4-b]pyridin-6-yl)-3-methylbutanoate



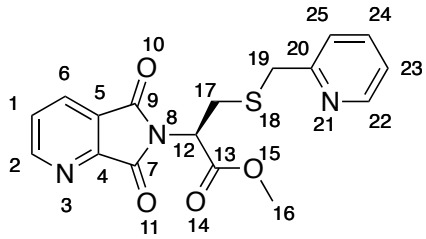
L-Valine methyl ester hydrochloride (100 mg, 0.60 mmol), 2,3-pyridine dicarboxylic anhydride (90 mg, 0.60 mmol) were reacted with TEA (0.5 ml) in MeCN (3 ml) according to the General Procedure. After 10mins acetic anhydride was added (5 ml). After 1 hr, reaction solvents were removed and the residue was purified to give a clear oil (84 mg, 0.32 mmol, 54%). $\mathbf{R}_f$ 0.65 (100% EtOAc). **^{1}H-NMR** ($CDCl_3$, 400 MHz) δ = 0.86 (3 H, d, *J* = 7.0 Hz, C(18)H_3), 1.09 (3 H, d, *J* = 7.0 Hz, C(19)H_3), 2.64 - 2.78 (1 H, m, C(17)*H*), 3.65 (s, 3 H, C(16)*H*), 4.58 (1 H, d, *J* = 8.0 Hz, C(12)*H*), 7.60 (1 H, dd, *J* = 7.5, 5.0 Hz, C(1)*H*), 8.13 (1 H, dd, *J* = 7.5, 1.5 Hz, C(6)*H*), 8.94 (1 H, dd, *J* = 5.0, 1.5 Hz, C(2)*H*) ppm. **^{13}C-NMR** ($CDCl_3$, 101 MHz) δ =19.4, 20.9, 28.6, 52.6, 57.8, 126.8, 127.3, 127.6, 131.5, 151.3, 155.6, 165.6, 165.7, 165.7, 168.9 ppm. **FT-IR** ν_{max} (film) 2987, 1720, 1378, 1075, 735 cm^{-1}. **HRMS** (ESI-TOF) calcd for $C_{13}H_{14}N_2O_4Na$ $[M+Na]^+$: 285.0846, found 285.0848.

Methyl (S)-2-(5,7-dioxo-5,7-dihydro-6H-pyrrolo[3,4-b]pyridin-6-yl)-3-phenylpropanoate



L-Phenylalanine methyl ester hydrochloride (100 mg, 0.61 mmol), 2,3-pyridine dicarboxylic anhydride (91 mg, 0.61 mmol), TEA (0.5 ml) and MeCN (3 ml). After 10 mins acetic anhydride was added (5 ml). After 1 hr, reaction solvents were removed and the residue was purified to give a yellow oil (114 mg, 0.37 mmol, 60%). $\mathbf{R}_f$ 0.50 (100% EtOAc). **^{1}H-NMR** ($CDCl_3$, 400 MHz) δ = 3.52 - 3.67 (2 H, m, C(17)H_2), 3.80 (3 H, s, C(16)H_3), 5.24 (1H, dd, J = 11.5, 5.5 Hz, C(12)H), 7.12 - 7.21 (5H, m, C(19)H + C(20)H + C(21)H + C(22)H + C(23)H), 7.59 (1 H, dd, J = 7.5, 5.0 Hz, C(1)H) 8.09 (1 H, d, J = 7.5 Hz, C(6)H), 8.94 (1 H, d, J = 4.0 Hz, C(2)H) ppm. **^{13}C-NMR** ($CDCl_3$, 101 MHz) δ = 34.5 , 53.1, 53.52, 126.9, 127.0, 127.6, 128.7, 128.8, 131.4, 136.4, 151.1, 155.5, 165.3, 165.4, 168.9 ppm. **FT-IR** ν_{max} (film) 2921, 1723, 1383, 733 cm^{-1}. **HRMS** (ESI-TOF) calcd for $C_{17}H_{14}N_2O_4Na$ $[M+Na]^+$: 333.0846, found 333.0848.

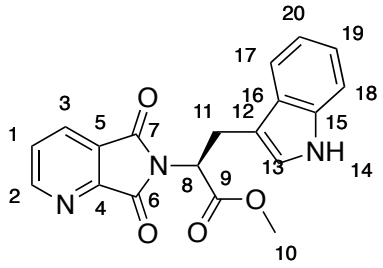
(34) *Methyl (R)-2-(5,7-dioxo-5,7-dihydro-6H-pyrrolo[3,4-b]pyridin-6-yl)-3-((pyridin-2-ylmethyl)thio)propanoate*



Methyl *S*-(pyridin-2-ylmethyl)-L-cysteinate (100 mg, 0.44mmol) and 2,3-pyridine dicarboxylic anhydride (100 mg, 0.44 mmol) were reacted with TEA (0.25 ml) in MeCN (3 ml) according to the General Procedure. After 10 mins acetic anhydride was added (5 ml). After 1 hr, reaction solvents were removed and the residue was purified to give a pale

orange oil (84 mg, 0.23 mmol, 54%). $\mathbf{R}_f$ 0.40 (100% EtOAc). **^{1}H-NMR** ($CDCl_3$, 400 MHz) δ = 3.28 - 3.38 (2 H, m, C(17)H_2), 3.76 (3 H, s, C(16)H_3), 3.75 - 3.79 (1 H, m, C(19)H_A), 3.92 (1 H, d, J = 13.5 Hz, C(19)H_B), 5.22 (1 H, dd, J =10.0, 5.5 Hz, C(12)*H*), 7.14 - 7.20 (1 H, m, C(24)*H*), 7.33 (1 H, d, J = 7.5 Hz, C(1)*H*), 7.63 - 7.69 (2 H, m, C(23)*H* + C(25)*H*), 8.20 (1 H, dd, J=7.5, 1.5 Hz, C(6)*H*), 8.49 - 8.53 (1 H, m, C(22)*H*), 9.02 (1 H, dd, J = 5.0, 1.5 Hz, C(2)*H*) ppm. **^{13}C-NMR** ($CDCl_3$, 101 MHz) δ = 29.0, 50.2, 52.1, 121.1, 122.1, 126.2, 126.5, 130.5, 135.9, 148.3, 150.4, 154.5, 156.7, 164.3, 164.4, 167.2 ppm. **FT-IR** ν_{max} (film) 2997, 1721, 1592, 1383, 1250, 1096, 731 cm^{-1}. **HRMS** (ESI-TOF) calcd for $C_{17}H_{15}N_3O_4SNa$ $[M+Na]^+$: 380.0675, found 380.0672.

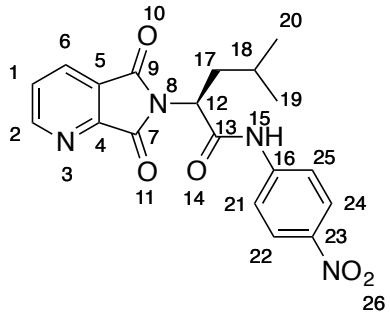
Methyl (S)-2-(5,7-dioxo-5,7-dihydro-6H-pyrrolo[3,4-b]pyridin-6-yl)-3-(1H-indol-3-yl)propanoate



L-Tryptophan methyl ester hydrochloride (100 mg, 0.39 mmol) and 2,3-pyridine dicarboxylic anhydride (58 mg, 0.39 mmol) were reacted with TEA (0.25 ml) in MeCN (3 ml) according to the General Procedure. After 10 mins acetic anhydride was added (5 ml). After 1 hr, reaction solvents were removed and the residue was purified to give a pale yellow oil (45 mg, 0.18 mmol, 45%. $\mathbf{R}_f$ 0.50 (100% EtOAc). **^{1}H-NMR** ($CDCl_3$, 400 MHz) δ = 3.72 - 3.88 (2 H, m, C(11)H_2), 3.84 (3 H, s, C(10)H_3), 5.38 (1 H, dd, J = 11.0, 5.0 Hz, C(8)*H*), 6.99 - 7.07 (2 H, m, C(19)*H* + C(20)*H*), 7.11 (1 H, s, C(13)*H*), 7.25 (1 H, d, J = 7.5 Hz, C(18)*H*), 7.48 - 7.55 (1 H, m, C(17)*H*), 7.58 (1 H, d, J = 7.5 Hz, C(1)*H*), 7.96 - 8.05 (1 H, m, C(3)*H*), 8.20 (1 H, br. s., N*H*), 8.89 (1 H, m, C(2)*H*) ppm. **^{13}C-NMR** ($CDCl_3$, 101 MHz) δ = 24.6, 52.9, 53.0, 110.5, 111.1, 118.3, 119.4, 122.0, 122.7, 126.8, 126.9, 127.3,

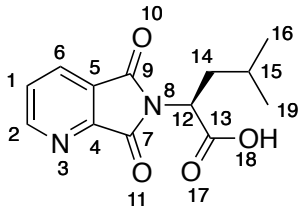
131.2, 136.0, 151.0, 155.1, 165.3, 165.5, 169.2 ppm. **FT-IR** ν_{max} (film) 3045, 1719, 1602, 1382, 1233, 1010, 727 cm^{-1}. **HRMS** (ESI-TOF) calcd for $C_{19}H_{15}N_3O_4Na$ $[M+Na]^+$: 372.0955, found 372.0956.

(S)-2-(5,7-Dioxo-5,7-dihydro-6H-pyrrolo[3,4-b]pyridin-6-yl)-4-methyl-N-(4-nitrophenyl)pentanamide



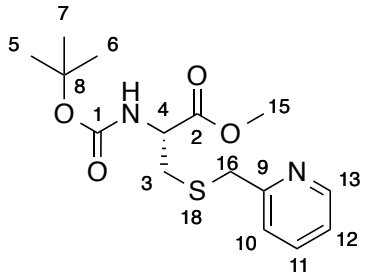
L-Leucine-4-nitroanilide (100 mg, 0.40 mmol), 2,3-pyridine dicarboxylic anhydride (60 mg, 0.40 mmol), TEA (0.25 ml) and MeCN (3 ml). After 10 mins acetic anhydride was added (5 ml). After 1 hr, reaction solvents were removed and the residue was purified to give a yellow oil (85 mg, 0.22 mmol, 56%). $\mathbf{R}_f$ 0.70 (100% EtOAc). **^{1}H-NMR** ($CDCl_3$, 400 MHz) δ = 0.95 (6 H, t, *J* = 7.0 Hz, C(19)H_3 + C(20)H_3), 1.46 - 1.57 (1 H, m, C(18)*H*), 1.98 - 2.09 (1 H, m, C(17)H_A), 2.39 - 2.50 (1 H, m, C(17)H_B), 5.17 (dd, *J* = 11.0, 5.5 Hz, 1 H, C(12)*H*), 7.66 (1 H, dd, *J* = 7.5, 5.0 Hz, C(1)*H*), 7.72 (2 H, d, *J* = 9.0 Hz, C(21)*H* + C(25)*H*), 8.13 (2 H, d, *J* = 9.0 Hz, C(22)*H* + C(24)*H*), 8.19 (1 H, dd, *J* = 7.5, 1.5 Hz, C(6)*H*), 8.95 (1 H, dd, *J* = 5.0, 1.5 Hz, C(2)*H*), 9.02 (1 H, s, N*H*) ppm. **^{13}C-NMR** ($CDCl_3$, 101 MHz) δ = 21.2, 23.0, 25.3, 37.6, 54.7, 119.6, 125.0, 127.0, 128.1, 131.9, 143.5, 143.7, 150.9, 155.8, 165.9, 166.8, 167.7 ppm. **FT-IR** ν_{max} (film) 3420, 2997, 1721, 1596, 1507, 1340, 725 cm^{-1}. **HRMS** (ESI-TOF) calcd for $C_{19}H_{18}N_4O_5Na$ $[M+Na]^+$: 405.1175 found 405.1176.

(S)-2-(5,7-Dioxo-5,7-dihydro-6H-pyrrolo[3,4-b]pyridin-6-yl)-4-methylpentanoic acid



Methyl (*S*)-2-(5,7-dioxo-5,7-dihydro-6H-pyrrolo[3,4-b]pyridin-6-yl)-4-methylpentanoate (50 mg, 0.18 mmol) was dissolved in MeCN (3 ml), distilled water (1 ml) and conc. HCl (0.5 ml). The mixture was then stirred overnight at 90°C. After removal of volatiles the crude material was purified *via* flash column chromatography (1:5:94, AcOH/MeOH/CH_2Cl_2) to give a pale yellow oil (29 mg, 0.11 mmol, 60%). $\mathbf{R}_f$ 0.05 (1:9, MeOH/CH_2Cl_2). **^{1}H-NMR** ($CDCl_3$, 400 MHz) δ = 0.94 (6 H, dd, *J* = 8.5, 6.5 Hz, C(16)H_3+C(19)H_3), 1.42 - 1.56 (1 H, m, C(15)*H*), 1.94 - 2.04 (1 H, m, C(14)H_A), 2.39 (1 H, m, C(14)H_B), 5.06 (1 H, dd, *J* = 11.5, 4.5 Hz, C(12)*H*), 7.67 (1 H, dd, *J* = 7.5, 5.0 Hz, C(1)*H*), 8.21 (1 H, dd, *J* = 7.5, 1.5 Hz, C(6)*H*), 9.03 (1 H, dd, *J* = 5.0, 1.5 Hz, C(2)*H*), 10.78 (1 H, br. s, O*H*) ppm. **^{13}C-NMR** ($CDCl_3$, 101 MHz) δ = 20.5, 20.6, 24.8, 36.6, 50.5, 126.8, 127.4, 131.4, 150.7, 155.0, 165.1, 165.2, 177.4 ppm. **FT-IT** ν_{max} (film) 2960, 1722, 1383, 733 cm^{-1}. **HRMS** (ESI-TOF) calcd for $C_{13}H_{14}N_2O_4Na$ $[M+Na]^+$: 285.0851, found 285.0852.

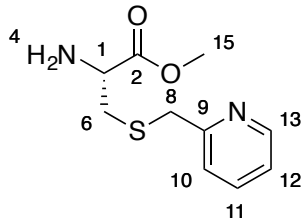
Methyl N-(tert-butoxycarbonyl)-S-(pyridin-2-ylmethyl)-L-cysteinate[2]



To a solution of boc-L-cysteine methyl ester (290 mg, 1.2 mmol) in MeCN (15 ml) was added 2-(bromomethyl)pyridine hydrobomide (340 mg, 1.3 mmol) and TEA (0.36 ml, 2.6 mmol). The solution was stirred at room temperature overnight under an atmosphere of N_2. The reaction solvent was then dried under *vacuo* and the resulting solid purified using flash

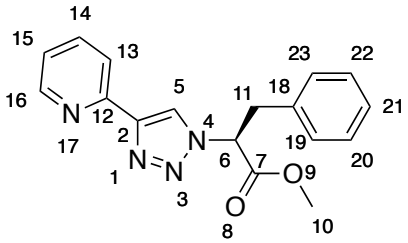
column chromatography (3:1, cyclohexane/EtOAc). The product was obtained as a pink oil (272 mg, 1.04 mmol, 80%). $\mathbf{R}_f$ 0.50 (1:1, cyclohexane/EtOAc,). ^{1}H-NMR ($CDCl_3$, 400 MHz) δ = 1.41 (9H, s, C(5)H_3 + C(6)H_3 + C(7)H_3), 2.84 (2H, s, C(16)H_2), 2.85 - 3.01 (2H, m, C(3)H_2), 3.68 (3H, s, C(15)H_3), 4.39 - 4.48 (1H, m, C(4)*H*), 6.62 - 6.71 (1 H, br s., N*H*), 7.23 - 7.28 (1 H, m, C(12)*H*), 7.43 (1 H, d, *J* = 8.0 Hz, C(10)*H*), 7.76 (1H, td, *J* = 7.0, J = 2.0 Hz, C(11)*H*), 8.49 - 8.53 (1 H, m, C(13)*H*) ppm. **^{13}C-NMR** ($CDCl_3$, 101 MHz) δ = 28.6, 48.1, 52.5, 56.5, 61.9, 92.6, 123.0, 124.0, 137.8, 139.0, 158.2, 205.5, 205.7 ppm. **FT-IR** ν_{max} (film) 3329, 2977, 1745, 1711, 1508, 1215, 1165 cm^{-1}. **HRMS** (ESI-TOF) calcd for $C_{15}H_{22}N_2O_4SNa$ $[M+Na]^+$: 349.1192, found: 349.1195.

(34a) *Methyl S-(pyridin-2-ylmethyl)-L-cysteinate*[2]



To a solution of methyl *N*-(tert-butoxycarbonyl)-*S*-(pyridin-2-ylmethyl)-L-cysteinate (272 mg, 1.04 mmol) in CH_2Cl_2 (6 ml) was added TFA (1.2 ml, 16.2 mmol) and stirred for 30 minutes at room temperature. The solvents were then removed in vacuo and the product was isolated as a colourless oil (223mg, 0.99mmol, 95%). $\mathbf{R}_f$ 0.05 (1:1, cyclohexane/EtOAc). **^{1}H-NMR** (D_2O, 400 MHz) δ = 2.93 - 3.13 (2 H, m, C(6)H_2), 3.72 (3 H, s, C(15)H_3), 4.13 (2 H, s, C(8)H_2), 4.29 - 4.34 (1 H, m, N*H*), 7.88 (1 H, t, *J* = 6.5 Hz, C(12)*H*), 7.96 (1 H, d, *J* = 8.0 Hz, C(10)*H*), 8.47 (1 H, t, *J* = 8.0 Hz, C(11)*H*), 8.64 (1 H, d, *J* = 6.0 Hz, C(13)*H*). **^{13}C-NMR** (D_2O, 101 MHz) δ = 31.1, 32.6, 52.2, 54.2, 126.3, 128.0, 127.9, 142.1, 147.7, 169.0 ppm. **FT-IR** ν_{max} (film) 2962, 1752, 1669, 1139 cm^{-1}. **LRMS** (ESI^+, *m/z*) calcd for $C_{10}H_{14}N_2O_2S$ $[M+H]^+$ 226.3 found $[M+H]^+$ 227.3.

(35) *Methyl (S)-3-phenyl-2-(4-(pyridin-2-yl)-1H-1,2,3-triazol-1-yl)propanoate*

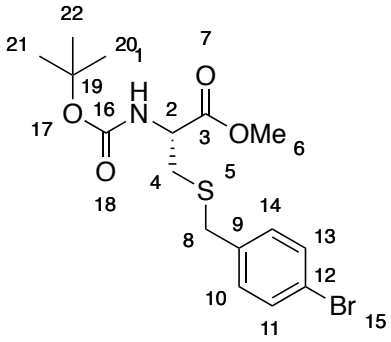


To a solution of L-phenylalanine methyl ester hydrochloride (200 mg, 0.9 mmol) in MeOH (4.7 ml) was added K_2CO_3 (347 mg, 2.5 mmol) and the resulting suspension stirred until dissolution of the starting material was observed. 1M (aq)$CuSO_4$ (50 µL) and 1*H*-imidazole-1-sulfonyl azide hydrochloride[16] (233 mg, 1.2 mmol) were then added to the reaction mixture and stirred overnight at room temperature. The reaction was then neutralised using 1M (aq) HCl, before the organic materials were extracted using EtOAc (3 x 5 ml), dried over Na_2SO_4, filtered and concentrated to dryness. Azide (**38**) was obtained as a crude yellow oil, which was used immediately without further purification.

To a solution of crude methyl 2-azido-3-phenylpropanoate (**38**) (20 mg, 0.1 mmol), in a 1:1 mixture of H_2O/*t*-BuOH (5 ml), was added 2-ethynyl pyridine (10 mg, 0.1 mmol), di-sodium *L*-ascrobate (20 mg, 0.1 mmol), and 1M (aq) $CuSO_4$ (50 µL). The reaction mixture was stirred overnight before being neutralised with 1M (aq) HCl, extracted with EtOAc (3 x 5 ml) and purified *via* flash column chromatography (0-100% EtOAc in cyclohexane over 10 CV's). The appropriate fractions were collected and dried to yield (**35**) as yellow oil. (10mg, 0.03mmol, 30%). **^{1}H-NMR** ($CDCl_3$, 500 MHz) δ = 3.49 - 3.55 (1 H, m, C(11)H_A), 3.59 - 3.64 (1 H, m, C(11)H_B), 3.77 (3 H, s, C(10)), 5.63 (1 H, dd, *J* = 9.0, 6.0 Hz, C(6)*H*), 7.09 - 7.13 (2 H, m, C(19)*H* + C(23)*H*), 7.21 - 7.26 (3 H, m, C(20)*H* + C(21)*H* + C(22)*H*), 7.78 (1 H, td, *J* = 8.0, 2.0 Hz, C(15)*H*), 8.16 (1 H, d, *J* = 8.0 Hz, C(14)*H*), 8.29 (s, 1 H, C(5)*H*), 8.52 - 8.64 (m, 1 H, C(16)*H*) ppm. **^{13}C-NMR** ($CDCl_3$, 126 MHz) δ = 38.7, 53.1, 64.3, 120.3, 121.9, 122.9, 127.5, 128.8, 134.7, 136.9, 148.2, 149.4, 150.0, 168.5 ppm. **FT-**

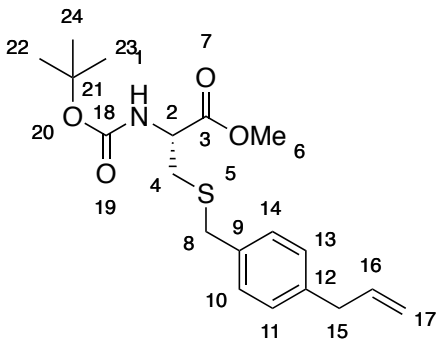
IR ν_{max} (film) 2869, 1752, 1745, 1165, 736 cm^{-1}. **LRMS** (ESI^+, *m/z*) calcd for $C_{17}H_{16}N_4O_2$ $[M]^+$ 308.1, found $[M+H]^+$ 309.1.

Methyl S-(4-bromobenzyl)-N-(tert-butoxycarbonyl)-L-cysteinate (41)



To a solution of boc-L-cysteine methyl ester (1.0 g, 4.2 mmol) and 4-bromobenzyl bromide (1.3 g, 5.1 mmol) in MeCN (14 ml) was added triethylamine (1.34 ml). The mixture was placed under N_2 and left to stir at room temperature under overnight. The reaction was then concentrated and purified *via* flash column chromatography (2-100% EtOAc in cyclohexane over 10 CVs). The appropriate fractions were collected and dried to give a colourless oil (1.68 g, 4.1 mmol, 99%). **^{1}H NMR** ($CDCl_3$, 400 MHz) δ = 1.45 (9H, s, C(21-22)*H*), 2.73 – 2.90 (2H, m, (4)), 3.67 (2H, s, (8)), 3.75 (3H, s, C(6)H_3), 4.49 – 4.58 (1H, m, C(2)*H*), 5.28 (1H, d, *J* = 8.0 Hz, N(1)*H*), 7.18 (2H, d, *J* = 8.5 Hz, C(10)*H*+C(14)*H*), 7.43 (2H, d, *J* = 8.5 Hz, C(11)*H* +C(12)*H*) ppm. **^{13}C NMR** ($CDCl_3$, 101 MHz) δ = 28.5, 33.8, 36.4, 52.7, 53.3, 80.3, 121.4, 125.6, 128.7, 134.7, 150.3, 171.8 ppm. **LRMS** (ESI^+, *m/z*) calcd for $C_{16}H_{22}BrNO_4S$ $[M+H]^+$ 404.1, found $[M+H]^+$ 404.1.

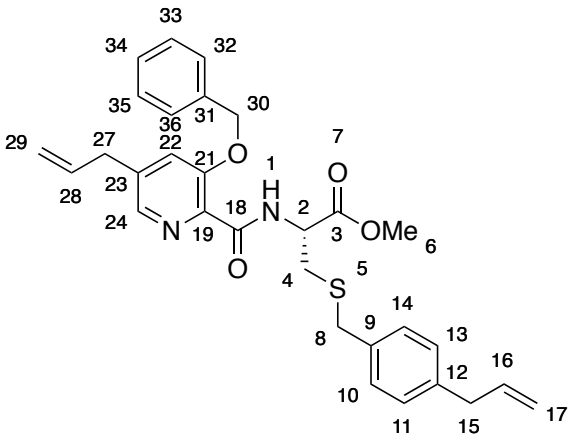
Methyl S-(4-allylbenzyl)-N-(tert-butoxycarbonyl)-L-cysteinate (42)



(**41**) (200 mg, 0.50 mmol), Pd(dppf)Cl_2 (25.4 mg, 0.035 mmol), K_2CO_3 (207 mg, 1.50 mmol), allylboronic acid pinacol ester (168 mg, 1.00 mmol) were dissolved in a mixture of Dioxane/H_2O (9:1, 1.25 ml). The resulting mixture was stirred in a microwave reactor and heated to 120°C for 20 minutes. The reaction was cooled to room temperature before being extracted with EtOAc (3 x 3 ml). The organic fractions were collected, dried over $MgSO_4$, filtered and concentrated before being purified *via* flash column chromatography (0-100% EtOAC in cylcohexane over 12 CVs). The appropriate fractions were collected and dried to give a pale yellow oil. (134 mg, 0.37 mmol, 74%)

^{1}H NMR ($CDCl_3$, 400 MHz) δ = 1.38 (9H, s, C(22-24)*H*), 2.69 – 2.88 (2H, m, C(4)*H*), 3.32 (2H, d, *J* = 6.5 Hz, C(15)*H*), 3.65 (2H, s, C(7)*H*), 3.70 (3H, s, C(6)H_3), 4.45 – 4.53 (1H, m, C(2)*H*), 4.99 – 5.06 (2H, m, C(17)H_2), 5.21 – 5.30 (1H, m, N(1)*H*), 5.85 – 5.98 (1H, m, C(16)*H*), 7.09 (2H, d, *J* = 8.0 Hz, C(9)*H*+C(14)*H*), 7.18 (2H, d, *J* = 8.0 Hz, C(11)*H*+C(13)*H*) ppm. **^{13}C NMR** ($CDCl_3$, 101 MHz) δ 28.4, 33.7, 36.4, 40.0, 52.66, 53.2, 80.3, 116.0, 128.9, 129.1, 135.4, 137.40, 139.2, 155.3, 171.7 ppm. **LRMS** (ESI^+, *m/z*) calcd for $C_{19}H_{27}NO_4SNa$ $[M+Na]^+$ 388.1, found $[M+Na]^+$ 388.1.

Methyl N-(5-allyl-3-(benzyloxy)picolinoyl)-S-(4-allylbenzyl)-L-cysteinate (43)



To a solution of (**42**) (120 mg, 0.33 mmol) in CH_2Cl_2 (2 ml) was added TFA (224 µL, 3.30 mmol) and the resulting mixture was stirred at room temperature for 15 minutes before the reaction was concentrated under *vacuo*. H_2O (2 ml) was then added followed by CH_2Cl_2 (4

ml). The organic material was collected, dried over $MgSO_4$ and concentrated to give a yellow oil which was then dissolved in CH_2Cl_2 (2 ml). HATU (247 mg, 0.65 mmol), (**39**) (89 mg, 0.33 mmol) and DBU (107 μL, 0.72 mmol) were then added before the reaction was stirred at room temperature until complete consumption of the starting material was observed by TLC (1:9, MeOH/CH_2Cl_2). The reaction was then concentrated to dryness before being purified by flash column chromatography (0-100% EtOAc in cyclohexane over 10 CVs). The appropriate fractions were collected and dried to give a yellow oil (127 mg, 0.25 mmol, 75% over two steps). **^{1}H NMR** ($CDCl_3$, 400 MHz) δ = 2.88 (1H, dd, *J* = 14.0, 5.0 Hz, C(4)H_A), 2.97 (1H, dd, *J* = 14.0, 5.0 Hz, C(4)H_B), 3.31 (2H, d, *J* = 6.5 Hz, C(15)H_2), 3.37 (2H, d, *J* = 6.5 Hz, C(27)H_2), 3.68 (2H, s, C(8)H_2), 3.71 (3H, s, C(6)H_3), 4.99 – 5.14 (5H, m, C(2)*H*+C(17)H_2+C(29) H_2), 5.22 (2H, s, C(30)H_2), 5.79 – 5.98 (2H, m, C(16)*H*, C(28)*H*), 7.04 – 7.09 (2H, m, C(10)*H*+ C(14)*H*), 7.16 – 7.21 (3H, m, C(11)*H*+C(13)*H*+C(34)*H*), 7.25 – 7.51 (6H, m, C(22)*H*+ C(32)*H*+C(33)*H*+C(35)*H*+C(36)*H*), 8.10 (1H, d, *J* = 1.5 Hz, C(24)*H*) ppm. **^{13}C NMR** ($CDCl_3$, 101 MHz) δ = 33.4, 36.3, 37.0, 39.9, 52.1, 52.6, 71.1, 127.4, 128.2, 128.8, 129.1, 129.6, 135.2, 135.5, 135.8, 136.6, 137.4, 139.0, 140.0, 141.4, 155.0, 163.7, 16, 171.4 ppm. **LRMS** (ESI^+, *m/z*) calcd for $C_{30}H_{33}N_2O_4S$ $[M+H]^+$ 517.2, found $[M+H]^+$ 517.2.

1.10 References

1. M. Dambrova, E. Liepinsh and I. Kalvinsh, Mildronate: cardioprotective action through carnitine-lowering effect, *Trends Cardiovasc. Med.*, 2002, **12**, 275-279.
2. A. M. Rydzik, R. Chowdhury, G. T. Kochan, S. T. Williams, M. A. McDonough, A. Kawamura and C. J. Schofield, Modulating carnitine levels by targeting its biosynthesis pathway - selective inhibition of gamma-butyrobetaine hydroxylase, *Chem. Sci.*, 2014, **5**, 1765-1771.
3. H. K. Greenblatt and D. J. Greenblatt, Meldonium (Mildronate): A Performance-Enhancing Drug?, *Clin. Pharm. Drug Dev.*, 2016, **5**, 167-169.

4. W. Schobersberger, T. Dunnwald, G. Gmeiner and C. Blank, Story behind meldonium-from pharmacology to performance enhancement: a narrative review, *Br. J. Sports Med.*, 2017, **51**, 22-25.

5. K. Tars, J. Rumnieks, A. Zeltins, A. Kazaks, S. Kotelovica, A. Leonciks, J. Sharipo, A. Viksna, J. Kuka, E. Liepinsh and M. Dambrova, Crystal structure of human gamma-butyrobetaine hydroxylase, *Biochem. Biophys. Res. Commun.*, 2010, **398**, 634-639.

6. A. M. Rydzik, I. K. Leung, G. T. Kochan, A. Thalhammer, U. Oppermann, T. D. Claridge and C. J. Schofield, Development and application of a fluoride-detection-based fluorescence assay for gamma-butyrobetaine hydroxylase, *Chem. Bio. Chem*, 2012, **13**, 1559-1563.

7. K. Tars, J. Leitans, A. Kazaks, D. Zelencova, E. Liepinsh, J. Kuka, M. Makrecka, D. Lola, V. Andrianovs, D. Gustina, S. Grinberga, E. Liepinsh, I. Kalvinsh, M. Dambrova, E. Loza and O. Pugovics, Targeting Carnitine Biosynthesis: Discovery of New Inhibitors against gamma-Butyrobetaine Hydroxylase, *J. Med. Chem.*, 2014, **57**, 2213-2236.

8. R. Vilskersts, J. Kuka, E. Liepinsh, M. Makrecka-Kuka, K. Volska, E. Makarova, E. Sevostjanovs, H. Cirule, S. Grinberga and M. Dambrova, Methyl-gamma-butyrobetaine decreases levels of acylcarnitines and attenuates the development of atherosclerosis, *Vascul. Pharmacol.*, 2015, **72**, 101-107.

9. S. F. Ng, H. M. Hanauskeabel and S. Englard, Cosubstrate Binding-Site of Pseudomonas Sp Ak1 Gamma-Butyrobetaine Hydroxylase - Interactions with Structural Analogs of Alpha-Ketoglutarate, *J. Biol. Chem.*, 1991, **266**, 1526-1533.

10. A. Khan, R. K. Lesniak, J. Brem, A. M. Rydzik, H. Choi, I. K. H. Leung, M. A. McDonough, C. J. Schofield and T. D. W. Claridge, Development and application of ligand-based NMR screening assays for gamma-butyrobetaine hydroxylase, *Med. Chem. Comm*, 2016, **7**, 873-880.

11. A. M. Rydzik, J. Brem, W. B. Struwe, G. T. Kochan, J. L. Benesch and C. J. Schofield, Ejection of structural zinc leads to inhibition of gamma-butyrobetaine hydroxylase, *Bioorg. Med. Chem. Lett.*, 2014, **24**, 4954-4957.

12. X. L. Luo, Y. X. Liu, S. Kubicek, J. Myllyharju, A. Tumber, S. Ng, K. H. Che, J. Podoll, T. D. Heightman, U. Oppermann, S. L. Schreiber and X. Wang, A Selective Inhibitor and Probe of the Cellular Functions of Jumonji C Domain-Containing Histone Demethylases, *J. Am. Chem. Soc.*, 2011, **133**, 9451-9456.

13. L. Henry, I. K. Leung, T. D. Claridge and C. J. Schofield, gamma-Butyrobetaine hydroxylase catalyses a Stevens type rearrangement, *Bioorg. Med. Chem. Lett.*, 2012, **22**, 4975-4978.
14. E. D. Goddard-Borger and R. V. Stick, An efficient, inexpensive, and shelf-stable diazotransfer reagent: Imidazole-1-sulfonyl azide hydrochloride, *Org. Lett.*, 2007, **9**, 3797-3800.
15. M. Demetriades, I. K. H. Leung, R. Chowdhury, M. C. Chan, M. A. McDonough, K. K. Yeoh, Y. M. Tian, T. D. W. Claridge, P. J. Ratcliffe, E. C. Y. Woon and C. J. Schofield, Dynamic Combinatorial Chemistry Employing Boronic Acids/Boronate Esters Leads to Potent Oxygenase Inhibitors, *Angew. Chem. Int. Ed.*, 2012, **51**, 6672-6675.
16. T. Wang, D. Y. W. Ng, Y. Z. Wu, J. Thomas, T. TamTran and T. Weil, Bis-sulfide bioconjugates for glutathione triggered tumor responsive drug release, *Chem. Commun.*, 2014, **50**, 1116-1118.